Cosmology with CMB and Large Scale Structure

Yin-Zhe Ma

Institute of Astronomy and Kavli Institute for Cosmology,
Trinity College

University of Cambridge

A thesis submitted for the degree of

Doctor of Philosophy

May 2011

I hereby declare that my thesis entitled '*Cosmology with CMB and Large Scale Structure*' is not substantially the same as any that I have submitted for a degree or diploma or other qualification at any other University. I further state that no part of my thesis has already been, or is concurrently being, submitted for any such degree, diploma or other qualification. Most of the original material in this thesis is based on papers that have either been published or submitted for publication as follows

1. **Large-Angle Correlations in the Cosmic Microwave Background**,
G. Efstathiou, Y.Z. Ma, and D. Hanson, MNRAS 407 (2010) 2530;

2. **Testing a direction-dependent power spectrum with Planck**,
Y.Z. Ma, G. Efstathiou, and A. Challinor, Phys. Rev. D 83 (2011) 083005;

3. **Constraints on the standard and non-standard early Universe models from CMB B-mode polarization**,
Y.Z. Ma, W. Zhao and M. Brown, JCAP 10 (2010) 007;

4. **Peculiar velocity field: constraining the tilt of the Universe**,
Y.Z. Ma, C. Gordon and H. Feldman, Phys. Rev. D 80 (2011) 103002;

5. **Cosmic Mach Number as A Sensitive Test of Growth of Structure**,
Y.Z. Ma, J. P. Ostriker and G.B. Zhao, 1106.3327 [arXiv:astro-ph.CO], submitted to Phys. Rev. Lett;

Although the original work listed here has been done in collaboration as described above, most of it has been done by the author. Various figures throughout the text are reproduced from the work of other authors, for illustration or discussion. Such figures are always credited in the associated caption. This thesis contains fewer than 60,000 words.

Acknowledgements

This thesis is about the stories that happened in the early and late time of the Universe, and it should be started by acknowledging the help, support and encouragement from all of my supervisors, family and friends which were invaluable to me.

Beyond all of the acknowledgement, I would like to make my greatest thanks to my thesis supervisor, George Efstathiou. As a distinguished cosmologist and accomplished supervisor, he always mentors me to choose projects with the highest level of impact, and teaches me to tackle the problems in a distinctive way. His inspiring speeches and broad knowledge of astronomy also influence me a lot. I am looking forward to learning more from George in the years to come.

I would also sincerely thank my second supervisor, Anthony Challinor for his help on many difficult problems that I could not solve by myself without his hints and inspiration. At the start of my PhD, I also enjoyed very much his lectures on large scale structure formation which got me quickly involved in real precision cosmology. I would also like to thank the cosmologists at IoA Cambridge with whom I had invaluable discussions: Michael Brown, Donald Lynden-Bell, Simeon Bird, Michael Bridges, Martin Haehnelt, Steven Gratton, Duncan Hanson, Lindsay King, Antony Lewis, Andrew Pontzen, Martin Rees, Richard Shaw. Among these people I would make special thanks to Duncan Hanson, who really helped me a lot with CMB programming at the start of my project; and Prof. Donald Lynden-Bell, for telling me of many interesting topics of astronomy and for inviting me to family gatherings.

The Institute of Astronomy at Cambridge University is such an encouraging and thoughtful place where many outstanding scientists have been working. During discussions with Andrew Fabian, Gerry Gilmore, Paul Hewett, Robert Kennicutt and Carolin Crawford, I felt my knowledge of astronomy, was greatly broadened. I also enjoy the friendships with my peer graduate student, Becky Canning, Alex Calverley, Ryan Cooke, Stephanie Hunt, James Mead and James Owen. In addition, I thank the computing team for solving so many technical problems during my 3-year PhD (Hardip, Andrew and Sue). Furthermore, sincere thanks to the administrators of the Institute, Mrs. Margaret Harding, Susan Leatherbarrow, Sian Owen, Paula Younger, and Mr. Mark Hurn for their patient help and great strength of support for my travelling and for my scientific career in general. Margaret is always helpful in making travel arrangements for me to conferences and visits. Paula worked very hard for me to send references and arrange supervisor meetings even when she was several months pregnant. Mark always brings useful books to me when I need them. Before I came to Cambridge, I suffered a lot from bureaucracy imposed by various administrators, and I never encountered supporting staff who were as efficient and helpful as those at Institute of Astronomy. I can say that they are the best secretaries that I have ever met.

College life and activities are also very much an important part of three year PhD at Cambridge.

Trinity College Cambridge, is not only a prestigious and wealthy college, but also a wonderful place to meet many smart and eminent people in every different subject, and develop personal and professional networks. It is a place to learn about the world and I always feel that I was so lucky to be admitted. I would sincerely give thanks for the financial support from the College and the Cambridge Overseas Trust, and I could not have come to Cambridge for my degree without these funding schemes. In the college life, I am grateful to my English supervisor, Ms. Margaret de Vaux, for her efforts in improving my English reading, speaking and writing. I especially thank Lord Martin Rees, the Master of Trinity College and Astronomer Royal, for discussions on many exciting and important topics in astronomy as well as general science. As a world-famous cosmologist, Martin delivers articulate speeches on various occasions which have taught me how to make the science understandable and appreciated by the general public. At the end of my PhD, I got a "best-speaker" award at Trinity College Annual Science Symposium which I attribute to Martin's inspiration and influence. His well-known formula, "ability$\times$impact" on how to search for suitable projects, also impressed me a lot. I would like to thank my friends from Trinity with whom I have shared my three-year time with. In particular, I would like to thank my fantastic friends Johanna Tudeau, Juggs Ravalia, Lindsay Chura, Peng Zhao, Ena Hodzik, Sina Bonyadi, Sara Ahmadi, Rebekah Clements, Yang Xia, Xuxiao Zhang, Fangyuan Cheng, Hao Wu, Mao Zeng, Bo Zheng and Mingjie Dai et al.. I know they are less likely to read this thesis but they really deserve thanks.

Collaborations are essential to a cosmologist and I have been lucky to work/discuss with many excellent researchers throughout the world during the PhD course. First I must thank Christopher Gordon, Hume Feldman and Douglas Scott for mentoring me closely on a number of occasions, offering new ideas, revising paper drafts, and supporting me in navigating postdoc jobs. I especially thank Douglas Scott and CITA office to support me as the CITA national fellow subsequent my degree. I must also thank Jeremiah Ostriker, Gongbo Zhao, Wen Zhao, Laurie Shaw, Houjun Mo, Xingang Chen, Baojiu Li, Xuelei Chen and Pengjie Zhang for the help and discussion they have given me on various occasions. I really gained much valuable knowledge of cosmology and astronomy from these collaborators.

Last but not least, completing a PhD is not possible without the unwavering support from my family and closest people. I would like to thank my parents, Jian-Ming Ma and Yu-Qin Lu, as well as other family members, for their constant love and support.

Abstract

Cosmology has become a precision science due to a wealth of new precise data from various astronomical observations. It is therefore important, from a methodological point of view, to develop new statistical and numerical tools to study the Cosmic Microwave Background (CMB) radiation and Large Scale Structure (LSS), in order to test different models of the Universe. This is the main aim of this thesis.

The standard inflationary Λ-dominated Cold Dark Matter (ΛCDM) model is based on the premise that the Universe is statistically isotropic and homogeneous. This premise needs to be rigorously tested observationally. We study the angular correlation function $C(\theta)$ of the CMB sky using the WMAP 5-year data, and find that the low-multipoles can be reconstructed from the data outside the sky cut. We apply a Bayesian analysis and find that $S_{1/2}$ statistic ($S_{1/2} = \int [C(\theta)]^2 d\cos\theta$, used by various investigators as a measure of correlations at large angular scales) cannot exclude the predictions of the ΛCDM model. We clarify some issues concerning estimation of correlations on large angular scales and their interpretation.

To test for deviation from statistical isotropy, we develop a quadratic maximum likelihood estimator which we apply to simulated Planck maps. We show that the temperature maps from Planck mission should be able to constrain the amplitude of any spherical multipole of a scale-invariant quadrupole asymmetry at the 1% level (2σ). In addition, polarization maps are also precise enough to provide complimentary constraints. We also develop a method to search for the direction of asymmetry, if any, in Planck maps.

B-mode polarisation of the CMB provides another important test of models of the early Universe. Different classes of models, such as single-field inflation, loop quantum cosmology and cosmic strings give speculative but testable predictions. We find that the current ground-based experiments such as BICEP, already provided fairly tight constraints on these models. We investigate how these constraints might be improved with future observations (e.g. Planck, Spider).

In addition to the CMB related research, this thesis investigates how peculiar velocity fields can be used to constrain theoretical models of LSS. It has been argued that there are large bulk flows on scales of $\gtrsim 50$ Mpc/h. If true, these results are in tension with the predictions of the ΛCDM model. We investigate a possible explanation for this result: the unsubtracted intrinsic dipole on the CMB sky may source this apparent flow, leading to the illusion of the tilted Universe. Under the assumption of a superhorizon isocurvature fluctuation, the constraints on the tilted velocity require that inflation lasts at least 6 e-folds longer (at the 95% confidence interval) than that required to solve the horizon problem.

Finally, we investigate Cosmic Mach Number (CMN), which quantifies the ratio between the mean velocity and the velocity dispersion of galaxies. We find that CMN is highly sensitive to the growth of structure on scales $(10, 150)$ Mpc/h, and can therefore be used to test modified gravity models and neutrino masses. With future CMN data, it should be possible to constrain the growth factor of linear perturbation, as well as the sum of the neutrino mass to high accuracy.

Contents

Contents **v**

List of Figures **ix**

1 Introduction **1**

1.1 Friedmann-Robertson-Walker models . . . 2
1.2 Inflation . . . 4
1.2.1 Problems of the Big Bang model . . . 4
1.2.1.1 Horizon Problem . . . 4
1.2.1.2 Flatness Problem . . . 6
1.2.1.3 Homogeneity Problem . . . 6
1.2.2 Inflation models . . . 7
1.2.2.1 Inflationary Scenario . . . 7
1.2.2.2 Single field description of inflation . . . 8
1.2.2.3 Inflation Models . . . 14
1.2.3 The properties of the observable Fluctuations . . . 16
1.2.3.1 Gaussian Fluctuations . . . 16
1.2.3.2 Linear perturbation . . . 17
1.2.3.3 Adiabatic Initial conditions . . . 17
1.2.3.4 Close to Scale-invariant . . . 18
1.2.3.5 Small but non-zero tensor modes . . . 18
1.3 The Cosmic Microwave Background Radiation (CMB) . . . 19
1.3.1 CMB temperature power spectrum . . . 19
1.3.1.1 Scenario of recombination . . . 19
1.3.1.2 Mathematical Treatment . . . 22
1.3.2 CMB polarization . . . 25
1.3.3 Prospects of constraining inflation . . . 29
1.4 The Growth of Structure . . . 31
1.4.1 Mass Fluctuations and Matter Power Spectrum . . . 31
1.4.2 Linear growth of structure . . . 34

1.4.2.1 Jeans equation 34
1.4.2.2 Sub-Hubble-length modes 35
1.4.3 Non-linear growth of the structure 38
1.4.3.1 Spherical Collapse model 38
1.4.3.2 Dark Matter halo abundance 43
1.4.3.3 Gas Physics 45
1.5 Dark matter and Galaxy formation 46
1.5.1 Dark Matter Particles 46
1.5.2 Dark Matter on Small Scales 47
1.5.2.1 Population of sub-halos and satellites: how cold is cold dark matter? 47
1.5.2.2 Cusp and Core problem 48
1.6 Overview 49
1.6.1 Classification of problems in Cosmology 49
1.6.1.1 Known Physics but unknown details 49
1.6.1.2 Unknown Physics 50
1.6.2 Aims and Structure of the Thesis 51

2 Large-Angle Correlations in the CMB 55
2.1 Introduction 55
2.2 Estimators of the Correlation Function 56
2.3 Reconstructing low-order multipoles on a cut sky 62
2.4 Analysis of the $S_{1/2}$ statistic 69
2.4.1 Approximate Bayesian analysis 70
2.4.2 Frequentist analysis 71
2.5 Discussion and Conclusions 73

3 Testing a direction-dependent primordial power spectrum with CMB observations 75
3.1 Introduction 75
3.2 The anisotropic model 77
3.2.1 Covariance matrix 77
3.2.2 Quadratic estimators and the Fisher matrix 78
3.3 Forecasts for Planck 79
3.3.1 Constraints on the anisotropy amplitude 79
3.3.2 Constraints on scale-dependence 81
3.3.3 Axisymmetric models 83
3.4 Conclusions 84

4 Constraints on the standard and non-standard models of the early Universe from CMB B-mode polarisation **87**

4.1 Introduction . . . 87
4.2 B-mode polarization and its observations . . . 89
4.2.1 B-mode polarization . . . 89
4.2.2 Constraints on the B-mode signal . . . 90
4.2.3 Data Analysis Methodology . . . 92
4.2.3.1 χ^2 analysis and hyper-parameters . . . 92
4.2.3.2 Fisher information matrix . . . 94
4.3 Constraining the SFI model . . . 95
4.3.1 Scalar and tensor primordial power spectra in the SFI model . . . 95
4.3.2 Constraints on SFI from current data . . . 97
4.3.3 Prospects for future observations . . . 98
4.3.4 Single-field slow-roll inflationary models . . . 102
4.4 Loop Quantum Gravity and its observational probes . . . 105
4.4.1 Primordial tensor perturbations in LQG models . . . 105
4.4.2 Constraints from current data . . . 107
4.4.3 Prospects for future experiments . . . 109
4.5 Cosmic strings and their detection . . . 111
4.5.1 B-mode polarization from cosmic strings . . . 111
4.5.2 Constraints from current data . . . 112
4.5.3 Prospects for future experiments . . . 114
4.6 Conclusion . . . 115

5 Peculiar Velocity Field: Constraining the tilt of the Universe **117**

5.1 Introduction . . . 117
5.2 Likelihood and mock catalogues . . . 118
5.3 Data Analysis . . . 119
5.4 Discussion . . . 123
5.5 Conclusion . . . 125

6 Cosmic Mach Number as A Sensitive Test of Growth of Structure **127**

6.1 Introduction . . . 127
6.2 Statistics of Cosmic Mach Number . . . 128
6.3 A sensitive test of growth of structure . . . 131
6.4 Conclusion . . . 133

7 Conclusions and Outlook **135**

A Instrumental Characteristics of CMB Experiments **141**

B Statistics of the conventional χ^2 and the hyper-parameter χ^2 **145**

B.1 χ^2 statistics 145

B.2 Hyper-parameter χ^2 146

C Analytic formulas of the correlated Window Function $f_{12}(k)$ **149**

References **153**

List of Figures

1.1 WMAP 7-year Internal Linear Combination (ILC) Map. The colour scale is from -200 K to 200 K. Figure taken from [196]. 5

1.2 Solution of the horizon problem. The scales of interest were greater than the Hubble radius before $a \sim 10^{-5}$, but fairly early on, all of the scales were inside the Hubble radius and were sensitive with microscopic physics. 7

1.3 Generic shapes of potentials for different inflation models. Left: large Field (Chaotic) Inflation; Middle: small field inflation; Right: hybrid inflation. Figure taken from [42]. 14

1.4 Left: Expected 95% uncertainty on the inflationary parameters n_s and r from WMAP and Planck in 1990s. Each model has a unique prediction for n_s and r. Figure taken from [66]. Right: Current constraints on $r - n_s$ parameter space from WMAP 7-year results. Figure taken from [72]. 15

1.5 The CMB temperature power spectrum (red line), which displays the amplitude of the CMB temperature fluctuation $\Delta T/T$ as a function of angular scale on the sky. The acoustic peaks suggest the interplay of the gravity and radiation pressure and they are very sensitive to cosmological parameters. The black dots are WMAP 7-year data, and blue band is the cosmic-variance. Figure taken from [52]. 19

1.6 Density contrast in conformal Newtonian gauge. The photon, baryon, and CDM density perturbations are plotted in red, green and blue respectively. The upper figure is long wave length case (k=0.01 Mpc^{-1}), and lower figure is the short wave length case (k=1.0 Mpc^{-1}). Figure taken from [62]. 20

1.7 Contribution of different terms in Eq. (1.81) to the temperature anisotropies from adiabatic initial conditions: $\delta_\gamma/4+\psi$ (Sachs-Wolfe effect, magenta line); v_b (Doppler effect, blue line); Integration term (Integrated Sachs-Wolfe effect, green line); total effect (black line). Figure taken from [62]. 21

1.8 Thomson scattering of radiation with a quadrupole anisotropy generates linear polarization. Red colors (thick lines) represent hot radiation, and blue colors (thin lines) cold radiation. Figure taken from [76]. 26

1.9 The power spectrum of the cross-correlation between temperature and E-mode polarization anisotropies. The anti-correlation at $100 < l < 200$ and the positive correlation at $200 < l < 400$ are due to the phase coherence of fluctuation generated during inflation [53]. The data is WMAP 7-year result [52]. 27

1.10 WMAP 5-year measurements of the temperature and polarization power spectrum to constrain the tensor-to scalar ratio. Left: Contours show 68% and 95% C.L of the parameter space. The gray region is the constraint from the low-l multipole data (TE, EE, BB at $l \leq 23$) only, and the red region is from the low-l data plus the high-l TE data at $24 \leq l \leq 450$. Finally, the blue region is the constraint from the low-l polarization data, the high-l TE correlation data, and the low-l temperature data at $l \leq 23$. Right: the gray curves show (r, τ)=(10,0.050), the red curves (r, τ)=(1.2,0.075) and the blue curves (r, τ)=(0.2,0.080), where τ is the optical depth $\tau = \int_0^{\eta_0} n_e \sigma_T a d\eta$. Figure taken from [3]. 28

1.11 The marginalised likelihood of tensor-to-scalar ratio r in WMAP 7-year data and 5-year data, from the polarization data (BB, EE and TE) alone. All the other cosmological parameters, including the optical depth, are fixed at the 5-year best-fit ΛCDM model [3]. The vertical axis $-2\ln(L/L_{max})$ is the standard χ^2 under the Gaussian approximation. The dashed line $-2\ln(L/L_{max}) = 4$ corresponds to the 2σ CL. The solid, dashed and dot-dashed lines show the likelihood as a function of r from the BB-only, BB+EE, and BB+EE+TE data. (Left) The 7-year polarization data. WMAP 7-year data shows $r < 2.1$, 1.6, and 0.93 (95.4% CL) from the BB-only, BB+EE, and BB+EE+TE data, respectively. (Right) The 5-year polarization data. $r < 4.7$, 2.7, and 1.6 (95.4% CL). Figure taken from [72]. 28

1.12 Comparison of matter power spectrum $P(k)$, inferred from the CMB temperature anisotropy to constraints from other observations, including the observed galaxy distributions. The consistency of independent results shows that the density perturbations are the seeds for structure growth. Figure taken from [5]. 30

1.13 Power spectrum (upper-left), transfer function (upper-right), and root-mean-square of mass fluctuation in linear perturbation theory at different redshift. Here we adopt ΛCDM model with WMAP 5-year parameters $\Omega_b = 0.0449$, $\Omega_c = 0.222$,$\Omega_\Lambda = 0.734$,$h = 0.71$,$\sigma_8 = 0.801$ and $n_s = 0.963$ [3]. 33

1.14 Inhomogeneous 1-D density fluctuation. The dark (light) curve is the field smoothed (not smoothed) on large scales. Small scale fluctuations that have density contrast over δ_{crit} collapse first, while the large scale fluctuation cannot collapse since their overdensity does not exist this threshold. Figure taken from [44]. 43

1.15 Left: Two-dimensional slice of the baryon distribution at z = 2.5 in a ΛCDM hydrodynamical simulation of structure formation. The low and high density regions are shown as dark and bright colours. The voids and filaments are typically associated with material in the Inter-Galactic Medium (IGM) and are observable in quasar absorption spectra. The luminous baryonic material (stars and galaxies) forms in the highest density regions, which is shown as the knots and sheets where many filaments converge. Right: The underlying dark matter distribution. The baryon distribution is slightly more diffuse (less small scale structure) compared to the underlying dark matter due to gas pressure support. In the simulation, the cosmological parameters are: $\Omega_m = 0.26$, $\Omega_\Lambda = 0.74$, $\Omega_b = 0.0463$, $h = 0.72$. The box size is 60 Mpc/h. The number of gas and dark matter particles are 2×400^3. The softening length is 2.5 kpc/h. Figure taken from [87]. 44

1.16 The cumulative number of Milky way satellite galaxies as a function of halo circular velocity. Left panel: Missing satellite problem; Right panel: the effect of reionization. Figure taken from [104]. 47

2.1 The figure to the left shows the correlation functions computed using the pixel estimator (2.3) applied to the 5 year WMAP ILC map (degraded as described in the text) over the full sky and with the WMAP KQ85 and KQ75 masks imposed. The figure to the right shows the correlation functions computed from the pseudo-power spectra (2.5). 59

2.2 Covariance matrix for the pixel correlation estimator (2.3) computed for full sky maps. The scale on the right is in units of $(\mu\mathrm{K})^4$. 60

2.3 The figure to the left in the top row shows the WMAP 5 year ILC temperature map smoothed by a Gaussian of FWHM 10° and repixelized to a Healpix resolution of NSIDE=16. The figure to the right in the top panel shows the degraded resolution WMAP KQ75 mask used in this Chapter. The remaining figures to the left show the reconstructed all-sky maps computed from data outside the KQ85 sky cut, using the harmonic coefficients computed from equation (2.19) with the coupling matrices truncated to (from top to bottom) $\ell_{\rm max} = 5$, 10, 15 and 20. The figures to the right show equivalent plots for the reconstructed all-sky maps computed from data outside the KQ75 sky cut. 64

2.4 Reconstructions of the correlation function from equation (2.22) for various choices of $\ell_{\rm max}$ and sky cut. 66

2.5 As Figure 2.1 but using the QML estimator of equation (2.14). 68

2.6 The temperature power spectrum at low multipoles computed from the low resolution WMAP 5-year ILC map. The points (corrected for the 10° FWHM smoothing and slightly displaced in ℓ for clarity) show QML power spectrum estimates for three sky cuts: no mask; KQ85 mask; KQ75 mask. Error bars show the diagonal components of the inverse of the Fisher matrix (2.29). The solid red line shows the power spectrum computed from the all-sky ILC map (which is identical to the QML all-sky estimates). The solid green and blue lines show the power spectra computed for the $\ell_{\max} = 10$ reconstructions of Fig. 2.3. 69

2.7 (a) Posterior distributions of $S^T_{1/2}$ computed as discussed in the text. The red (solid) histogram shows the distribution of $S^T_{1/2}$ from an analysis of the whole sky. The blue (dotted) histogram shows the distribution computed with the KQ75 sky cut applied. The vertical dashed lines in the figures shows the value $S^T_{1/2} \sim 49000\ (\mu\mathrm{K})^4$ for the best fitting ΛCDM model as determined from the 5-year WMAP analysis [3]. (b) Frequency distributions of $S_{1/2}$ for statistically isotropic, Gaussian, realizations of the ΛCDM model [3]. The red (solid) histogram shows the frequency distribution for the pixel ACF estimator applied to the whole sky. The blue (dotted) histogram shows the distribution computed with the pixel ACF estimator with the KQ75 sky cut applied. 71

2.8 Pixel based estimates ACF estimates for the WMAP ICL map corrected for the local ISW contribution for redshift $z < 0.3$ as described by [132]. 72

3.1 Noise-free simulation of a model with scale-invariant quadrupole asymmetry in the primordial power with $g_{LM} = 0.1\delta_{L2}\delta_{M0}$. The isotropic component of the temperature map is shown on the left, and the anisotropic component on the right. The colour scales are in μK. 80

3.2 Anisotropic components of the Q (left) and U (right) polarization maps in a noise-free simulation of the model in Fig. 3.1. The maps have been smoothed here with a Gaussian beam of FWHM 3° to enhance the imprint of the preferred axis in the Q map. The colour scales are in μK. 80

3.3 Estimates of the G_{20} (left) and $G_{2\,-2}$ (right) anisotropy parameters (shown with points) and their (one-sigma) Fisher errors ([Red] solid lines) as a function of $l_{\max}$ from five simulations of the model in Fig. 3.1 for one year of Planck data. The input parameters $G_{20} = 0.1$ and $G_{2\,-2} = 0.0$ are shown with horizontal [Blue] solid lines. From top to bottom we analyse temperature only, E-mode polarization only and temperature plus polarization. 81

3.4 Fisher errors for G_{20} from temperature, E-mode polarization, and temperature plus polarization in models with power-asymmetry spectral indices $q = 0$ (left), $q = 1$ (middle) and $q = 2$ (right). For $q = 0$ and $q = 1$ we show results for one and two years of observations; for $q = 2$ we show only the one-year errors since they improve very little with further observing time. Note that the one- and two-year errors from temperature alone are indistinguishable when $q \geq 0$. 82

3.5 Marginal distributions for the direction (left) and amplitude (g_{*2}, right) from a simulation of the nominal (one-year) Planck survey for a model with an axisymmetric quadrupole asymmetry aligned with the polar axis ($g_{LM} = 0.1\delta_{L2}\delta_{M0}$). We parameterise the direction with the equal-area projection $x = 2\sin(\beta/2)\cos(\alpha)$ and $y = 2\sin(\beta/2)\sin(\alpha)$ and show in solid lines the 68% [Red], 95% middle [Blue] and 99% outer [Green] contours from the temperature alone; dashed-line contours are from the E-mode polarization alone. For the amplitude (right), we plot the marginal distributions from T alone (solid line) and E alone (dashed line). 85

4.1 Comparison of different theoretical predictions, and the currently available data for the B-mode power spectrum. The unit for m is $\mathrm{M_{pl}}$ and k_* is Mpc^{-1}. Note that the error-bars are plotted in log-log scale. 90

4.2 Polarization noise power spectra for forthcoming experiments. Note that these curves include uncertainties associated with the instrumental beam. The blue curves show the B-mode power spectrum for the standard inflationary model with $r = 0.03$. In the left panel, we plot the instrumental noise for the Planck and CMBPol satellites, as well as the lensing B-mode signal and the noise level for the ideal experiment. In the right panel, we plot the instrumental noise for the ground-based PolarBear and QUIET experiments, and the balloon-borne Spider experiment. We fix the other parameters at WMAP 7-year best-fit values ($\Omega_b h^2 = 0.02258$, $\Omega_c h^2 = 0.1109$, $n_s = 0.963$, $A_s(k_0) = 2.43 \times 10^{-9}$ (pivot scale $k_0 = 0.002, \mathrm{Mpc}^{-1}$), $h = 0.71$, and $\tau = 0.088$). 91

4.3 The current constraints on r from BICEP and QUaD data. 97

4.4 The signal-to-noise ratio $r/\Delta r$ for different experiments, calculated using the Fisher matrix of Eq. (4.13). Left: The parameter r is treated as a free parameter but n_t is kept fixed at its fiducial value; Right: Both r and n_t are treated as free parameters. The atmospheric noise in PolarBear and QUIET is not included in the plot. . . . 100

4.5 The signal-to-noise ratio $r/\Delta r$ for different experiments, and the combination of Planck and ground-based experiments, calculated using the Fisher matrix of Eq. (4.13). Left: The parameter r is treated as a free parameter but n_t is kept fixed at its fiducial value; Right: Both r and n_t are treated as free parameters. 101

4.6 Forecasted joint constraints on the parameters of the SFI model. The contours indicate the 68% (1σ) confidence levels. The input models are indicated by the black points (Left: $r = 0.01$ and $n_t = 0$, Right: $r = 0.001$ and $n_t = 0$). 102

4.7 Forecasted uncertainty on the tensor spectral index, Δn_t, for different experiments, calculated using the Fisher matrix of Eq. (4.13). Here, both r and n_t are treated as free parameters. 103

4.8 Left: the primordial tensor power spectrum for different models of inflation. Right: the corresponding B-mode angular power spectrum generated by different inflationary models. Note the lensing B-mode signal which acts as an effective noise for detecting the primordial C_l^{BB} signal. The units for m and k_* are $\mathrm{M_{pl}}$ and Mpc^{-1} respectively. 107

4.9 Probability distribution function (PDF) for the parameters in the LQG model. Left: constraints on the mass parameter $\tilde{m} = m/\mathrm{M_{pl}}$. Right: constraints on k_*. The red, green, and brown curves overlap with each other, indicating that the vast majority of the constraining power for the combined data sets comes from the BICEP data. 108

4.10 2D constraints on the parameters $\tilde{m} = m/\mathrm{M_{pl}}$ and $k_*[\mathrm{Mpc}^{-1}]$ of the LQG model. The red line (BICEP 1σ CL) overlaps with the brown line (BICEP+QUaD, 1σ CL). 109

4.11 Predicted signal-to-noise ratios for the parameters in LQG for forthcoming and future experiments. Here $\tilde{m}$ is the mass parameter, and k_* is the position of the bump in the BB power spectrum. 110

4.12 Forecasted 2D constraints for the LQG model. The input models are indicated with the black points. (Left: $\tilde{m} = 10^{-8}$ and $k_* = 0.002\mathrm{Mpc}^{-1}$. Right: $\tilde{m} = 10^{-8}$ and $k_* = 0.0002\mathrm{Mpc}^{-1}$). 111

4.13 Current constraints from B-mode polarization on the cosmic string tension. To obtain the constraints, we have fixed the wiggling parameter at $\alpha = 1.9$. 113

4.14 Forecasts of the signal-to-noise ratio for the cosmic string tension $G\mu$ potentially achievable with future CMB polarization experiments. 114

5.1 The SN data plotted in Galactic coordinates.. The red points are moving away from us and the blue ones are moving towards us. The size of the points is proportional to the magnitude of the line-of-sight peculiar velocity. "X" is our estimate of the direction of the tilted velocity estimated from the SN data. 119

5.2 The simulation of the bulk flow velocity and test of likelihood (5.4). We input a particular set of parameters (σ_*, $\mathbf{u}$) and do 300 simulations of the underlying density field with the mean value of this set of parameters. One can see that the peaks of the average likelihood are very close to the input values ([Blue] dashed lines). 120

5.3 The 1-D marginalized posterior probability distribution functions of the parameters : (a) σ_*, (b) magnitude of $\mathbf{u}$, (c) $\mathrm{Cos}(\theta)$, (d) ϕ. 121

5.4 (a) The 68%, 95% and 99.7% Bayesian confidence interval contours for parameters σ_*-u. (b) The 68% contours for Cos(θ)-ϕ. The black dot is the direction of the bulk flow found by [244]. 122

6.1 (a): The 1-D posterior distribution of the CMN $M(r)$ from 5 different catalogues. The unit of r is [Mpc/h]. (b): The comparison between the CMN data (3σ CL.) and theoretic prediction: blue data points are the CMN data from posterior distributions shown in panel (a); red data points are the data used in Ostriker and Suto 1990 [270]; the black line is the CMN prediction from WAMP 7-yr best-fit values [72]; the green dashed line is calculated by using 'popular' CDM cosmological parameters $n_s = \Omega_m = 1$ and $h = 0.5$ in 1990s [270]; the brown dashed and purple dot-dashed lines are the CMN from $f(R)$ model with $B_0 = 10^{-4}$ and from ΛCDM model with neutrino mass $\sum_\nu m_\nu = 0.2$eV. 130

6.2 (a): Forecast 1σ errors of the CMN from 6dF survey, in which we assume the data is around our local region of the universe. Beside ΛCDM model, we plot $B_0 = 10^{-4}$ ([Brown] dashed line) and 10^{-3} ([Red] dashed line) for the $f(R)$ model, and $\sum_\nu m_\nu = 0.2$eV ([Purple] dot-dashed line) and 0.3eV ([Green] dashed line). (b): $P_{\theta\theta}$ [Black], and $f(k,a)$ [Red] in ΛCDM (real line), $f(R)$ (dashed line) and massive neutrino (dot-dashed line) models. (c): fractional difference between the $f(R)$ and massive neutrino models with ΛCDM. 131

7.1 Demonstration of potential effects associated with Malmquist bias. Panel (a): bulk flow magnitude as a function of depth R. By placing the galaxies at their redshifts ([Blue] triangle points) rather than distance ([Red] square points), the bulk flow magnitude is consistent with ΛCDM prediction. However, if we place the galaxies at their TF distances, we find large flows on scales $\gtrsim 50$Mpc/h. Panel (b): If we place the galaxies at their redshifts, the directions of the observed bulk flow at different depths is consistent with CMB dipole direction. Panel (c): Parameter estimation of σ_8 by using the COMPOSITE catalogue, SFI++ group galaxies (SFI++$_\mathrm{G}$), and SFI++ field galaxies (SFI++$_\mathrm{F}$) (see description of the catalogues in [244] for details). By using COMPOSITE catalogue, placing the galaxies at TF distance, and generating mock catalogues from Gaussian window function, Ref.[244] obtains the distribution ([Black] dashed line) which excludes WMAP 5-yr best-fit $\sigma_8 = 0.796$ at 3σ CL. However, by using the redshift as the true distances and adopting a top-hat window function, one finds a consistency with ΛCDM ([Black] solid line). Here we fix the cosmological parameters to be WMAP 5-yr results ($\Omega_m = 0.258$, $h = 0.719$, $n_s = 0.963$, $\Omega_b = 0.0441$) in order to compare with the results in [244]. 137

Chapter 1

Introduction

In the last two decades, cosmologists have been making great efforts that have established a standard cosmological model (ΛCDM) which describes the contents of the Universe. A wide variety of observations have tested the model to a very high degree of precision. These include measurements of the cosmic microwave background temperature anisotropy (hereafter CMB) [1; 2; 3]; observations of galaxy clustering, for example, from the 2dF Galaxy Redshift Survey [4] and the Sloan Digital Sky Survey [5; 6]; evidence for the accelerating expansion of the Universe from the distant Type Ia supernovae [7; 8; 9]. In addition, complementary CMB experiments [10], weak lensing measurements [11; 12; 13], X-ray measurements of rich galaxy clusters [14; 15; 16; 17] and Lyα forest data [18; 19; 20; 21] have given further precise constraints on cosmological parameters. The observational data provide strong support for a Universe which is spatially flat and accelerating at the present day, consisting of approximately 73% dark energy, 23% cold dark matter (hereafter CDM), and 4% baryons. In addition, the data favour the cosmological constant Λ as the candidate for dark energy, which leads to the generic concordance model ΛCDM.

According to the concordance model, the inhomogeneous large scale structure of the current Universe was seeded by tiny quantum fluctuations in the early Universe, which were amplified in scales during a special period of time when the Universe was expanding almost exponentially. This period of time is known as inflation [22; 23]. The primordial perturbations generated during inflation leave two important signatures on the sky that we can observe today. One is the imprint on the CMB, where acoustic oscillation peaks are generated in the angular power spectrum of the CMB. The other is the cosmic structure that we observe today, which was amplified by gravitational instability to produce non-linear structures, such as galaxies and clusters [26]. The simplest inflationary paradigm predicts an adiabatic, Gaussian and nearly scale-invariant power spectrum, which is consistent with the CMB observations.

Information from the CMB sky can be used to probe the physics of the early Universe. Many observational projects have been done to measure the power spectrum, C_l, of the CMB temperature fluctuations, such as the satellite observations (WMAP [1; 2; 3] and Planck [27]), ground-based telescopes (ACBAR [10], BICEP-II [28], QUIJOTE [29], PolarBear [30], QUIET [31]), and balloon-borne experiments (EBEX [32] and Spider [33]). The theory for the prediction of the power spectrum is now well developed and so it is possible to compute the linear evolution of the CMB anisotropy to a high precision. Various authors have developed Boltzmann codes, such as CMBFAST [24] and CAMB [25], to compute the linear part of the power spectrum. Therefore, it is feasible to estimate cosmological parameters accurately by using the current CMB data from WMAP and other experiments.

In addition to the CMB observations, the cosmic structure that we see today is also a manifestation of primordial perturbations. According to structure formation theory, after the photons decouple from baryonic matter, gravitational instability causes the dark matter to concentrate, and the curvature perturbation provides the potential wells for baryons to collapse and form galaxies and stars. The matter power spectrum is one of the simplest and most important measures of large-scale structure. Many observations have been made to infer the matter power spectrum of the cosmic structure [4; 5; 6] to a fairly high precision, which can be used to constrain cosmological parameters quite precisely. In addition, it is possible to go beyond the matter power spectrum and measure the peculiar velocities of galaxies which become another important probe of cosmic structure.

In this chapter, we shall first introduce the standard cosmology, and then present the inflationary paradigm and its predictions. Then we discuss measurements of the CMB angular power spectrum, and how these can be used to constrain cosmological parameters. We review the linear and non-linear theory of structure formation, and discuss how the ΛCDM model predicts cosmic structure from large (Gpc) to small (Mpc) scales. Then we discuss how observations of galaxies on kpc scale or smaller can be used to constrain the properties of dark matter. Finally, we summarize the aims of this thesis.

1.1 Friedmann-Robertson-Walker models

In the standard hot big bang theory, the Universe is expanding from the initial hot and dense state to the current cool and clumpy state. Mathematically, the standard big bang cosmology is formulated under the assumption of the cosmological principle, which assumes that the Universe is homogeneous and isotropic on large scales. Under this assumption, the space-time interval between two events is expressed as

$$ds^2 = -dt^2 + R^2(t)\left[\frac{dr^2}{1-kr^2} + r^2(d\theta^2 + \sin^2\theta d\phi^2)\right], \tag{1.1}$$

where (r, θ, ϕ) are comoving coordinates and $R(t)$ is the scale factor which describes the dynamical expansion of the Universe, and we use units in which $c = 1$. The dimensionless parameter k describes the curvature of the Universe: $k > 0$ describes a finite, positively curved space which corresponds to a closed Universe; $k = 0$ describes an infinite, zero-curvature space which corresponds

Content	EoS	a	ρ (density)	$H(t)$
Matter	$w = 0$	$a \sim t^{2/3}$	$\rho \sim a^{-3}$	$H(t) = 2/3t$
Radiation	$w = 1/3$	$a \sim t^{1/2}$	$\rho \sim a^{-4}$	$H(t) = 1/2t$
Λ	$w = -1$	$a = \exp(H(t - t_0))$	$\rho \sim$ const	$H(t)$ =const

Table 1.1: The evolution of each type of matter.

to a flat Universe; $k < 0$ describes an infinite, negatively curved space which corresponds to an open Universe. The scale factor $R(t)$ is related to the cosmological redshift z, and the normalized scale factor $a(t)$ as $R(t)/R_0 = a(t) = (1+z)^{-1}$. If we substitute the metric (1.1) into the Einstein field equations, we can derive the following Friedmann Equation

$$H^2 = \left(\frac{\dot{R}}{R}\right)^2 = \frac{8\pi G}{3}\rho - \frac{k}{R^2}, \tag{1.2}$$

where $H = H(t)$ is the Hubble parameter which describes the expansion rate of the Universe, k/R^2 is the spatial curvature for any time slice, and Λ is the cosmological constant. We can interpret the cosmological constant Λ as another component of the Universe with energy density $\rho_\Lambda = \Lambda/8\pi G$. By assuming the content of the Universe is an ideal fluid, the energy conservation equation $T^{\mu}_{\nu;\mu} = 0$ gives the relationship between the energy density ρ and the pressure p

$$\dot{\rho} + 3H(\rho + p) = 0. \tag{1.3}$$

Therefore, by differentiating Eq. (1.2) with respect to time and using Eq. (1.3), we determine the second derivative of the scale factor with respect to time

$$\frac{\ddot{R}}{R} = -\frac{4\pi G}{3}(\rho + 3p), \tag{1.4}$$

which characterizes the acceleration of the expanding Universe. From Eq. (1.4), we can see that the sign of $(\rho + 3p)$ determines whether the Universe is decelerating ($\ddot{R} < 0$) or accelerating ($\ddot{R} > 0$). If $p > -\frac{1}{3}\rho$, the expansion of the Universe will gradually slow down under the action of gravity; on the other hand, if $p < -\frac{1}{3}\rho$, the pressure can act as an 'anti-gravity' term leading to the accelerated expansion. For instance, the pressure from cosmological constant ($p_\Lambda = -\rho_\Lambda$) always acts as an anti-gravity which drives the Universe accelerated expansion. For each component of the Universe, cold dark matter, radiation and dark energy, we can define their equation of state (hereafter EoS) parameter $w = p/\rho$. Since the Friedmann equations (1.2) and (1.4) are related to the energy density and pressure, it is easy to relate the EoS parameter to the density and scale factor evolution, as shown in Table 1.1.

Here we assume the dark energy EoS $w = -1$, i.e. the cosmological constant. However, constraining the dark energy EoS and providing an explanation for dark energy are active current areas in astrophysics. If we substitute the above relations between energy density and scale factor, we can get the following evolution equation for Hubble parameter

$$H(z) = H_0[\Omega_{m0}(1+z)^3 + \Omega_{\Lambda 0} + \Omega_{r0}(1+z)^4]^{\frac{1}{2}}, \tag{1.5}$$

where H_0 is the present day Hubble parameter. Ω_{m0} is the present day fractional matter density, Ω_{r0} is the present day fractional radiation density, and $\Omega_{\Lambda 0}$ is the present day fractional vacuum energy density. They are defined as the ratio between the present-day matter density and critical density: $\Omega_{i0} = \rho_{i0}/\rho_{crit}$ ($\rho_{crit} = 3H_0^2/8\pi G, \quad i = m,r,\Lambda$). Here we assume the spatially flat Universe ($k = 0$, $\Omega_{m0} + \Omega_{\Lambda 0} + \Omega_{r0} = 1$) which is motivated by the inflation model and also consistent with the current observational data [3].

Since the density of different types of matter varies with the scale factor in different ways (see Table 1.1), the Universe does not have a constant EoS. In reality, the Universe went through a radiation dominated phase at early times, then a matter dominated phase and finally a dark energy dominated era. There are three classic pieces of evidence to support this standard model, the expansion of the Universe [34; 35], the abundance of the light elements [36; 37; 38], and the CMB radiation [2; 39; 40; 41].

Despite the observational support for the standard hot big bang scenario, explanations of the flatness, isotropy and homogeneity of the Universe requires a deeper understanding of cosmic evolution. Therefore, theoretical physicists proposed a new model, termed the inflationary Universe, which provides solutions to these problems and also provides a viable mechanism for structure formation.

1.2 Inflation

Let us first examine the problems with the standard hot big bang model and then introduce the inflationary scenario. We will discuss how inflation can provide solutions for these difficulties.

1.2.1 Problems of the Big Bang model

1.2.1.1 Horizon Problem

To analyze the horizon problem, let us consider the distance from the last scattering surface to us in the comoving coordinates (see [42] for more discussion)

$$\int_{t_{LS}}^{t_0} \frac{dt}{a} = \int_{\tau_{LS}}^{\tau_0} d\tau = \tau_0 - \tau_{LS}, \tag{1.6}$$

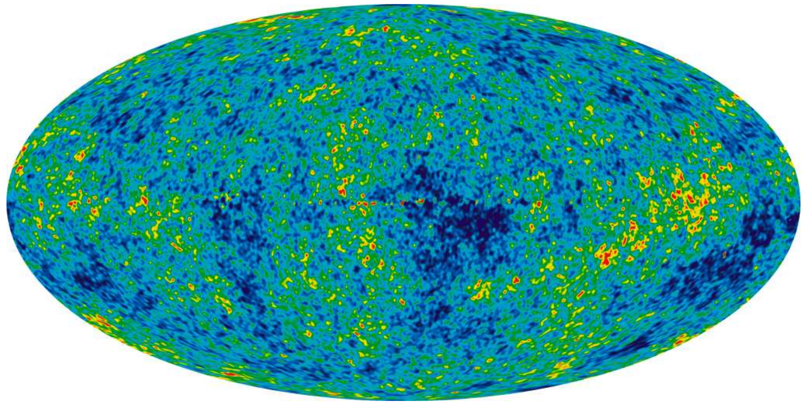

Figure 1.1: WMAP 7-year Internal Linear Combination (ILC) Map. The colour scale is from -200 K to 200 K. Figure taken from [196].

where τ_0 is the current conformal time and τ_{LS} is the conformal time at last scattering surface. A given comoving scale projected on the last scattering surface corresponds to an angular scale

$$\theta \simeq \frac{\lambda}{\tau_0 - \tau_{LS}}, \tag{1.7}$$

where the curvature effect has been neglected. Since before recombination baryons are tightly coupled to photons, the sound speed in the plasma is very close to that of a relativistic fluid $c_s = c/\sqrt{3}$. Take λ to be the comoving sound horizon which has the magnitude $c_s\tau_{LS} \sim \tau_{LS}/\sqrt{3}$, the angular acoustic scale becomes

$$\theta \simeq \frac{c_s\tau_{LS}}{\tau_0 - \tau_{LS}} \simeq c_s\frac{\tau_{LS}}{\tau_0}, \tag{1.8}$$

where the last equality holds since $\tau_0 \gg \tau_{LS}$. At the time of last scattering, the Universe has already entered into the matter dominated phase, and so the scale factor a and the temperature T scale with the conformal time as $a \sim \tau^2 \sim T^{-1}$. The angle corresponding to the sound horizon at the last scattering surface is

$$\theta_{hor} \simeq c_s\frac{\tau_{LS}}{\tau_0} = \frac{1}{\sqrt{3}}\left(\frac{T_0}{T_{LS}}\right)^{\frac{1}{2}} \simeq 1^0, \tag{1.9}$$

where we use $T_0 \simeq 3$ K and $T_{LS} \simeq 3000$ K. This corresponds to a multipole l_{hor} of

$$l_{hor} = \frac{2\pi}{\theta_{hor}} \simeq 300. \tag{1.10}$$

This means that the two photons at last scattering surface separated by angle $\theta > 1^0$ (or equivalently $l_{hor} \leq$300) were not in causal contact. However, from measurements of the CMB temperature field (Fig. 1.1), we know that temperature anisotropies on these scales are not bigger than $\Delta T/T \sim 10^{-5}$. This means that photons at the last scattering surface that were apparently not in causal contact have very nearly the same temperature. This is the horizon problem.

1.2.1.2 Flatness Problem

The current CMB experiments and SNe Ia constraints strongly favour a spatially flat Universe, which imposes strong constraints on the initial conditions. To understand the nature of this fine-tuning problem, we transform Eq. (1.2) into the following form

$$\Omega(a) - 1 = \frac{k}{(aH)^2}. \tag{1.11}$$

In the standard FRW model, the Universe contains only matter and radiation, so the comoving Hubble radius $(aH)^{-1}$ grows with time, and the quantity $|\Omega(a) - 1|$ must diverge with time. Thus, $\Omega(a) = 1$ is an unstable point. If the current spatial curvature is very close to zero, the density parameter needs to be close to unity to incredibly high precision. For instance, if we consider the time of Big Bang nucleosynthesis (BBN, $T \sim 0.1$ MeV), the Grand Unification era (GUT, $T \sim 10^{15}$ GeV) and the Planck scale ($T \sim 10^{19}$ GeV), the fractional density $\Omega(a)$ should satisfy the following conditions [43; 44]

$$|\Omega(a_{BBN}) - 1| \leq \mathcal{O}(10^{-16}), \tag{1.12}$$

$$|\Omega(a_{GUT}) - 1| \leq \mathcal{O}(10^{-55}), \tag{1.13}$$

$$|\Omega(a_{Pl}) - 1| \leq \mathcal{O}(10^{-61}). \tag{1.14}$$

Thus, if $\Omega_0 \sim 1$, the energy density at early times needs to be close to unity to an extraordinary fine precision. This needs an explanation.

1.2.1.3 Homogeneity Problem

The entropy of the current observable Universe is about 10^{80} in Planck units (estimated by considering the entropy contributed by radiation) [45]. If we put all of the matter of the observable Universe into a black hole, the entropy is related to the surface area of the black hole as

$$S = \frac{A}{4l_p^2} \sim 10^{120}, \tag{1.15}$$

where A is the surface area and l_p is the Planck length. This is very much larger than the observable value 10^{80}. This tells us that our Universe had an an extraordinary low entropy state at early times. Our Universe could have been more disordered and inhomogeneous than observed. This is the homogeneity problem.

1.2.2 Inflation models

1.2.2.1 Inflationary Scenario

Based on the hypothesis that in the early Universe there was a short period of time (perhaps about 10^{-35} second) when the Universe was exponentially expanding, it is possible that a patch as small as the Planck scale would have grown to be many orders of magnitude larger than our observable Universe. As the exponential expansion ended, matter and radiation were created during a period of "reheating", and the expansion rate slowed down to the moderate rate of the radiation dominated era [46]. The flatness, horizon and homogeneity problems can be solved if the Universe underwent an inflationary phase of quasi-exponential expansion.

According to Eq. (1.11), during the inflation period, the Hubble parameter H is nearly a constant, and the scale factor evolves as $a \sim e^{Ht}$, so it will drive the Universe towards flatness since

$$|1 - \Omega(a)| \sim \frac{1}{a^2} = e^{-2Ht} \to 0 \text{ as } t \to \infty. \tag{1.16}$$

Thus, if inflation occurred, $\Omega(a) = 1$ is an attractor, solving the flatness problem.

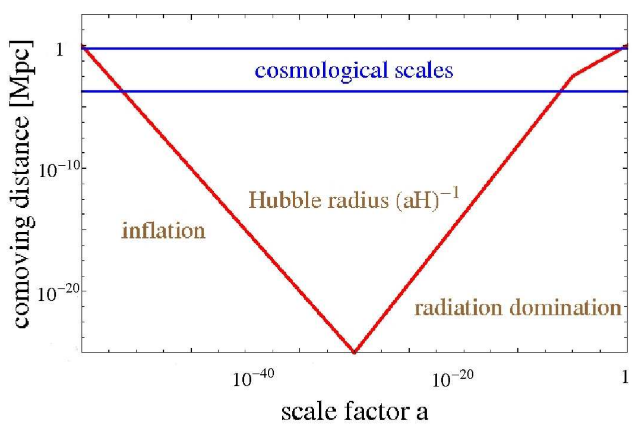

Figure 1.2: Solution of the horizon problem. The scales of interest were greater than the Hubble radius before $a \sim 10^{-5}$, but fairly early on, all of the scales were inside the Hubble radius and were sensitive with microscopic physics.

During the inflationary period, physical scales grow faster than the Hubble radius (in comoving coordinate, the Hubble radius is $(aH)^{-1}$), so quantum fluctuations are inflated on scales beyond the Hubble radius, when they become the classical fluctuations. After inflation ended and the Universe entered into the radiation dominated era, the frozen fluctuations reentered the Hubble radius and evolved under the action of gravity and pressure (see Fig. 1.2). Thus, scales that were apparently outside the Hubble radius at the decoupling time were in fact well within the Hubble radius during inflation. Inflation therefore provides an explanation of the origin of classical fluctuations and the horizon problem.

In addition, inflation partially solves the homogeneity problem. As we have shown above, the current Universe entropy 10^{80} is many order of magnitude smaller than the entropy 10^{120} if all of the cosmic structure is put into a black hole, which is a puzzle for standard ΛCDM cosmology. If the curvature of the Universe before inflation is not very fractal like, the Universe can be inflated to a homogeneous low-entropy state. However, this requires a low-entropy initial state, which is not explained by inflation so needs to be explained in the new physics.

1.2.2.2 Single field description of inflation

To understand how inflation might work, one should bear in mind that in General Relativity, gravity couples to both energy and pressure. Inflation might therefore arise if a scalar field dominates the dynamics of the early Universe. Therefore, we shall consider simple models in which inflation is driven by a single scalar field. First, let us write down the action for a single scalar field

$$S = \int d^4x\sqrt{-g}\mathcal{L} = \int d^4x\sqrt{-g}\left[\frac{1}{2}\partial_\mu\phi\partial^\mu\phi + V(\phi)\right], \tag{1.17}$$

where $\sqrt{-g} = a^3$ for the spatially flat FRW metric. From the Euler-Lagrange equation, we can derive the equation of motion for the scalar field ϕ

$$\ddot{\phi} + 3H\dot{\phi} - \frac{\nabla^2\phi}{a^2} + V'(\phi) = 0, \tag{1.18}$$

where $V'(\phi) = dV(\phi)/d\phi$. In Eq. (1.18), the $3H\dot{\phi}$ term describes the 'friction' caused by the expansion of the Universe as the scalar field rolls down the potential $V(\phi)$. Since the energy-momentum tensor is

$$T_{\mu\nu} = \partial_\mu\phi\partial_\nu\phi - g_{\mu\nu}\mathcal{L}, \tag{1.19}$$

we can write down the energy density ρ_ϕ and the pressure p_ϕ as follows [1]

$$\rho_\phi = T_{00} = \frac{\dot{\phi}^2}{2} + V(\phi) + \frac{(\nabla\phi)^2}{2a^2}, \tag{1.20}$$

$$p_\phi = -\frac{T_{ii}}{a^2} = \frac{\dot{\phi}^2}{2} - V(\phi) - \frac{(\nabla\phi)^2}{6a^2}. \tag{1.21}$$

Now we can split the inflaton ϕ into the following two parts

$$\phi = \phi_0(t) + \delta\phi(\mathbf{x}, t), \tag{1.22}$$

where ϕ_0 is the the classical scalar field and $\delta\phi(\mathbf{x}, t)$ is the quantum fluctuation. The classical scalar field ϕ_0 is the expectation value of the field at the initial homogeneous and isotropic state [42], whereas the $\delta\phi(\mathbf{x}, t)$ is the much smaller quantum fluctuation around the classical field ϕ_0.

[1] In the space-time with metric (1.1), the isotropic energy-momentum tensor can be written as $T^\mu_\nu = \mathrm{diag}(-\rho, p, p, p)$.

ϕ_0 plays the main role in determining the evolution of the 'background' (unperturbed) Universe, whereas the quantum fluctuation $\delta\phi$ is relevant to the formation of structure. Since at the moment we are interested in the dynamical evolution of the Universe, we shall neglect the $\delta\phi$ term and drop the subscript to keep the notation simple. Thus, the energy density and pressure can be expressed as

$$\rho_\phi = \frac{\dot{\phi}^2}{2} + V(\phi), \;\; p_\phi = \frac{\dot{\phi}^2}{2} - V(\phi). \tag{1.23}$$

If

$$V(\phi) \gg \frac{1}{2}\dot{\phi}^2, \tag{1.24}$$

the EoS of the scalar field is

$$p \approx -V(\phi) \approx -\rho, \tag{1.25}$$

leading to exponential expansion (Eq.(1.4)). Thus, inflation happens when the potential energy dominates over the kinetic energy, so that the Universe is dominated by the vacuum energy.

Since the spatial derivatives of the classical field are assumed to be negligible, the equation of motion for inflaton is simply (Eq. (1.18))

$$\ddot{\phi} + 3H\dot{\phi} + V'(\phi) = 0. \tag{1.26}$$

Under "slow-roll" approximation, we require $\ddot{\phi} \ll V'(\phi)$, so that Eq. (1.26) becomes

$$3H\dot{\phi} \simeq -V'(\phi). \tag{1.27}$$

In simple single field models, inflation ends when the potential energy of the inflaton becomes smaller than the kinetic energy. Couplings between inflaton and matter provide a friction for the motion of inflaton, which make the inflaton decay into relativistic particles. Generally, the dynamic friction effect is much greater than the Hubble expansion, so at the end of inflation the Hubble expansion can be neglected, and the energy of the Universe is dominated by the coherent oscillation of the inflaton around the minimum of its potential. This process is called reheating.

To distinguish different inflation models and to constrain these models, one needs to compute the power spectrum of the primordial fluctuation and other observables that can be tested by observational data. To do this, we define the following slow-roll parameters

$$\epsilon = -\frac{\dot{H}}{H^2} \simeq \frac{M_{pl}^2}{2}\left(\frac{V'}{V}\right)^2, \tag{1.28}$$

$$\eta = M_{pl}^2\left(\frac{V''}{V}\right), \tag{1.29}$$

$$\delta = \eta - \epsilon = -\frac{\ddot{\phi}}{H\dot{\phi}}, \tag{1.30}$$

where $M_{pl}^2 = 1/8\pi G$. The number of e-folds which characterize the duration of accelerated expansion can be calculated as

$$\begin{aligned} N_e &= \ln\left(\frac{a_f}{a_i}\right) \\ &= \int_{t_i}^{t_f} H dt \\ &\simeq H \int_{\phi_i}^{\phi_f} \frac{d\phi}{\dot{\phi}} \\ &\simeq -8\pi G \int_{\phi_i}^{\phi_f} \frac{V}{V'} d\phi, \end{aligned} \tag{1.31}$$

where in the last step we use the slow-roll approximation [1] and Friedmann equation $H^2 \simeq (8\pi G/3)V$.

As we have seen, the classical field is the driver of inflation, whereas the quantum fluctuation ($\delta\phi$ in Eq. (1.22)) induces the metric perturbation around the homogenous and isotropic FRW background as follows

$$\begin{aligned} ds^2 &= g_{\mu\nu} dx^\mu dx^\nu \\ &= -(1+2\psi)dt^2 + 2aB_i dt dx^i + a^2[(1-2\phi)\delta_{ij} + E_{ij}]dx^i dx^j, \end{aligned} \tag{1.32}$$

where ϕ and ψ are scalar perturbations, B_i is the vector perturbation, and E_{ij} is the symmetric and trace-free tensor perturbation. It is also proved that since the FRW metric possesses a great deal of symmetry, perturbations can always be decomposed into scalar, vector and tensor parts [57]. We shall describe each of the scalar, vector, and tensor perturbation and see how they affect the growth of structure.

For the scalar perturbation, the spatial part of the perturbed metric can be written as [56; 62]

$$g_{ij} = a^2(t)[1 + 2\zeta]\delta_{ij}, \tag{1.33}$$

where ζ is the spatial curvature of the constant hypersurface density, and $\zeta = -\phi$. The comoving curvature perturbation is defined as the spatial derivative of this spatial curvature as

$${}^{(3)}R = \frac{4}{a^2}\nabla^2\zeta. \tag{1.34}$$

The key property is that ζ is constant outside the Hubble radius [57; 62]. The power spectrum of

[1]Usually, we say inflation at least should last about 60 number of e-folds, which is the number of e-folds between the comoving scale of our observable Universe crosses the Hubble radius and the time that inflation ends. The total number of e-folds of inflation can be much longer. Also see discussion in Chapter 5.

the scalar fluctuation is

$$\langle \zeta_{\mathbf{k}} \zeta_{\mathbf{k}'} \rangle = (2\pi)^3 \delta^3(\mathbf{k} - \mathbf{k}') \frac{2\pi^2}{k^3} P_s(k), \tag{1.35}$$

and the scale dependence of the power spectrum can be described by the scalar spectral index n_s

$$n_s - 1 = \frac{d \ln P_s(k)}{d \ln k}, \tag{1.36}$$

and its running

$$\alpha_s = \frac{dn_s}{d \ln k}. \tag{1.37}$$

A full calculation of the primordial power spectrum for single scalar field models of inflation [42] leads to the following relation between the spectral index and the slow-roll parameters

$$n_s = 1 - 4\epsilon + 2\delta. \tag{1.38}$$

Then, the power spectrum is approximated as a power law form

$$P_s(k) = A_s(k_*) \left(\frac{k}{k_*} \right)^{n_s(k_*)-1}, \tag{1.39}$$

where k_* is an arbitrary pivot scale and A_s is the normalization. The WMAP team chose k_*=0.002Mpc^{-1}, and determined the amplitude of scalar fluctuation at this scale (WMAP 7-year data, see [72])

$$A_s(k_*) = (2.43 \pm 0.11) \times 10^{-9}. \tag{1.40}$$

If the primordial fluctuations are Gaussian, $\langle \zeta \zeta^* \rangle$ (power spectrum) contains all of the statistical information [56]. However, if primordial fluctuation is not purely Gaussian, the higher order correlations of ζ will encode information on this non-Gaussianity.

To analyze vector perturbations, well within the Hubble radius, we can describe the non-relativistic matter by using Newtonian perturbation theory. In this theory, the linearized Euler equation reduces to [62]

$$\partial_t \mathbf{v} + H\mathbf{v} = -\frac{1}{a\bar{\rho}} \nabla \delta P - \frac{1}{a} \nabla \phi, \tag{1.41}$$

where ϕ is the gravitational potential. We can decompose the velocity perturbation into the scalar part and the vector part as

$$\mathbf{v} = \nabla v + \mathbf{v}_\perp, \tag{1.42}$$

where $\nabla \cdot \mathbf{v}_\perp = 0$. The vector part of $\mathbf{v}$ does not lead to the clumping of the matter since the vorticity decays as the Universe expands. Taking the curl of the perturbation equation (1.41), we shall get

$$\nabla \times \partial_t \mathbf{v} = \partial_t (\nabla \times \mathbf{v}) = -H \nabla \times \mathbf{v}_\perp. \tag{1.43}$$

It follows that the vorticity decays by the Hubble flow since $\nabla \times \mathbf{v}_\perp$ scales as $1/a$. For general types of inflation models, the vector modes are not excited by inflation initially, but they can be excited by the perturbations introduced by topological defects [56; 62].

Tensor perturbations are described by a trace-free metric perturbation h_{ij} ($\partial_i h_{ij} = h^i_i = 0$) as [42; 56]

$$g_{ij} = a^2[\delta_{ij} + h_{ij}], \tag{1.44}$$

where h_{ij} corresponds to the gravitational wave perturbation. The power spectrum for the two polarization modes of h_{ij} ($h_{ij} = h^+ e^+_{ij} + h^\times e^\times_{ij}$, $h = h^+\ \ , h^\times$) is

$$\langle h_{\mathbf{k}} h_{\mathbf{k}'} \rangle = (2\pi)^3 \delta^3(\mathbf{k} - \mathbf{k}') \frac{2\pi^2}{k^3} P_t(k), \tag{1.45}$$

and its scale-dependence is defined as

$$n_t = \frac{d \ln P_t(k)}{d \ln k}, \tag{1.46}$$

i.e., the tensor power spectrum is the following power law form

$$P_t(k) = A_t(k_*) \left(\frac{k}{k_*}\right)^{n_t(k_*)}. \tag{1.47}$$

CMB experiments can, in principle, measure the ratio of the tensor to scalar fluctuation amplitude

$$r = \frac{P_t}{P_s}. \tag{1.48}$$

The value of r depends on the energy scale of inflation, and is important for distinguishing different inflationary models (see Section 1.2.2.3 and Chapter 4). We shall describe how CMB B-mode polarization observations can be used to constrain or measure the tensor-to-scalar ratio r (see Section 1.3.2).

Suppose that inflation is driven by a single inflaton field, then a calculation gives the following result for the primordial power spectrum of density fluctuations for slow-roll inflation [62]

$$\begin{aligned} P_s(k) &\simeq \left.\frac{H^4}{(2\pi\dot{\phi})^2}\right|_{k=aH} \\ &\simeq \left.\frac{9}{(2\pi)^2}\frac{1}{(3M_{pl}^2)^3}\frac{V^3}{V'^2}\right|_{k=aH} \\ &\simeq \frac{8}{3\epsilon}\left(\frac{V^{\frac{1}{4}}}{\sqrt{8\pi}M_{pl}}\right)^4, \end{aligned} \tag{1.49}$$

and the tensor fluctuation is

$$P_t(k) \simeq \frac{8}{M_{pl}^2}\left(\frac{H}{2\pi}\right)^2\Bigg|_{k=aH} \simeq \frac{2}{3}\frac{V}{\pi^2 M_{pl}^4}\Bigg|_{k=aH}. \tag{1.50}$$

Then we can calculate the tensor-to-scalar ratio

$$r = \frac{P_t}{P_s} \simeq 8M_{pl}^2\left(\frac{V'}{V}\right)^2. \tag{1.51}$$

The tensor-to-scalar ratio r is related to the slow-roll parameter ϵ as

$$r \simeq 16\epsilon. \tag{1.52}$$

On the other hand, since the power spectrum for scalar perturbation is normalized at the current Hubble radius to be $P_s \sim 2 \times 10^{-9}$, we can use this normalization with the Eq. (1.49) to derive the relationship between energy scale and r as

$$V^{\frac{1}{4}} = 1.06 \times 10^{16}\mathrm{GeV}\left(\frac{r}{0.01}\right)^{\frac{1}{4}}. \tag{1.53}$$

Thus, a detectable large tensor-to-scalar ratio would show that inflation happened at very high energy scale, comparable to the Grand Unification energy scale $\sim 10^{16}$GeV.

In addition, we can use the slow-roll approximation to obtain the following relation which characterizes the distance in field space from the end of inflation to the time when scales of CMB fluctuation were created [63; 64]

$$\frac{\Delta\phi}{M_{pl}} \gtrsim \left(\frac{r}{0.01}\right)^{\frac{1}{2}}. \tag{1.54}$$

This is called Lyth bound [63; 64]. Thus, if the tensor-to-scalar ratio is greater than ~ 0.01, it directly indicates a super-Planckian field evolving from ϕ_{CMB} to ϕ_{end}, which may give some observational clues about the nature of quantum gravity. Thus, the benchmark value $r \sim 0.01$ is so important that it may rule out a wide class of high field inflation models (see discussions in Section 1.2.2.3).

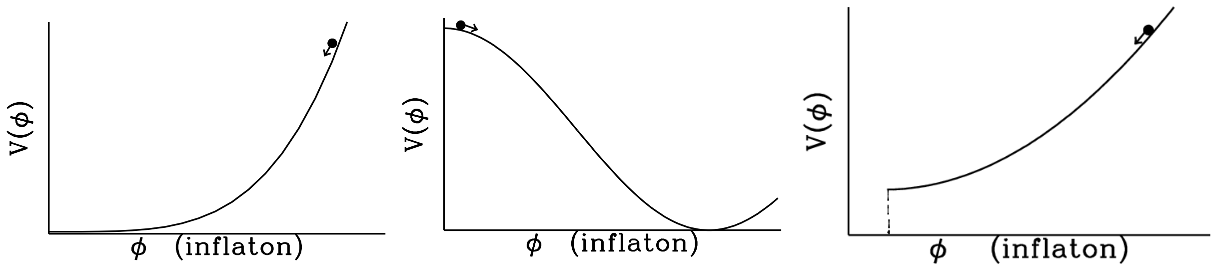

Figure 1.3: Generic shapes of potentials for different inflation models. Left: large Field (Chaotic) Inflation; Middle: small field inflation; Right: hybrid inflation. Figure taken from [42].

1.2.2.3 Inflation Models

For single-field inflation, a large number of models can be constructed, we can summarize their features with the following general potential

$$V(\phi) = \Lambda^4 f\left(\frac{\phi}{\mu}\right), \tag{1.55}$$

where Λ^4 is the vacuum energy density (characterizing the energy scale of inflation), and μ is a 'width' which characterizes the change in magnitude of the field value $\Delta\phi$ during inflation. Many variants of single field inflation can be encoded in the function f. Figure 1.3 summarizes three general types of simple inflation potential (see also [42]):

Large Field Inflation (Chaotic Inflation) Large field inflation corresponds to potentials (such as the left panel of Fig. (1.3)), where the inflaton is displaced initially from the minimum of the potentials by an amount of order the Planck mass. The potential in the left panel of Fig. (1.3) satisfies $V''(\phi) > 0$ and $-\epsilon < \delta \leq \epsilon$, and specific potentials that satisfy the conditions include $V(\phi) = \Lambda^4 \exp(\phi/\mu)$ and $V(\phi) = \Lambda^4(\phi/\mu)^p (p > 1)$. In chaotic inflation, the Universe is assumed to be generated at the quantum gravitational state with energy density comparable to Planck density [42], i.e. $V(\phi) \sim M_{pl}^4$ and $\Delta\phi \sim \mathcal{O}(1)M_{pl}$. The simplest type of chaotic inflation is a free scalar field with quadratic potential $V(\phi) = m^2\phi^2/2$, where m is the mass of the scalar field. However, from the constraints on the amplitude of the CMB power spectrum, the mass of this scalar field should be of order $m \simeq 10^{-6}M_{pl}$. If the Universe was driven by a chaotic inflation potential at an early time, the present observable Universe is only a portion of the entire Universe. In addition, since the change in magnitude of the field is order of Planck mass M_{pl}, it may be possible to probe Planckian physics in this model.

Small Field Inflation The small field inflation models correspond to the type of potentials that arise from the spontaneous symmetry breaking [67; 68] and from the pseudo Nambu-Goldstone modes [69]. The field starts from an unstable equilibrium state and rolls, initially very slowly, down the potential to a stable minimum [42; 67; 68; 69]. Thus, the potential is characterized as $V''(\phi) < 0$ and $\delta < -\epsilon$ as shown in the middle panel of Fig. 1.3. The generic potential is $V(\phi) = \Lambda^4[1 - (\phi/\mu)^p](p > 1)$ which can be viewed as the lowest order expansion of any potential around the origin.

Hybrid Inflation The hybrid inflation model has been proposed in the light of supersymmetry [70] and supergravity [71]. In the hybrid inflation model, the scalar field responsible for inflation evolves toward a minimum with nonzero vacuum energy, and ends as the result of the instability of a second field (Right panel of Fig. 1.3). The typical features for the hybrid inflation models are $V''(\phi) > 0$ and $0 < \epsilon < \delta$.

All of the above models are examples of slow-roll inflation, and can be distinguished by their predictions of the spectral index n_s and the tensor-to-scalar ratio r.

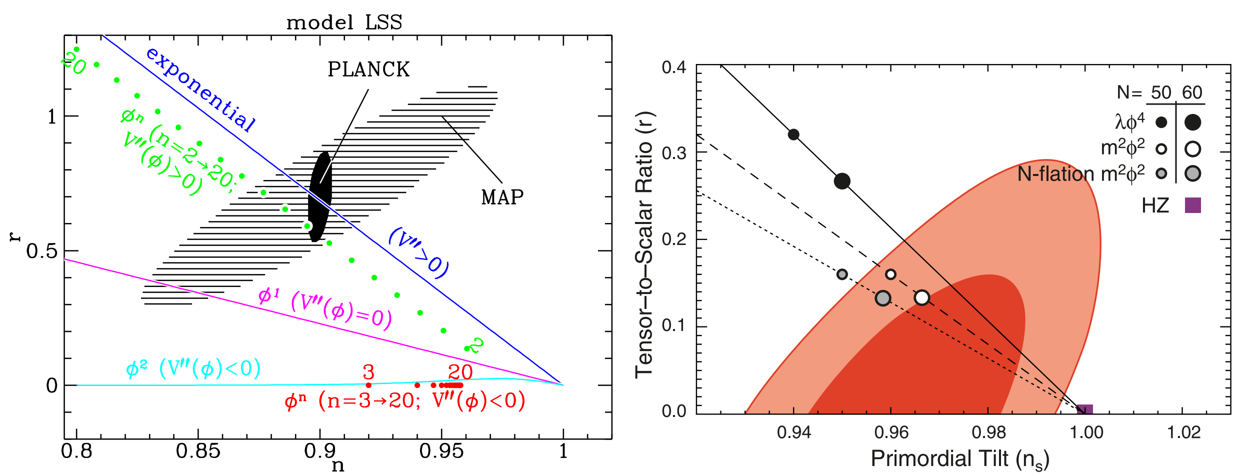

Figure 1.4: Left: Expected 95% uncertainty on the inflationary parameters n_s and r from WMAP and Planck in 1990s. Each model has a unique prediction for n_s and r. Figure taken from [66]. Right: Current constraints on $r - n_s$ parameter space from WMAP 7-year results. Figure taken from [72].

Figure 1.4 shows the predictions of different inflation models and compares them with the observational constraints. In the left panel of figure, the whole parameter space r-n_s is divided by three lines. The dark blue line corresponds to the model with $\delta = \epsilon$, i.e. the inflaton potential is exponential form $V(\phi) \sim e^{\phi}$, so the region above the blue line corresponds to the models with the potentials $V''/V > (V'/V)^2$, i.e. $\delta > \epsilon$, which corresponds to the hybrid type of potentials. The purple line corresponds to the model with $\delta = -\epsilon$, i.e. $V'' = 0$, which leads to the potential $V(\phi) \sim \phi$. So the region within the two boundary lines corresponds to the model with $0 < V''/V < (V'/V)^2$, i.e. $-\epsilon < \delta < \epsilon$, which corresponds to the large field inflation potentials. Finally, the light blue line corresponds to the model with $r = \epsilon = 0$, and the region above the light blue line and below the purple line corresponds to the models with $\eta < \delta < -\epsilon$, i.e. $V'' < 0$, which corresponds to the small field inflation potentials. Therefore, for each single field inflation model, we can compute the prediction of the model on the r-n_s plane and compare it with observational constraints. The left panel shows the forecasted error of Planck and WMAP data in 1990s, while the right panel shows the WAMP 7-year constraints, which nearly rules out $\lambda\phi^4$ inflation model.

However, these slow-roll inflation models are purely schematic. Many important theoretical questions remain unsolved. For example, what is the nature of the inflaton? How is the shape of the potential related to the fundamental physics, etc? At present, the vast majority of inflationary models are phenomenological with tenuous links to fundamental physics.

Other inflationary models In addition to the scalar field models described above, theorists have attempted to embed the inflationary scenario within string theory. For instance, brane-inflation models have been developed in the context of Type IIB superstring theory. The $D3$-branes in a warped geometry break supersymmetry, then lift the AdS vacuum to a metastable de Sitter vacuum with a sufficiently long lifetime. The anti-brane is fixed at the bottom of a warped throat, while the brane is mobile and experiences a small attractive force towards the anti-brane. Inflation ends when the brane and the anti-brane collide and annihilate, initiating the hot Big Bang epoch. The annihilation of the brane and anti-brane causes the Universe settle down to the string vacuum state that describes our universe. During the process of the brane collision, cosmic strings may be copiously produced [47; 48].

The key difference between the scalar field description of inflation and models of brane inflation is that the potential of the latter can, in principle, be derived from speculative but nevertheless microphysical principles. In addition, in this type of model, the inflaton has a fundamental geometric interpretation. For reviews of recent progress on brane inflation, see [49; 50].

1.2.3 The properties of the observable Fluctuations

At present, observations suggest that the fluctuation have the following properties: Gaussian statistics, linear on large scales, adiabatic, nearly scale-invariant power spectrum with small tensor modes. We shall illustrate how these properties are related to the predictions of inflation.

1.2.3.1 Gaussian Fluctuations

In the linear perturbation theory [44; 62], the perturbation is considered to be small so that the different Fourier modes of the curvature perturbation ζ_k evolve independently. Statistically independent Fourier modes of ζ_k imply that the curvature perturbation in real space $\zeta(\mathbf{x})$ satisfy Gaussian statistics. However, higher order perturbations will induce a small degree of non-Gaussianity.

The bispectruum of curvature perturbation ζ is

$$\langle \zeta_{\mathbf{k_1}} \zeta_{\mathbf{k_2}} \zeta_{\mathbf{k_3}} \rangle = (2\pi)^3 \delta^D(\mathbf{k_1} + \mathbf{k_2} + \mathbf{k_3}) B_\zeta(\mathbf{k_1} + \mathbf{k_2} + \mathbf{k_3}). \tag{1.56}$$

There are various shapes of the primordial bispectrum. Physically motivated models for producing non-Gaussian perturbations often produce signals that peak at particular configurations of triangle defined by the three wavenumbers in (1.56). The three often-discussed types of non-Gaussianity shapes are

Local form: This type of non-Gaussianity can arise from a curvature perturbation of the form $\zeta = \zeta_L + f_{NL}^{local} \zeta_L^2$ (ζ_L is the linear Gaussian curvature perturbation), which is expanded in a local region of space-time. This type of bispectrum peaks at the squeeze limit $k_3 \ll k_2 \approx k_1$. WMAP 7-year best estimate for the local form is $f_{NL}^{local} = 32 \pm 21$ (68% CL).

Equilateral form: The amplitude of this form of bispectrum peaks at equilateral triangle shapes ($k_1 = k_2 = k_3$). The f_{NL} is constrained by WMAP 7-year data as $f_{NL}^{equil} = 26 \pm 140$ (68% CL).

Folded shape: The signal of this form of bispectrum peaks at folded a shape $k_1 \approx 2k_2 \approx 2k_3$.

In the future, the Planck satellite is expected to reduce the uncertainty of the non-Gaussianity parameter by a factor of four [27; 73]. Note that although the standard single field slow-roll inflation model produces very small non-Gaussianity, there are various other physical mechanisms which can generate large non-Gaussianity, such as double-inflation models [74] and topological defeats [75]. Proposing and testing various types of non-Gaussianity mechanisms is one of the important frontiers of cosmology.

1.2.3.2 Linear perturbation

Since inflation causes the Universe to expand exponentially (Fig. 1.2), the comoving Hubble radius decreases during inflation while the comoving perturbation wavelength remains constant, therefore perturbations are stretched beyond the Hubble radius, remain frozen until inflation ends and then enters the Hubble radius at later time. Therefore, the observed anisotropy on the very large scale of the CMB should be fairly small ($\mathcal{O}(10^{-5})$).

In ΛCDM cosmology, the temperature anisotropy on the CMB last scattering surface is dominated by the Sachs-Wolfe effect on very large scales $\delta T/T \approx -\zeta(\mathbf{x}_{ls})/5$, where $\zeta(\mathbf{x}_{ls})$ is the comoving curvature perturbation and $\mathbf{x}_{ls}$ is the position vector of any point on the last scattering surface [62]. In Section 1.3, we will review the imprints on the CMB sky produced by the linear perturbations.

1.2.3.3 Adiabatic Initial conditions

Imagine at the starting point of structure formation, the Universe is full of a uniform distribution of matter and radiation; the simplest way to perturb the density would be to compress (or expand) a region within the volume adiabatically. This would perturb the curvature of the Universe while keeping the entropy (also the equation of state) constant. The complimentary mode is to perturb the entropy of the Universe while keep the curvature unchanged, which is the isocurvature perturbation.

For adiabatic mode, since the entropy per-baryon

$$S = \frac{n_r}{n_b} \sim \frac{\rho_r^{\frac{3}{4}}}{\rho_b} \tag{1.57}$$

is fixed, one requires $\delta_m = 3\delta_r/4$.

For the isocurvature mode, since the total energy density $\rho_m + \rho_r$ is constant, $\delta\rho_m = -\delta\rho_r$ at the time that the perturbation is generated. Single-field inflation model predicts that the initial condition of fluctuation should follow adiabatic initial conditions, while the double-field inflation and topological defects can generate isocurvature modes.

1.2.3.4 Close to Scale-invariant

As we have seen in Eq. (1.49), the power spectrum of scalar perturbation P_s is proportional to the Hubble parameter H and field "speed" $\dot{\phi}$, while these two quantities are nearly constant during inflation. Therefore, slow-roll inflation predicts an almost scale-invariant spectrum of curvature perturbations. The current tightest constraints on the spectral index (Eqs. (1.36) and (1.38)) from WAMP 7-year data [72] (at pivot scale $k_0 = 0.002$ Mpc^{-1}) is

$$n_s \simeq 0.967 \pm 0.014. \tag{1.58}$$

A scale-invariance spectrum $n_s = 1$ is excluded at 2.4σ. This slight violation of scale-invariance suggests that during inflation, there is some variation of the Hubble parameter H and inflaton speed $\dot{\phi}$. The logarithmic scale-dependence of $n_s(k)$, known as the "running" of spectral index α_s, is constrained to be [72]

$$\alpha_s = \frac{dn_s}{d\ln k} \simeq -0.034 \pm 0.026, \tag{1.59}$$

which suggests that there is marginal evidence of the running of spectral index. However, these constraints only apply on relatively large scales and actually say nothing about the spectrum on small scales. Therefore, to test for scale-invariance, one needs more small scale observations for a larger lever-arm.

1.2.3.5 Small but non-zero tensor modes

As we have already seen in Section 1.2.2.2, the tensor perturbation in the space-time metric can also source primordial fluctuations. According to Eqs. (1.48) and (1.52), the amplitude of tensor modes is suppressed by a factor related to slow-roll parameters; it is therefore expected that the

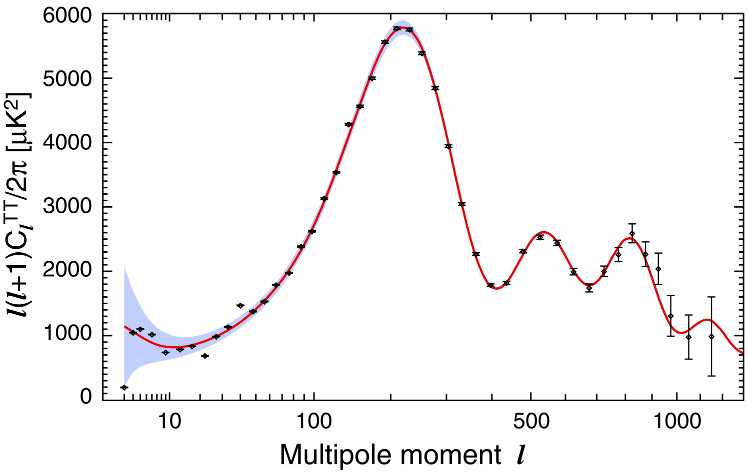

Figure 1.5: The CMB temperature power spectrum (red line), which displays the amplitude of the CMB temperature fluctuation $\Delta T/T$ as a function of angular scale on the sky. The acoustic peaks suggest the interplay of the gravity and radiation pressure and they are very sensitive to cosmological parameters. The black dots are WMAP 7-year data, and blue band is the cosmic-variance. Figure taken from [52].

tensor modes predicted by inflation are small but non-zero. Physically, the tensor modes are the tensor perturbations of space-time in the primitive Universe, where the stretching and squeezing of space-time produces gravitational waves, propagating at the speed of light. In Chapter 4, we shall see how the current and future CMB polarization data can be used to constrain different models of the early Universe.

1.3 The Cosmic Microwave Background Radiation (CMB)

1.3.1 CMB temperature power spectrum

1.3.1.1 Scenario of recombination

From the measurement of the Far-InfraRed Absolute Spectrophotometer (FIRAS) on board the Cosmic Background Explorer (COBE), the CMB was found to be accurately described as the blackbody radiation, which is characterized by the Planck function

$$I_\omega = \frac{\hbar\omega^3}{2\pi^2 c^2}\frac{1}{e^{\frac{\hbar\omega}{K_B T}} - 1}. \tag{1.60}$$

From [58; 59; 60], we know that the data points match the blackbody shape with $T = 2.725K$ incredibly well over the frequencies range 1 to 600 GHz. This tells us that before last scattering, the photons were in thermal equilibrium so the Universe was in a hot and dense status. This provides strong empirical support for the hot Big Bang model.

To understand the physics of CMB, we describe the following statistical aspects. (see [44; 46] for more discussions).

First, let us expand the temperature fluctuation on the sky in terms of spherical harmonics as

$$\Delta T(\mathbf{n}) = \sum_{l,m} a_{lm} Y_{lm}(\mathbf{n}), \tag{1.61}$$

where (θ, ϕ) are the spherical coordinates, and $Y_{lm}(\theta, \phi)$ are the spherical harmonics. If the coefficients a_{lm} describe a pure Gaussian random field which preserves the rotational invariance and translational invariance, all of the statistical information will be contained in the angular power spectrum

$$C_l = \frac{1}{2l+1} \sum_m \langle |a_{lm}|^2 \rangle. \tag{1.62}$$

From the analyzes of the WMAP data, we know empirically that the temperature anisotropies are close to Gaussian [3; 72].

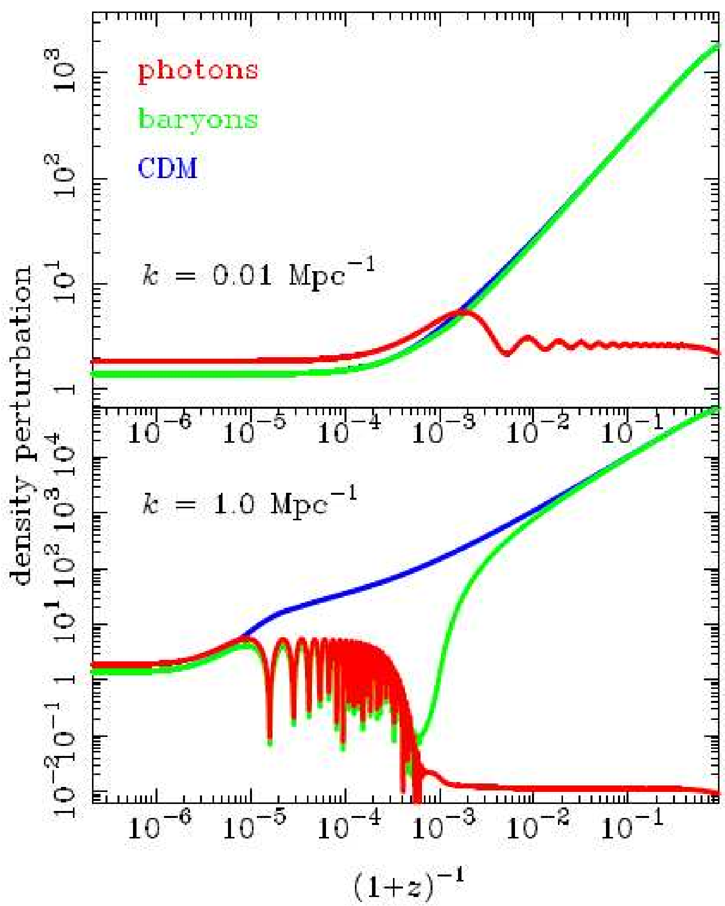

Figure 1.6: Density contrast in conformal Newtonian gauge. The photon, baryon, and CDM density perturbations are plotted in red, green and blue respectively. The upper figure is long wave length case (k=0.01 Mpc^{-1}), and lower figure is the short wave length case (k=1.0 Mpc^{-1}). Figure taken from [62].

In Fig. 1.5, we see that the power spectrum of temperature anisotropies have peaks and troughs between the multipole moments l from 100 to 1500. The explanation of these peaks is as follows: On super-Hubble-length scales, the comoving curvature perturbation is conserved for adiabatic scalar fluctuations, and on the sub-Hubble-length scales, the CDM perturbation grew very slowly. (This is known as the Meszaros effect, see Section 1.4.2.2). However, the gravitationally-driven collapse of the perturbations in the tightly coupled photon-baryon fluid is resisted by the pressure of the radiation, so the gravitational compression and collapse of the fluid is halted by the pressure of the photons. The pressure of the radiation causes the fluid to rebound till recombination when photons become decoupled from the baryons (Fig. 1.6). Therefore, before decoupling, since the perturbations were larger than the Hubble radius at earlier times and formed coherent phase oscillation, the density perturbation of baryons and radiation underwent a period of 'baryon acoustic oscillation', which leave an imprint in the CMB power spectrum in the form of acoustic peaks (Fig. 1.5).

After the photons decouple with baryons and the Universe is deeply into the matter dominated era, the photon perturbations decay rapidly as a result of free-streaming. In contrast, as the Universe entered the matter dominated era, the CDM perturbations grew in amplitude proportional to the scale factor a. The baryons fell into the potential well of CDM perturbations, so the baryon perturbation quickly tracks the perturbation of CDM. The baryons and CDM then grew together at late times (Fig. 1.6).

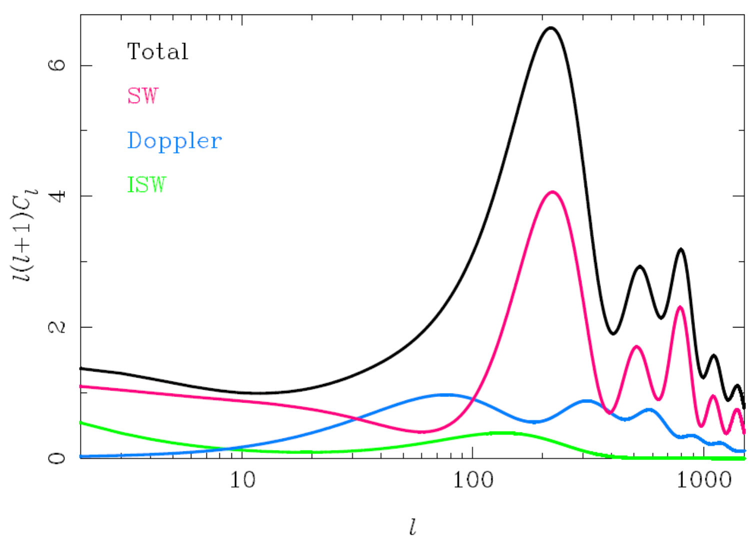

Figure 1.7: Contribution of different terms in Eq. (1.81) to the temperature anisotropies from adiabatic initial conditions: $\delta_\gamma/4 + \psi$ (Sachs-Wolfe effect, magenta line); v_b (Doppler effect, blue line); Integration term (Integrated Sachs-Wolfe effect, green line); total effect (black line). Figure taken from [62].

1.3.1.2 Mathematical Treatment

In this section we calculate the CMB temperature fluctuation caused by scalar perturbation (For more detail descriptions, see [44; 62]). In Eq. (1.32), we retain the scalar potential ϕ and ψ, and set the vector perturbation B_i and tensor perturbation E_{ij}, to zero. We first construct an orthogonal frame of 4−vector $(E_0)^\mu$ and $(E_i)^\mu$ in the perturbed metric (Eq. (1.32)). We take the timelike vector $(E_0)^\mu$ to be the 4−velocity u^μ of an observer at rest with respect to the coordinate system, so it should be parallel to the δ_0^μ. To first order, it is [1]

$$(E_0)^\mu = a^{-1}(1-\psi)\delta_0^\mu, \tag{1.63}$$

since to first order $g_{\mu\nu}(E_0^\mu)(E_0^\nu) = 1$, the spacelike orthogonal basis is

$$(E_i)^\mu = a^{-1}(1+\phi)\delta_i^\mu. \tag{1.64}$$

[We can easily confirm that $g_{\mu\nu}(E_i)^\mu(E_j)^\nu = -\delta_{ij}$, and $g_{\mu\nu}(E_0)^\mu(E_j)^\nu = 0$.]

Based on the above orthogonal basis, we parameterize the photon 4−momentum in terms of the energy E seen by an observer in the observer's rest frame, and the propagation direction e^i seen by the same observer on the $(E_i)^\mu$ basis of spacial coordinate [62]. Note that $\delta_{ij}e^ie^j = 1$. We have the photon 4−momentum

$$\begin{aligned} p^\mu &= E\left[(E_0)^\mu + e^i(E_i)^\mu\right] \\ &= Ea^{-1}\left[(1-\psi)\delta_0^\mu + e^i(1+\phi)\delta_i^\mu\right]. \end{aligned} \tag{1.65}$$

Now we introduce the comoving energy $\epsilon \equiv Ea$ which is constant in the background evolution [62].

Photon moves along geodesics of the perturbed metric so

$$\frac{dp^\mu}{d\lambda} + \Gamma^\mu_{\nu\rho}p^\nu p^\rho = 0, \tag{1.66}$$

where λ is the affine parameter of the geodesic so that $p^\mu = dx^\mu/d\lambda$. Using the parameterization of Eq. (1.65), we have the following equations in the first order

$$\begin{aligned} \frac{d\eta}{d\lambda} &= \frac{\epsilon}{a^2}(1-\psi), \\ \frac{dx^i}{d\lambda} &= \frac{\epsilon}{a^2}(1+\phi)e^i, \\ \Rightarrow \frac{dx^i}{d\eta} &= (1+\phi+\psi)e^i. \end{aligned} \tag{1.67}$$

[1] The perturbed space-time metric is written as $ds^2 = a^2(\eta)[(1+2\psi)d\eta^2 - (1-2\phi)\delta_{ij}dx^idx^j]$.

Therefore the geodesic equation to first order is

$$(1-\psi)\frac{\epsilon}{a^2}\frac{dp^\mu}{d\eta}+\Gamma^\mu_{\nu\rho}p^\nu p^\rho=0. \tag{1.68}$$

Now we can figure out the 0 and i component of the geodesic equation (1.68). By using an equation of the time-derivative of the gravitational potential

$$\frac{d\psi}{d\eta}=\dot{\psi}+e^i\partial_i\psi, \tag{1.69}$$

one can reach the simplified geodesic equations

$$\frac{1}{\epsilon}\frac{d\epsilon}{d\eta}=-\frac{d\psi}{d\eta}+(\dot{\psi}+\dot{\phi}), \tag{1.70}$$

$$\frac{de^i}{d\eta}=-(\delta^{ij}-e^ie^j)\partial_j(\phi+\psi), \tag{1.71}$$

where the overdot means ∂_η.

Equation (1.70) describes how the comoving energy ϵ evolves along the photon path in the presence of metric perturbations. In absence of perturbation, ϵ is constant, but this is modified if there is either (a) metric perturbations along the photon path, or (b) time-evolving gravitational potentials. The latter case can be important at the later dark energy dominant era and at the matter-radiation equality epoch. This leads to the Integrated Sach-Wolfe effect that we have seen in Section 1.3.1.1 and Fig. 1.7. Equation (1.71) describes how the photon direction is deflected if the gradient of gravitational potential is perpendicular to the line of sight.

Integrating Eq. (1.70) from emission point E at the last scattering surface to the observed point 0, we get

$$\frac{\epsilon_0}{\epsilon_E}=1+(\psi_E-\psi_0)+\int_E^0(\dot{\phi}+\dot{\psi})d\eta. \tag{1.72}$$

Therefore, the comoving photon energy changes due to either (a) gravitational redshifting, or (b) time-varying gravitational potentials. For the former case, if the gravitational potential at the emission point is deeper than observing point $\psi_E<\psi_0$, there is a net loss of energy, and vice versa. For the latter, for a decaying gravitational potential ($\dot{\psi}+\dot{\phi}<0$), a photon will be blueshifted since it gains more energy when falling in a potential and loses less energy when climbing out [44; 62].

Therefore, in the CMB rest frame, the ratio of the temperature of the CMB received by an observer with zero redshift $T(\mathbf{e})$ to the mean temperature of the CMB at last scattering surface $\overline{T}_*$ is just the ratio of the proper energy of photon received by an observer at $z=0$ to that emitted at the last scattering surface (in the CMB rest frame):

$$\left.\frac{T(\mathbf{e})}{\overline{T}_*}\right|_{CMBframe} = \frac{\epsilon_0}{\epsilon_E}\frac{a_E}{a_0}$$

$$= \frac{a_E}{a_0}\left(1 + (\psi_E - \psi_0) + \int_E^0 (\dot{\phi} + \dot{\psi}) d\eta\right). \tag{1.73}$$

Now let us take into account two different effects that could change the observed temperature anisotropy [62]. The first thing we should consider is the Doppler effect. The key quantity here is the Lorentz-invariant quantity $p^\mu u_\mu$ (p^μ is the photon's 4-momentum and u_μ is observer's 4-velocity). Suppose in the CMB rest frame a photon is moving in direction $\mathbf{n}$ with energy E, $p^\mu = E(1, \mathbf{n})$, and observer is moving at velocity $\mathbf{v}$, so $u^\mu = \gamma(1, \mathbf{v})$ and $u_\mu = \gamma(1, -\mathbf{v})$ where $\gamma = (1 - v^2)^{-1/2}$ is the Lorentz-factor. Therefore,

$$E_{CMB} = p^\mu u_\mu = E\gamma(1 - \mathbf{v} \cdot \mathbf{n}), \tag{1.74}$$

and photon distribution (also Lorentz-invariant) is

$$f(p^\mu) \propto \frac{1}{e^{E_{CMB}/T_{CMB}} - 1} = \frac{1}{e^{E\gamma(1+\mathbf{v}\cdot\mathbf{e})/T_{CMB}} - 1}, \tag{1.75}$$

which makes the photon distribution like a blackbody but the observed temperature varies over the sky as $T(\mathbf{e}) = T_{CMB}/\gamma(1 + \mathbf{v} \cdot \mathbf{e}) \simeq T_{CMB}(1 - \mathbf{v} \cdot \mathbf{e})$. Since $\mathbf{v} = -\mathbf{v_b}$, in the observer's rest frame, the CMB temperature on direction $\mathbf{e}$ is

$$\frac{T(\mathbf{e})}{\overline{T}_*} = \frac{a_E}{a_0}\left(1 + (\psi_E - \psi_0) + e_i v_b^i + \int_E^0 (\dot{\phi} + \dot{\psi}) d\eta\right). \tag{1.76}$$

The second thing is to determine how the scale factor a varies on the perturbed last scattering surface, i.e. we need to find the relation between a_E and a_*, where a_* is the scale factor of the unperturbed space-time at the last scattering surface [62]. Due to the perturbed space-time, the photon energy density at the last scattering surface E is

$$\overline{\rho}_\gamma(\eta_* + \Delta\eta)(1 + \delta_\gamma) = \overline{\rho}_\gamma(\eta_*), \tag{1.77}$$

where we have used the fact that energy density of photons is uniform over the last scattering surface and equal to the background value. Taylor expanding the above equation one can get the first order perturbation

$$\Delta\eta = -\frac{\delta_\gamma}{\dot{\overline{\rho}}_\gamma/\overline{\rho}_\gamma} = \frac{\delta\rho_\gamma}{4\mathcal{H}}, \tag{1.78}$$

therefore we have

$$a_E = a(\eta + \Delta\eta) = a(\eta)(1 + \mathcal{H}\Delta\eta) = a_*(1 + \frac{\delta_\gamma}{4}). \tag{1.79}$$

Substituting this equation into Eq. (1.76), we have

$$\frac{T(\mathbf{e})}{\overline{T}_*} = \frac{a_*}{a_0}\left(1 + \frac{\delta_\gamma}{4} + (\psi_E - \psi_0) + e_i v_b^i + \int_E^0 (\dot{\phi} + \dot{\psi}) d\eta\right) \tag{1.80}$$

$$\Longrightarrow T(\mathbf{e}) \;\; = \;\; \overline{T}_0 \left(1 + \frac{\delta_\gamma}{4} + (\psi_E - \psi_0) + e_i v_b^i + \int_E^0 (\dot{\phi} + \dot{\psi}) d\eta \right),$$

where $\overline{T}_0 = \overline{T}_* a_* / a_0$ is the background CMB temperature at the reception point. Thus, the observed temperature fluctuation is [62]

$$\frac{\Delta T(\mathbf{n})}{\bar{T}_0} = \frac{T(\mathbf{n}) - \bar{T}_0}{\bar{T}_0} = \frac{1}{4}\delta_r + (\psi_E - \psi_0) + e_i v_b^i + \int_E^0 (\dot{\phi} + \dot{\psi}) d\eta, \tag{1.81}$$

where $T(\mathbf{n})$ is the observed temperature in direction $\mathbf{n}$, $\bar{T}_0$ is the CMB background temperature at the point of reception. The four contributions in Eq. (1.81) can be summarized as follows: $\delta_r/4$ is the intrinsic temperature fluctuation on the last scattering surface, ψ_E is the gravitational redshift when the photons climb out of a potential well. The two terms together $\delta_r/4 + \psi_E$ are called the 'Sachs-Wolfe' effect. $e^i v_b^i$ is the Doppler effect due to the relative motion of the observer with respect to CMB rest frame. Finally, the integration term is the 'Integrated Sachs-Wolfe' effect which describes the gravitational redshift arising from the time-varying potential.

It is important to recognize that the perfect fluid approximation of photons and matter is idealized and that in reality, the two components are not perfectly coupled. This imperfect coupling leads to the damping of the temperature fluctuations on small scales (often called Silk damping [65]). In fact, on scales smaller than the damping scale ($\lambda_{damp} = c\sqrt{t_{rec} t_s}$, t_{rec} and t_s are recombination time and photon scattering time scale), the photons diffuse and erase small scale perturbations so that the temperature power spectrum at high multipoles ($l > 2500$) decline as l^{-4} (see Figs. 1.5 and 1.7).

The CMB power spectrum therefore encodes much information on early Universe physics, the matter content of the Universe, as well as geometrical information that relates physical scales to angular scales on the sky.

1.3.2 CMB polarization

CMB polarization has become a very powerful tool to probe the physics of the early Universe. Since the CMB temperature anisotropies are sourced by the primordial fluctuations, the anisotropy of Thomson scattering can generate quadrupole anisotropy of the CMB photons [56; 76]. Therefore, the polarization signal and the cross-correlation of the polarization with temperature provide an effective check of the standard cosmology paradigm, and supply a powerful tool to constrain cosmological parameters. Furthermore, since the polarization pattern on the sky encodes much information on the primordial perturbations, it may strongly constrain models of inflation.

The relationship between the temperature anisotropies and polarization pattern is determined by the properties of Thomson scattering [56; 76]. If the incoming radiation field is isotropic, then the outgoing radiation remains unpolarized since the orthogonal polarization pattern cancels out. However, if the incoming radiation field has a quadrupole component, such as shown in Fig. 1.8,

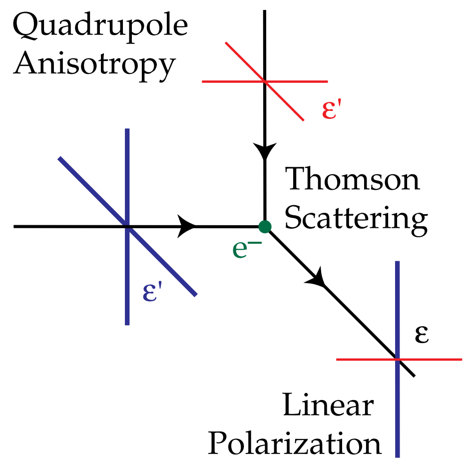

Figure 1.8: Thomson scattering of radiation with a quadrupole anisotropy generates linear polarization. Red colors (thick lines) represent hot radiation, and blue colors (thin lines) cold radiation. Figure taken from [76].

the outgoing radiation field will gain a net polarization pattern due to the anisotropic Thomson scattering. Thus, a linear polarization pattern of the radiation field is generated when the photons decouple from the baryons just before the recombination. The polarization anisotropies correlate with the temperature anisotropies since both of them are related to the density fluctuation.

The polarized radiation field can be described by a 2×2 intensity matrix $I_{ij}(\mathbf{n})$, where $\mathbf{n}$ denotes the direction on the sky, and $I_{ij}(\mathbf{n})$ is based on the two orthogonal basis $\mathbf{e}_1$ and $\mathbf{e}_2$ that are perpendicular to $\mathbf{n}$. Linear polarization is related to two Stokes parameter $Q = \frac{1}{4}(I_{11} - I_{22})$ and $U = \frac{1}{2}I_{12}$, whereas the temperature anisotropy is $T = \frac{1}{4}(I_{11} + I_{22})$. Thus, the polarization magnitude and angle are $P = \sqrt{Q^2 + U^2}$ and $\alpha = \frac{1}{2}\tan^{-1}(U/Q)$. The temperature anisotropy is a scalar field which is invariant under the rotation perpendicular to $\mathbf{n}$, so we expand the temperature in terms of spin-0 spherical harmonics as Eq. (1.61).

However, the Stokes parameters Q and U transform under a rotation ψ as $(Q \pm iU)(\mathbf{n}) \to e^{\mp 2i\psi}(Q \pm iU)(\mathbf{n})$. Thus, $(Q \pm iU)(\mathbf{n})$ requires an expansion with spin-2 spherical harmonics

$$(Q + iU)(\mathbf{n}) = \sum_{lm} a_{lm}^{(\pm 2)}\,{}_{\pm 2}Y_{lm}(\mathbf{n}). \tag{1.82}$$

We can introduce the linear combinations of the two coefficients $a_{lm}^{(2)}$ and $a_{lm}^{(-2)}$ as

$$a_{lm}^{E} = -\frac{1}{2}(a_{lm}^{(2)} + a_{lm}^{(-2)}),\ a_{lm}^{B} = -\frac{1}{2i}(a_{lm}^{(2)} - a_{lm}^{(-2)}), \tag{1.83}$$

then the polarization field is expressed in terms of two scalar fields E and B instead of spin-2 quantity Q and U

$$E(\mathbf{n}) = \sum_{lm} \left[\frac{(l+2)!}{(l-2)!}\right]^{\frac{1}{2}} a^E_{lm} Y_{lm}(\mathbf{n}), \;\; B(\mathbf{n}) = \sum_{lm} \left[\frac{(l+2)!}{(l-2)!}\right]^{\frac{1}{2}} a^B_{lm} Y_{lm}(\mathbf{n}). \tag{1.84}$$

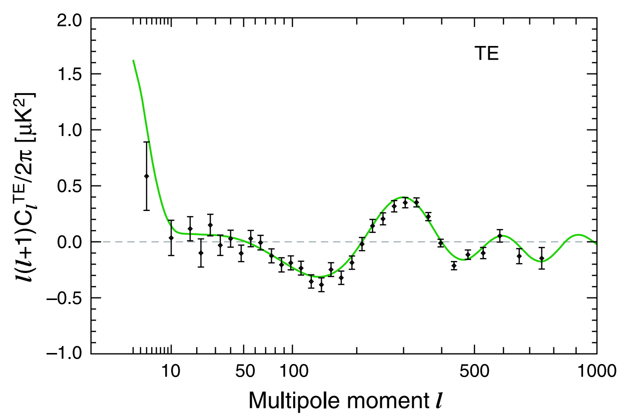

Figure 1.9: The power spectrum of the cross-correlation between temperature and E-mode polarization anisotropies. The anti-correlation at $100 < l < 200$ and the positive correlation at $200 < l < 400$ are due to the phase coherence of fluctuation generated during inflation [53]. The data is WMAP 7-year result [52].

The E and B-modes completely describe the polarization field. The E mode is the curl-free mode with polarization vector radial for a cold spot and tangential for a hot spot. The B-mode is the divergence-free mode with polarization vector vortical around a given point on the sky.

Since both the temperature fluctuation and the polarization pattern are sourced by the primordial fluctuations, it is possible to cross-correlate these different modes. Due to the reason of symmetry, there are only four non-zero cross-correlation: TT, TE, EE, BB.[1]

The angular power spectrum is defined for temperature and polarization as

$$C_l^{X,Y} = \frac{1}{2l+1} \sum_{lm} \left\langle a^X_{lm} a^Y_{lm} \right\rangle, \;\; X, Y = T, E, B. \tag{1.85}$$

Figure 1.9 shows the WMAP 7-year measurement of the TE correlation [52]. We can see that the theoretical prediction for the phase coherence generated during inflation is consistent with the observational data to high accuracy, providing strong support for the inflationary model. As we have seen in Fig. 1.5, the standard ΛCDM prediction of the temperature power spectrum fits the data at all angular scales very well. However, the other polarization power spectra have not been measured as accurately as the TT power spectrum. So far, the EE spectrum has been measured, but only upper limits have been placed on the BB spectrum (Fig. 1.10 and 1.11) [3; 51; 52; 56].

[1]This assumes the parity-conservative processes in the early Universe. Since both T and E has parity factor $(-1)^l$ under rotation, while B has parity $(-1)^{l+1}$ under rotation, the TB and EB should vanish for symmetry reasons. See more discussion in [3].

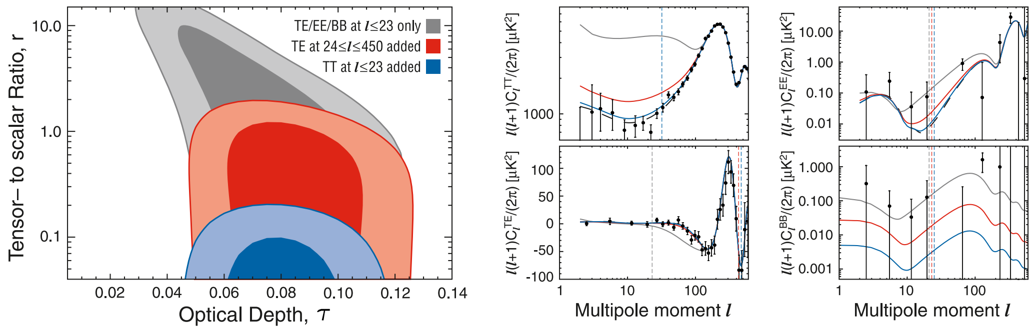

Figure 1.10: WMAP 5-year measurements of the temperature and polarization power spectrum to constrain the tensor-to scalar ratio. Left: Contours show 68% and 95% C.L of the parameter space. The gray region is the constraint from the low-l multipole data (TE, EE, BB at $l \leq 23$) only, and the red region is from the low-l data plus the high-l TE data at $24 \leq l \leq 450$. Finally, the blue region is the constraint from the low-l polarization data, the high-l TE correlation data, and the low-l temperature data at $l \leq 23$. Right: the gray curves show (r, τ)=(10,0.050), the red curves (r, τ)=(1.2,0.075) and the blue curves (r, τ)=(0.2,0.080), where τ is the optical depth $\tau = \int_0^{\eta_0} n_e \sigma_T a d\eta$. Figure taken from [3].

The dependence on cosmological parameters of these various power spectrum differs. The current measurement of TT and TE power spectrums provides the most powerful constraints on cosmological parameters. In the near future, Planck will measure the EE and BB polarization spectrum more precisely than WMAP, which will help to break parameter degeneracies [27].

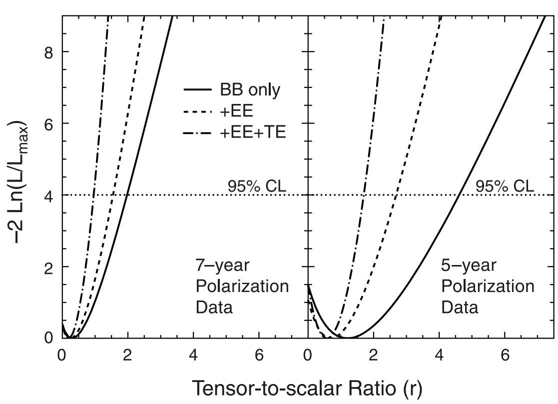

Figure 1.11: The marginalised likelihood of tensor-to-scalar ratio r in WMAP 7-year data and 5-year data, from the polarization data (BB, EE and TE) alone. All the other cosmological parameters, including the optical depth, are fixed at the 5-year best-fit ΛCDM model [3]. The vertical axis $-2\ln(L/L_{max})$ is the standard χ^2 under the Gaussian approximation. The dashed line $-2\ln(L/L_{max}) = 4$ corresponds to the 2σ CL. The solid, dashed and dot-dashed lines show the likelihood as a function of r from the BB-only, BB+EE, and BB+EE+TE data. (Left) The 7-year polarization data. WMAP 7-year data shows $r < 2.1$, 1.6, and 0.93 (95.4% CL) from the BB-only, BB+EE, and BB+EE+TE data, respectively. (Right) The 5-year polarization data. $r < 4.7$, 2.7, and 1.6 (95.4% CL). Figure taken from [72].

Parameters	WMAP7 Only	WMAP7+BAO+H_0
n_s	0.967 ± 0.014	0.968 ± 0.012
n_s r	$0.982^{+0.020}_{-0.019}$ < 0.36 (95% CL)	0.973 ± 0.014 < 0.24 (95% CL)
n_s α_s	$1.027^{+0.050}_{-0.051}$ -0.034 ± 0.026	1.008 ± 0.042 -0.022 ± 0.020
n_s r α_s	1.076 ± 0.065 < 0.49 (95% CL) -0.048 ± 0.029	1.070 ± 0.060 < 0.49 (95% CL) -0.042 ± 0.024

Table 1.2: WMAP 7-year constraints on n_s, r and α_s [72]. All of the other cosmological parameters in ΛCDM model are marginalized.

In addition to the temperature and E-mode power spectrum, the B-mode power spectrum can also provide a very powerful tool to constrain the inflation model and probe the physics of the early Universe. Scalar perturbation produces only E-mode polarization pattern, while tensor perturbation produces both E and B-modes. Therefore, probing B-mode polarization is an important test of primordial gravitational waves. The current measurement of B-mode polarization can provide only upper limits (Figs. 1.10 and 1.11), but the next generation of CMB polarization measurements should improve these limits substantially [27; 56].

1.3.3 Prospects of constraining inflation

Current cosmological observations of the temperature power spectrum, combined with the other astrophysical measurements, such as the distant Type Ia supernovae and the angular diameter distance data from baryon acoustic oscillations (BAO) can place precise constraints on cosmological parameters. Here, we give a brief review of the current tightest constraints.

Komatsu et al. [72] used the WMAP 7-year data, combined with the angular diameter distance data of BAO at $z = 0.2$ and 0.35 [78] and a Gaussian prior on the present-day Hubble constant $H_0 = 74.2 \pm 3.6$ km/s/Mpc (68% CL, [77]) to constrain cosmological parameters. Here, we present their 1σ constraints on spectral index n_s, its running α_s (Eq. (1.37)) and tensor-to-scalar ratio r in Table 1.2, since these parameters are related to the inflation models.

Several points should be noticed concerning their results [72]:

- Assuming zero running of the spectral index ($\alpha_s = 0$), the best-fits of scalar spectral index are around 0.967 (i.e. a red power spectrum). If no tensors (r=0) are assumed, the scale-invariant Harrison-Zel'dovich power spectrum, $n_s = 1$, is excluded from the peak likelihood at the 99.5% confidence level.

- There is no strong evidence for the running index α_s, since for any combination of data sets, α_s is always very close to zero.

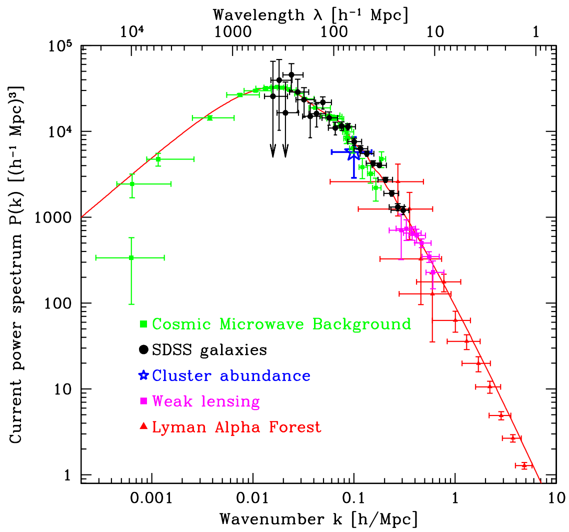

Figure 1.12: Comparison of matter power spectrum $P(k)$, inferred from the CMB temperature anisotropy to constraints from other observations, including the observed galaxy distributions. The consistency of independent results shows that the density perturbations are the seeds for structure growth. Figure taken from [5].

- The current tightest constraint on r ($r < 0.24$) comes almost exclusively from the combined measurements of TT+TE+EE+BB power spectrum (Fig. 1.11 and Table 1.2) and BAO measurement and H_0 prior. The direct B-mode polarization limits make a negligible contribution to the constraints on r. WMAP data is able to rule out $\lambda\phi^4$ inflation model [72], while a large class of models is still consistent with WMAP 7-year data.

- Since r is degenerated with n_s and τ(optical depth, defined as $\tau = \int_0^{\eta_0} n_e \sigma_T a d\eta$), a better constraint on these two quantities will improve the constraints on r.

By using the WMAP parameter constraints, we can compute the matter power spectrum according to the WMAP type parameters. This is found to be in good agreement with power spectrum measurements from galaxy surveys (Fig. 1.12). This agreement suggests that the primordial density perturbations were the seeds of structure formation in the late Universe.

The future for CMB observations is promising, since many high precision observations are planned over the next few years. The Planck satellite of European Space Agency [27] will provide very much improved measurements on the E- and B-modes polarization, and it may be possible to detect a tensor-to-scalar ratio of about 0.05 magnitude [54; 55]. The Planck satellite will be supplemented by many ground-based measurements of the small scale fluctuations and polarization data (such as EBEX [32] and Spider [33]). In addition, the CMBPol satellite proposes to improve the sensitivity of B-modes by almost two orders of magnitude [46; 56].

1.4 The Growth of Structure

1.4.1 Mass Fluctuations and Matter Power Spectrum

We define the density contrast of the fluctuations which source the structure formation

$$\delta(\mathbf{x}) = \frac{\rho(\mathbf{x}) - \overline{\rho}}{\overline{\rho}}, \tag{1.86}$$

where $\overline{\rho}$ is the mean density and $\rho(\mathbf{x})$ is the density at position $\mathbf{x}$. Inflation predicts Gaussian fluctuations whose power spectrum is statistically homogeneous and isotropic. This means that each of the Fourier modes of the fluctuation $\delta_{\mathbf{k}}$ has no correlation with other modes. Thus, we can further understand why it is convenient to work in Fourier space

$$\delta_{\mathbf{k}} = \int \delta(\mathbf{x}) e^{-i\mathbf{k}\cdot\mathbf{x}} d^3\mathbf{x}, \tag{1.87}$$

rather than in real space. Statistical isotropy implies

$$\langle \delta_{\mathbf{k}} \delta_{\mathbf{k}'} \rangle = (2\pi)^3 P(k) \delta^3(\mathbf{k} - \mathbf{k}'), \tag{1.88}$$

i.e. the power spectrum is described by a scalar function $P(k)$.

Now we can calculate the mass fluctuation within some volume to quantify the amplitude of the fluctuations[1] [79]

$$\begin{aligned}
\left\langle \left(\frac{\delta\rho}{\rho} \right)^2 \right\rangle &= \langle \delta^2(\mathbf{x}) \rangle = \int \frac{d^3\mathbf{x}}{V} \delta^2(\mathbf{x}) \\
&= \int \frac{d^3\mathbf{x}}{V} \int \frac{d^3\mathbf{k}}{(2\pi)^3} \frac{d^3\mathbf{q}}{(2\pi)^3} \delta_{\mathbf{k}} \delta^*_{\mathbf{q}} e^{i(\mathbf{k}-\mathbf{q})\cdot\mathbf{x}} \\
&\simeq V^{-1} \int \frac{d^3\mathbf{k}}{(2\pi)^3} |\delta_k|^2 = V^{-1} \int \frac{k^3 |\delta_k|^2}{(2\pi^2)} \frac{dk}{k},
\end{aligned}$$

where the second equality is valid for sufficiently large volume [2] V. The integrand is the dimensionless power spectrum

$$\Delta^2(\mathbf{k}) = \frac{V^{-1}}{2\pi^2} k^3 |\delta_k|^2, \tag{1.89}$$

which is the power spectrum popular in the early Universe community. In the large scale structure community, the k^{-3} factor is often added so that it has the dimension k^{-3} [44], i.e. $P(k) =$

[1] In the above calculation, we have used the Fourier transformation $\delta(\mathbf{x}) = \int d^3\mathbf{k} \delta_{\mathbf{k}} e^{i\mathbf{k}\cdot\mathbf{x}}/(2\pi)^3$, and delta function $\delta^3(\mathbf{x}) = \int e^{i\mathbf{k}\cdot\mathbf{x}} d^3\mathbf{x}/(2\pi)^3$.

[2] Here the second equality actually uses the "Ergodic Hypothesis": the ensemble average of many different realization can be expressed as an average over a sufficient large volume of a single realization.

$V^{-1}|\delta_k|^2$. In the following, we shall use the dimensional power spectrum $P(k)$.

To quantify the magnitude of the fluctuation, we calculate the fluctuations on some particular scale R, i.e. we filter the density fluctuation with some *window function*. In real space, the simplest window function, a top-hat window function is defined by

$$\begin{aligned} W(r) &= 1 \text{ if } r \leq R, \\ &= 0 \text{ if } r > R. \end{aligned} \tag{1.90}$$

The Fourier transform of this function is

$$W_k(R) = 4\pi R^3 \left[\frac{\sin kR}{(kR)^3} - \frac{\cos kR}{(kR)^2} \right]. \tag{1.91}$$

Now the total mass in a volume R with window function $W(|\mathbf{y}|)$ is

$$M_R = \int d^3\mathbf{y} \rho_b W(|\mathbf{y}|) = V_w \rho_b, \tag{1.92}$$

and the mass fluctuation within a volume centered at some point $\mathbf{x}$ is

$$\delta M_R(\mathbf{x}) = \rho_b \int d^3\mathbf{y} \delta(\mathbf{x}+\mathbf{y}) W(|\mathbf{y}|). \tag{1.93}$$

Therefore, the Fourier transformation of mass contrast is

$$\left(\frac{\delta M}{M}\right)_R = \int \frac{d^3\mathbf{k}}{(2\pi)^3} \left(\frac{\delta_k W_k}{V_w}\right) e^{i\mathbf{k}\cdot\mathbf{x}}, \tag{1.94}$$

from which one can reach the mean square fluctuation as

$$\begin{aligned} \sigma^2(M) \equiv \sigma^2(R) &= \left\langle \left(\frac{\delta M}{M}\right)^2_R \right\rangle \\ &= \int \frac{dk}{2\pi^2} k^2 P(k) \left(\frac{3 j_1(kR)}{kR}\right)^2, \end{aligned} \tag{1.95}$$

which characterize the strength of fluctuations on different scales R.

We will now turn to the matter power spectrum. In Sections 1.2 and 1.3, we have shown that the primordial power spectrum from inflation is nearly scale-invariant (Eq. (1.39)), i.e. the strength of primordial perturbation is approximately equal on different scales. However, the cosmic evolution acts like a filter which can suppress and enhance the strength of the perturbation spectrum on different scales by a variety of processes: growth under self-gravitation, Silk damping, free-streaming etc. The "filtering" causes the spectrum in the late times to have more power on some scales, and less power on other scales (We shall summarize the main effect in the next

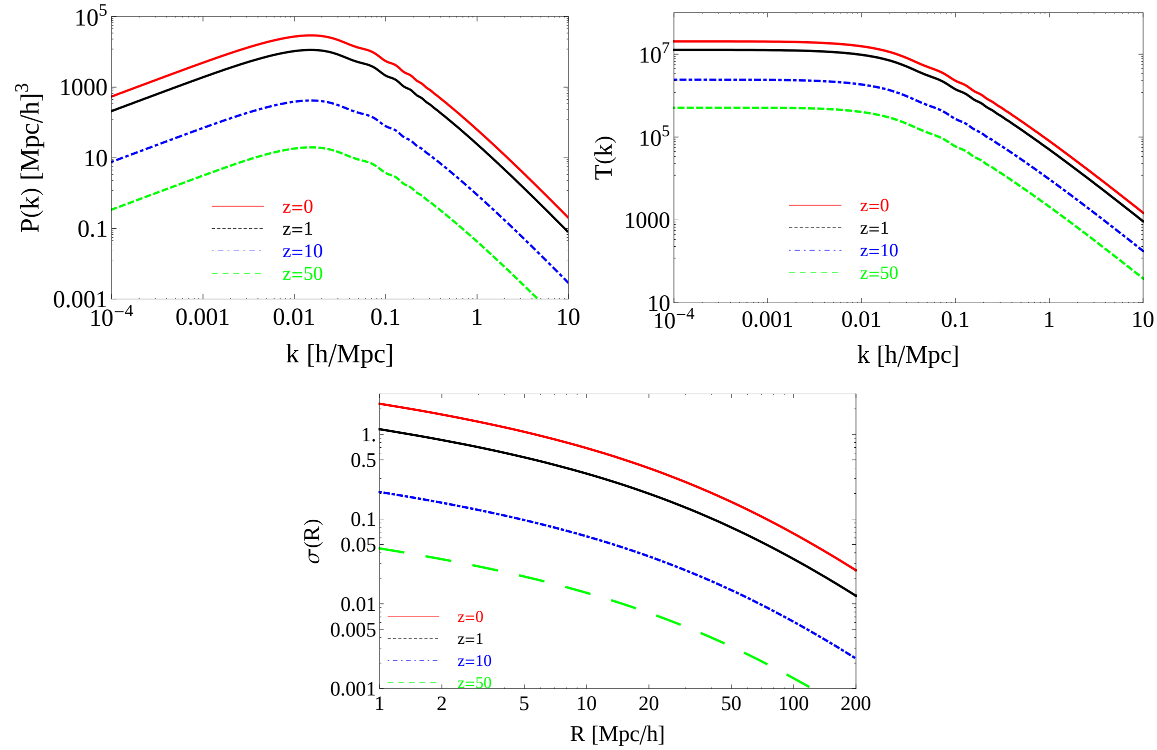

Figure 1.13: Power spectrum (upper-left), transfer function (upper-right), and root-mean-square of mass fluctuation in linear perturbation theory at different redshift. Here we adopt ΛCDM model with WMAP 5-year parameters $\Omega_b = 0.0449$, $\Omega_c = 0.222$,$\Omega_\Lambda = 0.734$,$h = 0.71$,$\sigma_8 = 0.801$ and $n_s = 0.963$ [3].

subsection). The overall filter can be encapsulated in the *transfer function* $T(k, z)$ [1] , so that the power spectrum at redshift z can be written as

$$P(k, z) = P_s(k)T^2(k, z), \tag{1.96}$$

where $P_s(k)$ is the power spectrum of primordial fluctuations. To accurately calculate the transfer function and thus matter power spectrum, one needs to solve a set of Boltzmann hierarchy equations to follow the evolution of various components of the Universe. People have developed several Boltzmann codes to solve this problem, such as CMBFAST [24] and CAMB [25]. In practice, it has been figured out semi-analytic formulae that fit the numerical results for the transfer function quite precisely [81].

In Fig.1.13, we plot the matter power spectrum (upper-left), transfer function (upper-right) and variance of mass fluctuation (lower panel) from linear perturbation theory at different redshift z. The cosmic evolution as a filtering effect can be seen from the upper-right panel of Fig. 1.13. Since the growth function $D(t) \propto a$ for matter-dominated Universe, the difference between power spectra at different redshifts is just a time-evolution factor which enhances or suppresses power on all scales. In the lower panel of Fig. 1.13, we plot the root-mean-square of mass fluctuation

[1]Only when all of the physical process responsible for filtering has finished, the transfer function can be separate as $T(k, t) = T(k)D(t)$, while in general this is not true.

as a function of scale R [Mpc/h] through Eq. (1.95). The density perturbations detach from the background when they reach the overdensity of unity, the perturbations become non-linear and begin to form dark matter halos.

1.4.2 Linear growth of structure

Now let us briefly summarize the evolution of adiabatic perturbations of a perfect fluid in the expanding Universe, i.e. Jeans theory. We will then apply this theory to the spatially flat, CDM dominant Universe. We shall first ignore the effect of cosmological constant Λ, since it makes a negligible contribution to the energy density before $z \sim 2$, then describe the growth of structure for models with nonzero Λ in Section 1.4.2.2.

1.4.2.1 Jeans equation

Linear perturbation theory gives the following Jeans equation from the combination of continuity, Euler and Poisson equations for a single perfect fluid in an expanding Universe [62; 79]

$$\ddot{\delta} + 2\frac{\dot{a}}{a}\dot{\delta} + \left(\frac{c_s^2 k^2}{a^2} - 4\pi G\overline{\rho}\right)\delta = 0, \tag{1.97}$$

where c_s is the sound speed of the perfect fluid, $\overline{\rho}$ is the background density, the a is the cosmic scale factor, and the dot refers to the derivative with respect to cosmic time. This is the equation for a damped oscillator in an expanding Universe provided that $c_s^2 k^2/a^2 > 4\pi G\overline{\rho}$, since in this situation, the pressure support leads to acoustic oscillation in the fluid system. In contrast, if $c_s^2 k^2/a^2 < 4\pi G\overline{\rho}$ the system is unstable and gravitational collapse will occur. Therefore, the critical wavelength, *the Jeans wavelength* is defined as

$$\lambda_J \equiv c_s\sqrt{\frac{\pi}{G\overline{\rho}}}, \tag{1.98}$$

so that if the proper wavelength $2\pi a/k$ exceeds λ_J, gravitational collapse will take place. It is also common to express the Jeans criterion in terms of Jeans mass as

$$M_J = \frac{4\pi}{3}\rho\left(\frac{\lambda_J}{2}\right)^3. \tag{1.99}$$

In an expanding Universe, the Jeans wavelength changes with time. The evolution of a given perturbation with wavelength λ can be studied by solving the full relativistic perturbation equations [44; 79]. In the following discussions, we will discuss the evolution of the sub-Hubble radius modes ($\lambda < H^{-1}$) in various cases. For super-Hubble-length modes, the curvature perturbation remains constant until it crosses the Hubble radius.

1.4.2.2 Sub-Hubble-length modes

CDM perturbation

Radiation dominant era— Meszaros effect The Meszaros effect describes how the CDM grows only logarithmically during the radiation dominant era on scales smaller than the Hubble radius [62]. Since the radiation is assumed to dominate over CDM, and the pressure of CDM can be neglected, the Jeans equation (1.97) becomes

$$\ddot{\delta}_c + 2\frac{\dot{a}}{a}\dot{\delta}_c - 4\pi G \sum_{j=r,c} \overline{\rho}_j \delta_j = 0, \tag{1.100}$$

in which the summation includes both the radiation and matter. However, the Jeans length for radiation in the baryon-radiation fluid ($c_s = 1/\sqrt{3}$) during the radiation dominant era is the order of the Hubble radius (Eq. (1.98)), so perturbations with scales much smaller than this will oscillate as sound waves so that the average contribution on δ_c is negligible. Therefore, in the summation of Eq. (1.100), we can neglect the radiation term so the equation becomes

$$\ddot{\delta}_c + \frac{1}{t}\dot{\delta}_c - 4\pi G\overline{\rho}_c\delta_c = 0, \tag{1.101}$$

where we use $a \propto t^{1/2}$ and $H = 1/(2t)$. Since this is radiation domination ($\overline{\rho}_\gamma \gg \overline{\rho}_c$),

$$\ddot{\delta}_c \sim \frac{1}{t}\dot{\delta}_c \sim H^2\delta_c \gg 4\pi G\overline{\rho}_c\delta_c. \tag{1.102}$$

Therefore, we can neglect the last term in Eq. (1.101), and the final equation has the solution

$$\delta_c \propto \text{const}, \quad \text{and} \quad \ln(t), \tag{1.103}$$

i.e. the rapid expansion due to the unclustering radiation leads to logarithmic growth rate of δ_c.

Matter dominant era Perturbations within the Hubble-length can grow more rapidly once the Universe becomes matter dominated. This can also be easily derived from Jeans equation (1.97) by using the fact $a \propto t^{2/3}$, $H = 2/(3t)$ and $4\pi G\overline{\rho} = 2/(3t^2)$

$$\ddot{\delta}_c + \frac{4}{3t}\dot{\delta}_c - \frac{2}{3t^2}\delta_c = 0. \tag{1.104}$$

By substituting a power law form $\delta_c \propto t^p$, one can get two independent solutions $\delta_c \propto t^{-1}$(decaying mode) and $\delta_c \propto t^{2/3} \propto a$. The *growing mode* of CDM perturbation grows as a and $t^{2/3}$ in an expanding Universe, which is fundamentally different from the non-expanding Universe, since in

Sub-Hubble-length	Radiation	Matter		Λ
	$t < t_{eq}$	$t_{eq} < t < t_{dec}$	$t_{dec} < t < t_\Lambda$	$t > t_\Lambda$
δ_b	oscillation	oscillation	a	constant
M_{Jb}	a^3	$a^{3/2}$	$a^{-3/2}$	constant
δ_c	const	a		constant

Table 1.3: The summary of the evolution of sub-Hubble-length density contrast and Jeans mass.

the latter case, Eq. (1.97) has exponential solution ($\dot{a} = 0$)

$$\delta(t) \propto e^{\pm t/\tau}, \quad \tau = 1/\sqrt{4\pi G\rho_0}. \tag{1.105}$$

Baryonic perturbation

Radiation dominant era The baryons and photons remain tightly coupled through Thomson scattering until the epoch of decoupling $z_{dec} \simeq 1100$. The sound speed for the mixed baryon-photon fluid is [44]

$$c_s \simeq \frac{c}{\sqrt{3}} \left(1 + \frac{3}{4}\frac{\rho_b}{\rho_\gamma}\right)^{-\frac{1}{2}}. \tag{1.106}$$

Therefore, during the radiation domination, $\rho_\gamma \gg \rho_b$ so $c_s = c/\sqrt{3}$, i.e. the tightly coupled photon-baryon plasma supports the propagation of sound waves.

Now let us compute the evolution of Jeans mass. Since Jeans wavelength is $\lambda_J = (c/\sqrt{3})\sqrt{\pi/G\rho_\gamma} \propto a^2$, Jeans mass becomes [79]

$$M_{Jb} = 3.2 \times 10^{14} M_\odot \left(\frac{\Omega_b}{\Omega_m}\right) \left(\Omega_m h^2\right)^{-2} \left(\frac{a}{a_{eq}}\right)^3. \tag{1.107}$$

Such a high mass threshold prohibits the growth of structure.

Matter dominant era Let us calculate how the Jeans wavelength and Jeans mass changed during this period. Since the decoupling of photon-baryon plasma can substantially change the sound speed and Jeans mass, we separate this period into two stages: (A) $t_{eq} < a < t_{dec}$ (before decoupling); (B) $t_{dec} < t < t_\Lambda$ (after decoupling).

- $t_{eq} < a < t_{dec}$. Although the dark matter has already started to collapse, the pressure from the photons prevents the collapse of the baryons, and causes the perturbation in the photon-baryon fluid to oscillate as sound waves. Therefore, the sound speed is close to that in radiation $c_s \simeq c/\sqrt{3}$, so the Jeans wavelength becomes $\lambda_J = c_s\sqrt{\pi/G\rho_{rad}} \propto a^{3/2}$ and the Jeans mass $M_J \propto a^{3/2}$ is the order of $10^{14}M_{\odot}$. Therefore, the solution of the density contrast δ_b from non-relativistic perturbation theory shows oscillatory behavior over this period of time, which can be seen in the lower panel of Fig. 1.6.

- $t_{dec} < t < t_\Lambda$. This is the period when the photons decouple from the baryon, so the sound speed in the baryons is no longer the sound speed of relativistic fluid, but rather the velocity dispersion in the gaseous mixture of hydrogen of helium, which drops as the Universe expands. Thus, the baryonic Jeans mass drops dramatically after recombination and the baryonic perturbation grows and catches up the CDM perturbation.

  Since the perturbations in dark matter during this stage grow as the scale factor a, the baryons decouple from photon-baryon plasma and fall into the dark matter potential wells quickly, so the growth of the baryon perturbation also scales as factor a. To see this, one can apply Jeans equation (1.97) to both baryon and dark matter as [62]

$$\ddot{\delta}_b + \frac{4}{3t}\dot{\delta}_b = 4\pi G(\overline{\rho}_b\delta_b + \overline{\rho}_c\delta_c), \tag{1.108}$$

$$\ddot{\delta}_c + \frac{4}{3t}\dot{\delta}_c = 4\pi G(\overline{\rho}_b\delta_b + \overline{\rho}_c\delta_c). \tag{1.109}$$

  We can decouple the equation by introducing the "total density contrast" $\delta_m = (\overline{\rho}_b\delta_b + \overline{\rho}_c\delta_c)/(\overline{\rho}_b + \overline{\rho}_c)$ and density contrast difference $\Delta = \delta_c - \delta_b$, then by subtracting Eq. (1.109) from (1.108) one can get

$$\ddot{\Delta} + \frac{4}{3t}\dot{\Delta} = 0 \implies \Delta \propto \text{const}, \text{ or } t^{-\frac{1}{3}}. \tag{1.110}$$

  δ_m can be solved from Eq. (1.104) therefore has the solution $\delta_m \propto t^{-1}$ and $t^{2/3}$. Therefore, the ratio between δ_c and δ_b becomes

$$\frac{\delta_c}{\delta_b} = \frac{\overline{\rho}_m\delta_m + \overline{\rho}_b\Delta}{\overline{\rho}_m\delta_m - \overline{\rho}_c\Delta} \longrightarrow \frac{\delta_m}{\delta_m} = 1, \tag{1.111}$$

  so we see that δ_b is catching up δ_c and therefore falling into the dark matter potential well quickly. This can be seen from the lower panel of Fig. (1.6).

We summarize these two solutions in the 3^{rd} and 4^{th} column in Table 1.3.

Λ dominant era At a later time when the cosmological constant Λ becomes the dominant component in the Universe, the baryon perturbations have caught up with the perturbations in the dark matter, so we can consider them as a single matter perturbation δ_m. In the Λ dominant era, $H^2 \gg 4\pi G\overline{\rho}_m$, the Jeans equation is simplified as

$$\ddot{\delta}_m + 2H\dot{\delta}_m = 0, \tag{1.112}$$

for which the solutions are $\delta_m \propto$ const and $\delta_m \propto e^{-2t\sqrt{\Lambda/3}} \propto a^{-2}$. Therefore, Λ suppress the growth of structure which implies that the gravitational potential decays as $a^2\overline{\rho_m} \propto a^{-1}$. This leaves an imprint on the CMB sky as the Integrated Sachs-Wolfe effect, which can be seen in Fig. 1.7.

1.4.3 Non-linear growth of the structure

The linear perturbation theory developed in Section 1.4.2 fails when the density contrast reaches order unity. The cosmic structures that we see today — galaxies, clusters etc — have density contrasts much greater than unity. They can be analyzed by performing numerical simulations. However, non-linear evolution can be studied analytically if some simplifying assumptions are made. We shall first review the spherical collapse model (Section 1.4.3.1), and then discuss dark matter halo abundances (Section 1.4.3.2). Finally, we will review briefly some of the gas physics associated with the collapse of baryonic systems (Section 1.4.3.3).

1.4.3.1 Spherical Collapse model

In Section 1.4.2.2, we have seen that during the matter dominant era, the density perturbation δ grows as the scale factor a, therefore at some point, the density contrast will exceed unity and the linear perturbation description will fail.

Consider the density contrast $\delta(\mathbf{x}, t_i)$ of an overdense region at some time t_i. In the overdense region, the self-gravity of the local dense region make the matter within this region expand more slowly than the background expansion [79], i.e. the self-gravity works against the cosmic expansion, which makes the overdense region "decouple" from the background. The properties of collapsed object should be related to the initial condition of the overdense region. We therefore have to specify this condition before we analyze the time evolution.

Initial condition Let us suppose that the overdense region we are interested in is spherically symmetrical and has the initial density distribution at time t_i $\rho(r, t_i) = \rho_m(t_i) + \delta\rho(r, t_i) = \rho_m[1 + \delta_i(r)]$, where $\delta_i(r)$ is the initial density contrast at radius r. Therefore, the total mass M interior to radius r and total density contrast δ_i of the region (radius r_i) become

$$M = \left(\frac{4\pi}{3}\rho_m r_i^3\right)(1 + \delta_i), \;\; \delta_i = \left(\frac{3}{4\pi r_i^3}\right)\int_0^{r_i} \delta_i(r) 4\pi r^2 dr. \tag{1.113}$$

In the spherical collapse model, we assume no shell-crossing, so that M is a constant during the evolution of the shell. The specific energy of the shell [1] is

$$\frac{1}{2}\left(\frac{dr}{dt}\right)^2 - \frac{GM}{r} = E, \tag{1.114}$$

where the sign of E determines whether the mass shell will expand forever ($E > 0$) or decouple from expansion and collapse ($E < 0$). Suppose the peculiar velocity of the shell v_i is negligible at initial time $t = t_i$, then $\dot{r}_i = (\dot{a}/a)r_i = H(t_i)r_i = H_i r_i$, so the initial kinetic energy per unit mass is

$$K_i = \left(\frac{\dot{r}^2}{2}\right) = \frac{H_i^2 r_i^2}{2}, \tag{1.115}$$

and the potential energy at $t = t_i$ is ($U = -|U|$)

$$\begin{aligned} |U| &= \left(\frac{GM}{r}\right)_{t_i} = G\frac{4\pi}{3}\rho_m(t_i)r_i^2(1+\delta_i) \\ &= \frac{1}{2}H_i^2 r_i^2 \Omega_i(1+\delta_i) = K_i\Omega_i(1+\delta_i), \end{aligned} \tag{1.116}$$

where $\Omega_i = \rho_m(t_i)/\rho_c(t_i)$ is the initial matter density parameter of the background Universe. Therefore, the specific energy of the mass shell becomes

$$E = K_i - |U| = K_i\Omega_i\left[\Omega_i^{-1} - (1+\delta_i)\right], \tag{1.117}$$

from which the condition of collapsing object ($E < 0$) can be expressed as $\delta_i > [\Omega_i^{-1} - 1]$. Obviously, in a closed or a flat Universe ($\Omega_i \geq 1$), this condition is always satisfied for an overdense region $\delta_i > 0$, but for an open Universe ($\Omega_i < 1$), the above condition sets a threshold for the overdense region which can collapse eventually. Let us consider a collapsing mass shell with $E < 0$, which will expand till some maximal radius and collapse. One can get the "turn-around" radius by setting $\dot{r} = 0$ in Eq. (1.114) and using Eq. (1.117)

$$r_{turn} = r_i \times \frac{(1+\delta_i)}{\delta_i - (\Omega_i^{-1} - 1)}. \tag{1.118}$$

Since we work in a matter dominated Universe, we shall set $\Omega_i = 1$ in the following calculations.

The time evolution of the mass shell can be found by solving Eq. (1.114). The solution can be given in a parametric form as [79; 80][2]

$$r = A(1-\cos(\theta)), \;\; t = B(\theta - \sin(\theta)); \;\; A^3 = GMB^2, \tag{1.119}$$

[1] energy per unit mass of the shell

[2] In principle, an integration constant can be added to either r or T expressions, but the constant can be proved to be very small if the initial condition of the mass shell is set up to (t_i,r_i) in a matter dominant Universe, see [79].

where A and B are constants. The time t increases if the parameter θ increases, and r increases to r_{turn} before decreasing to zero. Therefore, from the condition $r(\pi) = r_m = 2A$, and $A^3 = GMB^2$, one can find out the coefficients from the initial condition

$$A = \frac{r_i}{2}\left(\frac{1+\delta_i}{\delta_i}\right) \simeq \frac{r_i}{2\delta_i}, \quad B = \frac{1}{2H_i}\frac{1+\delta_i}{\delta_i^{\frac{3}{2}}} \simeq \frac{3t_i}{4\delta_i^{\frac{2}{3}}}, \tag{1.120}$$

where the "$\simeq$" is under the approximation of a small initial fluctuation.

Time evolution With the above initial conditions, one can work out the evolution of the mean density contrast within the shell. The mean density within a shell is

$$\overline{\rho}(r,t) = \frac{3M}{4\pi r^3} = \frac{3M}{4\pi A^3(1-\cos(\theta))^3}, \tag{1.121}$$

and the background density is $\rho_m(t) = 1/(6\pi G t^2)$ ($a \propto t^{2/3}$). Therefore, the mean density contrast within the mass shell is

$$1 + \delta(r,t) = \frac{\overline{\rho}(r,t)}{\rho_m(t)} = \frac{3M}{4\pi A^3}\frac{6\pi G t^2}{(1-\cos(\theta))^3}, \tag{1.122}$$

and by substituting Eq.(1.119) into Eq.(1.122), one finds that the density contrast evolves as

$$\delta(r,t) = \frac{9}{2}\frac{(\theta-\sin(\theta))^2}{(1-\cos(\theta))^3} - 1, \quad t = B(\theta - \sin(\theta)). \tag{1.123}$$

The linear evolution of the density contrast can be recovered in the small limit of θ, and by expanding Eqs. (1.123) and using Eq. (1.120), one can find that in the linear approximation,

$$\delta = \frac{3}{5}\delta_i\left(\frac{t}{t_i}\right)^{\frac{2}{3}} \propto a(t), \tag{1.124}$$

which recovers the linear growth law for the linear perturbation theory (Section 1.4.2.2).

Now let us change the notation of initial conditions to match the current observables. We use the current comoving radius of the mass shell to replace r_i: $x = r_i[a(t_0)/a(t_i)]$, and current magnitude of the initial density perturbation to replace the δ_i: $\delta_0 = (a(t_0)/a_{t_i})(3\delta_i/5) = (1+z_i)(3\delta_i/5)$. From these relations, one can find the time evolution equations (1.119) and (1.120) become

$$r(t) = \frac{3x}{10\delta_0}(1-\cos(\theta)), \quad t = \left(\frac{3}{5}\right)^{\frac{3}{2}}\frac{3t_0}{4\delta_0^{\frac{3}{2}}}(\theta - \cos(\theta)). \tag{1.125}$$

From Eq.(1.124) and the relation $(t/t_i)^{2/3} = (1+z_i)(1+z)^{-1}$, one can find the relationship between parameter θ and redshift z as

$$(1+z) = \left(\frac{5}{3}\right)\left(\frac{4}{3}\right)^{\frac{2}{3}} \frac{\delta_0}{(\theta - \sin(\theta))^{\frac{2}{3}}}. \tag{1.126}$$

Therefore, Eqs. (1.123) and (1.126) give a complete solution for the density contrast evolution, by assuming an initial value of perturbation δ_0, one can get the time evolution $\delta(z)$. Equations (1.125) give the solution for how the radius of the mass shell evolves under self-gravity.

The mass shell of the overdense region expands due to cosmic expansion, but at some point it reaches its maximum radius r_m $(\theta = \pi)$ and begins to collapse due to self-gravity. By substituting $\theta = \pi$ into Eqs. (1.123) and (1.126), one finds the "turn-around" redshift, radius and density contrast as

$$\begin{aligned}(1+z_{turn}) &\simeq \frac{\delta_0}{1.062}, \quad r_{turn} = \frac{3x}{5\delta_0}. \\ 1+\delta &= \left(\frac{\overline{\rho}}{\rho_m}\right)_{turn} = \frac{9\pi^2}{16} \simeq 5.6.\end{aligned} \tag{1.127}$$

After the mass shell reaches its "turn-around" radius, it begins to contract and Eq. (1.125) suggests that at $\theta = 2\pi$ all of the mass collapses to a singular point. However, in reality, the spherical collapse scenario will break down well before the system reaches a singularity because of density and velocity irregularities. The dark matter will experience a collisionless process called "violent relaxation"[85], which broadens the energy distribution of the dark matter particles and finally realizes the virialised state. The final virialised state can be modelled to describe the dark matter structure that we see today. At the "turn-around" point, the total energy is equal to the potential energy $E_{turn} = U_{turn} \approx -(3GM^2)/(5r_{turn})$. From energy conservation equation and the virial theorem, one has

$$E_{turn} = -K \simeq -\frac{Mv^2}{2} \simeq -\frac{3GM^2}{5r_{turn}}, \quad U = -2K \simeq -Mv^2 \simeq \frac{3GM^2}{5r_{vir}}. \tag{1.128}$$

Therefore, the random velocity of the particles within the dark matter halo and the virial radius become

$$v \simeq \left(\frac{6GM}{5r_{turn}}\right)^{\frac{1}{2}}, \quad r_{vir} \simeq \frac{r_{turn}}{2}. \tag{1.129}$$

Important quantities There are several important quantities that are predicted from this spherical collapse model [79; 83]. The first one is the time taken for the fluctuation to reach virial equilibrium $\theta = 2\pi$. From Eq. (1.126) we find

$$(1 + z_{col}) = \frac{\delta_i(1 + z_i)}{(2\pi)^{\frac{2}{3}}(\frac{3}{4})^{\frac{2}{3}}} = 0.63(1 + z_{turn}) = \frac{\delta_0}{1.686}. \tag{1.130}$$

Therefore, $\delta_{\rm crit} = 1.686/D(z)$ ($D(a = 1) = 1$ is the current growth factor) is the density contrast extrapolated from linear theory, at which the perturbation reaches turnaround [1]. The second important quantity is the mean density of the collapsed object, which is $\rho_{col} = 8\rho(t_{turn}) = 8 \times 5.6\rho_m(t_{turn}) = 8 \times 5.6 \times [(1 + z_{turn})/(1 + z_{col})]^3\rho_m(t_{col})$, where the $\rho(t_{turn})$ is the density of the collapsing object at turn-around time, $\rho_m(t_{turn})$ is the cosmic background density at the turn-around time, and the $\rho_m(t_{col})$ is the cosmic background density at collapsed time. From these relations, we can find the density of the collapsed object

$$\rho_{col} \simeq 170\rho_m(t_{col}) = 170\rho_{m0}(1 + z_{col})^3, \tag{1.131}$$

where the ρ_0 is the present matter density. Therefore, at the present epoch, the density of a collapsed and virialised object should be about 170 times the background matter density.

We can summarize the above results as follows: the comoving radius of the initial mass shell with mass M is

$$x = r_i\left(\frac{a_{t_0}}{a_{t_i}}\right) = \left(\frac{M}{\frac{4\pi}{3}\rho_{m0}}\right)^{\frac{1}{3}} = 0.086\left(\frac{M}{10^8M_\odot}\right)^{\frac{1}{3}} \text{Mpc}. \tag{1.132}$$

The virial radius of the collapsed object rms of the velocity dispersion of the dark matter particles are

$$r = \frac{3x}{10\delta_0} = 1.5\left(\frac{M}{10^8M_\odot}\right)^{\frac{1}{2}}\left(\frac{1 + z_{col}}{10}\right)^{-1} \text{kpc}, \tag{1.133}$$

$$v = 13.0 \times \left(\frac{M}{10^8M_\odot}\right)^{\frac{1}{3}}\left(\frac{1 + z_{col}}{10}\right)^{\frac{1}{2}} \text{km/s}. \tag{1.134}$$

And the binding energy of the halo is

$$E = 3 \times 10^{53}\left(\frac{M}{10^8M_\odot}\right)^{\frac{5}{3}}\left(\frac{1 + z_{col}}{10}\right) \text{erg}. \tag{1.135}$$

Finally, we consider the gas properties during the collapse. The gaseous mixture of hydrogen and helium develops shocks and provides pressure to prevent further collapse [2]. Therefore, the thermal energy can be comparable to the gravitational potential energy. Let μ be the mean

[1] The real density contrast is greater than 1.686 since at turnaround point it already reaches $9\pi^2/16$ (Eq. (1.127)).

[2] Under the assumption that the cooling can be neglected

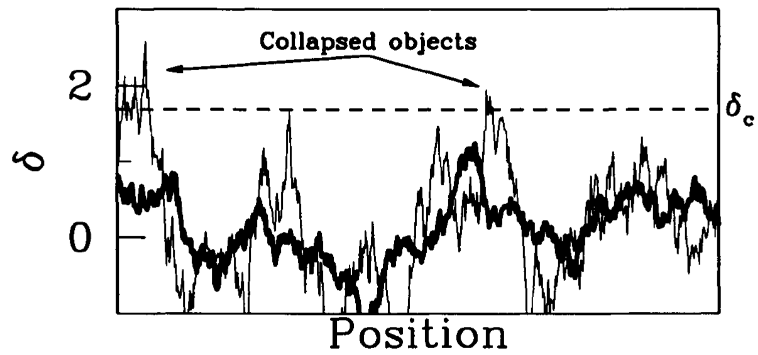

Figure 1.14: Inhomogeneous 1-D density fluctuation. The dark (light) curve is the field smoothed (not smoothed) on large scales. Small scale fluctuations that have density contrast over δ_{crit} collapse first, while the large scale fluctuation cannot collapse since their overdensity does not exist this threshold. Figure taken from [44].

molecular weight in units of hydrogen mass,

$$\mu = \frac{m_H n_H + m_{He} n_{He}}{(2n_H + 3n_{He})m_H} = \frac{1}{2}\left(\frac{1+Y}{1+0.375Y}\right) \simeq 0.57, \tag{1.136}$$

where we use helium faction $Y = 0.25$. Therefore, the pressure equilibrium suggests $3\rho_{gas} k_B T_{vir}/(2\mu m_H) = \rho_{gas} v^2/2$, from which we can obtain the virial temperature

$$T_{vir} = 3.9 \times 10^3 \left(\frac{\mu}{0.57}\right)\left(\frac{M}{10^8 M_\odot}\right)^2 \left(\frac{1+z_{col}}{10}\right) \mathrm{K}. \tag{1.137}$$

The spherical collapse model captures some of the physics responsible for the formation of halos. In reality, cosmic structures form hierarchically: at early time, low mass halos formed, and they have continuously accreted and merged to form higher mass halos. In Section 1.5, we will discuss hierarchial halo formation and universal dark matter density profile, and review galaxy formation in a bit more detail.

1.4.3.2 Dark Matter halo abundance

The above spherical collapse model provides a rough description of the evolution of individual halos, but a theory of structure formation should also predict the statistical properties of halos, for example, their number density as a function of mass at different redshifts. One can, of course, compute such statistics from numerical simulations, but to gain a physical understanding, an analytic model is needed [83].

A key advance in computing halo abundances was made in the seminal paper by Press and Schechter in 1974 [86], which is based on the linear perturbation theory, spherical collapse model and Gaussian statistics. Once an object with mass reaches a threshold amplitude, it will collapse and form a virialised object. Therefore, one can expect to find various density peaks in the final volume of interest. Small scale density fluctuations would typically have a higher amplitude than

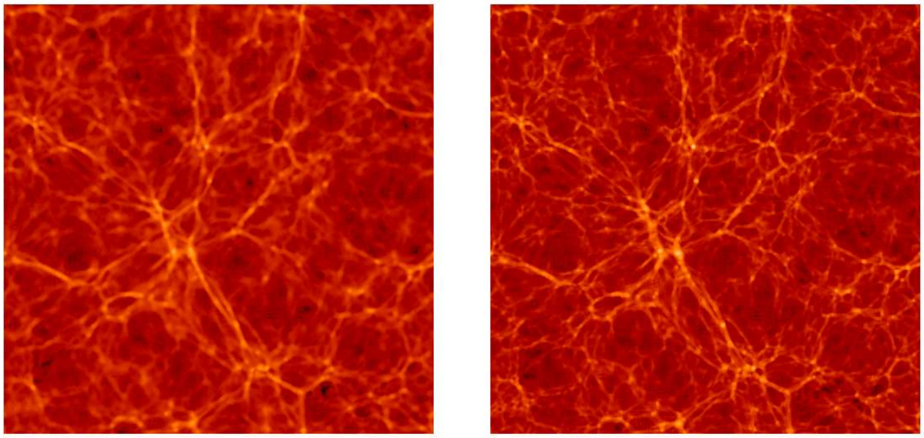

Figure 1.15: Left: Two-dimensional slice of the baryon distribution at z = 2.5 in a ΛCDM hydrodynamical simulation of structure formation. The low and high density regions are shown as dark and bright colours. The voids and filaments are typically associated with material in the Inter-Galactic Medium (IGM) and are observable in quasar absorption spectra. The luminous baryonic material (stars and galaxies) forms in the highest density regions, which is shown as the knots and sheets where many filaments converge. Right: The underlying dark matter distribution. The baryon distribution is slightly more diffuse (less small scale structure) compared to the underlying dark matter due to gas pressure support. In the simulation, the cosmological parameters are: $\Omega_m = 0.26$, $\Omega_\Lambda = 0.74$, $\Omega_b = 0.0463$, $h = 0.72$. The box size is 60 Mpc/h. The number of gas and dark matter particles are 2×400^3. The softening length is 2.5 kpc/h. Figure taken from [87].

the large scale smoothed fluctuations (Fig. 1.14). Therefore small scale fluctuations would collapse first and merge to form denser and larger halos. To understand this scenario, we consider a 1-D density fluctuation as shown in Fig. 1.14. The average of the inhomogeneity is zero, but there are some regions with large fluctuations whose density contrast is comparable or greater than δ_{crit}, and also some underdense regions with density contrast negative (Note that $\delta = (\rho - \overline{\rho})/\overline{\rho}$ cannot be smaller than -1). It is just these rare regions with large density contrast that will "decouple" from the Hubble expansion and collapse first. Since the density contrast in the matter dominated regime will grow as the scale factor a, the large scale inhomogeneity also grows and eventually collapses.

The Press-Schechter theory predicts the fraction of the volume that collapses at redshift z, i.e. the mass fraction above M is

$$\begin{aligned} f_{col}(> M, z) &= \frac{2}{\sqrt{2\pi}\sigma(R,z)} \int_{\delta_{crit}}^{\infty} d\delta \exp\left(-\frac{\delta^2}{2\sigma^2(R,z)}\right), \\ &= \mathrm{erfc}\left(\frac{\delta_{crit}}{\sqrt{2}\sigma(R,z)}\right), \end{aligned} \tag{1.138}$$

where "erfc" is the error function. There are several assumptions involved in computing this distribution. The most important assumption is relating a filter scale $\sigma^2(R,z)$ to a collapsed non-linear mass $M(R,z)$. Often people use the top-hat filter and the spherical collapse model to derive a relation between σ^2 and M, but to do it more accurately numerical simulations are needed. The second assumption is an "ad-hoc" factor of two in Eq. (1.138) in order to recover the mean density of the Universe. The excursion set formulism developed by [88] gives a more satisfactory explanation (see also [83]). If a halo with given mass M has density contrast $\delta_M < \delta_{crit}$, it may still collapse if it has an inner region with density contrast $\delta_L \geq \delta_{crit}$ and mass $M_L \geq M$. In this case, the region with mass M would be counted as belonging to the halo with mass M_L. Therefore, the fraction of the volume that has collapsed is greater than the Gaussian distribution without the factor of two [83; 88]. However, in practice, Press-Schetcher formulism works pretty well in matching the numerical simulations [89]. We can get the number density of the collapsed objects with mass in between M and $M + dM$ as

$$\begin{aligned} \frac{dn}{dM}dM &= -\frac{\rho_m}{M}\frac{df_{col}(M(R),z)}{dM}dM \\ &= -\sqrt{\frac{2}{\pi}}\frac{\rho_m}{M}\frac{d\ln\sigma(R,z)}{dM}\nu e^{-\nu^2/2}dM, \end{aligned} \tag{1.139}$$

where $M = (4\pi/3)\rho_m R^3$ and $\nu = \delta_{crit}/\sigma(R,z)$. The rms $\sigma(R,z)$ depends on cosmological parameters, so by measuring the galaxy cluster abundance, one can quantify cosmological parameters [44], in particular the matter content Ω_m and amplitude of fluctuation σ_8.

The Press-Schetcher formulism can fit observations quite well, but it underestimates the rare halos that host galaxies at high reshift. Therefore, people have proposed various other mass functions in order to match simulation results better, one of which was proposed by Sheth and Tormen in 1999 [82]

$$f_{col}(>M,z) = A\frac{\nu}{\sigma^2(R,z)}\sqrt{\frac{a'}{2\pi}}\left[1+\frac{1}{(a'\nu^2)^{q'}}\right]e^{-a'\nu^2/2}, \tag{1.140}$$

where the best-fit parameters are $a' = 0.75$, $q' = 0.3$ and the normalization requires $A = 0.322$.

1.4.3.3 Gas Physics

When the dark matter halo collapses, the gas falls into the dark matter potential well with a streaming velocity of order v (Eq. (1.134)). In order to form stars, the collapsed gas has to cool until its Jeans mass drops to the mass of a typical star [83]. This is important because if the cooling is ignored, we would expect the gas to shock and produce a pressure support atmosphere in hydrostatic equilibrium.

Before the first stars were formed, no element existed to cool the gas (Big Bang Nucleosynthesis cannot produced enough heavy elements to cool the first stars), so the gas can be only cooled by atomic transitions in hydrogen and helium and molecular hydrogen transition. However, below $\sim 10^4$ K (Eq. (1.137)), atomic cooling is inefficient and therefore cannot provide an effective way to cool and fragment the gas into stars. The only way of cooling the gas with $T < 10^4$ K is via molecular hydrogen cooling. After recombination, there are residual free electrons e^- which can act as a catalyst to combine with the neutral hydrogen and release photons $H + e^- \longrightarrow H^- + \gamma$ and $H^- + H \longrightarrow H_2 + e^-$. Through this mechanism, free electrons can catalyze H_2 and cool the gas to the temperature or about a few hundred K [83].

For a halo with virial temperature greater than $10^4\ K$, atomic transitions and free-free emission are effective ways of cooling the gas, but when the temperature drops below $10^4\ K$, molecular hydrogen becomes important [83].

In the ΛCDM model, structures on small scales build up hierarchically and form filamentary structure (Fig. 1.15). Gas cooling defines a characteristic mass of order $10^{12} M_\odot$ for the baryonic content of galaxies. Below this mass scale, the gas can cool so efficiently that it nearly collapses at the free-fall rate. For larger masses, the gas cannot cool efficiently so galaxies may still be forming at very low redshift [84].

In summary, structure formation theory of ΛCDM predicts the hierarchial formation of dark matter halos, and within these halos stars form in the dense, cold knots of gas. By mapping the density peaks of the distribution from observations, one can test the theory of structure formation and measure the cosmological parameters. In addition, mapping the cosmic diffuse gas by observing the emission and absorption lines in either quasar spectrum or in the 21cm line of molecular hydrogen is also an important way of probing the first structure formation.

1.5 Dark matter and Galaxy formation

In the above introduction, we have reviewed large scale structure formation and sketched some of the basic physical processes involved in the formation of hierarchial structure. An essential step in confirming this scenario is to check whether the theory is consistent with observations in the nearby Universe, since experimentally nearby objects are usually easier to observe in detail. This task is closely related to the understanding of dark matter properties on Galactic scales since the dark matter may reveal more microscopic physics on this scale via its effect on small scale structure formation. In this Section, we shall first look at dark matter from a particle physics perspective, and then discuss some potential problems posed by observations of small scale structures. For more discussion in detail, we refer to [90; 92].

1.5.1 Dark Matter Particles

Dark matter is not new to cosmologists. It was as early as the 1930s that Fritz Zwicky discovered the existence of the dark matter ("missing mass") in clusters of galaxies by using viral theorem [94]. In 1970s, astronomers discovered flat galaxy rotation curves and proposed that they might be explained by an invisible dark matter halo [95]. Currently, there are two popular dark matter candidates from the considerations of elementary particle physics perspective. One is the lightest

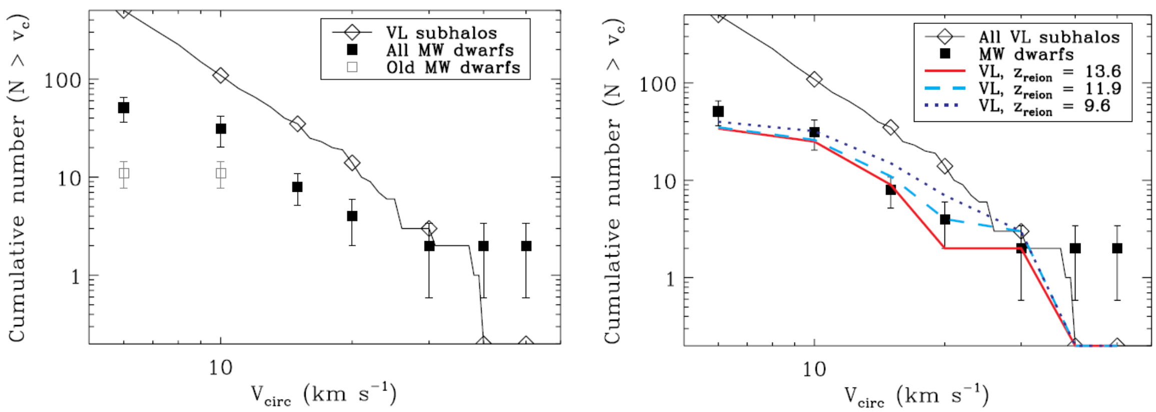

Figure 1.16: The cumulative number of Milky way satellite galaxies as a function of halo circular velocity. Left panel: Missing satellite problem; Right panel: the effect of reionization. Figure taken from [104].

supersymmetric partner particle, which is called WIMP (Weakly Interacting Massive Particle) [93; 101]; and the other is the cosmological axion [102; 103].

The WIMP model is proposed under the supersymmetry (SUSY) principle of particle physics. SUSY can allow the unification of the electroweak and strong interactions and naturally explains why the electroweak scales is much smaller than the Planck scale. The predictions of the WIMP mass is typically between 100 to 1000 GeV.

Axion were first proposed to solve the strong interaction CP problem in SU(3) gauge theory. Axion like fields appear to be common in string theory and so remain a possible candidate for the dark matter.

1.5.2 Dark Matter on Small Scales

There are two major issues that have challenged the ΛCDM scenario, namely the abundance of the dark matter halos and satellite galaxies and the existence of the density cusps at the centres of galaxies [90]. In this subsection, we shall review these problems and discuss how they might relate to the properties of dark matter particles.

1.5.2.1 Population of sub-halos and satellites: how cold is cold dark matter?

Many fewer satellite galaxies have been detected in the Local Group than the number of sub-halos predicted from numerical simulations (Fig. 1.16), and this is considered by some to be a serious problem for ΛCDM cosmology. However, the suppression of star formation in small dwarf galaxies after reionization can account for the observed abundance of satellites for ΛCDM [90; 104]. This is possibly related to the "common mass" scale discovered by [105] which may further reveal the properties of the baryonic physics.

The properties of dark matter halo depend on the mass of the dark matter particles. For example, warm dark matter with high thermal velocities, can suppress the formation of sub-halos. However, it is not clear whether we need to suppress the formation of small dark halos. What we can observe is the stars, and not all of the dark matter halos host stars. In particular, feedback from star formation may drive out most of the gas from a low velocity dispersion dark halo. Therefore, the 'missing satellite' problem may be either due to the thermal velocity of dark matter, or baryonic feedback resulting from the star formation process.

Sterile neutrinos, provide an example of warm dark matter. Sterile neutrinos may have been produced in the very early stage of the Universe, and have been proposed as a candidate for dark matter [96]. The main effect of the thermal velocities of such warm dark matter particles would be to suppress structures below Mpc scale. The Lyman-alpha absorption produced by the intervening neutral hydrogen in the spectrum of quasars (also known as Lyman-alpha forest), can probe the matter power spectrum in the mildly nonlinear regime down to small scales (~ 1Mpc/h) over the redshift $z = 2-6$ [91]. Therefore, the statistics of the Lyman-alpha forest at redshift $2.0 < z < 6.4$ can be used to set a lower limit on the sterile neutrino mass $m_s \geq 28$ keV [91]. On the other hand, the sterile neutrino can decay into X-rays and light neutrinos, so the null results of X-ray observations (such as $XMM-Newton$ observation of Ursa Minor and Milky Way [98; 99]) can give an upper limit on the sterile neutrino mass $m_s \leq 3.5$ keV [97]. Therefore, the sterile neutrino is nearly ruled out as a dark matter candidate, although some windows of parameter space remain open [90].

The epoch of reionsation, can provide another constraint on the dark matter particle mass. Since the thermal velocities of the warm dark matter strongly suppress the formation of low-mass halos, the absence of the mini-halos can delay the formation of the first stars, and therefore delay the reionisation epoch [90].

Therefore, the populations of sub-halos and satellite galaxies can set important constraints on the clustering properties of dark matter.

1.5.2.2 Cusp and Core problem

In 1996, Navarro et al. investigated the structure of dark matter halos from N-body simulations of the ΛCDM model. They found a universal profile of dark matter density

$$\rho(r) = \rho_{crit} \frac{\delta_c}{(r/r_s)(1+r/r_s)^2}, \tag{1.141}$$

which has a slope r^{-1} as small radii. However, observations of nearby galaxies [106] suggest a core-dominated halo with a central profile $\rho(r) \propto (r_0^2 + r^2)^{-1}$.

One possible reason for this problem may be the neglect of baryonic physics in pure dark matter simulations. There are three mechanisms that have been proposed to solve the cusp problem [90]:

- Dynamical friction: By comparing the pure dark matter and baryon+ dark matter simulations [107; 108], Ramano-Diaz et al. claim that dynamical friction causes infalling baryon and dark matter clumps to transfer energy and angular momentum to the dark matter. As a result, the dark matter radial profile at low redshift is transformed into an isothermal with a flat core at low redshift.

- Starburst removal: The rapid blowout of a large amount of gas in the centre of the density profile due to a starburst can cause the dark matter distribution in the inner region of the halo to expand [109].

- Bulk gas motion: Supernovae-driven gas bulk motions can smooth out dark matter cusps in the forming galaxy regions as a consequence of resonant heating of dark matter in the resulting fluctuating potential. This may provide an explanation of the dark matter cores in the dwarf spheroidal (dSph) galaxies such as the Ursa Minor satellites of the Milky Way [90; 110].

All of these mechanisms are very speculative, however, in order to determine the distribution of dark matter in low surface brightness disks and gas-rich dwarf galaxies, one needs to compare numerical simulations that model baryonic process with observations.

1.6 Overview

1.6.1 Classification of problems in Cosmology

In the above we have presented an extensive review of our current understanding of cosmic evolution: from quantum fluctuation in the early Universe to the subsequent formation of non-linear structure. However, the many unresolved questions in cosmology provide great challenges and opportunities for further research. Below, I give examples of two types of problems in cosmology, namely as "unknown physics" and "known physics but unknown details". Both classes of problem provide fertile ground for novel research.

1.6.1.1 Known Physics but unknown details

Cosmic reionization As we have seen in Section 1.3, at a redshift about 1100, electrons began to recombine with protons to form neutral hydrogen, so the free electron density began to drop and radiation decoupled from the baryons. The dark ages began at this point, since there was no light source in the Universe apart from the gradually dimming CMB radiation.

When the redshift decreased to about 20, gravitational instability caused the formation of the first non-linear objects. It is believed that the light from the first stars reionised the neutral hydrogen at a redshift $z \gtrsim 10$. Understanding the process of reionization would provide important information on how the first galaxies and stars formed [83]. The spectrum of quasars can be an important way of probing the reionization epoch. Quasars release an extraordinary amount of energy and may be the brightest objects in the very early Universe. They emit the light in which the blueward of the spectrum can be absorbed by the neutral hydrogen in the line-of-sight. This is known as the Gunn-Peterson effect and the rapid increase in optical depth in the spectrum of quasar suggests that the end of reionization occurs at a redshift of ~ 6 [111; 112].

The 21-cm line of neutral hydrogen offers a promising way of studying the dark ages and the early stages of reionization. The 21-cm transition of hydrogen arises from two separate hyperfine states of the ground-state. This transition is highly temperature dependent, due to the fact that as objects form in the "dark ages" and emit photons that heat the surrounding neutral hydrogen, it causes 21-cm line emissions in the surrounding area [83]. The 21-cm line can be detected in emission or absorption, depending on the spin temperature of the neutral gas [100]. On-going experiments, such as LOFAR [113], are constructed to detect such signals.

Gravitational Waves Gravitational waves are fluctuations of the curvature of the space-time predicted by Einstein's theory of general relativity. They propagate as the speed of light, while their frequency is determined by the mass of the object(s) and the power is determined by the geometry and distance of the emitting object(s). On-going projects such as the Laser Interferometer Gravitational-Wave Observatory (LIGO), Advanced LIGO, and the future Laser Interferometer Space Antenna (LISA) will constrain the signals over a wide range of frequencies. The direct detection of gravitational waves will open up a new window to study strong gravity and compact astrophysical objects.

1.6.1.2 Unknown Physics

Inflation models and the early Universe process To describe the fundamental field that drove inflation in the early Universe, theoretical physicists have proposed hundreds of models. However, these phenomenological models are still far from fundamental microscopic physics. In addition, some theorists try to avoid inflation and propose a non-trivial early universe mechanism (such as Cyclic Model [114]) to generate primordial fluctuations. The difference between this model and inflation is the amplitude of the tensor modes. Single-field inflation predicts a tensor mode $r \sim \mathcal{O}(0.1)$, while the cyclic model predicts undetectable amplitude $r \sim \mathcal{O}(10^{-5})$. Therefore, perhaps the most realistic way to distinguish the models is to measure the B-mode polarization signals in the CMB map to infer the energy level and field configuration of the inflaton. This is a frontier of cosmology for the coming decades since space-mission (Planck [27]), and ground-based experiments (QUIET [31], PolarBear [30]) are dedicated to measuring this signal. In Chapter 4, we are going to discuss the current and prospective constraints on the CMB B-mode signals and its constraints on the models of the early Universe.

Dark Matter As we have shown above, dark matter is known to exist around galaxies and in galaxy clusters. However, although astrophysical observations may set some limit on the microscopic properties of dark matter, the nature of dark matter is still very speculative. Perhaps the most promising way of discovering its nature lies in particle physics experiments such as the Large Hadron Collider (LHC) [115], and the Cryogenic Dark Matter Search (CDMS) [116].

Dark Energy The dark energy problem is one of the most serious problems in modern physics. If it is caused by the vacuum fluctuations (cosmological constant Λ), it should take a value of about M_{pl}^4, which is an order of 120 times higher than what we observe today. People have proposed dynamic field (such as quintessence) to explain dark energy, but these models have to be contrived and fine-tuned to match the observable fluctuations [118]. In addition, these models are all phenomenological and lack a basis in fundamental physics. The combination of on-going CMB observations Planck [27] and future galaxy redshift surveys can constrain the dark energy equation of state to a high precision [117].

1.6.2 Aims and Structure of the Thesis

In the above sections, we have reviewed the standard ΛCDM cosmology in detail, including the inflation, CMB cosmology and large scale structure formation. We have also given a brief review of the aspects of the ΛCDM model that requires new physics.

However, although the ΛCDM model can successfully pass most of the observational tests of cosmology, a number of inconsistencies between the ΛCDM model and different astronomical observations have been discussed in the literatures. Some authors argue that there is a lack of large angular correlations in the CMB, and some authors argue that there is a broken symmetry pattern in the CMB. In addition, on $\gtrsim 50$ Mpc scales, it has been argued that there is a very large amplitude of the bulk flow, which seems to be inconsistent with the linear perturbation theory of structure formation.

Discovering inconsistencies with an established model is of course extremely important. It is only by establishing such inconsistencies that the subject can develop and a new paradigm can emerge. In this thesis, we will compare the ΛCDM model with a number of cosmological tests, and investigate the constraints on the plausible new physics. In the remaining Chapters of the thesis, I will investigate the following topics:

- In Chapter 2, we discuss the issue of whether there is really a lack of angular correlations in the CMB sky. We compare various estimators of the temperature correlation function showing how they depend on assumptions of statistical isotropy and how they perform on the WMAP 5-yr Internal Linear Combination (ILC) maps with and without a sky cut. We further reconstruct the low-multipole harmonics that determine the large scale features of the temperature correlation accurately from the data that lie outside the sky cuts. The reconstruction results are in good agreement with those computed from the ILC map over the whole sky. A Bayesian analysis of the large-scale correlations is presented, which shows that the data cannot exclude the standard ΛCDM model. Therefore, we conclude that irrespective of the assumption of statistical isotropy, there is marginal evidence for the lack of large angular correlation which is inconsistent with ΛCDM model.

- In Chapter 3, we discuss the test of the statistical isotropy of CMB and develop a method to access the statistical significance of any broken isotropy. We construct simple quadratic estimators to reconstruct asymmetry in the primordial power spectrum from CMB temperature and polarization data and verify their accuracy by using simulations with quadrupole power asymmetry. We show that the Planck mission, with its millions of signal-dominated modes of the temperature anisotropy, should be able to constrain the amplitude of any spherical multipole of a scale-invariant quadrupole asymmetry at the 1% level (2σ). Almost independent constraints can be obtained from polarization at the 3% level after four complete sky surveys, providing an important consistency test. If the amplitude of the asymmetry is large enough, constraining its scale-dependence should become possible. In scale-free quadrupole models with 1% asymmetry, consistent with the current limits from WMAP temperature data (after correction for beam asymmetries), Planck should constrain the spectral index q of power-law departures from asymmetry to $\Delta q = 0.3$. Finally, we show how to constrain models with axisymmetry in the same framework. For scale-free quadrupole models, Planck should constrain the direction of the asymmetry to a 1σ accuracy of about 2 degrees using one year of temperature data.

- Chapter 4 investigates at the issue of how well the current and future CMB B-mode polarization experiments are able to detect the features of inflation and early Universe models. We investigate the observational signatures of three models of the early Universe in the B-mode polarization of the CMB radiation: standard single field inflation, loop quantum cosmology (from loop quantum gravity) and cosmic strings as predicted from brane inflation. We further use current B-mode polarization data from the BICEP and QUaD experiments to constrain the parameters of these models. We also examine the detectability of the primordial B-mode signal predicted by these models with future CMB polarization experiments. We find that although the current CMB experiments cannot distinguish between the models, they can already set strong constraints. Future space-satellites (e.g. Planck and CMBPol), ground-based experiments (PolarBear and QUIET), and balloon-borne experiments can set important limits on the fundamental parameters of inflation and other alternatives and perhaps even distinguish them.

- A large bulk flow, which is in tension with the ΛCDM cosmology, has been reported by some authors. In Chapter 5, we provide a physically plausible explanation of this bulk flow, based on the assumption that some fraction of the observed dipole in the cosmic microwave background is due to an intrinsic fluctuation, so that the subtraction of the observed dipole leads to a mismatch between the CMB defined rest frame and the matter rest frame. We investigate a model that takes into account the relative velocity (hereafter the tilted velocity) between the two frames, and develop a Bayesian statistic to explore the likelihood of this tilted velocity.

By studying various independent peculiar velocity catalogs, we find that (1) the magnitude of the tilted velocity u is around 400 km/s, and its direction is close to what is found from previous bulk flow analyzes; for most catalogs analyzed, $u = 0$ is excluded at about the 2.5σ level; (2) constraints on the magnitude of the tilted velocity can result in constraints on the duration of inflation, due to the fact that inflation can neither be too long (no dipole effect) nor too short (very large dipole effect); (3) under the assumption of a superhorizon isocurvature fluctuation, the constraints on the tilted velocity require that inflation lasts at least 6 e-folds longer (at the 95% confidence interval) than that required to solve the horizon problem. This opens a new window for testing inflation and models of the early Universe from observations of large scale structure.

- In Chapter 6, we investigate the potential power of the Cosmic Mach Number (CMN), which is the ratio between the mean velocity and the velocity dispersion of galaxies as a function of cosmic scales, to constrain cosmologies. We first measure the CMN from 5 catalogues of galaxy peculiar velocity surveys at low redshift ($z \in (0.002, 0.03)$), and use them to contrast cosmological models. Overall, current data is consistent with the WMAP7 ΛCDM model. We find that the CMN is highly sensitive to the growth of structure on scales $k \in (0.01, 0.1)$ h/Mpc in Fourier space. Therefore, modified gravity models, and models with massive neutrinos, in which the structure growth generally deviate from that in the ΛCDM model in a scale-dependent way, can be well differentiated from the ΛCDM model using future CMN data.

- In the conclusion Chapter 7, we will give an outlook of the further tests of standard ΛCDM cosmology and other possible variations.

Chapter 2

Large-Angle Correlations in the CMB

2.1 Introduction

Following the discovery by the COBE team of temperature anisotropies in the cosmic microwave background (CMB) radiation [41; 119], Ref. [120] noticed that the temperature angular correlation function, $C(\theta)$, measured from the COBE maps was close to zero on large angular scales. This result attracted little attention until the publication of the first year results from WMAP [1; 61]. The results from WMAP confirmed the lack of large-scale angular correlations in the temperature maps and led [1] to introduce the statistic

$$S_{1/2} = \int_{-1}^{1/2} [C(\theta)]^2 d\cos\theta. \tag{2.1}$$

The form of the statistic and the upper cut-off, $\mu = \cos\theta = 1/2$, were chosen *a posteriori* by [1] 'in response' to the observed shape of the temperature correlation function computed using a particular estimator and sky cut (as described in further detail in Section 2.2). To assess the statistical significance of the lack of large-scale power, [1] computed a 'p-value', *i.e.* the fraction of models in their Monte Carlo Markov chains which had a value of $S_{1/2}^{\rm model} < S_{1/2}^{\rm data}$, using the same estimator and sky cut that they applied to the data. For their standard six-parameter inflationary ΛCDM cosmology, they found a p-value of 0.15%, suggesting a significant discrepancy between the model and the data.

This problem was revisited by [121]. The main focus of the [121] was to improve on the pseudo-harmonic power spectrum analysis used by the WMAP team [122] by using quadratic maximum likelihood (QML) estimates of the power spectrum, with particular emphasis on the statistical significance of the low amplitude of the quadrupole anisotropy. As an aside, Ref. [121] computed angular correlation functions from the QML power spectrum estimates and showed that they were insensitive to the presence of a sky cut. Similarly the $S_{1/2}$ statistic computed from these correlation functions was found to be insensitive to the size of the sky cut giving p-values of a few percent. Ref. [121] concluded that the correlation function and $S_{1/2}$ statistic offered no compelling evidence against the concordance inflationary ΛCDM model. Ref. [121] did not explore in any detail the low p-value for the $S_{1/2}$ statistic reported by [1], but commented that it was probably simply an 'unfortunate' consequence of the particular choice of statistic, estimator and sky cut chosen by these authors (in other words, a result of various *a posteriori* choices).

The CMB temperature correlation function and S statistic have been reanalyzed in two recent papers [124; 125]. The arguments in the two papers are quite similar, and so for the most part we will refer to the later paper [125] (since, as in this work, it analyzes the 5-year WMAP temperature data, [123]). The [124; 125] papers are largely motivated by evidence for a violation of statistical isotropy in the WMAP temperature maps, in particular evidence of alignments amongst the low order CMB multipoles (*e.g.* [126; 127; 128; 129]), although the statistical significance of these alignments has been questioned ([130; 132; 133]). Refs. [124; 125] make the valid point that statistical isotropy is often implicitly assumed in defining what is meant by the term 'correlation function' and in defining estimators. They argue further that different estimators contain different information. They then focus on pixel-based estimates of the correlation function applied to the WMAP data, including a sky cut, and find p-values for the $S_{1/2}$ statistic of $\sim$ 0.025–0.04%, depending on the choice of CMB map and sky cut. If no sky cut is applied, they find p-values of $\sim 5\%$ (similar to the p-values reported in [121]). Ref. [125] comments that the full-sky results are apparently inconsistent with the cut-sky analysis suggesting a violation of statistical isotropy.

Any analysis which claims to strongly rule out the simple inflationary ΛCDM model deserves careful scrutiny, since a confirmed discordance would have profound consequences for our understanding of the early Universe. The purpose of this Chapter is to investigate carefully the analysis presented in [125]. In Section 2.2 we discuss estimators of the correlation function and relate the pixel-based estimator used by [125] to the pseudo-power spectrum computed on a cut sky. In Section 2.3, we explicitly reconstruct the individual low order multipole coefficients $a_{\ell m}$ from cut-sky maps using a technique first applied by [131]. This allows us to test the sensitivity of the large-angle correlation function to the presence of a sky cut, largely independent of assumptions concerning statistical isotropy or Gaussianity. The results of this analysis are compared with the QML estimates of the correlation function used in [121]. Section 2.4 describes a Bayesian analysis of the $S_{1/2}$ statistic and contrasts it with the frequentist analysis applied by [1] and [125]. Our conclusions are summarized in Section 2.5. A recent paper by Pontzen and Peiris [134] extends the analysis presented here to general anisotropic Gaussian theories with largely similar conclusions.

2.2 Estimators of the Correlation Function

If we assume statistical isotropy, the ensemble average of the temperature angular correlation function (ACF) measured over the whole sky $\langle C(\theta)\rangle$ is related to the ensemble average of the angular power spectrum $\langle C_\ell \rangle$ by the well known relation

$$\langle C(\theta) \rangle = \frac{1}{4\pi} \sum_\ell (2\ell+1) \langle C_\ell \rangle P_\ell(\cos\theta). \tag{2.2}$$

However, we have only one realization of the sky and we may further choose to impose a sky cut to reduce possible contamination from regions of high Galactic emission. If we relax the assumptions of statistical isotropy and complete sky coverage, there is no unique definition or estimator of the ACF. One can write down a number of estimators that, given certain assumptions concerning the underlying statistics of the fluctuations, may average to the ensemble mean when applied to data on an incomplete sky.

Ref.[125] uses a direct pixel based correlation function [1] on the cut sky

$$C^{\rm pix}(\theta) = \langle x_i x_j \rangle, \tag{2.3}$$

where x_i denotes the temperature value in pixel i and the angular brackets denote an average over all pixel pairs outside the sky cut with an angular separation that lies within a small interval of θ.

If the underlying temperature field is statistically isotropic, equation (2.3) provides an unbiased estimate of the correlation function, i.e. the average over a large number of independent realizations is unbiased, irrespective of the sky cut. However, if the fluctuations are statistically isotropic and Gaussian, Eq. (2.3) is not an optimal estimator of $\langle C(\theta) \rangle$. To see this, expand the temperature field in spherical harmonics

$$x_i = \sum_{\ell m} a_{\ell m} Y_{\ell m}(\boldsymbol{\theta}_i), \ \ \langle |a_{\ell m}|^2 \rangle = \langle C_\ell \rangle. \tag{2.4}$$

Then, from the rotation properties of the spherical harmonics, it is straightforward to prove

$$C^{\rm pix}(\theta_{ij}) = \langle x_i x_j \rangle = \frac{\sum_\ell (2\ell+1) \tilde{C}^P_\ell P_\ell(\cos\theta_{ij})}{\sum_\ell (2\ell+1) \tilde{W}_\ell P_\ell(\cos\theta_{ij})}, \tag{2.5}$$

where $\tilde{C}^P_\ell$ is the pseudo-power spectrum (PCL) estimate on the cut sky:

$$\tilde{C}^P_\ell = \frac{1}{(2\ell+1)} \sum_m |\tilde{a}_{\ell m}|^2, \ \ \tilde{a}_{\ell m} = \sum_i x_i w_i Y^*_{\ell m}(\boldsymbol{\theta}_i) \Omega_i, \tag{2.6}$$

where w_i is a window function that is zero or unity depending on whether a pixel (of area Ω_i) lies inside or outside the sky cut. The function $\tilde{W}_\ell$ in (2.5) is the pseudo-power spectrum of the

[1] More generally, one can define a bi-polar correlation function $C(\boldsymbol{\theta}_i, \boldsymbol{\theta}_j)$, which can be used as a test of statistical isotropy (see [135])

window function w_i:

$$\tilde{W}_\ell = \frac{1}{(2\ell+1)}\sum_m |\tilde{w}_{\ell m}|^2, \;\; \tilde{w}_{\ell m} = \sum_i w_i \Omega_i Y^*_{\ell m}(\boldsymbol{\theta}_i). \tag{2.7}$$

The relation (2.5) is an identity and does not depend on the assumption of statistical isotropy.

In fact, the pixel estimator (2.5) is mathematically identical[1] to the PCL estimator used by [1] and [121]

$$C^P(\theta) \equiv C^{\text{pix}} \equiv \frac{1}{4\pi}\sum_\ell (2\ell+1)\hat{C}^P_\ell P_\ell(\cos\theta), \;\; \hat{C}^P_\ell = M^{-1}_{\ell\ell'}\tilde{C}^P_{\ell'}, \tag{2.8}$$

where the matrix M is

$$M_{\ell\ell'} = \frac{1}{(2\ell+1)}\sum_{mm'}|K_{\ell m\ell' m'}|^2. \tag{2.9}$$

The equivalence between the estimators (2.5) and (2.9) demonstrates that for isotropic Gaussian random fields, the pixel estimator (2.3) is suboptimal since PCL power-spectrum estimates are suboptimal when applied to the cut sky (for extensive discussions see [121; 136] and references therein).

The coefficients $\tilde{a}_{\ell m}$ are related to the coefficients $a_{\ell m}$ on the uncut sky by the coupling matrix $\mathbf{K}$,

$$\tilde{a}_{\ell m} = \sum_{\ell' m'} a_{\ell' m'} K_{\ell m \ell' m'}, \tag{2.10}$$

where

$$K_{\ell_1 m_1 \ell_2 m_2} = \sum_i w_i \Omega_i Y^*_{\ell_1 m_1}(\boldsymbol{\theta}_i) Y_{\ell_2 m_2}(\boldsymbol{\theta}_i). \tag{2.11}$$

Under the assumption of statistical isotropy and Gaussianity, it is straightforward to calculate the covariance matrix of the estimator (2.3)

$$\langle \Delta\tilde{C}(\theta_i)\Delta\tilde{C}(\theta_j)\rangle = \left(\sum_{\ell_1\ell_2}(2\ell_1+1)(2\ell_2+1)\langle\tilde{\Delta}C^P_{\ell_1}\tilde{\Delta}C^P_{\ell_2}\rangle P_{\ell_1}(\cos\theta_{ij})P_{\ell_2}(\cos\theta_{ij})\right) \Bigg/ \left(\sum_\ell (2\ell+1)\tilde{W}_\ell P_\ell(\cos\theta_{ij})\right)^2 \tag{2.12}$$

where

$$\langle\Delta\tilde{C}^P_\ell \Delta\tilde{C}^P_{\ell'}\rangle = \frac{2}{(2\ell+1)(2\ell'+1)}\sum_{mm'}\sum_{\ell_1 m_1}\sum_{\ell_2 m_2} C_{\ell_1}C_{\ell_2}K_{\ell m \ell_1 m_1}K^*_{\ell' m' \ell_1 m_1}K^*_{\ell m \ell_2 m_2}K_{\ell' m' \ell_2 m_2} \tag{2.13}$$

Figure 2.1(a) shows the direct pixel based estimator (2.3) applied to the 5-year WMAP ILC map after smoothing with a Gaussian filter of 10° FWHM and repixelising at a Healpix [137]

[1] We are grateful to Anthony Challinor for pointing this out. See Appendix B of [134] for a proof.

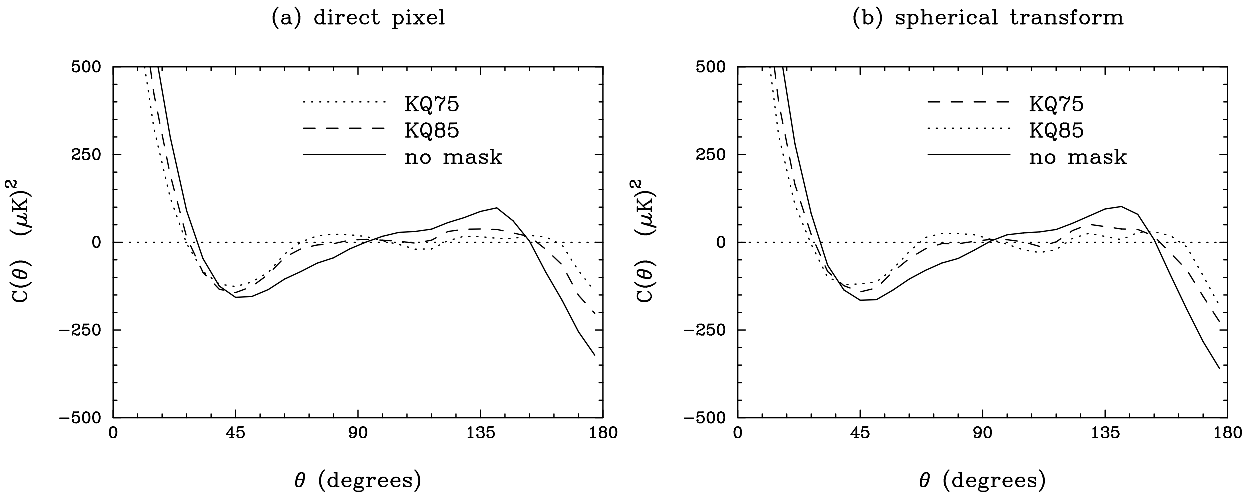

Figure 2.1: The figure to the left shows the correlation functions computed using the pixel estimator (2.3) applied to the 5 year WMAP ILC map (degraded as described in the text) over the full sky and with the WMAP KQ85 and KQ75 masks imposed. The figure to the right shows the correlation functions computed from the pseudo-power spectra (2.5).

resolution NSIDE=16. The results of Fig. 2.1 are consistent with those of [125]. With the WMAP KQ85 and KQ75 masks[1] applied (retaining about 82% and 71% of the sky respectively [138]), there is little power over the angular range 60°-160°. However, there is some non-zero correlation if the pixel estimator is evaluated over the full sky. Fig. 2.1(b) shows the correlation functions determined from the pseudo-spectra (2.5). This simply confirms the equivalence of the two estimators (2.3) and (2.5) (apart from minor differences arising from the finite angular bin widths). The covariance matrix for these estimators for the full sky is shown in Fig. 2.2, using the C_ℓ for the six parameter ΛCDM model that provides the best fit to the WMAP data ([72]). The large angle ACF for a nearly scale invariant temperature spectrum is dominated by a small number of modes leading to large correlations between different angular scales. The main effect of a KQ75-type sky cut on the covariance matrix is to increase its overall amplitude. The angular structure of the covariance matrix is insensitive to the precise size and shape of the sky cut.

The main differences between the various ACF estimates plotted in Figs. 2.1 come from application of the sky cuts. With the sky cuts applied, the ACF's are close to zero on angular scales $\geq 60°$. This lack of power leads to particular low values for the $S_{1/2}$ statistic of about 1000-2000 $(\mu K)^4$, as listed in Table 2.1[2]. If no sky cut is applied, the value of the $S_{1/2}$ statistic is substantially higher at around 8000 $(\mu K)^4$. It is worth noting that the values listed in Table 2.1 are very similar to the values obtained from the WMAP first year data (see Table 5 in [121]). The low multipole anisotropies that contribute to the ACF at large angular scales have remained stable as the data have improved. The low multipoles are signal dominated and stable to improved gain

[1]We used degraded resolution (NSIDE=16) versions of these masks. The degraded resolution KQ75 mask is plotted in Fig. 2.3.

[2]For maps degraded to Healpix resolution of NSIDE= 16 and smoothed with a Gaussian of FWHM 10°.

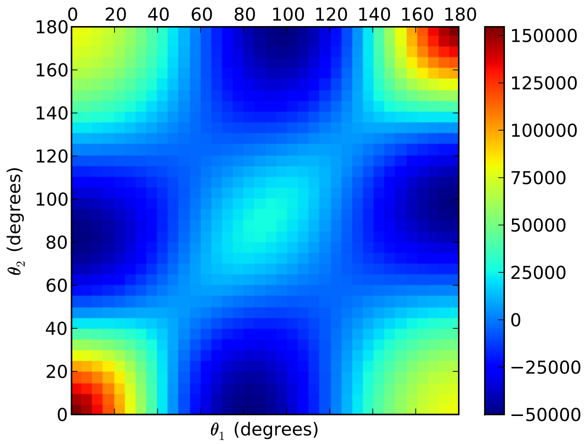

Figure 2.2: Covariance matrix for the pixel correlation estimator (2.3) computed for full sky maps. The scale on the right is in units of $(\mu\mathrm{K})^4$.

corrections, foreground separation and small perturbations to the Galactic mask.

	$S_{1/2}$ statistic in $(\mu\mathrm{K})^4$						
sky cut	Pixel ACF (Eq. (2.3))	Pixel ACF (Eq. (2.5))	Harmonic Reconstruction $\ell_{\max}=5$	$\ell_{\max}=10$	$\ell_{\max}=15$	$\ell_{\max}=20$	QML ACF (Eq. (2.14))
full sky	7373	8532	8170	7777	7649	7606	8532
KQ85	1401	1781	8250	6953	7612	6383	7234
KQ75	647	963	7913	6914	8233	5139	5764

Table 2.1: Values of the $\mathbf{S_{1/2}}$ statistic for WMAP 5-year ILC maps.

As discussed in the Introduction, Refs. [124; 125] argue that the pixel estimates of the ACF computed from the masked regions of the sky lead to p-values with respect to the standard ΛCDM cosmology of $\sim 0.1\%$ or less, suggesting a significant discrepancy between the model and the data. However, the p-values computed for the unmasked sky are much less significant ($\sim 5\%$). Various interpretations of this result have been proposed:

(i) The interpretation put forward by [124; 125] is that either correlations have been introduced in reconstructing the full sky maps from the observations, or that there are highly significant departures from statistical isotropy that are correlated with the Galactic sky cut leading to an ACF that is very close to zero for regions outside the sky cut.

(ii) The interpretation put forward by [121] is that the ACF computed over the whole sky is accurate and unaffected by Galactic contamination. The low p-values arise from are a consequence of using a sub-optimal estimator of the ACF on a cut sky, combined with a posteriori choices of the form of the $S_{1/2}$ statistic.

In support of point (ii), Ref. [121] used a quadratic maximum likelihood (QML) estimator of the power spectrum, $\hat{C}^Q_\ell$, and computed the ACF

$$C^Q(\theta) = \frac{1}{4\pi}\sum_\ell (2\ell+1)\hat{C}^Q_\ell P_\ell(\cos\theta). \tag{2.14}$$

For Gaussian, statistically isotropic, temperature maps, the QML estimates $\hat{C}^Q_\ell$ have a significantly smaller variance than the PCL estimates $\hat{C}^P_\ell$ if a sky cut is applied to the data[1]. Hence the estimator $C^Q(\theta)$ will generally be closer to the truth, i.e. closer to the ensemble mean $\langle C(\theta)\rangle$, than the estimator (2.8). (Ref. [134] argues more generally that the QML estimator will be close to optimal for any theory with a power spectrum close to that of the concordance ΛCDM cosmology). Applied to the first year WMAP ILC map, [121] found that the ACF estimates derived from (2.14) are insensitive to a sky cut and lead to p-values for the S-statistic of $\sim 5\%$, *i.e.* no strong evidence against the concordance ΛCDM model.

The reason that the QML estimator has significantly smaller 'estimator induced' variance than the PCL estimator is easy to understand (see [136]). For noise-free band limited data, it is possible to reconstruct the low multipole coefficients $a_{\ell m}$ exactly from data over an incomplete sky. This is, in effect, what the QML estimator does, though it implicitly assumes statistical isotropy in weighting the $a_{\ell m}$ coefficients to form the power-spectrum (see equation (2.26) below) . For low multipoles, the assumption of statistical isotropy is unimportant, and for the noise-free data and sky cuts relevant to WMAP, the low order multipole coefficients and the power spectrum C_ℓ can be reconstructed almost exactly from data on the incomplete sky. In this Chapter, we will extend the analysis of [121] by explicitly reconstructing the low order coefficients $a_{\ell m}$ over the entire sky. This analysis will confirm that the ACF at large angular scales is insensitive to a sky cut and leads to p-values of marginal significance.

The 'estimator induced' variance of the pixel estimator of the ACF (2.3) is also easy to understand intuitively. (This problem has been discussed extensively in the literature in the context of angular clustering analysis of galaxy surveys [139; 140; 141; 142]). The ACF is a pair-weighted statistic. Consider the analysis of data on an incomplete sky. An overdensity, or underdensity, close to the boundary of the sky cut will almost certainly continue as an overdensity, or underdensity, across the cut. If the pair count is merely corrected by the missing area that lies within the cut region of sky (as in the estimator (2.3)) overdense and underdense regions close to the boundary will be underweighted. This causes no bias to the estimator, but increases the sample variance. The analysis presented in the next Section shows that it is possible reduce this sampling variance by reconstructing the low multipoles across a sky cut in a way that is numerically stable and free of assumptions concerning statistical isotropy.

[1] For noise-free data over the full sky, the QML and PCL estimators are identical.

2.3 Reconstructing low-order multipoles on a cut sky

The aim of this Section is to reconstruct the large-scale features of the temperature anisotropies over the whole sky using only the incomplete data that lies outside a chosen sky cut. This can be done in a number of ways, for example, by Weiner or 'power equalization' filtering [143], Gibbs sampling [144; 145] or by 'harmonic inpainting' [146]. Here we apply a direct inversion method, which is insensitive to assumptions concerning the statistical properties of the temperature field.

Let the vector $\mathbf{x}$ denote the temperature field on the sky and let the vector $\mathbf{a}$ denote the spherical harmonic coefficients $a_{\ell m}$. The vectors $\mathbf{x}$ and $\mathbf{a}$ are related by the spherical transform $\mathbf{Y}$,

$$\mathbf{x} = \mathbf{Y}\mathbf{a} + \mathbf{n}, \tag{2.15}$$

where $\mathbf{n}$ represents 'noise' in the data.

Now consider the reconstruction $\mathbf{a^e}$

$$\mathbf{a^e} = (\mathbf{Y}^T\mathbf{A}\mathbf{Y})^{-1}\mathbf{Y}^T\mathbf{A}\mathbf{x}, \tag{2.16}$$

for any arbitrary square matrix $\mathbf{A}$. The reconstruction is related to the true coefficients $\mathbf{a}$ by

$$\mathbf{a^e} = \mathbf{a} + (\mathbf{Y}^T\mathbf{A}\mathbf{Y})^{-1}\mathbf{Y}^T\mathbf{A}\mathbf{n}. \tag{2.17}$$

If the data is noise free, (2.16) recovers the true vector $\mathbf{a}$ exactly. If, further, we choose $\mathbf{A}$ to be the identity matrix, then

$$\mathbf{a^e} = \mathbf{K}^{-1}\tilde{\mathbf{a}}, \tag{2.18}$$

where $\mathbf{K}$ is the coupling matrix (2.11).

The reconstruction of (2.18) is closely related to the problem of defining an orthogonal basis set of functions on the cut sky, which has been studied extensively in the literature (see *e.g.* [147; 148; 149]). If the sky cut is relatively small, and the data are noise-free and band-limited, the coupling matrix $\mathbf{K}$ will be non-singular and can be inverted to yield the full-sky harmonics $\mathbf{a}$ exactly. If the data are noise-free but not band-limited, the matrix $\mathbf{K}$ will become numerically singular on the incomplete sky as $\ell_{\max} \to \infty$. (As a rule-of-thumb the matrix will become singular if $\ell_{\max}$ exceeds the inverse of the width of the sky cut in radians.) This simply tells us that there are 'ambiguous' harmonic coefficients that are unconstrained by the data outside the sky cut. For noise-free data that are not strictly band-limited, the solution (2.16) truncated to a finite value of ℓ_{max} will amplify some of the high frequency signal which will appear as 'noise' within the sky cut in the reconstruction $\mathbf{x^e} = \mathbf{Y}\mathbf{a^e}$. The amplitude of this 'noise' can be reduced by an appropriate choice of the matrix $\mathbf{A}$. If we assume that the signal and noise are Gaussian, the optimal solution of (2.15) is the familiar 'map-making' solution [131]

$$\mathbf{a^e} = (\mathbf{Y}^T\mathbf{C}^{-1}\mathbf{Y})^{-1}\mathbf{Y}^T\mathbf{C^{-1}x}, \tag{2.19}$$

$$\mathbf{C} = \langle \mathbf{x}\mathbf{x}^T \rangle = \mathbf{S} + \mathbf{N}. \tag{2.20}$$

If Gaussianity and statistical isotropy holds, the variance of the (2.19) is

$$\langle \mathbf{a}^e \mathbf{a}^{eT} \rangle = \mathbf{C_a} = (\mathbf{Y^T}\mathbf{C}^{-1}\mathbf{Y})^{-1}. \tag{2.21}$$

The statement that the estimator (2.19) is 'optimal' and the expression for the variance (2.21), do of course depend on the assumptions of Gaussianity and statistical isotropy. However, as long as the noise term in (2.17) is negligible, the reconstructed harmonic coefficients will be identical to the true harmonic coefficients *independent* of any assumptions concerning statistical isotropy. Figure 2.3 illustrates the application of this machinery. The upper row shows the smoothed WMAP 5-year ILC map (to the left) and the degraded resolution KQ75 mask (to the right). The remaining figures show the reconstructed maps from the harmonic coefficients (2.19) for the KQ85 mask (figures to the left) and for the KQ75 mask (figures to the right). The figures show the reconstructions with $\ell_{\max}$ truncated at 5, 10, 15 and 20. The maps for the two sky cuts at $\ell_{\max} = 5$ and 10 are virtually identical, and by $\ell = 10$ the reconstructions look visually similar to the ILC map over the entire sky. For $\ell_{\max} = 15$ and 20, the reconstructions for the KQ85 mask are stable and, again, look very similar to the WMAP ILC map over the whole sky. For the KQ75 mask, one can see 'noise' (*i.e.* reconstruction errors) beginning to appear inside the sky cut when $\ell_{\max}$ is increased to $\ell_{\max} = 15$ and 20.

However, the high harmonics that contribute to the 'noise' in Fig. 2.3 make very little contribution to the correlation function at large angular scales. This is illustrated in Fig. 2.4, which shows the dependence of the correlation functions

$$C^e(\theta) = \frac{1}{4\pi}\sum_{\ell=2}^{\ell_{\max}}(2\ell+1)C^e_\ell P_\ell(\cos\theta), \quad C^e_\ell = \frac{1}{(2\ell+1)}\sum_m |a^e_{\ell m}|^2, \tag{2.22}$$

on $\ell_{\max}$ for each of the each of the sky cuts. In the case of zero sky cut, the correlation function stabilises to its final shape by $\ell_{\max} = 10$; higher multipoles make a negligible contribution to the correlation function at large angular scales. The reconstructed correlation functions for the KQ85 and KQ75 masks are almost identical to the all-sky correlation function for $\ell_{\max} = 5$, 10 and 15. For the KQ75 mask, one can begin to see the effects of reconstruction noise in $C^e(\theta)$ for $\ell_{\max} = 20$, but the correlation function for the KQ85 mask remains stable.

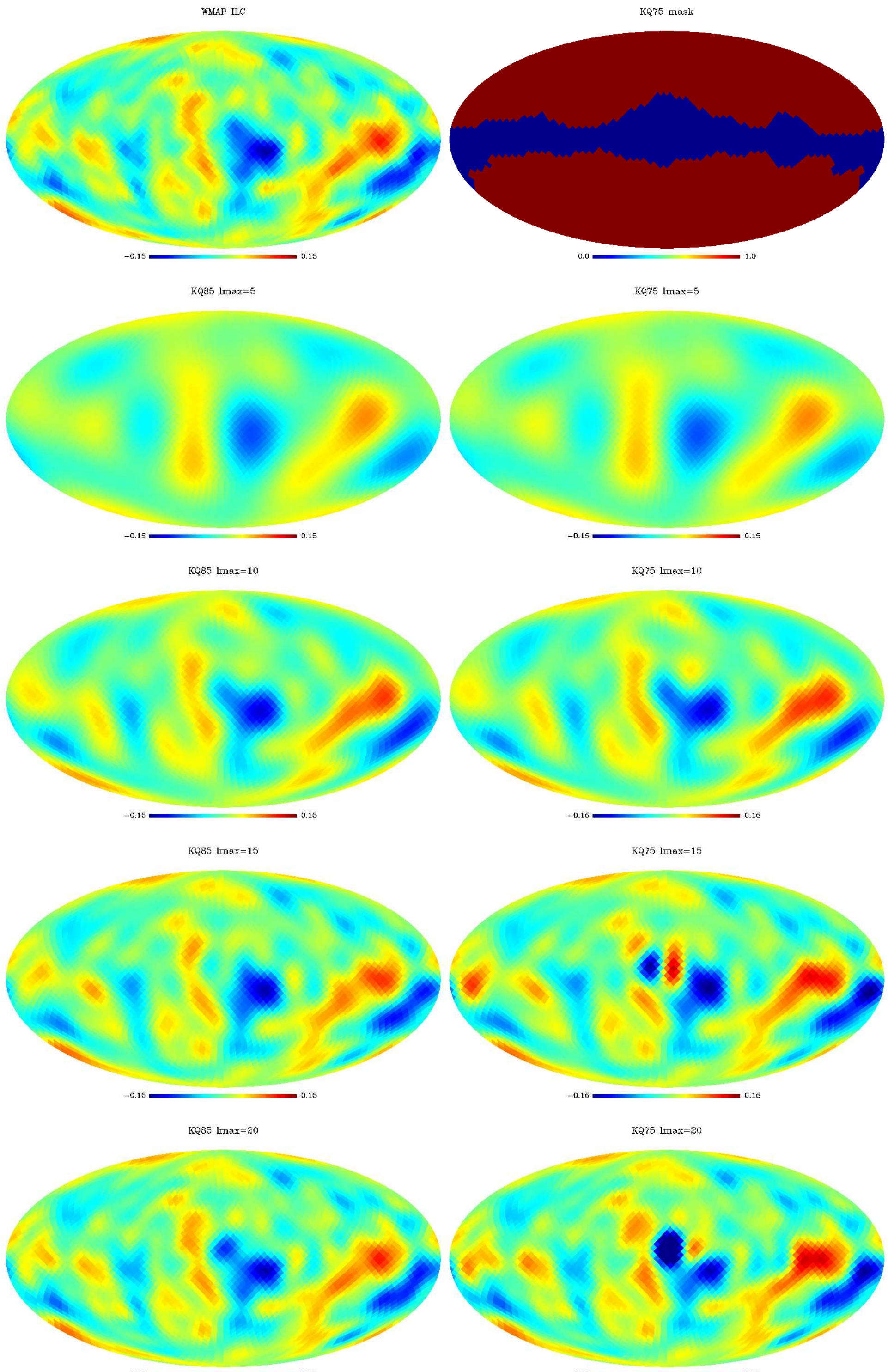

Figure 2.3: The figure to the left in the top row shows the WMAP 5 year ILC temperature map smoothed by a Gaussian of FWHM 10° and repixelized to a Healpix resolution of NSIDE=16. The figure to the right in the top panel shows the degraded resolution WMAP KQ75 mask used in this Chapter. The remaining figures to the left show the reconstructed all-sky maps computed from data outside the KQ85 sky cut, using the harmonic coefficients computed from equation (2.19) with the coupling matrices truncated to (from top to bottom) $\ell_{\rm max} = 5$, 10, 15 and 20. The figures to the right show equivalent plots for the reconstructed all-sky maps computed from data outside the KQ75 sky cut.

ℓ	$(\Delta T^2)_\ell$	$\delta(\Delta T^2)_\ell$ Harmonic Reconstruction KQ85				$\delta(\Delta T^2)_\ell$ Harmonic Reconstruction KQ75			
ℓ	ILC	$\ell_{\max} = 5$	$\ell_{\max} = 10$	$\ell_{\max} = 15$	$\ell_{\max} = 20$	$\ell_{\max} = 5$	$\ell_{\max} = 10$	$\ell_{\max} = 15$	$\ell_{\max} = 20$
2	98.8	0.28	0.04	0.29	0.22	6.5	2.0	5.0	5.4
3	292.2	0.14	0.26	0.31	0.58	2.4	4.0	15.0	14.1
4	150.3	0.57	0.51	0.99	1.09	13.8	3.9	36.2	38.1
5	254.3	0.36	1.18	1.69	1.41	3.4	13.2	23.6	35.8
6	79.6	–	0.88	1.89	1.85	–	4.8	63.1	39.2
7	132.4	–	1.96	2.80	2.28	–	13.9	37.7	42.8
8	55.3	–	1.72	3.65	2.25	–	9.3	67.8	65.6
9	44.0	–	1.77	2.84	2.17	–	10.6	30.0	44.7
10	45.6	–	1.23	2.89	1.69	–	4.3	43.5	33.3

Table 2.2: Residuals of harmonic reconstructions (all in $(\mu K)^2$).

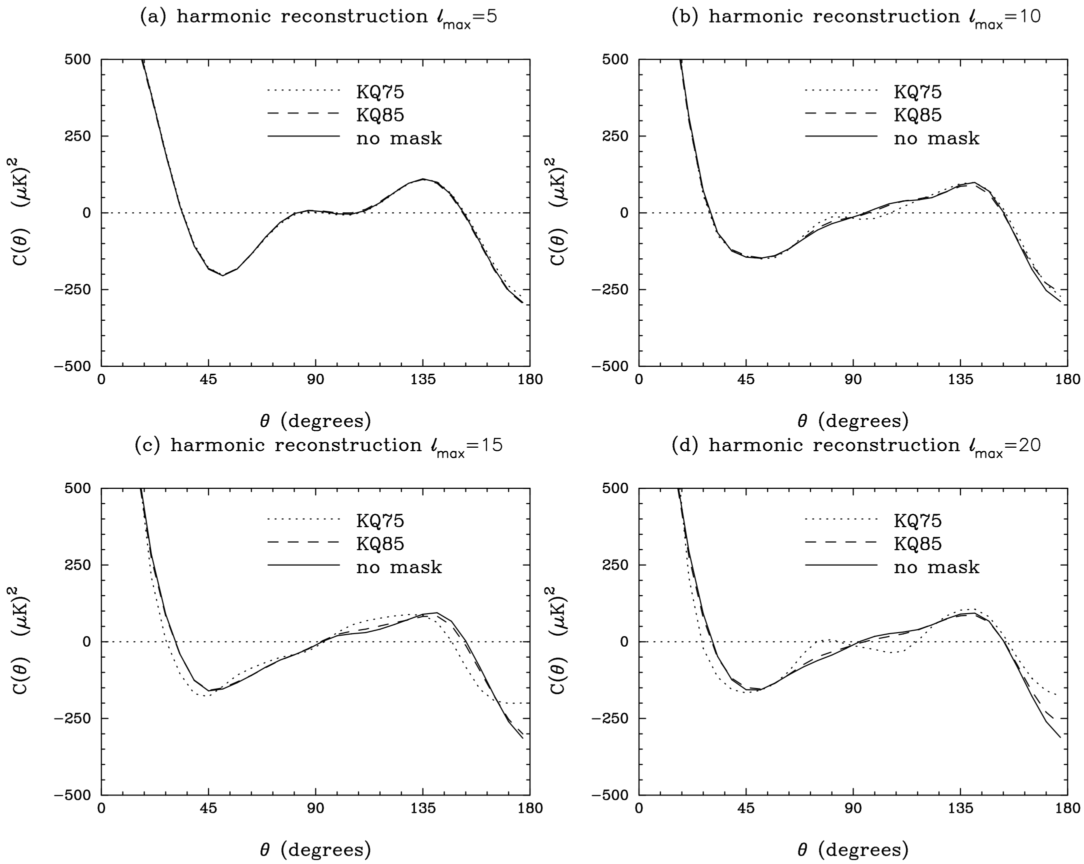

Figure 2.4: Reconstructions of the correlation function from equation (2.22) for various choices of $\ell_{\max}$ and sky cut.

In Table 2.2, we list the mean square temperature at each multipole

$$(\Delta T)^2_\ell = \frac{1}{4\pi}\sum_m |a^{\rm ILC}_{\ell m}|^2, \tag{2.23}$$

for the first few multipoles ($\ell \leq 10$) computed from the ILC map, and the residuals

$$\delta(\Delta T)^2_\ell = \frac{1}{4\pi}\sum_m |a^{\rm ILC}_{\ell m} - a^{\rm e}_{\ell m}|^2, \tag{2.24}$$

for our reconstructed maps. For the KQ85 mask, all multipoles with $\ell \leq 10$ are reconstructed to high accuracy, with residuals $\delta(\Delta T)^2_\ell \sim 2\mu{\rm K}^2$ or less. For the KQ75 mask, the reconstruction begins to break down for multipoles $\ell \geq 6$ if $\ell_{\max} \geq 15$ because of the coupling with 'ambiguous' modes that cannot accurately be reconstructed within the sky cut. Nevertheless, since the shape of the correlation function is dominated by the low multipoles, the shape remains reasonably stable even for $\ell_{\max} = 20$ (Fig. 2.4d).

This analysis shows that it is possible to reconstruct the low order harmonic coefficients that contribute to the large angle correlation functions accurately from data on the cut sky. The sky cut is basically irrelevant and so the all-sky form of the correlation function can be reconstructed from the cut sky irrespective of any assumptions concerning Gaussianity or statistical isotropy and with only a very weak dependence on the assumed shape of the covariance matrix C_{ij}. Values for the $S_{1/2}$ statistic for each of the cases shown in Fig. 2.4 are listed in Table 2.1.

Notice that if we define weighted harmonic coefficients,

$$\boldsymbol{\beta} = \mathbf{C_a}^{-1}\mathbf{a^e} = Y^*_{\ell m}(\boldsymbol{\theta}_i)C^{-1}_{ij}x_j, \tag{2.25}$$

then the power spectrum computed from these weighted coefficients is

$$y_\ell = \frac{1}{2}\sum_m |\beta_{\ell m}|^2 = x_p x_q E^\ell_{pq}, \tag{2.26}$$

where

$$\mathbf{E}^\ell = \frac{1}{2}\mathbf{C}^{-1}\frac{\partial \mathbf{C}}{\partial C_\ell}\mathbf{C}^{-1}. \tag{2.27}$$

In other words, the power spectrum of the weighted coefficients is identically equivalent to the QML power spectrum estimator [131; 150]. If statistical isotropy holds, and the data is noise-free, the quantity

$$\hat{\mathbf{C}}^{\mathbf{Q}} = \mathbf{F}^{-1}\mathbf{y}, \tag{2.28}$$

provides an unbiased estimate of the power spectrum, where $\mathbf{F}$ is the Fisher matrix,

$$F_{\ell\ell'} = \frac{1}{2}\mathrm{Tr}\left[\mathbf{C}^{-1}\frac{\partial \mathbf{C}}{\partial C_\ell}\mathbf{C}^{-1}\frac{\partial \mathbf{C}}{\partial C_{\ell'}}\right]. \tag{2.29}$$

Notice that for the complete sky, and for noise-free data

$$\mathbf{C_a} = C_\ell \delta_{\ell\ell'}\delta_{mm'}, \tag{2.30}$$

in the limit $\ell_{max} \to \infty$, *i.e.* the variance on the $a_{\ell m}$ is just the cosmic variance. The Fisher matrix is

$$F_{\ell\ell'} = \frac{(2\ell+1)}{2C^2_\ell}\delta_{\ell\ell'}, \tag{2.31}$$

and so the QML estimates $\hat{C}^Q_\ell$ are identical to the PCL estimates. For relatively small sky cuts such as the KQ85 and KQ75 masks, the Fisher matrix at low multipoles will be *almost* diagonal [136] and the recovered power spectrum from the cut sky will be almost identical to the true power spectrum computed from the whole sky. The QML estimator effectively performs the reconstruction $\mathbf{a^e}$ of equation (2.19), but uses the assumption of statistical isotropy to downweight 'ambiguous' modes that are poorly constrained by the sky cut.

For small sky cuts, we would therefore expect the QML correlation function estimate (2.14) to be almost identical at large-angular scales to the correlation functions computed from the

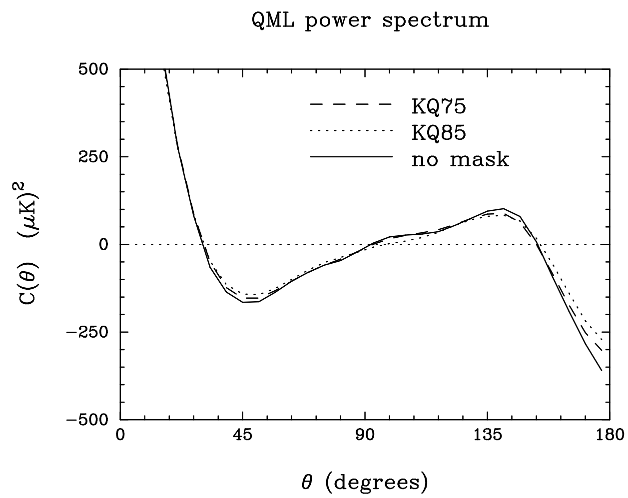

Figure 2.5: As Figure 2.1 but using the QML estimator of equation (2.14).

reconstructed coefficients $\mathbf{a}^{\mathrm{e}}$. (They are, of course, mathematically identical for zero sky cut.) $C^{Q}(\theta)$ is expected to behave more stably than $C^{e}(\theta)$ as the sky cut is increased, since the QML correlation function downweights ambiguous modes. This is exactly what we see when we apply the QML estimate to the WMAP ILC 5-year ILC maps (see Fig. 2.5). The ACF is almost independent of the sky cut, confirming the results of [121]. Values of the $S_{1/2}$ statistic for the QML ACF estimates are listed in the final column of Table 2.1.

The QML power spectrum estimates are plotted in Fig. 2.6. The power spectrum coefficients $\hat{C}^{Q}_{\ell}$ are extremely stable to the sky cut, varying by only a few tens of $(\mu\mathrm{K})^2$ for $\ell \leq 10$. The figure compares these estimates to the power spectrum estimates for the reconstructed all-sky maps using equation (2.19). We plot the results for $\ell_{\max} = 10$, since this value is large enough to determine the shape of the ACF at large angular scales, but small enough to limit the noise in the reconstructed maps at high multipoles. The power spectra of the reconstructed maps are very close to the QML estimates at $\ell \leq 8$, though one can begin to see the effects of reconstruction noise in the KQ75 case at $\ell > 8$. (However, as Fig. 2.4b shows, this reconstruction noise has very little effect on the shape of the ACF at large angular scales.)

The results of this section show that the low-order multipole coefficients that determine the behaviour of the correlation function at large angular scales can be reconstructed to high accuracy from data on the incomplete sky, independent of any assumptions concerning statistical isotropy. The usual motivation for applying a sky cut is to remove regions of the sky that may be contaminated by residual Galactic emission. However, for the KQ85 and KQ75 sky cuts, the missing area of sky leads to little loss of information at low multipoles. The low multipoles can therefore be reconstructed from the data on the incomplete sky. The imposition of the sky cuts does not remove foreground contamination at these low multipoles: any residual Galactic contribution to the low multipoles in the ILC map is, like the CMB signal, faithfully reproduced by the reconstructions shown in Fig. 2.3. What a Galactic cut can do is to mask out localized Galactic

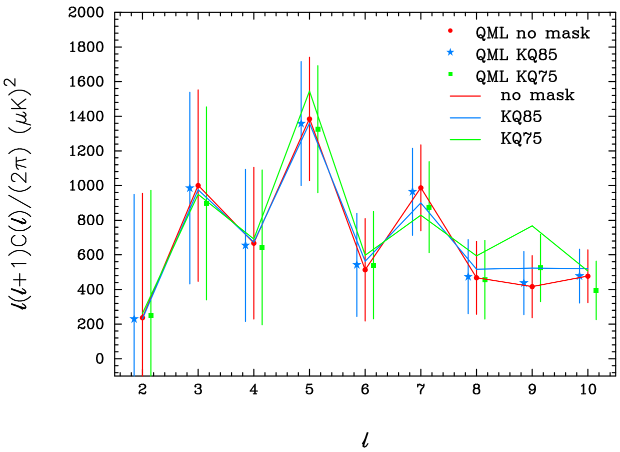

Figure 2.6: The temperature power spectrum at low multipoles computed from the low resolution WMAP 5-year ILC map. The points (corrected for the 10° FWHM smoothing and slightly displaced in ℓ for clarity) show QML power spectrum estimates for three sky cuts: no mask; KQ85 mask; KQ75 mask. Error bars show the diagonal components of the inverse of the Fisher matrix (2.29). The solid red line shows the power spectrum computed from the all-sky ILC map (which is identical to the QML all-sky estimates). The solid green and blue lines show the power spectra computed for the $\ell_{\max} = 10$ reconstructions of Fig. 2.3.

emission ('ambiguous' modes) that could, in principle, couple to the low multipoles in a way that depends on the estimator (*e.g.* via the coupling matrix $\mathbf{K}$ in the simple inversion of equation (2.18)). The similarities between the reconstructions of Fig. 2.3 and the full-sky ILC map (and the correlation functions and power spectra plotted in Figs. 2.5 and 2.6) show that the ILC map has removed Galactic emission successfully at low Galactic latitudes, since there is no evidence of high amplitude 'ambiguous' modes in the ILC map within the region of the sky cut.

If suitable estimators are applied to noise-free data, a sky cut of the size of the KQ85 or KQ75 masks has little impact on the reconstruction of the low order multipoles or the all-sky ACF. The imposition of a sky cut does, however, lead to a loss of information if a poor estimator is used to estimate the ACF. This is what happens when the pixel estimator (2.3) is used to estimate the ACF on the cut sky [124; 125; 151]. The analysis presented in this Section provides compelling evidence that the true value of the $S_{1/2}$ statistic for our realization of the sky is in the region of 6000-8000$(\mu\mathrm{K})^4$, independent of the sky cut. The remaining question is whether the anomalously low p-values implied by the cut-sky pixel ACF are the result of a statistical fluke, or indicative of new physics.

2.4 Analysis of the $\mathbf{S_{1/2}}$ statistic

In this Section we analyze the $S_{1/2}$ statistic, first from a Bayesian point of view, and then from a frequentist point of view. We then discuss the interpretation of the low frequentist p-values found by [125].

2.4.1 Approximate Bayesian analysis

We begin by performing an approximate Bayesian analysis to compute the posterior distribution of the $S_{1/2}$ given the data on the assumption that the fluctuations are Gaussian and statistically isotropic. If the data were noise-free and covered the entire sky then, under the assumptions of statistical isotropy and Gaussianity, the data power spectrum C_ℓ^d provides a loss-free description of the data. Assuming uniform priors on each of the C_ℓ^T, the posterior distribution of the theory power spectrum coefficients C_ℓ^T is given by the inverse Gamma distribution

$$dP(C_\ell^T|C_\ell^d) \propto \left(\frac{C_\ell^d}{C_\ell^T}\right)^{\frac{2\ell-1}{2}} \exp\left[-\frac{(2\ell+1)}{2}\left(\frac{C_\ell^d}{C_\ell^T}\right)\right]\frac{1}{C_\ell^T}. \tag{2.32}$$

Each of the C_ℓ^T is statistically independent and the mean value is

$$\langle C_\ell^T \rangle = \left(\frac{2\ell+1}{2\ell-3}\right) C_\ell^d. \tag{2.33}$$

The distribution (2.32) will therefore favour theory values that are larger than the observed values C_ℓ^d.

The results of the previous Section (and Fig. 2.6 in particular) show that the low multipoles are well determined and insensitive to the application of a sky cut. We can therefore use the measurements C_ℓ^d computed over the whole sky to represent the data [1]. The multipole expansion is truncated at $\ell_{\max} = 20$ (although as discussed in the previous Section, multipoles greater than $\ell \approx 10$ make very little contribution to the ACF at large angular scales) and statistically independent C_ℓ^T values are generated from the inverse Gamma distribution (2.32). These values are then used to generate Gaussian $a_{\ell m}^T$ from which we synthesize real-space maps x_i at a Healpix resolution of NSIDE=16 smoothed with a Gaussian of FWHM 10°. We then compute $S_{1/2}$ from the pixel correlation function (2.3). This methodology provides a test of statistically isotropic, Gaussian models, with no additional constraints imposed on the theory C_ℓ^T apart from uniform priors.

The posterior distributions of $S_{1/2}^T$ is shown in Fig. 2.7a for the analysis of all-sky maps (red histogram) and for maps with the KQ75 mask applied (blue histogram). The distribution for the trials with the sky cut applied is slightly broader than the distribution for the all-sky trials, as expected since the pixel ACF estimator is sub-optimal on a cut sky. The peaks of the distributions occur at $S_{1/2}^T \approx 6000$ $(\mu\mathrm{K})^4$ and so low values of $S_{1/2}^T$ are clearly preferred by the data. However, the posterior distributions have a very long tail to high values (as expected from the inverse Gamma distribution 2.32). The best fitting six parameter ΛCDM model as determined from the 5-year WMAP analysis [3] has a value of $S_{1/2}^T \sim 49000$ $(\mu\mathrm{K})^4$. At this value (indicated by the

[1] It is in this sense that the analysis presented here is described as an 'approximate', *i.e.* any residual errors on the C_ℓ^d are ignored.

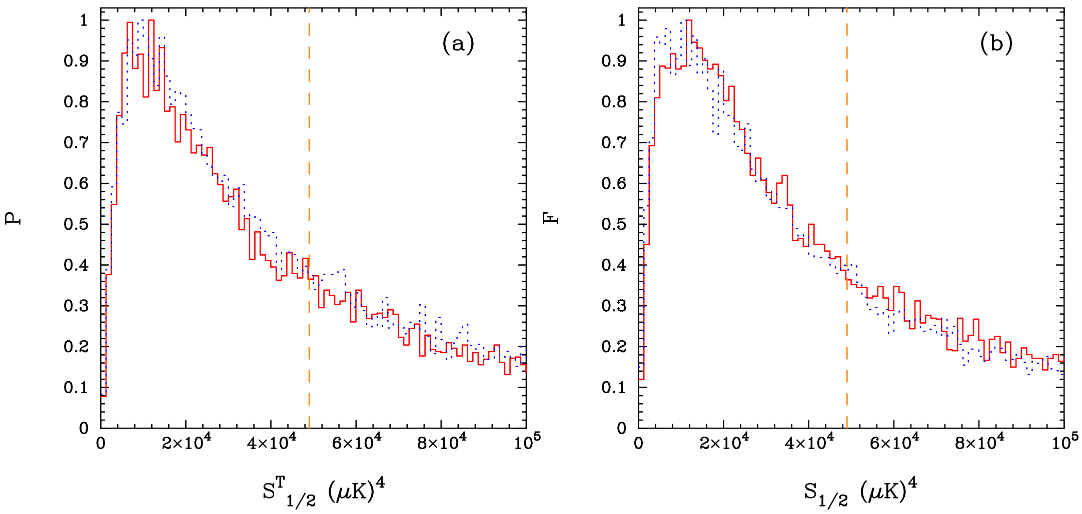

Figure 2.7: (a) Posterior distributions of $S^T_{1/2}$ computed as discussed in the text. The red (solid) histogram shows the distribution of $S^T_{1/2}$ from an analysis of the whole sky. The blue (dotted) histogram shows the distribution computed with the KQ75 sky cut applied. The vertical dashed lines in the figures shows the value $S^T_{1/2} \sim 49000$ $(\mu\mathrm{K})^4$ for the best fitting ΛCDM model as determined from the 5-year WMAP analysis [3]. (b) Frequency distributions of $S_{1/2}$ for statistically isotropic, Gaussian, realizations of the ΛCDM model [3]. The red (solid) histogram shows the frequency distribution for the pixel ACF estimator applied to the whole sky. The blue (dotted) histogram shows the distribution computed with the pixel ACF estimator with the KQ75 sky cut applied.

vertical dashed line in Fig. 2.7a), the posterior distribution has fallen to a value of about 0.4. Such high values of $S^T_{1/2}$ are evidently not favoured by the data, but they are not strongly disfavoured. Very low values of $S^T_{1/2}$, of ~ 1000 $(\mu\mathrm{K})^4$ are also not strongly disfavoured.

From the Bayesian point of view, the quantity $S_{1/2}$ is a poor discriminator of theoretical models and so is relatively uninformative. The posterior distributions of Fig. 2.7a are extremely broad with a long tail to high values. The data, irrespective of estimator or sky cut, clearly prefer low values of $S_{1/2}$ but cannot exclude the value of $S^T_{1/2} \sim 49000$ $(\mu\mathrm{K})^4$ expected for the concordance inflationary ΛCDM model.

2.4.2 Frequentist analysis

We now generate statistically isotropic Gaussian realizations with the C^T_ℓ constrained to those of the best fitting ΛCDM model. The frequency distributions of $S_{1/2}$ computed from the pixel estimator are plotted in Fig. 2.7b. The distributions of Figs. 2.7a and 2.7b look fairly similar, but the frequentist interpretation is very different. For the all-sky analysis, the p-value of finding $S_{1/2} < 7373$ $(\mu\mathrm{K})^4$ is 8% and hence is not statistically significant. However, if we apply the KQ75 mask, the p-value for $S_{1/2} < 647$ $(\mu\mathrm{K})^4$ is only 0.065%. This result appears strongly significant and, at face value, inconsistent with the p-value for the all-sky analysis.

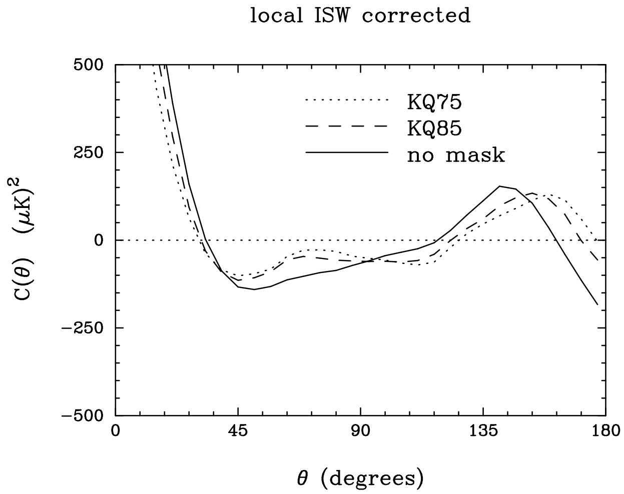

Figure 2.8: Pixel based estimates ACF estimates for the WMAP ICL map corrected for the local ISW contribution for redshift $z < 0.3$ as described by [132].

The low p-value found here and by [1] and [125] come exclusively from analyzing cut sky maps with 'sub-optimal' (in the sense of not reproducing the ACF for the whole sky) estimators. The sky cuts, ostensibly imposed to reduce any effects of Galactic emission at low Galactic latitudes, lead to a loss of information and to poorer estimates of the ACF *for our realization of the sky*. But as we have demonstrated, the information on the ACF at large angles for our realization of the sky is contained in the data outside the sky cuts. The imposition of a sky cut therefore has little to do with reducing the effects of Galactic emission on the ACF at large angular scales. If there is any cosmological significance to the low p-values, then one must accept that the Galactic cut aligns with the signal, *purely by coincidence*, in just such a way as to remove the large-scale angular correlations for particular choices of estimator of the ACF. This alignment may indicate a violation of statistical isotropy, as argued by [125], but if this is true the alignment with the Galactic plane must be purely coincidental.

It seems to us that a more plausible interpretation of the low p-values is that they are a consequence of the *a posteriori* selection of the $S_{1/2}$ statistic by [1] for a particular choice of estimator and sky cut. It is difficult to quantify the effects of *a posteriori* choices. However, numerical tests with the more general statistic

$$S^p_\mu = \left[\frac{2}{3}\int_{-1}^{\mu} [C(\theta)]^p \, d\cos\theta\right]^{2/p}, \tag{2.34}$$

(which reduces to $S_{1/2}$ for the choices $\mu = 1/2$ and $p = 2$) suggest that it is possible to alter p-values by an order of magnitude or more by selecting the parameters in response to the data. It would be possible to raise the p-values even more by varying the size and orientation of a sky cut.

Is there any way of testing this hypothesis further? In the ΛCDM model, the integrated Sachs-

Wolfe (ISW) effect [152] makes a significant contribution to the total temperature anisotropy signal at low multipoles. The ISW contribution from the time of last scattering ($t_{\rm LS}$) and the present day (t_0) is given by

$$\frac{\Delta T}{T}^{\rm ISW} = 2\int_{t_{\rm LS}}^{t_0} \frac{d\Phi}{dt}\, dt \tag{2.35}$$

where Φ is the Newtonian gravitational potential (see *e.g.* [153]). Recently, Ref. [132] has used the 2MASS near infrared all-sky survey [154], together with photometric redshift estimates to compute the ISW contribution from local structure at redshifts $z < 0.3$. If *a posteriori* choices are responsible for the low p-values, we should find large changes to the pixel ACF estimates for the masked sky when the WMAP ILC maps are corrected for the local ISW contribution. As shown in Fig. 2.8, this is indeed what we find when we subtract the local ISW contribution computed by [132] from the 5-year WMAP ILC map. The $S_{1/2}$ statistic computed from the ACFs shown in Fig. 2.8 are 10360 $(\mu{\rm K})^4$ (all-sky), 6463 $(\mu{\rm K})^4$ (KQ85 mask) and 5257 $(\mu{\rm K})^4$ (KQ75 mask), all consistent with the concordance ΛCDM model at the few percent level. This is consistent with our hypothesis that the [125] low p-values are a fluke, unless one is prepared to argue that there is a physical alignment of local structure with the potential fluctuations at the last scattering surface that conspires to remove large-angle temperature correlations in the regions outside the Galactic mask (which seems implausible to us). Francis and Peacock [132] discuss how the local ISW correction affects a number of other low multipole statistics, in particular reducing the statistical significance of the alignment between the quadrupole and octopole.

2.5 Discussion and Conclusions

The low amplitude of the temperature autocorrelation function at large angular scales has led to some controversy since the publication of the first year results from WMAP. This Chapter has sought to clarify the following points:

[1] We have compared different estimators of the ACF showing: (a) how they depend on assumptions of statistical isotropy; (b) how they are interrelated; (c) how they perform on the WMAP 5-year ILC maps with and without a sky cut.

[2] The imposition of the KQ85 and KQ75 sky masks leads to little loss of information on the low multipoles that contribute to the large-scale angular correlation function. As demonstrated in Section 2.3, the low multipole harmonics can be reconstructed accurately from the data that lie outside the sky cuts, independent of any assumptions concerning statistical isotropy and with only a weak dependence of the shape of the pixel covariance matrix C_{ij}. The ACFs computed from these reconstructions are in good agreement with the ACF computed from the whole sky and in good agreement with the maximum likelihood estimator (2.14). There can be little doubt that the large-scale ACF for our realization of the sky is very close to the all-sky results shown in Figs. 2.1 and 2.5.

[3] The lack of large-scale structure seen in the cut-sky pixel ACF arises from a particular alignment of the low order multipoles (see also [134]) which, as we have demonstrated, can be reconstructed accurately from the data outside the sky cut. The ACF at large angular scales is insensitive to high order modes localised within the sky cut.
[4] The Bayesian analysis presented in Section 2.4 shows that the posterior distribution of the $S^T_{1/2}$ is broad and cannot exclude the value $S^T_{1/2} \sim 49000\ (\mu\mathrm{K})^4$ appropriate for the [3] best fitting inflationary ΛCDM model. The breadth of the posterior distribution $S^T_{1/2}$ distribution shows that it is fairly uninformative statistic and so is not a particularly good discriminator of theoretical models.
[5] Unusually low values of the $S_{1/2}$ statistic are found only if 'sub-optimal' ACF estimators are applied to maps that include a Galactic mask. We have argued that the low p-values associated with these low values of $S_{1/2}$ are most plausibly a result of *a posteriori* choices of statistic. This seems plausible to us because: (a) S-type statistics are relatively uninformative and hence sensitive to *a posteriori* choices; (b) the all-sky ACF (which is compatible with the concordance ΛCDM model) can be recovered from the data outside the mask and so any physical model for the low p-values requires a fortuitous alignment of the temperature field with the Galaxy; (b) the analysis of the local ISW corrected maps presented in Section 2.4 suggests that any physical model of the low p-values requires a precise alignment of local structure with the large-scale potential fluctuations at the last scattering surface.
[6] If one does not accept that the low-p values are associated with *a posteriori* choices, then one must accept that they may be indicative of new physics as suggested by [125].

In summary, the results of this Chapter suggest to us that, irrespective of the imposition of Galactic sky cuts or assumptions of statistical isotropy, the large-scale correlations of the CMB temperature field provide unconvincing evidence against the concordance inflationary ΛCDM cosmology.

Chapter 3

Testing a direction-dependent primordial power spectrum with CMB observations

3.1 Introduction

In recent years, observations of the cosmic microwave background (CMB) radiation fluctuations by the Wilkinson Microwave Anisotropy Probe (WMAP) and a large number of ground-based and suborbital experiments have led to a precise measurement of the temperature anisotropy power spectrum up to multipoles of a few thousand ([10; 61; 155; 156; 157; 158]) . Apart from some claimed "anomalies" (see below) the observations are consistent with a dark-energy-dominated cosmology with statistically isotropic, Gaussian, adiabatic perturbations, as expected from simple models of inflation. (We will refer to this as the "concordance" ΛCDM model.) If statistical isotropy applies, then the harmonic coefficients of the temperature field,

$$a_{lm}^{T} = \int d\Omega Y_{lm}^{*}(\Omega)\Delta T(\Omega), \tag{3.1}$$

must satisfy

$$C_{lm,l'm'}^{TT} = \left\langle a_{lm}^{T} a_{l'm'}^{T*} \right\rangle = C_{l}^{TT} \delta_{ll'} \delta_{mm'}. \tag{3.2}$$

If the fluctuations are Gaussian and statistically isotropic, their statistical properties are completely described by the power spectrum C_l^{TT}.

There have been some hints of "anomalies" in the WMAP data, perhaps suggesting a violation of statistical isotropy. These include alignments of low-l multipoles [126; 128; 159; 160], evidence for power asymmetry [161; 162] and for a deep cold spot in the southern Galactic hemisphere [163; 164]. For the most part, these anomalies have been found by examining the data without reference to specific theoretical models. There is, therefore, an *a posteriori* aspect in computing their statistical significance which is difficult to assess [133]. Some authors have, however, claimed highly significant discrepancies between the CMB data and the concordance ΛCDM model [165].

Interest in the CMB anomalies has motivated theorists to build inflationary models that violate rotational invariance, either via the addition of a vector field [166; 167; 168] or via an isocurvature perturbation [169; 170]. In addition, a number of phenomenological models that violate statistical isotropy have been proposed, which can be tested against observations (e.g. [166; 171; 172]).

Reference [166] considers the phenomenological model in which the primordial power spectrum depends on a preferred direction,

$$\mathcal{P}(\mathbf{k}) = P_s(k)[1 + g(k)(\mathbf{k} \cdot \mathbf{n})^2], \tag{3.3}$$

where $g(k)$ is some arbitrary function of wavenumber, and $P_s(k)$ is the isotropic primordial power spectrum (1.35). There has been considerable interest in this model recently. The authors of [173] applied Gibbs sampling to the WMAP five-year maps to test models with $g(k) = g_* =$ constant, finding strong evidence for a preferred direction with $g_* = 0.15 \pm 0.039$ using multipoles $l \leq 400$. Hanson and Lewis [174] corrected some algebraic errors in the analysis of [173] and applied a simpler quadratic estimator to the WMAP 5-year data. These authors also found evidence for a highly significant (9σ) departure from statistical isotropy, but with a preferred direction suspiciously close to the ecliptic poles, suggestive of some type of systematic effect in the WMAP data. This analysis was confirmed by [175]. A subsequent analysis [176] showed that asymmetries in the WMAP beams fully account for the observed violation of statistical isotropy.

Despite this negative conclusion, it is still important to assess the prospects of constraining violations of statistical isotropy in the CMB with more precise experiments. In this Chapter, we focus on constraints from the Planck satellite, which was launched successfully in May 2009 and has recently completed its third full scan of the sky. The Planck satellite has much higher signal-to-noise ratio in both temperature and polarization than WMAP [27]. It also has higher angular resolution — 5 arcmin full-width at half-maximum (FWHM) at frequencies $\geq$ 217 GHz — so asymmetries on scales of the beam width should have little effect at multipoles $l \leq 1000$. It is also expected that the Planck beams will be calibrated to high precision from scans of bright planets [177]. Following the successful launch of Planck, the European Space Agency (ESA) has approved a mission extension until the on-board cryogens are depleted. Planck is therefore expected to produce almost five sky surveys, compared to the two sky surveys approved for the nominal mission. This combination of high sensitivity, high resolution and extended lifetime allows greater scope for testing for systematic effects than was possible with WMAP. For example, it becomes possible to use polarization maps independently of temperature maps to test for violations of statistical isotropy.

In this Chapter, we extend the analysis of [178] to assess how accurately an extended Planck mission can be used to test models with an anisotropic primordial power spectrum. This Chapter is organized as follows: In Section 3.2, we summarize some basic properties of the anisotropic model. Section 3.3 then applies the quadratic estimator of [174], extended to include polarization, to compute forecasts for Planck. Our conclusions are presented in Section 3.4.

3.2 The anisotropic model

3.2.1 Covariance matrix

We write the anisotropic primordial power spectrum as

$$\mathcal{P}(\mathbf{k}) = P_s(k)\left(1 + \sum_{LM} g_{LM}(k) Y_{LM}(\hat{\mathbf{k}})\right). \tag{3.4}$$

We assume that parity-invariance continues to hold in the mean so that L is restricted to even values such that $\mathcal{P}(-\mathbf{k}) = \mathcal{P}(\mathbf{k})$. In this Chapter, we consider a quadrupole modulation, i.e. $L = 2$, $|M| \leq 2$, with a power-law scale dependence on the wave number $g_{LM}(k) = g_{LM}(k_0/k)^q$ where the pivot scale $k_0 = 0.002\,\mathrm{Mpc}^{-1}$. Scale-invariant modulation corresponds to $q = 0$.

The harmonic coefficients of the CMB anisotropy can be expressed as

$$a^X_{lm} = 4\pi i^l \int \frac{d^3\mathbf{k}}{(2\pi)^3} \Delta^X_l(k)\zeta(\mathbf{k}) Y^*_{lm}(\hat{\mathbf{k}}), \tag{3.5}$$

where $\Delta^X_l(k)$ are the adiabatic transfer functions, either for temperature ($X = T$) or E-mode polarization ($X = E$). The primordial curvature perturbation is $\zeta(\mathbf{k})$ with statistically-homogeneous but anisotropic correlations

$$\langle \zeta(\mathbf{k})\zeta^*(\mathbf{k}')\rangle = (2\pi)^3\delta^3(\mathbf{k} - \mathbf{k}')\frac{2\pi^2}{k^3}\mathcal{P}(\mathbf{k}), \tag{3.6}$$

with $\mathcal{P}(\mathbf{k})$ given by Eq. (3.4). Thus, the covariance matrix of the harmonic coefficients is

$$\begin{aligned} C^{XX'}_{l_1m_1,l_2m_2} &= \left\langle a^X_{l_1m_1} a^{X'*}_{l_2m_2}\right\rangle \\ &= C^{XX'}_{l_1}\delta_{l_1l_2}\delta_{m_1m_2} + \delta C^{XX'}_{l_1m_1,l_2m_2}, \end{aligned} \tag{3.7}$$

where

$$C^{XX'}_{l_1} = 4\pi \int d\ln k P_s(k)\Delta^X_{l_1}(k)\Delta^{X'}_{l_1}(k) \tag{3.8}$$

is the usual isotropic power spectrum. The additional term in Eq. (3.7) due to the power asymmetry is

$$\delta C^{XX'}_{l_1m_1,l_2m_2} = i^{l_1-l_2}\tilde{C}^{XX'}_{l_1l_2}(q)\sum_{LM} g_{LM}\int d\Omega_k Y_{LM}(\hat{\mathbf{k}})Y^*_{l_1m_1}(\hat{\mathbf{k}})Y_{l_2m_2}(\hat{\mathbf{k}})$$

$$\begin{aligned} &= i^{l_1-l_2}\tilde{C}^{XX'}_{l_1l_2}(q)\sum_{LM} g_{LM}(-1)^{m_1} \\ &\quad\times\left[\frac{(2L+1)(2l_1+1)(2l_2+1)}{2\pi}\right]^{\frac{1}{2}}\begin{pmatrix} L & l_1 & l_2 \\ 0 & 0 & 0 \end{pmatrix}\begin{pmatrix} L & l_1 & l_2 \\ M & -m_1 & m_2 \end{pmatrix}, \end{aligned} \tag{3.9}$$

where

$$\tilde{C}^{XX'}_{l_1l_2}(q) = 4\pi\int d\ln k P_s(k)\Delta^X_{l_1}(k)\Delta^{X'}_{l_2}(k)\left(\frac{k_0}{k}\right)^q. \tag{3.10}$$

Since L is even, the anisotropic covariance is nonzero only for l_1-l_2 even as required by parity invariance. In the following it will also be convenient to introduce 2×2 matrices $\mathbf{C}_{l_1m_1,l_2m_2}$ and $\tilde{\mathbf{C}}_{l_1l_2}$ with elements $C^{X_1X_2}_{l_1m_1,l_2m_2}$ and $\tilde{C}^{X_1X_2}_{l_1l_2}(q)$ respectively.

3.2.2 Quadratic estimators and the Fisher matrix

Here we assume that the scale-dependence of the power asymmetry (i.e. q) is known. We can then use the quadratic estimator of Ref. [174], extended to polarization, to form estimates $\hat{g}_{LM}$ of the anisotropy parameters. For an isotropic survey and in the limit of small primordial anisotropy, these take the form

$$\hat{g}_{LM} = \frac{1}{2}\sum_{L'M'} F^{-1}_{LM,L'M'}\sum_{X_1l_1m_1}\sum_{X_2l_2m_2}\bar{a}^{X_1*}_{l_1m_1}\frac{\partial C^{X_1X_2}_{l_1m_1,l_2m_2}}{\partial g^*_{L'M'}}\bar{a}^{X_2}_{l_2m_2}. \tag{3.11}$$

Here, $\bar{a}^X_{lm} \equiv \sum_{X'}[(\mathbf{C}^{\rm tot}_l)^{-1}]^{XX'}a^{X'}_{lm}$ are the temperature and polarization multipoles after weighting with the inverse of their isotropic total (signal-plus-noise) covariance matrix. The Fisher matrix, evaluated at $g_{LM}=0$, is given by

$$F_{LM,L'M'} = \frac{1}{2}\sum_{l_1m_1}\sum_{l_2m_2}\mathrm{Tr}\left[(\mathbf{C}^{\rm tot}_{l_1})^{-1}\frac{\partial\mathbf{C}_{l_1m_1,l_2m_2}}{\partial g^*_{LM}}(\mathbf{C}^{\rm tot}_{l_2})^{-1}\frac{\partial\mathbf{C}_{l_2m_2,l_1m_1}}{\partial g_{L'M'}}\right]. \tag{3.12}$$

In the limit of vanishing primordial anisotropy, the inverse of this Fisher matrix equals the covariance of the errors on $\hat{g}_{LM}$, i.e. $F^{-1}_{LM,L'M'} = \langle\hat{g}_{LM}\hat{g}^*_{L'M'}\rangle$.

The assumed isotropy of the survey ensures that the Fisher matrix at $g_{LM}=0$ is diagonal. Using Eq. (3.9), the diagonal elements evaluate to

$$F_{LM,LM} = \sum_{l_1l_2}\left[\mathrm{Tr}\left(\tilde{\mathbf{C}}_{l_1l_2}(\mathbf{C}^{\rm tot}_{l_2})^{-1}\tilde{\mathbf{C}}_{l_2l_1}(\mathbf{C}^{\rm tot}_{l_1})^{-1}\right)\frac{(2l_1+1)(2l_2+1)}{8\pi}\begin{pmatrix} l_1 & l_2 & L \\ 0 & 0 & 0 \end{pmatrix}^2\right]. \tag{3.13}$$

Since g_{LM} is complex for $M\neq 0$, we present our simulation results in the next section in terms of $\hat{G}_{LM} = \sqrt{2}\mathrm{Re}(\hat{g}_{LM})$ and $\hat{G}_{L-M} = \sqrt{2}\mathrm{Im}(\hat{g}_{LM})$ for $M>0$, and $\hat{G}_{L0} = \hat{g}_{L0}$. The $\hat{G}_{LM}$ are uncorrelated and have the same variance as the $\hat{g}_{LM}$.

3.3 Forecasts for Planck

3.3.1 Constraints on the anisotropy amplitude

In this section, we consider forecasts for the Planck mission. We use the parameters for the 143 GHz channel (the most sensitive of the Planck frequency channels) as given in [27]. We therefore assume a Gaussian beam with FWHM of 7.1 arcmin and assume uncorrelated isotropic noise in the temperature and polarization maps with root-mean-square noise levels of σ_T and σ_P respectively. For the nominal two-sky-survey mission (one year of observation) we adopt $\sigma_T = 12.2\,\mu$K and $\sigma_P = 23.3\,\mu$K in 3.4 arcmin pixels (Healpix [137] resolution $N_{\rm side} = 1024$), corresponding to $42\,\mu$K-arcmin noise in temperature and $80\,\mu$K-arcmin in Stokes Q and U polarization. We also consider an extended mission of four complete sky surveys (two years of observation) with σ_T and σ_P reduced by a factor of $\sqrt{2}$.

To give a feel for the nature of the anisotropy signal, Figs. 3.1 and 3.2 show simulated sky maps for a noise-free realisation of a scale-invariant ($q = 0$) quadrupole-modulation model with $g_{20} = 0.1$ ($g_{2M} = 0$, $M \neq 0$). These maps have been generated using the prescription described in [174], generalized to polarization. This uses an approximate square root of the anisotropic covariance matrix, linear in the g_{LM}, to simulate maps as the sum of a statistically isotropic part and an anisotropic part. The isotropic component of a noise-free temperature map is shown on the left in Fig. 3.1 and the anisotropic component, clearly showing a preferred direction along the polar axis, is shown on the right.

The anisotropic contribution to the Stokes Q and U polarization maps is shown in Fig. 3.2. Here, we have smoothed the polarization maps with a Gaussian of FWHM 3 deg. to enhance the visual impact of the statistical anisotropy in the Q Stokes map. Because of the quadrupole asymmetry in the primordial power, modes of the primordial perturbation with wavevectors along the polar axis tend to have their amplitude enhanced. For such modes, the polarization generated by Thomson scattering is pure Q in the polar basis and varies in amplitude with the polar angle as $\sin^2\theta$ [76]. The dominant effect of the statistical anisotropy is therefore observed in the Q Stokes parameter and is concentrated toward the equatorial plane.

To illustrate the machinery summarised in Section 3.2.2, we have generated five simulations of the scale-invariant quadrupole-modulation model with $g_{2M} = 0.1\delta_{0M}$ and added instrumental noise appropriate to one year of observation with the Planck 143 GHz channel. We then estimate g_{2M} via Eq. (3.11) as a function of $l_{\rm max}$, the maximum multipole retained in the analysis. Since the only nonzero coefficient in these simulations is g_{20}, and the survey is assumed isotropic, the recovered estimates $\hat{g}_{2M}$ are statistically equivalent for $M \neq 0$ and so we show results only for the two (real) components $\hat{G}_{20}$ and $\hat{G}_{2-2}$ in Fig. 3.3. We analyse temperature alone (top panels), E-mode polarization alone (middle), and both jointly (bottom).

With temperature alone, the errors on G_{2M} decrease approximately as $1/l_{\rm max}$ over the range

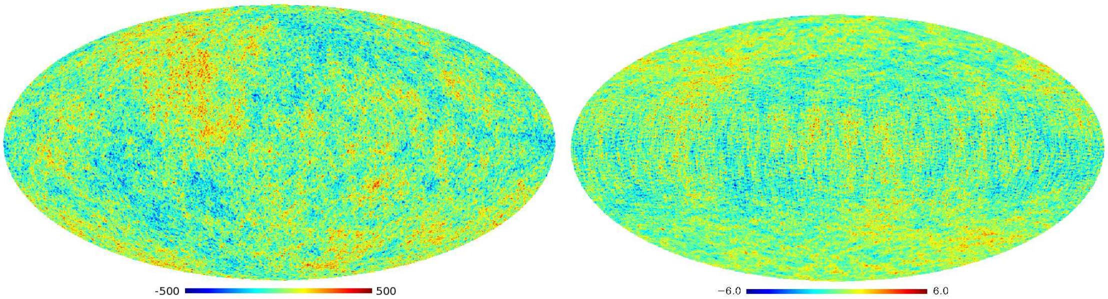

Figure 3.1: Noise-free simulation of a model with scale-invariant quadrupole asymmetry in the primordial power with $g_{LM} = 0.1\delta_{L2}\delta_{M0}$. The isotropic component of the temperature map is shown on the left, and the anisotropic component on the right. The colour scales are in μK.

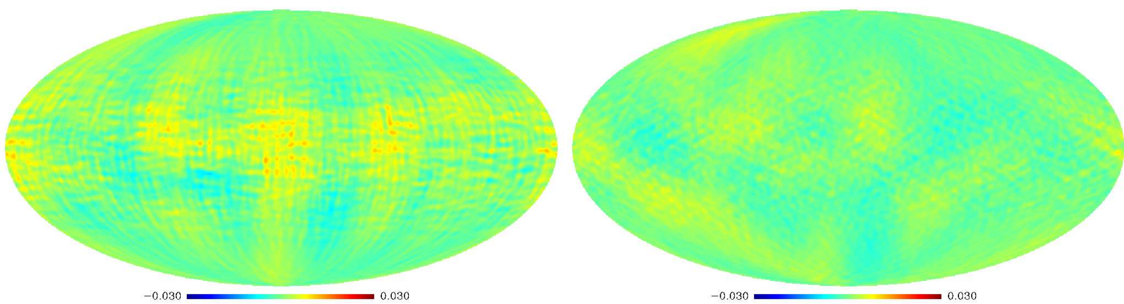

Figure 3.2: Anisotropic components of the Q (left) and U (right) polarization maps in a noise-free simulation of the model in Fig. 3.1. The maps have been smoothed here with a Gaussian beam of FWHM 3° to enhance the imprint of the preferred axis in the Q map. The colour scales are in μK.

plotted in Fig. 3.3 ($l \leq 1500$) reaching 0.005 by $l_{\max}$ (in agreement with the minimum-variance estimators of [178]). This behaviour follows from simple mode-counting since the temperature maps are signal-dominated over this multipole range.[1] However, the polarization maps are noise-dominated over much of this multipole range and so the errors approach constant values for $l_{\max} \gtrsim 600$. Nevertheless, the Planck polarization maps alone can provide (almost) independent constraints on an anisotropic modulation to the temperature maps. For two sky surveys, the errors on the g_{2M} from polarization are four times worse than in temperature. Consistency between temperature and polarization constraints would provide an important test of systematic effects should Planck show any evidence of an anisotropic power spectrum.

[1] For modes that are signal-dominated, the scale dependence of the trace term in the Fisher matrix, Eq. (3.13), is weak. Treating the trace as constant gives Fisher information varying as $l_{\max}^2$ which is proportional to the number of modes retained in the analysis.

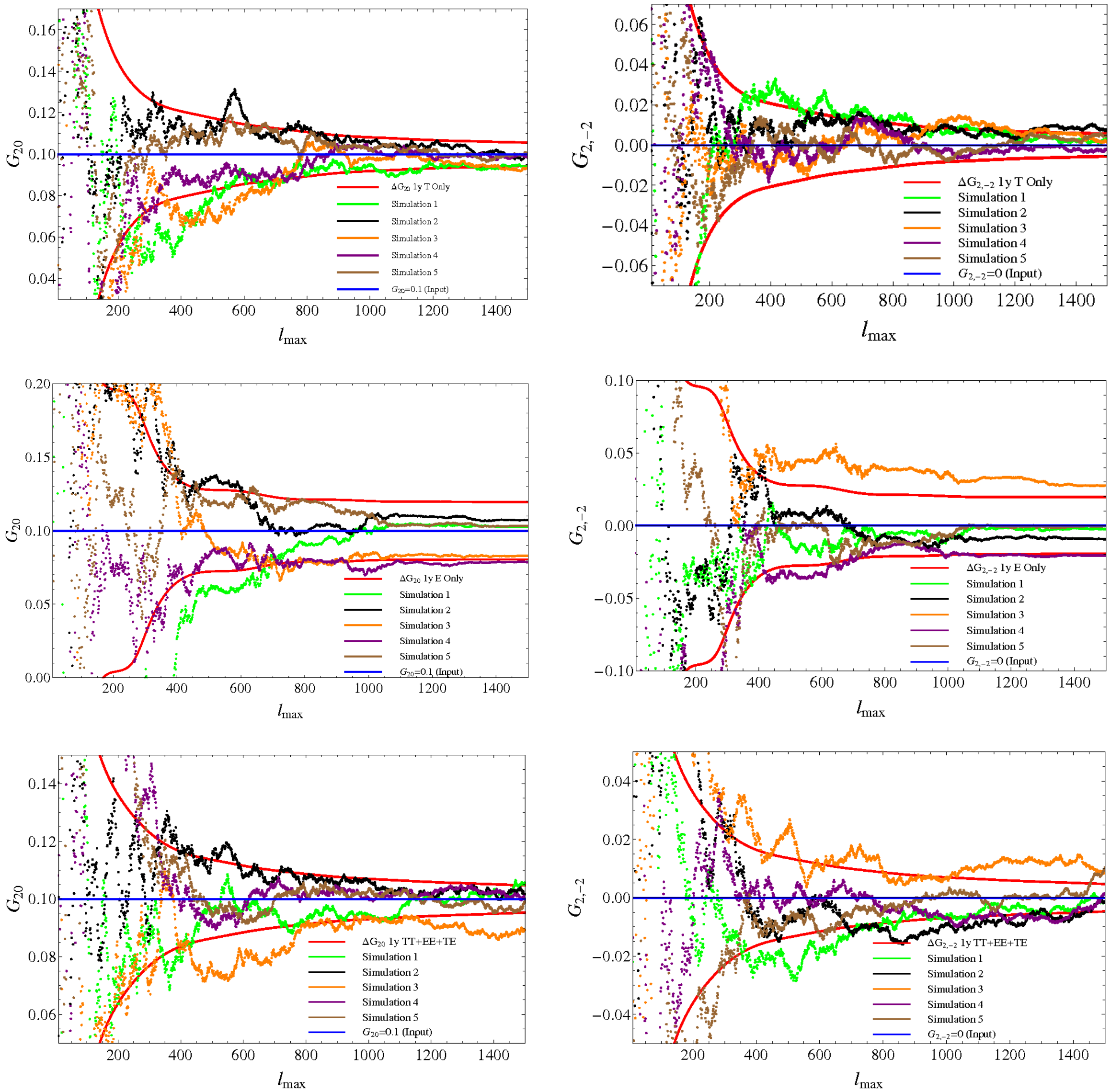

Figure 3.3: Estimates of the G_{20} (left) and $G_{2\,-2}$ (right) anisotropy parameters (shown with points) and their (one-sigma) Fisher errors ([Red] solid lines) as a function of $l_{\max}$ from five simulations of the model in Fig. 3.1 for one year of Planck data. The input parameters $G_{20} = 0.1$ and $G_{2\,-2} = 0.0$ are shown with horizontal [Blue] solid lines. From top to bottom we analyse temperature only, E-mode polarization only and temperature plus polarization.

3.3.2 Constraints on scale-dependence

In Fig. 3.4, we compare the Fisher errors on the amplitude of the modulation for a scale-invariant model ($q = 0$) and two models with scale-dependence ($q = 1$ and $q = 2$). For larger q, the asymmetry in the variance of the Fourier modes is confined to larger scales and so relatively more of the constraining power derives from low-l multipole moments. The low-l modes of polarization are enhanced by scattering at reionization [179] and are expected to be signal-dominated in the one-year Planck data. The polarization constraints on the g_{2M} therefore become more comparable

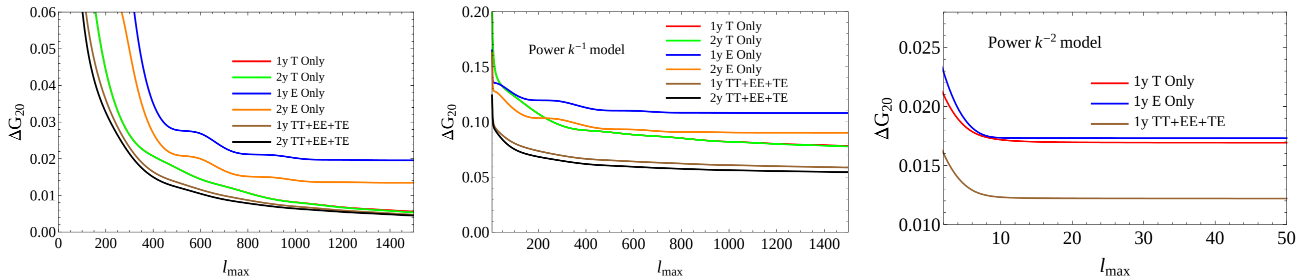

Figure 3.4: Fisher errors for G_{20} from temperature, E-mode polarization, and temperature plus polarization in models with power-asymmetry spectral indices $q = 0$ (left), $q = 1$ (middle) and $q = 2$ (right). For $q = 0$ and $q = 1$ we show results for one and two years of observations; for $q = 2$ we show only the one-year errors since they improve very little with further observing time. Note that the one- and two-year errors from temperature alone are indistinguishable when $q \geq 0$.

to those from the temperature as q increases and the improvement from observing for longer in polarization lessens.

If the amplitude of any primordial power asymmetry is high enough, it might be possible to constrain the scale-dependence of the asymmetry with Planck. To forecast constraints on the spectral index of the power asymmetry, q, we extend the Fisher matrix analysis of Sec. 3.2.2 to include q as a parameter. We must now evaluate the Fisher matrix at nonzero g_{LM} but we assume that the asymmetry is still small enough that we can neglect asymmetry in the $(\mathbf{C}^{\rm tot})^{-1}$ terms. The $F_{LM,L'M'}$ is then unchanged from Eq. (3.13) but the additional elements are

$$\begin{aligned} F_{LM,q} &= \frac{1}{2}\sum_{l_1m_1}\sum_{l_2m_2}\mathrm{Tr}\left[(\mathbf{C}^{\rm tot}_{l_1})^{-1}\frac{\partial \mathbf{C}_{l_1m_1,l_2m_2}}{\partial g^*_{LM}}(\mathbf{C}^{\rm tot}_{l_2})^{-1}\frac{\partial \mathbf{C}_{l_2m_2,l_1m_1}}{\partial q}\right] \\ &= \sum_{l_1l_2}\left[\mathrm{Tr}\left(\tilde{\mathbf{C}}_{l_1l_2}(\mathbf{C}^{\rm tot}_{l_2})^{-1}\partial_q\tilde{\mathbf{C}}_{l_2l_1}(\mathbf{C}^{\rm tot}_{l_1})^{-1}\right)g_{LM}\frac{(2l_1+1)(2l_2+1)}{8\pi}\begin{pmatrix} l_1 & l_2 & L \\ 0 & 0 & 0\end{pmatrix}^2\right] \quad (3.14) \\ F_{q,q} &= \frac{1}{2}\sum_{l_1m_1}\sum_{l_2m_2}\mathrm{Tr}\left[(\mathbf{C}^{\rm tot}_{l_1})^{-1}\frac{\partial \mathbf{C}_{l_1m_1,l_2m_2}}{\partial q}(\mathbf{C}^{\rm tot}_{l_2})^{-1}\frac{\partial \mathbf{C}_{l_2m_2,l_1m_1}}{\partial q}\right] \\ &= \sum_{l_1l_2}\left[\mathrm{Tr}\left(\partial_q\tilde{\mathbf{C}}_{l_1l_2}(\mathbf{C}^{\rm tot}_{l_2})^{-1}\partial_q\tilde{\mathbf{C}}_{l_2l_1}(\mathbf{C}^{\rm tot}_{l_1})^{-1}\right)\frac{(2l_1+1)(2l_2+1)}{8\pi}\right. \\ &\qquad \left.\times\sum_{LM}|g_{LM}|^2\begin{pmatrix} l_1 & l_2 & L \\ 0 & 0 & 0\end{pmatrix}^2\right]. \quad (3.15) \end{aligned}$$

Note that these elements vanish if $g_{LM} = 0$. From the scaling of the Fisher matrix elements with g_{LM}, we expect the error on q to scale as the inverse of the amplitude of the asymmetry.

As an example, we consider a fiducial model with scale-invariant quadrupole asymmetry with $G_{2M} = 0.03\delta_{M0}$. Such a model is compatible with the constraints on quadrupole asymmetry from the beam-corrected analysis of WMAP data in Ref. [176], but the amplitude should be detectable

Δq (1σ)	T only	E only	T and E
One year	0.399	1.300	0.322
Two years	0.389	0.878	0.299

Table 3.1: Fisher errors on the scale-dependence of the power asymmetry assuming a scale-invariant quadrupole asymmetry with $g_{2M} = 0.03\delta_{M0}$.

with Planck at the 6σ level (fixing $q = 0$). Forecasts for the (marginalised) errors on q for this model are given in Table 3.1. With temperature and polarization, Planck should constrain the spectral index to a 1σ accuracy of $\Delta q \sim 0.3$. The marginalised errors on the g_{LM} are similar to the case in which q is fixed.

3.3.3 Axisymmetric models

The preceding analysis makes no assumptions about axisymmetry of the primordial power asymmetry. However, if we have good reason to expect axisymmetry, so the model is described by a preferred axis $\hat{\mathbf{m}}$ and the $M = 0$ multipoles $\{g_{*L}\}$ in a frame with the polar axis along $\hat{\mathbf{m}}$, we can constrain these parameters by post-processing our estimates $\hat{g}_{LM}$. We illustrate how this works, assuming a fixed scale dependence for the primordial asymmetry.

For models with a nearly scale-invariant anisotropy spectrum, many small-scale modes contribute to the $\hat{g}_{LM}$, so we might expect the statistics of the $\hat{g}_{LM}$ to be approximately Gaussian. Expressing $\hat{\mathbf{m}}$ in terms of its azimuthal angle α and polar angle β, $\hat{\mathbf{m}} = D(\alpha, \beta, 0)\hat{\mathbf{z}}$ (i.e. a rotation of the $\hat{\mathbf{z}}$ direction through Euler angles α and β), in the Gaussian approximation we can write $\Pr(\{\hat{g}_{LM}\}|\hat{\mathbf{m}}, \{g_{*L}\}) \propto \exp(-\chi^2/2)$ where

$$\chi^2 = \sum_{LM}\sum_{L'M'}(\hat{g}^*_{LM} - \tilde{g}^*_{LM})F_{LM,L'M'}(\hat{g}_{L'M'} - \tilde{g}_{L'M'}). \tag{3.16}$$

Here,

$$\tilde{g}_{LM} \equiv D^L_{M0}(\alpha, \beta, 0)g_{*L} \tag{3.17}$$

are the multipoles of the primordial asymmetry rotated from their preferred frame. ($D^L_{MM'}(\alpha, \beta, \gamma)$ are the Wigner rotation matrices.) If we now assign a uniform prior on the direction $\hat{\mathbf{m}}$ [so that $\Pr(\alpha, \beta)d\alpha d\beta = (4\pi)^{-1}d\alpha d\cos\beta = (4\pi)^{-1}d\hat{\mathbf{m}}$] and a flat prior on the g_{*L}, Bayes' theorem gives for the posterior

$$\begin{aligned} \Pr(\hat{\mathbf{m}}, \{g_{*L}\}|\{\hat{g}_{LM}\})d\hat{\mathbf{m}} &= \Pr(\alpha, \beta, \{g_{*L}\}|\{\hat{g}_{LM}\})d\alpha d\beta \\ &\propto e^{-\chi^2/2}d\hat{\mathbf{m}}. \end{aligned} \tag{3.18}$$

For an isotropic survey (and assumed weak anisotropy), the Fisher matrix is isotropic and we can write $F_{LM,L'M'} = \delta_{LL'}\delta_{MM'}/\sigma^2_L$. Substituting Eq. (3.17) into Eq. (3.16) and using the addition theorem for the rotation matrices, we have

$$\chi^2 = \sum_L \frac{1}{\sigma_L^2}\left(g_{*L}^2 - 2g_{*L}\sum_M \Re\left[\hat{g}_{LM}D_{M0}^{L*}(\alpha,\beta,0)\right] + \sum_M |\hat{g}_{LM}|^2\right). \tag{3.19}$$

Noting that $D_{M0}^{L*}(\alpha,\beta,0) = \sqrt{4\pi/(2L+1)}Y_{LM}(\hat{\mathbf{m}})$, if we define

$$\hat{g}_L(\hat{\mathbf{m}}) \equiv \sum_M \hat{g}_{LM}Y_{LM}(\hat{\mathbf{m}}), \tag{3.20}$$

(i.e. a map of the estimated $\hat{g}_{LM}$ at multipole L), we can write the posterior as

$$\begin{aligned}\Pr(\hat{\mathbf{m}},\{g_{*L}\}|\{\hat{g}_{LM}\})d\hat{\mathbf{m}} \;\propto\; & \prod_L \exp\left(-\frac{2\pi}{(2L+1)\sigma_L^2}\left[g_{*L}Y_{L0}(\hat{\mathbf{z}}) - \hat{g}_L(\hat{\mathbf{m}})\right]^2\right) \\ & \times \exp\left(\frac{2\pi}{(2L+1)\sigma_L^2}\hat{g}_L^2(\hat{\mathbf{m}})\right) d\hat{\mathbf{m}}.\end{aligned} \tag{3.21}$$

The marginal distribution for the direction of the axis is given by integrating over g_{*L}:

$$\Pr(\hat{\mathbf{m}}|\{\hat{g}_{LM}\})d\hat{\mathbf{m}} \propto \prod_L \exp\left(\frac{2\pi}{(2L+1)\sigma_L^2}\hat{g}_L^2(\hat{\mathbf{m}})\right) d\hat{\mathbf{m}}, \tag{3.22}$$

so that contours of constant density are given by the contours of $\sum_L \hat{g}_L^2(\hat{\mathbf{m}})/[(2L+1)\sigma_L^2]$. For the simple case of a primordial power asymmetry at a single multipole L, e.g. a quadrupole asymmetry, $\ln \Pr(\hat{\mathbf{m}}|\{\hat{g}_{LM}\})$ is proportional to the square of the map of the reconstructed multipoles.

To illustrate these ideas, in Fig. 3.5 we plot the marginal distributions for the direction and amplitude of the model analysed in Sec. 3.3.1 using one of the simulations shown in Fig. 3.3. We parameterise the direction by the Cartesian components of the equal-area projection $x = 2\sin(\beta/2)\cos(\alpha)$ and $y = 2\sin(\beta/2)\sin(\alpha)$. With one year of simulated Planck temperature data, the constraints on the direction of the axis are $\Delta x \approx \Delta y = 0.032$ (i.e. $1.8°$) at 68% confidence and the x and y components are almost uncorrelated as expected from isotropy. The amplitude $g_{*2} = 0.1 \pm 0.005$ (68% confidence) with the error being very nearly σ_2. With polarization alone, these constraints weaken to $\Delta x \approx \Delta y = 0.10$ (i.e. $5.7°$) and $g_{*2} = 0.11 \pm 0.02$. The maximum of the posterior in this simulation is at $x = 0.042$, $y = -0.035$ and $g_{*2} = 0.099$ (T only) and $x = -0.033$, $y = 0.062$ and $g_{*2} = 0.11$ (E only) and the χ^2 at these values are 0.223 and 0.236 respectively, with $5 - 3 = 2$ degrees of freedom.

3.4 Conclusions

As summarized in Sec. 3.1, cosmological perturbations are usually assumed to satisfy statistical isotropy, as expected in simple models of inflation. Yet there is some tentative observational

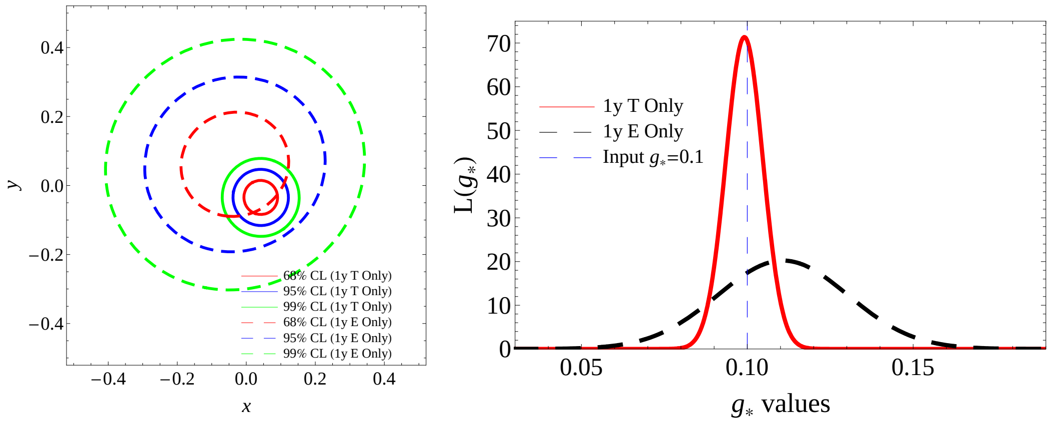

Figure 3.5: Marginal distributions for the direction (left) and amplitude (g_{*2}, right) from a simulation of the nominal (one-year) Planck survey for a model with an axisymmetric quadrupole asymmetry aligned with the polar axis ($g_{LM} = 0.1\delta_{L2}\delta_{M0}$). We parameterise the direction with the equal-area projection $x = 2\sin(\beta/2)\cos(\alpha)$ and $y = 2\sin(\beta/2)\sin(\alpha)$ and show in solid lines the 68% [Red], 95% middle [Blue] and 99% outer [Green] contours from the temperature alone; dashed-line contours are from the E-mode polarization alone. For the amplitude (right), we plot the marginal distributions from T alone (solid line) and E alone (dashed line).

evidence from the CMB suggesting possible departures from statistical isotropy. Here we have shown that Planck should be able to set strong constraints on small departures from statistical anisotropy and, under favourable circumstance, could set constraints on their scale dependence and any preferred direction.

In this Chapter we have developed and applied quadratic estimators to test for an asymmetry in the primordial power spectrum from temperature and polarization measurements of the CMB. Our estimators are optimal in the limit of isotropic primordial power. We have tested our methods against simulations that include a quadrupole power asymmetry.

We have analysed the ability of the Planck mission to constrain models with quadrupole power asymmetry using temperature and polarization data. Using temperature data alone, Planck should be able to constrain each multipole g_{2M} of a scale-invariant quadrupole anisotropy at the 0.01 level (2σ), well below the current constraints derived from WMAP ($|g_{2M}| < 0.07$ from Ref. [176]). Using polarization data alone from an extended Planck mission (four sky surveys) such an anisotropy can be constrained to an accuracy only about three times worse than from the temperature. This offers the possibility of a consistency check on the existence on any observed departure from statistical isotropy.

If the amplitude of a power asymmetry is large enough, it may be possible to constrain its scale dependence. We have estimated the Fisher errors when additionally constraining a free spectral index describing a power law modulation, $g_{LM}(k) = g_{LM}(k_0/k)^q$. For a scale-free quadrupole modulation with an amplitude of 1% (i.e. $g_{20}/\sqrt{4\pi} = 0.01$ in an axi-symmetric model), we find that an extended Planck mission can constrain the spectral index to a 1σ accuracy of $\Delta q \sim 0.3$.

Finally, we have considered the constraints on a preferred direction in models with a purely axisymmetric modulation of the primordial power spectrum. In a scale-free model with a 1% quadrupole modulation, the direction of the preferred axis can be determined from Planck data to a precision of about 2° using temperature observations alone and to about 6° using polarization data alone.

The quadratic estimators developed here for isotropic surveys can, in principle, be straightforwardly extended to deal with real-world effects such as anisotropic noise and Galactic masks. However, the calculation of the $\bar{a}^X_{lm}$ in Eq. (3.11) requires inverse weighting the temperature and polarization data with the full covariance matrix for the anisotropic survey. This has been done for the WMAP temperature data at its native resolution [174; 180] but extending this to polarization and the resolution required for Planck requires further work. In practice, fast estimators can still be constructed for anisotropic surveys, with moderate loss of performance, by replacing $\bar{a}^X_{lm}$ with some heuristically-weighted pseudo multipoles (i.e. those computed directly on the masked sky) following techniques used for CMB power spectrum estimation (e.g. see [136] for a review). In either case, care must be taken to subtract the mean-field response – that obtained on average for no primordial power asymmetry – from the quadratic estimator since this is no longer confined to the $L = 0$ mode for an anisotropic survey. The mean-field and the estimator normalisation are then generally best determined by Monte-Carlo simulations.

Chapter 4

Constraints on the standard and non-standard models of the early Universe from CMB B-mode polarisation

4.1 Introduction

Observations of the Cosmic Microwave Background (CMB) radiation have proved a valuable tool for studying the physics of the very early Universe. Scalar, vector and tensor perturbations generated in the early Universe have left observable imprints in the temperature and polarization anisotropies of the CMB. Recent experiments, including the Wilkinson Microwave Anisotropy Probe (WMAP) satellite [61; 72; 155], QUaD [156], BICEP [182] and others [183; 184; 185; 186; 187], have led to a precise determination of the basic parameters of the standard ΛCDM cosmological model, including the parameters describing the primordial density perturbations.

According to this concordance model, the Universe underwent a period of near-exponential expansion, termed inflation, at very early times. The standard model of inflation is based on the single field slow-roll scenario. In this scenario, the expansion is driven by a scalar field (the inflaton) gradually rolling down a flat potential during the inflationary stage. Inflation ended when the slow-roll conditions were broken, and the inflaton decayed into relativistic particles which re-heated the Universe.

In spite of many phenomenological successes of inflation based on effective field theory, serious problems remain concerning the origin of the scalar field driving inflation, namely the singularity problem [188] and the trans-Plankian problem [189]. Consequently, efforts have been made to realize inflation in a more natural way from some fundamental theory of microscopic physics. Brane inflation [50; 190; 191] from high dimensional string theory is a typical example. In this scenario, the Universe is embedded into a high dimensional warped space-time. The anti-brane is fixed at the bottom of a warped throat, while the brane is mobile and experiences a small attractive force towards the anti-brane. Inflation ends when the brane and the anti-brane collide and annihilate, initiating the hot big bang epoch. During the brane collision, cosmic strings would be copiously produced, and would leave an imprint on the CMB sky [47; 48]. Searching for this cosmic string signal in the CMB is an important way to test the correctness of this scenario.

Another approach for realizing a period of inflation, based on Loop Quantum Gravity (LQG) has been proposed recently (see [192] for instance). LQG is a non-perturbative and background-independent quantization of General Relativity. Based on a canonical approach, it uses Ashtekar variables, namely SU(2) valued connections and conjugate densitized triads. The quantization is obtained through holonomies of the connections and fluxes of the densitized triads. More importantly, when the energy density of the Universe was approaching the critical density ρ_c, the Universe entered into a bouncing period due to repulsive quantum geometrical effects. Thus, the big bang is replaced by a "big bounce". This, to some extent, avoids the singularity problem in the standard ΛCDM model.

Differentiating between these three classes of models (single field inflation, brane inflation and loop quantum cosmology), which are motivated by different microscopic physics, is a crucially important goal for modern cosmology. Since the primordial scalar, vector and tensor perturbations produced in these models are quite different from each other, they will in general leave different signatures in the CMB radiation. Numerous authors have constrained the parameters of single field inflation models from CMB and large scale structure observations. (See for example [72; 156; 193] for some recent analyses.) Most of these analyses have made use of both temperature and polarization CMB measurements and their constraints have been dominated by the temperature measurements. However, with the advent of a new generation of CMB polarization measurements [156; 182], it is now possible to obtain meaningful constraints from measurements of the polarization of the CMB. Since B-mode polarization on very large scale is generated only by tensor perturbations in the early Universe, this is a particularly attractive technique: a detection of B-mode polarization at large enough angular scales *must* be due to gravitational waves (tensor perturbations) and the connection with early Universe physics is then very clear. In addition, small scale B-mode polarization is possibly sourced by cosmic string. Note that on small scales, B-modes are also generated by gravitational lensing of the dominant E-mode polarization signal. Therefore, for testing models of the early Universe, large-angular scale measurements are required in order to avoid confusion from gravitational lensing.

In this Chapter, we extend the investigation of inflationary constraints from CMB B-mode polarization measurements alone by considering the constraints obtainable on the three classes of models described above. The Chapter is organized as follows. In Section 4.2.1, we briefly review the characterization of CMB polarization in terms of E- and B-modes. In Section 4.2.2, we present the currently available B-mode constraints, and the predicted noise levels for some current and future CMB experiments. In Section 4.2.3, we first present the likelihood and hyper-parameter analysis methods, which we will use in the parameter estimation. We then describe the Fisher information matrix formalism which we will use to forecast the constraints obtainable by using future experiments. In Section 4.3.1, we discuss the tensor perturbations which arise in the single field inflationary (hereafter SFI) model [1], and in Section 4.3.2, we constrain the parameters of the SFI model using the BICEP and QUaD data. In Section 4.3.3, we calculate the signal-to-noise ratio for a number of future CMB experiments and their combinations, and present forecasts for the constraints obtainable on the tensor-to-scalar ratio r with future observations. In Section 4.3.4, we discuss four types of single field slow-roll inflation models, and their detectability with future experiments. We then follow a similar line of discussion for the LQG model in Section 4.4 and the brane inflation/cosmic string model in Section 4.5. We summarize our results in Section 4.6.

4.2 B-mode polarization and its observations

4.2.1 B-mode polarization

Let us first briefly review the statistics of the CMB polarization field. The polarized radiation field can be described by a 2×2 intensity matrix $I_{ij}(\mathbf{n})$ [194], where $\mathbf{n}$ denotes the direction on the sky, and $I_{ij}(\mathbf{n})$ is defined with respect to the orthogonal basis $(\mathbf{e}_1, \mathbf{e}_2)$ which is perpendicular to $\mathbf{n}$. Linear polarization is related to the two Stokes parameters, $Q=\frac{1}{4}(I_{11}-I_{22})$ and $U=\frac{1}{2}I_{12}$, whereas the temperature anisotropy is $T=\frac{1}{4}(I_{11}+I_{22})$. The polarization magnitude and orientation are given by $P=\sqrt{Q^2+U^2}$ and $\alpha=\frac{1}{2}\tan^{-1}(U/Q)$.

As spin ± 2 fields, the Stokes parameters Q and U change under a rotation by an angle ψ as $(Q\pm iU)(\mathbf{n})\rightarrow e^{\mp 2i\psi}(Q\pm iU)(\mathbf{n})$. Thus, $(Q\pm iU)(\mathbf{n})$ requires an expansion with spin ± 2 spherical harmonics [195]

$$(Q\pm iU)(\mathbf{n})=\sum_{lm} a_{lm}^{(\pm 2)}\,{}_{\pm 2}Y_{lm}(\mathbf{n}). \tag{4.1}$$

The multipole coefficients $a_{lm}^{(\pm 2)}$ can be calculated as

$$a_{lm}^{(\pm 2)}=\int (Q\pm iU)(\mathbf{n})[{}_{\pm 2}Y_{lm}^{*}(\mathbf{n})]d\mathbf{n}. \tag{4.2}$$

The E- and B-mode multipoles are defined in terms of the coefficients $a_{lm}^{(\pm 2)}$ in the following manner:

$$a_{lm}^{E}=-\frac{1}{2}(a_{lm}^{(2)}+a_{lm}^{(-2)}),\ a_{lm}^{B}=-\frac{1}{2i}(a_{lm}^{(2)}-a_{lm}^{(-2)}). \tag{4.3}$$

One can now define the E-mode polarization sky map $E(\mathbf{n})$ and the B-mode polarization sky map

[1] Here we restrict our discussion to the single field slow-roll inflationary model. SFI models with non-trivial sound speed are not covered here. Thanks to the discussion with Daniel Baumann.

$B(\mathbf{n})$ as

$$E(\mathbf{n}) = \sum_{lm} \left[\frac{(l+2)!}{(l-2)!}\right]^{\frac{1}{2}} a_{lm}^{E} Y_{lm}(\mathbf{n}), \;\; B(\mathbf{n}) = \sum_{lm} \left[\frac{(l+2)!}{(l-2)!}\right]^{\frac{1}{2}} a_{lm}^{B} Y_{lm}(\mathbf{n}). \tag{4.4}$$

The scalar field $E(\mathbf{n})$ and the pseudoscalar field $B(\mathbf{n})$ completely describe the polarization field. E-modes are curl-free modes and appear as symmetric radial and tangential polarization patterns on the sky. B-modes are divergence-free modes with left-handed and right-handed vortical polarization patterns on the sky.

One constructs the various CMB power spectra by correlating the T, E and B modes in harmonic space. In the absence of parity-violating effects [1], there are only four non-zero cross-correlations: TT, TE, EE and BB. The angular power spectra of the polarization fields are defined as

$$C_l^{EE} \equiv \frac{1}{2l+1} \sum_m \langle a_{lm}^{E} a_{lm}^{E*} \rangle, \quad C_l^{BB} \equiv \frac{1}{2l+1} \sum_m \langle a_{lm}^{B} a_{lm}^{B*} \rangle, \tag{4.5}$$

where the brackets denote an ensemble average. If the fluctuations are Gaussian distributed, all of the cosmological information is encoded in the angular power spectra.

4.2.2 Constraints on the B-mode signal

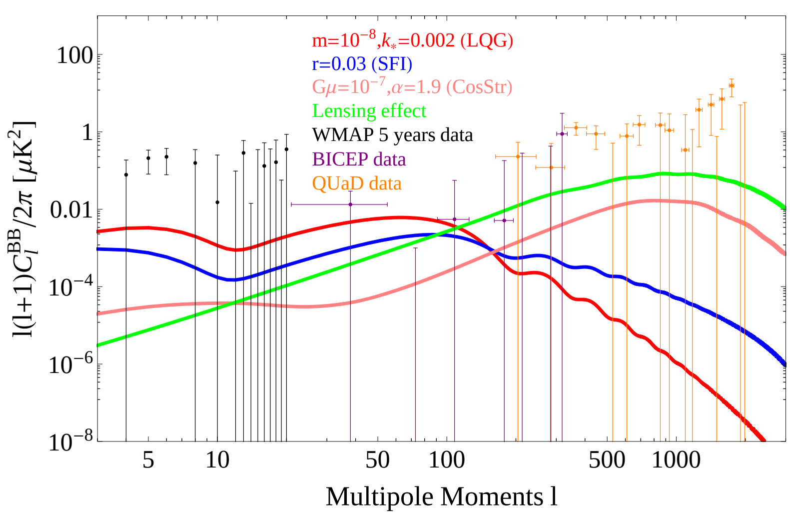

Figure 4.1: Comparison of different theoretical predictions, and the currently available data for the B-mode power spectrum. The unit for m is $\mathrm{M_{pl}}$ and k_* is Mpc^{-1}. Note that the error-bars are plotted in log-log scale.

In Fig. 4.1, we plot the current constraints on the B-mode power spectrum along with some representative B-mode signals from different theories. The red curve is the predicted C_l^{BB} calcu-

[1] Since both T and E have parity factor $(-1)^l$ under rotation, while B has parity $(-1)^{l+1}$, the TB and EB should vanish for symmetry reasons.

lated from LQG, with a mass parameter $m = 10^{-8}\,\mathrm{M_{pl}}$ and $k_* = 0.002\,\mathrm{Mpc}^{-1}$ (see Section 4.4.1 for a discussion on LQG). The blue curve is the predicted C_l^{BB} from SFI for a tensor-to-scalar ratio $r = 0.03$, and the pink curve is the BB power spectrum generated by cosmic strings for a string tension $G\mu = 10^{-7}$ and wiggling parameter $\alpha = 1.9$ (see Section 4.5 for a discussion on cosmic strings). The green curve is the B-mode signal from gravitational lensing which acts as a source of confusion when attempting to measure the primordial B-mode signal. The black, purple and orange points with associated error-bars are the currently available B-mode data from the WMAP 5-year observations ($l \leq 20$ [196]), the BICEP experiment (9 band powers [182; 197]), and the QUaD experiment (23 band powers [156; 198]).

The WMAP constraints are relatively weak due to instrumental noise, cosmic variance and residual foreground noise. In addition, the constraining power is further restricted by the uncertainty in the optical depth τ to the last scattering surface. We will therefore not use the WMAP data in the following likelihood analysis. The BICEP data probes intermediate scales ($21 \leq l \leq 335$) around the recombination bump in the primordial B-mode spectrum. On these scales, the primordial signal is less affected by cosmic variance and is comparable to or larger than the lensing signal for tensor-to-scalar ratios $r \gtrsim 0.01$. The QUaD experiment, whose primary aim was a high resolution measurement of the E-mode signal, probes small scales ($164 \leq l \leq 2026$). Its ability to constrain the primordial signal is thus severely restricted due to lensing confusion and the rapid decline in the primordial signal with inverse scale. It may however be useful for constraining the cosmic string signal which peaks on small scales.

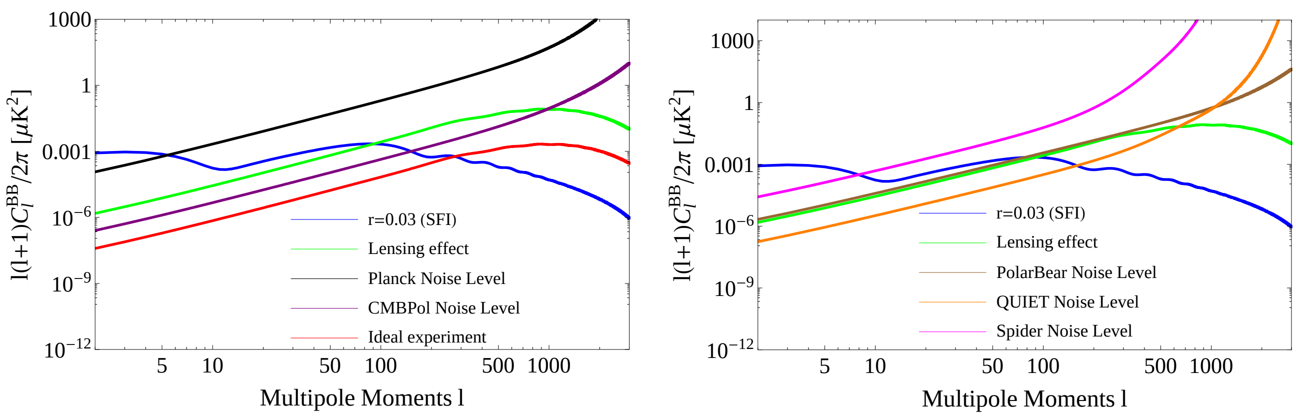

Figure 4.2: Polarization noise power spectra for forthcoming experiments. Note that these curves include uncertainties associated with the instrumental beam. The blue curves show the B-mode power spectrum for the standard inflationary model with $r = 0.03$. In the left panel, we plot the instrumental noise for the Planck and CMBPol satellites, as well as the lensing B-mode signal and the noise level for the ideal experiment. In the right panel, we plot the instrumental noise for the ground-based PolarBear and QUIET experiments, and the balloon-borne Spider experiment. We fix the other parameters at WMAP 7-year best-fit values ($\Omega_b h^2 = 0.02258$, $\Omega_c h^2 = 0.1109$, $n_s = 0.963$, $A_s(k_0) = 2.43 \times 10^{-9}$ (pivot scale $k_0 = 0.002, \mathrm{Mpc}^{-1}$), $h = 0.71$, and $\tau = 0.088$).

The constraints plotted in Fig. 4.1 are all consistent with zero signal at the $\sim 2\sigma$ level.

Detecting B-mode polarization therefore remains an outstanding experimental challenge, and represents a key goal for current and future CMB experiments including ground-based (BICEP-II [28], QUIJOTE [29], PolarBear [30], QUIET [31]), balloon-borne (EBEX [32], Spider [33], PIPER) and satellite (Planck [27], B-Pol [199], litebird [200], CMBPol [201]) experiments. In what follows, we will forecast the constraints potentially achievable with the following five representative experiments: the Planck and CMBPol satellite missions, the ground-based PolarBear and QUIET (Phase II) experiments, and the balloon-borne experiment, Spider. In addition, for reference, we shall consider the ideal (but unrealistic) case where there is no foreground contamination and no instrumental noise, and where the lensing signal can be cleaned to around 1 part in 40 [202]. The instrumental specifications which we use to model the various experiments are listed in Appendix A. Fig. 4.2 shows the noise levels of these experiments compared to the SFI signal for $r = 0.03$.

4.2.3 Data Analysis Methodology

In this subsection, we describe the methodology we use to constrain the models using current data, and to forecast constraints for future experiments. The parameters of the standard ΛCDM model have already been tightly constrained by CMB TT, EE and TE data [72] and the remaining uncertainties in these parameters have little impact on the B-mode power spectrum, e.g. [181]. Therefore, consistent with the approach adopted by Ref. [182], throughout this Chapter, we only vary those parameters which influence the level of primordial B-modes. We fix the other cosmological parameters at their WMAP 7-year best-fit values, which are derived under the assumption $r = 0$ and constant n_s across all wavelengths [72]: $\Omega_b h^2 = 0.02258$, $\Omega_c h^2 = 0.1109$, $n_s = 0.963$, $A_s(k_0) = 2.43 \times 10^{-9}$ (pivot scale $k_0 = 0.002\,\mathrm{Mpc}^{-1}$), $h = 0.71$, and $\tau = 0.088$.

4.2.3.1 χ^2 analysis and hyper-parameters

To constrain the three models using current data, we initially employ a conventional χ^2 analysis to obtain the likelihood function for each data set. For LQG and SFI, we use the CAMB code [25] to output the transfer function for the B-mode power spectrum. C_l^{BB} can then be calculated as

$$C_l^{BB} = \frac{\pi}{4} \int P_t(k) \Delta_l^B(k)^2 d\ln k, \tag{4.6}$$

where $\Delta_l^B(k)$ is the transfer function for each multipole l, and $P_t(k)$ is the primordial tensor power spectrum (see Eqs. (4.17) and (4.37)). For the cosmic string model, we use the publicly available code CMBACT [203] to generate the B-mode power spectrum.

We then follow the procedure of likelihood construction in Refs. [156; 182] to construct the expected bandpowers for each model, and we use the lognormal approximation (as illustrated in e.g. [182]) to calculate χ^2 according to

$$\chi^2(\alpha) = \left[\hat{\mathbf{Z}}^{BB} - \mathbf{Z}^{BB}(\alpha)\right]^T \mathbf{D}^{BB}(\alpha)^{-1} \left[\hat{\mathbf{Z}}^{BB} - \mathbf{Z}^{BB}(\alpha)\right], \tag{4.7}$$

where α is the parameter we wish to constrain, and $\mathbf{Z}^{BB}(\alpha)$ and $\hat{\mathbf{Z}}^{BB}$ are the model and observed band powers, transformed to the lognormal basis. $\mathbf{D}^{BB}(\alpha)$ is the covariance matrix of the observed bandpowers, once again transformed to the lognormal basis. Minimizing the χ^2 across all sampled values of α yields the best-fit model.

To obtain joint constraints from BICEP and QUaD, we can simply add the χ^2 values and minimize the resulting joint χ^2,

$$\chi^2_{\rm tot} = \chi^2_{\rm BICEP} + \chi^2_{\rm QUaD}. \tag{4.8}$$

The goodness of fit for each model can be ascertained by comparing the minimum χ^2 value with the number of degrees of freedom n. If the value of χ^2_{min}/n is close to unity within the range $(1-\sqrt{2/n}$,$1+\sqrt{2/n})$, we can say that the model provides a good fit to the data. If $\chi^2_{min}/n \gg 1+\sqrt{2/n}$, then the model is not a good fit to the data, while if $\chi^2_{min}/n \ll 1-\sqrt{2/n}$, then the model is overfitting the data which may happen if the model has redundant free parameters and/or the errors on the data have been overestimated.

Note that in the conventional joint χ^2 analysis of Eq. (4.8), we have weighted each data set equally. This may be problematic if the two data sets are not mutually consistent, or if there are unquantified systematics in the data [205; 206]. In such cases, one may wish to weight the data appropriately. The assignment of weights often occurs when two or more of the data sets are inconsistent, and is usually made in a somewhat ad-hoc manner [206]. Generally speaking, assigning the weights for each data set is a somewhat subjective way of performing a joint analysis, but one well-motivated approach to assigning weights is the "hyper-parameter" approach, formulated within a Bayesian context, which can objectively allow the statistical properties of each data set to determine its own weight in the analysis [205; 206].

In the hyper-parameter technique, the effective χ^2 is defined as

$$\chi^2_{\rm hyper} = \sum_j n_j \ln \chi^2_j, \tag{4.9}$$

where j sums over all of the data sets, χ^2_j is the χ^2 for each data set, and n_j is the number of degrees of freedom for each data set [1].

Once the χ^2 values for the combined data set have been obtained, we can find the posterior

[1] There is a subtle difference between our definition and those in [205] and [206]. In [205], n_j is the number of data points in each data set $n_{\rm data}$, while in [206], $n_j = n_{\rm data} + 2$. However, we prove in Appendix B that, when considering several constraint equations on the random variables, the distribution function form is not changed under the constraints, only if the hyper-parameter is defined as Eq. (4.9).

distribution for the parameter α using

$$-2\ln P(\alpha|D_1,\cdots,D_N)=\chi^2, \tag{4.10}$$

where χ^2 can be either the conventional $\chi^2_{\rm tot}$ or the hyper-parameter version $\chi^2_{\rm hyper}$ [205].

In Appendix B, we calculate the expectation value and variance (see Eq. (B.17)) of $\chi^2_{\rm hyper}$. This calculation shows that in the hyper-parameter case, a model can be said to be a good fit to the data if the minimum χ^2 is within the range $(1-\sqrt{V(n)}/E(n), 1+\sqrt{V(n)}/E(n))$, where n is the number of degrees of freedom for the data sets [1].

4.2.3.2 Fisher information matrix

In order to make forecasts for the constraints achievable with future experiments, one can calculate the Fisher information matrix under the assumption that each parameter is Gaussian-distributed. The standard Fisher matrix $F_{\alpha\beta}$ is defined as [207; 208],

$$F_{\alpha\beta}=\frac{1}{2}{\rm Tr}[C_{,\alpha}C^{-1}C_{,\beta}C^{-1}], \tag{4.11}$$

where C is the total covariance matrix, which includes both signal and noise contributions:

$$C_{l_1m_1l_2m_2}=(C^{BB}_{l_1,sig}+N^{BB}_{l_1,tot})\delta_{l_1l_2}\delta_{m_1m_2}. \tag{4.12}$$

Here, $N^{BB}_{l,tot}$ is the total noise contribution to the covariance matrix, which includes instrumental noise, foreground contamination as an effective noise, and confusion noise from lensing B-modes (see Appendix A for the details). In our case where we consider only B-mode polarization, the Fisher matrix can be simplified as [208; 209]

$$F_{\alpha\beta}=\sum_l\left(\frac{2l+1}{2}f_{\rm sky}\right)\frac{(C^{BB}_{l,sig})_{,\alpha}(C^{BB}_{l,sig})_{,\beta}}{(C^{BB}_{l,sig}+N^{BB}_{l,tot})^2}, \tag{4.13}$$

where $f_{\rm sky}$ is the fraction of sky observed. For Planck, CMBPol, Spider and the ideal experiment, since these are nearly full-sky observations, we perform the summation in Eq. (4.13) from $l=2$ to $l=3000$. For the ground-based PolarBear and QUIET experiments, the summation is performed from $l=21$ to $l=3000$. We restrict the summation for these experiments to $l>20$ since ground-based experiments are insensitive to the largest angular scales because of their finite survey areas (see [210] for instance).

The inverse of the Fisher matrix F^{-1} can, crudely speaking, be considered the best achievable covariance matrix for the parameters given the experimental specification. The Cramer-Rao

[1] The Bayesian Evidence (BE) is another important technique for discriminating between different models. However, the currently available data is clearly not constraining enough at present to *discriminate* between models. We therefore defer any discussion of the BE until more precise data becomes available.

inequality means that no unbiased method can measure the i^{th} parameter with an uncertainty (standard deviation) less than $1/\sqrt{F_{ii}}$ [207; 208]. If the other parameters are not known but are also estimated from the data, the minimum standard deviation rises to $(F^{-1})^{1/2}_{ii}$ [207; 208]. Therefore we can estimate the best prospective signal-to-noise ratio as $\alpha/\Delta\alpha$, where $\Delta\alpha = (F^{-1})^{1/2}_{\alpha\alpha}$. This formula will be used frequently in the following discussion.

4.3 Constraining the SFI model

4.3.1 Scalar and tensor primordial power spectra in the SFI model

In addition to nearly scale-invariant scalar perturbations, inflationary models also predict vector and tensor perturbations [211]. However, the vector perturbations are expected to be negligible since these modes decayed very rapidly once they entered the Hubble horizon. We will therefore ignore any vector component in what follows.

We will work in the perturbed Friedmann-Lemaitre-Robertson-Walker Universe, for which the metric can be written as

$$ds^2 = -c^2dt^2 + a^2(t)(\delta_{ij} + h_{ij})dx^i dx^j. \tag{4.14}$$

The tensor perturbations h_{ij} are described by two transverse-traceless components. The power spectrum for the two polarization modes of h_{ij} ($h_{ij} = h^+ e^+_{ij} + h^\times e^\times_{ij}$, $h = h^+ = h^\times$) is

$$\langle h_{\mathbf{k}} h_{\mathbf{k}'} \rangle = (2\pi)^3 \delta^3(\mathbf{k} - \mathbf{k}') \frac{2\pi^2}{k^3} P_t(k), \tag{4.15}$$

where $h_{\mathbf{k}}$ is the Fourier component of the perturbation field h. Standard inflationary models predict a nearly scale-invariant tensor power spectrum $P_t(k)$. In order to describe the weak scale-dependence of $P_t(k)$, we can define the tensor spectral index n_t in the usual way:

$$n_t \equiv \frac{d\ln P_t(k)}{d\ln k}. \tag{4.16}$$

The tensor power spectrum can then be written in the following power-law form

$$P_t(k) = A_t(k_0) \left(\frac{k}{k_0}\right)^{n_t}. \tag{4.17}$$

In the case where inflation is driven by a single inflaton field, the following calculation yields the primordial power spectrum of the scalar perturbations for slow-roll inflation (see [42; 56] for instance. For alternative calculations, see [212].)

$$P_s(k) \;=\; \left.\frac{H^4}{(2\pi\dot{\phi})^2}\right|_{k=aH}$$

$$
\begin{aligned}
&= \frac{9}{(2\pi)^2}\frac{1}{(3\mathrm{M}_{\rm pl}^2)^3}\frac{V^3}{V'^2}\bigg|_{k=aH} \\
&= \frac{8}{3\epsilon}\left(\frac{V^{\frac{1}{4}}}{\sqrt{8\pi}\mathrm{M}_{\rm pl}}\right)^4, \qquad (4.18)
\end{aligned}
$$

while the power spectrum of tensor perturbations is given by

$$
\begin{aligned}
P_t(k) &= \frac{8}{\mathrm{M}_{\rm pl}^2}\left(\frac{H}{2\pi}\right)^2\bigg|_{k=aH} \\
&= \frac{2}{3}\frac{V}{\pi^2\mathrm{M}_{\rm pl}^4}\bigg|_{k=aH}. \qquad (4.19)
\end{aligned}
$$

Here, $V(\phi)$ is the inflaton potential, and H is the Hubble parameter at the time of inflation. It is customary to define the tensor-to-scalar ratio r as

$$
r \equiv \frac{P_t}{P_s} = 8\mathrm{M}_{\rm pl}^2\left(\frac{V'}{V}\right)^2. \qquad (4.20)
$$

The tensor-to-scalar ratio and the tensor spectral index are related to the slow-roll parameter ϵ via [42; 56]

$$
r = 16\epsilon,\ \ n_t = -2\epsilon. \qquad (4.21)
$$

These expressions lead to the so-called consistency relation for single field slow-roll inflation [213]:

$$
n_t = -\frac{r}{8}. \qquad (4.22)
$$

Unfortunately, this consistency relation is extremely difficult to constrain observationally because of the small amplitude of the tensor power spectrum. We discuss the possibilities for testing this relation with future observations in Section 4.3.3.

The normalization of the power spectrum of scalar perturbations (defined at the pivot wavenumber $k_0 = 0.002$ Mpc^{-1}) is $P_s(k_0) = (2.43 \pm 0.11) \times 10^{-9}$($1\sigma$ CL, WMAP 7-year data [72]). We can use this normalization together with Eq. (4.18) to derive the relationship between the energy scale of inflation and the value of r:

$$
V^{\frac{1}{4}} = 1.06 \times 10^{16}\mathrm{GeV}\left(\frac{r}{0.01}\right)^{\frac{1}{4}}. \qquad (4.23)
$$

That relation indicates that a detection of the tensor-to-scalar ratio at $r \approx 0.01$ or greater would indicate that inflation happened at an energy scale comparable to the Grand Unification Theory (GUT) energy scale ($\mathcal{O}(10^{16})$GeV).

We can also use the slow-roll approximation to derive the following relation, which characterizes the distance in the field space from the end of inflation to the time when CMB scale fluctuations were created, namely the Lyth bound [63; 64]

$$\frac{\Delta\phi}{\mathrm{M_{pl}}} \gtrsim \left(\frac{r}{0.01}\right)^{\frac{1}{2}}. \tag{4.24}$$

Thus, a tensor-to-scalar ratio greater than ~ 0.01, would directly indicate a super-Planckian field evolving from ϕ_{CMB} to ϕ_{end}. Such a detection could provide important observational clues about the nature of quantum gravity. The boundary $r \sim 0.01$ is therefore an important benchmark value which can confirm or rule out a wide class of large field inflation models.

4.3.2 Constraints on SFI from current data

In this subsection, we present constraints on the tensor-to-scalar ratio r from BICEP and QUaD data. To obtain the constraints, we follow the methodology outlined in Section 4.2.3.1.

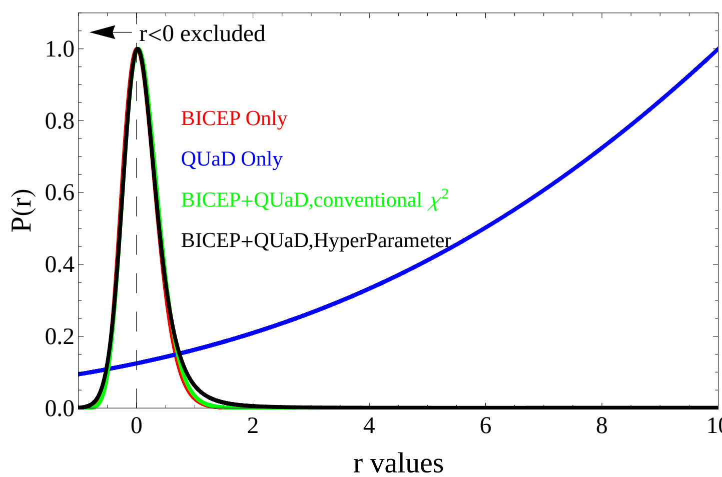

Figure 4.3: The current constraints on r from BICEP and QUaD data.

The results of the analysis are shown in Fig. 4.3. It is clear from the figure that the BICEP data provides a fairly strong upper limit on the value of r. The best-fit value is $r = 0.01^{+0.31}_{-0.26}$ (1σ CL), which is very close to the result obtained by the BICEP team themselves [182]. As expected, r is essentially unconstrained by QUaD, whose measurements are made at much smaller scales ($l \gtrsim 200$) than the scale at which the primordial B-mode signal peaks ($l \sim 80$). In producing joint constraints, we find that both the conventional χ^2 and the hyper-parameter version (χ^2_{hyper}) are completely dominated by the BICEP data. For the conventional χ^2 analysis, the best-fit of the joint analysis gives $r = 0.03^{+0.32}_{-0.27}$ (1σ CL), and for the hyper-parameter χ^2 analysis, we obtain $r = 0.02^{+0.31}_{-0.26}$ (1σ CL). The details of the constraints are listed in the first row of Table 4.1. Note that the tendency for the QUaD data to prefer larger values of r appears to be related to a marginal excess of power in the QUaD measurements over the multipole range $300 < l < 500$ (see Fig. 4.1). After a careful investigation, we find that this shift to higher value of r is due to this part of the data, specifically $l \sim 370$, which might suffer from the unaccounted systematic errors [1].

Comparing the BICEP result to the WMAP 7-year results [72], the tightest upper-bound on r that the WMAP team quote is $r \leq 0.24$ (2σ). This constraint is derived from a combination of the WMAP data with both large scale structure measurements and the HST key project constraint on the Hubble constant. It is clear that measurements of the TT and TE CMB spectra in combination with other astrophysical probes currently play a significant role in constraining the value of r. However, we note that the constraints obtained from B-mode polarization alone are already comparable to the combined constraints from all other cosmological probes and are likely to overtake them with the next generation of CMB polarization experiments.

In Table 4.2 we quote the goodness-of-fits for the various analyses and we quote the weights for the hyper-parameter analysis in Table 4.3. In Table 4.2, $E(n)$ is the expectation value for each fit, calculated using Eqs. (B.4) and (B.17). If the model provides a good fit to the data, the minimum χ^2 over the expectation value should be well within the range $(1 - \sqrt{V(n)}/E(n)$, $1 + \sqrt{V(n)}/E(n))$. Examining the table, we see that the SFI model can fit the BICEP data well, but that the fit to the QUaD data is relatively poor. This poor fit to the QUaD data adds further weight to our conclusion above regarding the anomalous power in the QUaD results in the range $300 < l < 500$.

4.3.3 Prospects for future observations

In this section, we discuss the detection capabilities of future CMB experiments. In order to forecast the error bars of the parameters r and n_t in the fiducial models, we use the Fisher matrix technique, introduced in Section 4.2.3.2.

In Fig. 4.4, we plot the signal-to-noise ratio ($r/\Delta r$) for a detection of tensors as a function of the fiducial value of r, for a number of current and forthcoming experiments. In the left panel, we only consider r as the free parameter, and keep n_t fixed at $n_t = 0$. We see that the Planck satellite can potentially detect the signal of the tensor perturbations at more than 3σ confidence level if $r > 0.05$. For $r = 0.1$, the value of $r/\Delta r$ becomes 5 which would constitute a robust detection. These results are consistent with those presented in [54; 55; 214]. The predicted constraints for PolarBear, QUIET and Spider are somewhat tighter with $r/\Delta r > 3$ for models with $r > 0.02$. The predicted constraints for the proposed CMBPol mission suggest that tensor perturbations could be detected (at the 3σ level) for values of r as low as $r \sim 0.002$. Such a measurement would provide an excellent opportunity to differentiate between various inflationary models. We also find that for the ideal CMB experiment which includes only a residual lensing noise contribution (after

[1] Thanks to the conversation with QUaD team member Michael L. Brown.

Models	Sampling Range	Conventional χ^2			hyper-parameter χ^2
		BICEP	QUaD (tot)	BICEP+QUaD	BICEP+QUaD
SFI: r	$(-1.0, 10.0)$	$0.01^{+0.31+0.68}_{-0.26-0.49}$	$10.0^{\times}_{-3.0-9.70}$	$0.03^{+0.32+0.70}_{-0.27-0.50}$	$0.02^{+0.31+0.75}_{-0.26-0.51}$
LQG: m $[10^{-8}\mathrm{M_{pl}}]$	$(0.01, 10^2)$	$0.18^{+1.16+5.74}_{\times}$	$47.5^{\times}_{-27.7\times}$	$0.22^{+1.14+5.72}_{\times}$	$0.20^{+1.16+5.96}_{\times}$
k_* $[10^{-4}\mathrm{Mpc}^{-1}]$	$(0.1, 10^2)$	$1.07^{+1.36+5.88}_{\times}$	$53.4^{+131.63\times}_{-23.3\times}$	$1.07^{+1.37+5.89}_{\times}$	$1.07^{+1.36+5.98}_{\times}$
Cosmic String $G\mu \times 10^7$	$(10^{-3}, 10^2)$	$(0.001)^{+5.586+9.961}_{\times}$	tot: $7.60^{+1.38+2.63}_{-1.56-3.60}$		
			(l>500): $4.32^{+2.41+4.25}_{\times}$	$2.98^{+2.82+4.74}_{\times}$	$2.32^{+3.45+5.69}_{\times}$

Table 4.1: The best-fit values for the parameters, and the 1σ and 2σ CL for the scalar field inflation (SFI), Loop Quantum Gravity (LQG) and cosmic string models. For the SFI and LQG models, we use all the QUaD data and combine these with BICEP using both a conventional joint χ^2 and the hyper-parameter approach (χ^2_{hyper}). For the cosmic strings model, in addition to the entire QUaD data set, we also examine the effect of removing the $l < 500$ QUaD data points. When combining the QUaD and BICEP data for the cosmic strings model, we also restrict the QUaD data to $l > 500$ (see the discussion in section 4.5.2). The notation "$\times$" indicates that the values of the parameters are out of sampling range.

Goodness of fits	Conventional χ^2			hyper-parameter χ^2
	BICEP	QUaD (tot)	BICEP+QUaD	BICEP+QUaD
SFI: $E(n)$	8	22	31	82.58
$\chi^2_{min}/E(n)$	1.00	1.64	1.56	1.26
Good-fits range	(0.5,1.5)	(0.70,1.30)	(0.75,1.25)	(0.89,1.11)
LQG: $E(n)$	7	21	30	75.49
$\chi^2_{min}/E(n)$	1.10	1.76	1.60	1.22
Good-fits range	(0.47,1.54)	(0.69,1.31)	(0.74,1.26)	(0.90,1.10)
CosStr: $E(n)$	8	18 (l >500)	27 (QUaD l >500)	66.6 (QUaD l >500)
$\chi^2_{min}/E(n)$	1.0	1.35	1.21	1.08
Good-fits range	(0.5,1.5)	(0.67,1.33)	(0.73,1.27)	(0.90,1.11)

Table 4.2: Reduced χ^2 as an indication of the goodness-of-fit for each analysis. $E(n)$ is the expectation value for each fit. If the model provides a good fit to the data, the values of $\chi^2_{min}/E(n)$ should be within the range $(1-\sqrt{V(n)}/E(n),\, 1+\sqrt{V(n)}/E(n))$.

$\alpha_{\rm eff}=n_{\rm A}/\chi^2_{\rm A}$	BICEP	QUaD
SFI	1.13	0.64
LQG	1.17	0.62
CosStr	1.13	0.95

Table 4.3: The values of the effective hyper-parameters $\alpha_{\rm eff}=n_{\rm A}/\chi^2_{\rm A}$ for the BICEP and QUaD data which reflect the relative weights assigned to each data set.

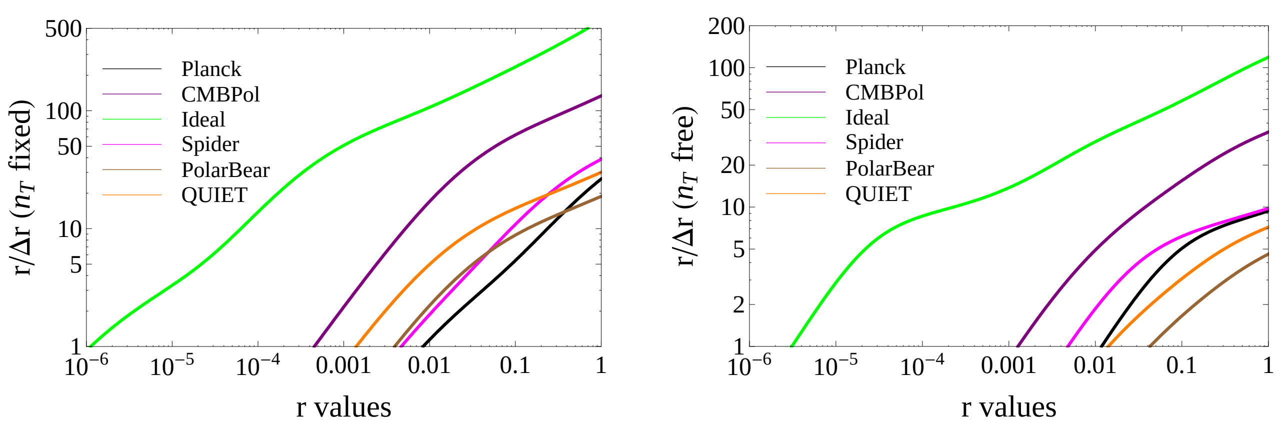

Figure 4.4: The signal-to-noise ratio $r/\Delta r$ for different experiments, calculated using the Fisher matrix of Eq. (4.13). Left: The parameter r is treated as a free parameter but n_t is kept fixed at its fiducial value; Right: Both r and n_t are treated as free parameters. The atmospheric noise in PolarBear and QUIET is not included in the plot.

de-lensing), the SFI primordial signal could be detected (at $> 3\sigma$) only if $r > 10^{-5}$ is satisfied.

In Fig. 4.5, we also plot the signal-to-noise ratio for the combination of Planck with the ground-based experiments (PolarBear and QUIET). The former is sensitive to the B-mode signal at the lowest multipoles $\ell < 20$, while the latter are sensitive to the recombination peak of C_l^{BB} at $l \sim 80$. Similar to [215], we find that the combination of these experiments yields little formal improvement in the signal-to-noise of the detection compared with the capabilities of the ground-based experiments on their own. However, a detection of *both* the recombination bump (e.g. from ground-based experiments) *and* the reionization bump (e.g. from Planck) would constitute much more compelling evidence for tensors than either detection would constitute on its own.

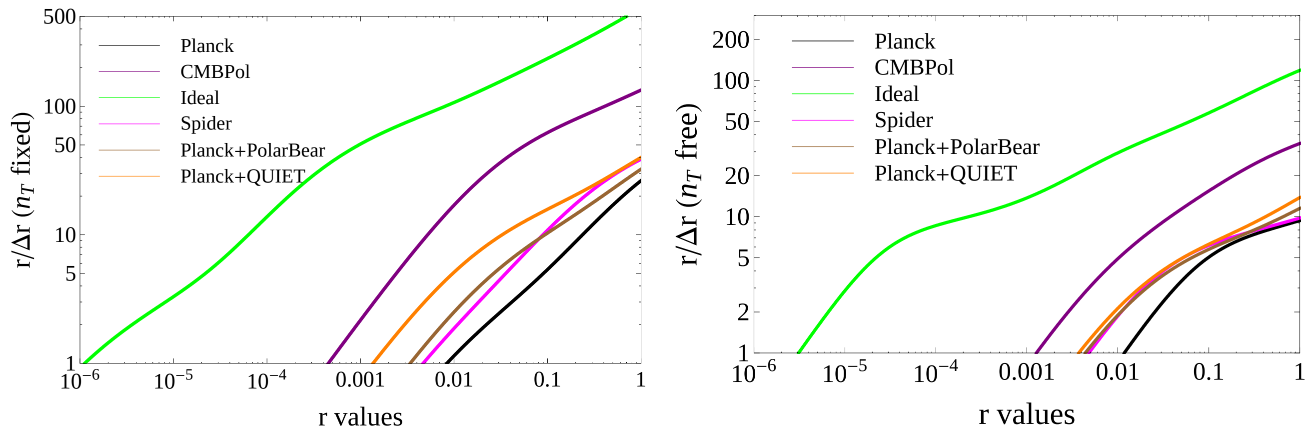

Figure 4.5: The signal-to-noise ratio $r/\Delta r$ for different experiments, and the combination of Planck and ground-based experiments, calculated using the Fisher matrix of Eq. (4.13). Left: The parameter r is treated as a free parameter but n_t is kept fixed at its fiducial value; Right: Both r and n_t are treated as free parameters.

In the right hand panels of Fig. 4.4 and Fig. 4.5, we have plotted the results for the case where we treat both r and n_t as free parameters. Comparing with the corresponding results in the left panels, we find (in agreement with previous works, e.g. [201; 216]) that the signal-to-noise ratios become much smaller due to correlations between the parameters. These correlations were investigated in some detail by [215] who also explored the optimal choice of pivot scale for which the two parameters become decorrelated. In Fig. 4.6, we show separately the forecasted joint constraints on r and n_t parameters given the Planck+QUIET, Planck+PolarBear, Spider, and CMBPol experiment.

In Fig. 4.7, we plot the values of Δn_t as a function of r for various cases. Here we find that, for Planck, PolarBear, QUIET and Spider, the constraint on n_t is relatively weak unless the value of r is very large. For example, the predicted constraint for Planck is $\Delta n_t = 0.13$, and for QUIET is $\Delta n_t = 0.18$ for a model with $r = 0.1$. The combination of Planck and QUIET could in principle do somewhat better with $\Delta n_t = 0.08$. The proposed CMBPol mission could achieve $\Delta n_t = 0.04$ while the limiting value of the ideal experiment is $\Delta n_t = 0.007$, which is comparable to the current constraint on the scalar spectral index n_s [72]. For lower values of r, the predicted constraints are correspondingly weaker. For example, for the CMBPol mission, the value of Δn_t increases from 0.04 to 0.1 if we replace the $r = 0.1$ model with $r = 0.01$.

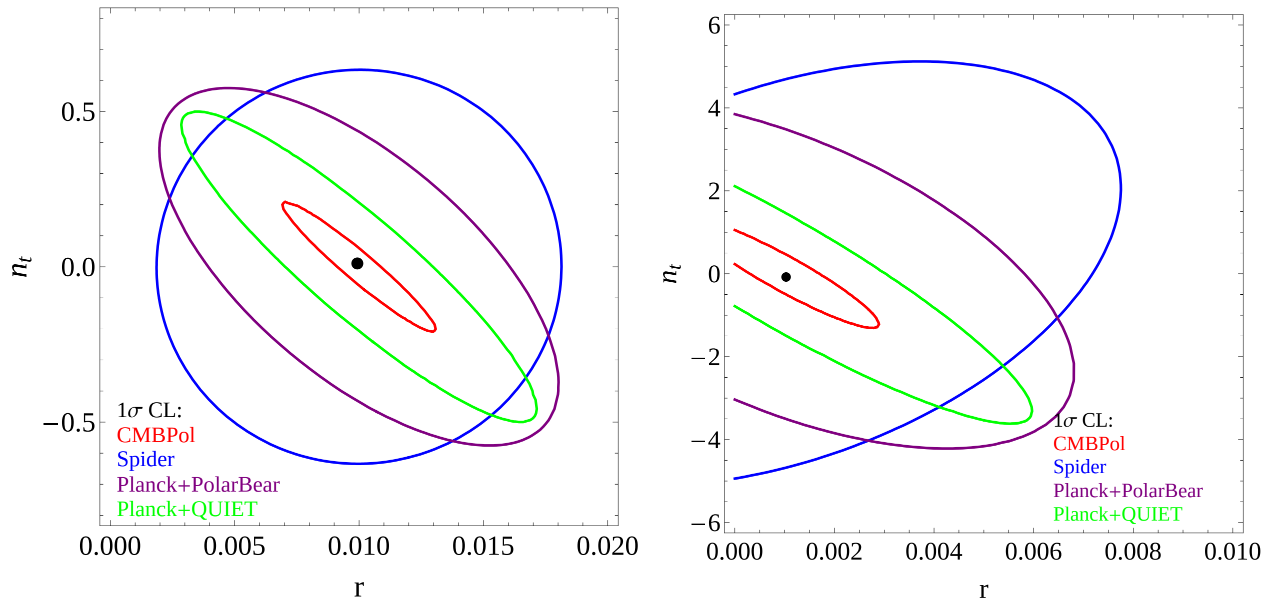

Figure 4.6: Forecasted joint constraints on the parameters of the SFI model. The contours indicate the 68% (1σ) confidence levels. The input models are indicated by the black points (Left: $r = 0.01$ and $n_t = 0$, Right: $r = 0.001$ and $n_t = 0$).

Testing the consistency relation $n_t = -r/8$ (see Eq. (4.22)) is potentially one of the most powerful ways to test the general SFI scenario. To assess whether future experiments might achieve this goal, in Fig. 4.7 we compare the values of Δn_t with $r/8$. If $\Delta n_t < r/8$, then the constraint on n_t is tight enough to allow the consistency relation to be tested. We find that $\Delta n_t < r/8$ is satisfied only if $r > 0.23$ for the CMBPol experiment, and only if $r > 0.06$ for the ideal experiment. An observational confirmation of the consistency relation is therefore extremely unlikely to be achieved with any of the currently envisaged future experiments.

4.3.4 Single-field slow-roll inflationary models

In single field slow-roll inflationary models, the observables depend on three slow-roll parameters [213]

$$\epsilon_V \equiv \frac{\mathrm{M}_{\rm pl}^2}{2}\left(\frac{V'}{V}\right)^2 , \qquad \eta_V \equiv \mathrm{M}_{\rm pl}^2\left(\frac{V''}{V}\right) , \qquad \xi_V \equiv \mathrm{M}_{\rm pl}^4\left(\frac{V'V'''}{V^2}\right) , \tag{4.25}$$

where $V(\phi)$ is the inflationary potential, and the prime denotes derivatives with respect to the field ϕ. Here, ϵ_V quantifies the "steepness" of the slope of the potential, η_V measures the "curvature" of the potential, and ξ_V quantifies the "jerk". Since the potential is fairly flat in the slow-roll inflation models, these three parameters must be much smaller than unity for inflation to occur. One of

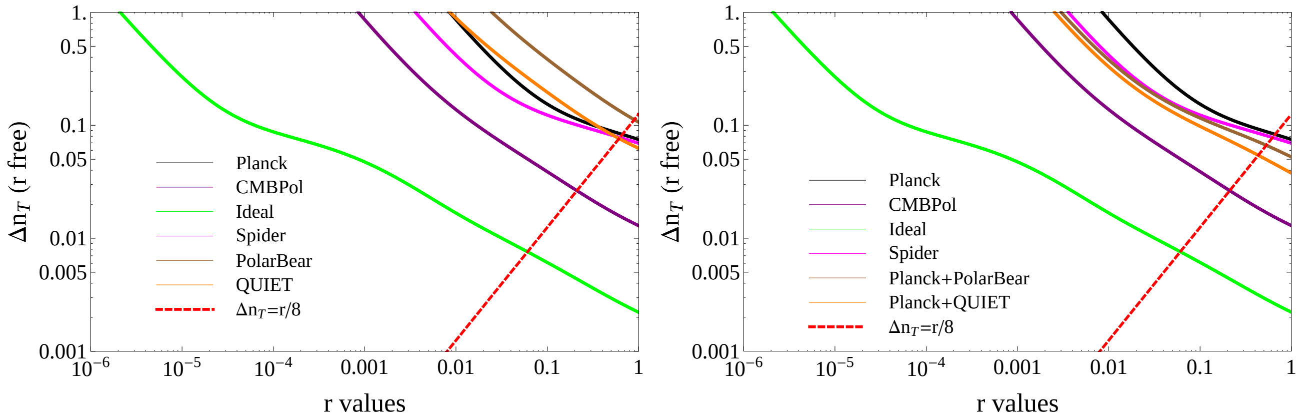

Figure 4.7: Forecasted uncertainty on the tensor spectral index, Δn_t, for different experiments, calculated using the Fisher matrix of Eq. (4.13). Here, both r and n_t are treated as free parameters.

the important predictions of SFI models is that the scalar perturbations are nearly scale-invariant, which has already been confirmed by WMAP results [72].

In SFI models, a standard slow-roll analysis yields the following relations

$$n_t = -\frac{r}{8}, \quad n_s = 1 + 2\eta_V - 6\epsilon_V, \quad r = \frac{8}{3}(1 - n_s) + \frac{16}{3}\eta_V, \quad \alpha_s = -24\epsilon_V^2 + 16\epsilon_V\eta_V - 2\xi_V, \tag{4.26}$$

where n_s is the tilt of primordial scalar power spectrum, and $\alpha_s = dn_s/d\ln k$ is the "running" of n_s. These formulae relate the tensor parameters n_t and r to the scalar parameters n_s and α_s; the latter can be constrained through CMB and large scale structure observations. As shown in Eq. (4.26), the relation between r and n_s involves the slow-roll parameter η_V which in turn depends on the specific inflationary potential.

The strength of the primordial tensor perturbations depends on the value of r. Observations have yielded quite tight constraints on n_s, but we currently only have upper limits on the value of r. The relation between n_s and r depends on the specific inflationary model, and different models predict very different values for r. In the following discussion, we categorize SFI models into four classes based on different regimes for the curvature of the potential $V(\phi)$, and discuss their individual constraints.

Case A: negative curvature models $\eta_V < 0$

The negative η_V models arise from a potential of spontaneous symmetry breaking. One type of often-discussed potentials is the form $V = \Lambda^4\left[1 - (\phi/\mu)^p\right]$ ($p \geq 2$). This type of model predicts a red tilt in the scalar spectrum ($n_s < 1$), which is consistent with the WMAP 7-year results [72]. In addition, these models predict relatively small values for r. For the model with $p = 2$ in Ref. [217],

$$r \simeq 8(1 - n_s)e^{-N_e(1-n_s)}\ , \tag{4.27}$$

where N_e is the number of e-folds, taken to be in the range $N_e \in [40,\ 70]$ based on current observations of the CMB [72; 218]. Here we choose the value $N_e = 60$. Using the result $n_s = 0.963 \pm 0.012$ [72] yields the constraint $r \in [0.021,\ 0.045]$. From Fig. 4.4 (right panel), we see that this is close to or even beyond the sensitivity range of the Planck satellite, but is within the sensitivity ranges of PolarBear, QUIET, Spider and CMBPol. In other models with $p > 2$, the predicted values of r are much smaller than that of the model with $p = 2$.

Case B: small positive curvature models $0 \leq \eta_V \leq 2\epsilon_V$

Two example potentials in this case are the monomial potentials $V = \Lambda^4(\phi/\mu)^p$ with $p \geq 2$ for $0 < \eta_V < 2\epsilon_V$ and the exponential potential $V = \Lambda^4 \exp(\phi/\mu)$ for $\eta_V = 2\epsilon_V$. In these models, to first order in slow roll, the scalar index is always red $n_s < 1$ and the following constraint on r is satisfied

$$\frac{8}{3}(1 - n_s) \leq r \leq 8(1 - n_s)\ . \tag{4.28}$$

Using the result $n_s = 0.963$ [72] , one finds that $r \in [0.1,\ 0.3]$, which is within the sensitivity range of the Planck satellite, as well as that of forthcoming CMB experiments. Thus, the Planck results may provide some constraints on these type of models.

Case C: intermediate positive curvature models $2\epsilon_V < \eta_V \leq 3\epsilon_V$

The supergravity-motivated hybrid models have a potential of the form $V \simeq \Lambda^4[1+\alpha\ln(\phi/Q)+\lambda(\phi/\mu)^4$, up to one-loop correction during inflation. In this case,

$$n_s < 1\ , \qquad r > 8(1 - n_s)\ , \tag{4.29}$$

are satisfied. Using the result $n_s = 0.963$ [72], one finds that $r > 0.3$, which is slightly in conflict with the current upper limit $r < 0.24$ (WMAP+BAO+H_0, 2σ CL) [72]. Fig. 4.4 shows that this model is also in the sensitivity range of the Planck satellite.

Case D: large positive curvature models $\eta_V > 3\epsilon_V$

This class of models has a typical monomial potential similar to those of Case A, but with a plus sign for the term $(\phi/\mu)^p$: $V = \Lambda^4\,[1 + (\phi/\mu)^p]$. This enables inflation to occur for small values of $\phi < \mathrm{M_{pl}}$. The model predicts a blue tilt in the scalar power spectrum $n_s > 1$ (Eq. (4.26)), which is in conflict with current constraints on n_s unless a running of n_s is allowed [72]. When a running in n_s is included, the WMAP 7-year results suggest a blue power spectrum ($n_s = 1.008 \pm 0.042$ for 1σ CL). Therefore, even though this model is not favoured by the WMAP 7-year results for the constant of n_s only, it is not excluded when a running of the spectral index is included. Planck and future CMB experiments should constrain both n_s and α_s to high precision and so should be able to rule out this model.

4.4 Loop Quantum Gravity and its observational probes

4.4.1 Primordial tensor perturbations in LQG models

Loop Quantum Gravity is a promising framework for constructing a quantum theory of gravity in theoretical physics. Based on the reformulation of General Relativity as a kind of gauge theory obtained by [219; 220], LQG is now a language and a dynamical framework which leads to a mathematically coherent description of the physics of quantum spacetime [221]. Constraining LQG theories experimentally is challenging because the quantum geometrical effect can only be tested at very high energy scales, beyond the reach of current accelerator experiments. In this section, we will calculate the possible observational signature of LQG in the CMB sky, which opens a new window for cosmological tests of quantum gravity.

There are two main quantum corrections in the Hamiltonian of LQG when dealing with the semi-classical approach, namely holonomy corrections and "inverse volume" corrections [221; 222]. The holonomy corrections lead to a dramatic modification of the Friedmann equation as [223]

$$H^2 = \frac{8\pi G}{3}\rho\left(1 - \frac{\rho}{\rho_c}\right), \tag{4.30}$$

where ρ is the energy density, and ρ_c is the critical energy density,

$$\rho_c = \frac{4\sqrt{3}}{\gamma^3}\mathrm{M}_{\mathrm{pl}}^4 \simeq 507.49\,\mathrm{M}_{\mathrm{pl}}^4. \tag{4.31}$$

Here $\gamma = 0.239$ is the Barbero-Immirzi parameter, which is derived from the computation of the black hole entropy [224]. Note that we use the reduced Planck mass in our calculation.

A generic picture for this model with the holonomy correction is the bouncing behavior exhibited when the energy density of the Universe approaches ρ_c. The negative sign in Eq. (4.30) is an appealing feature in the framework of LQG such that the repulsive quantum geometry effect becomes dominant in the Planck region [221; 222]. This triggers a contraction period before the bounce, during which time the Hubble parameter is negative and the Hubble radius is shrinking. As a result, the perturbation modes on the largest scales crossed the Hubble horizon and froze out during the contracting period, until the end of the contracting stage when the Hubble horizon increased again. For the very large scale modes, this pre-inflationary bounce may imprint distinctive features in the CMB sky, since they stretched out of the horizon at very early times [221; 222].

Unfortunately, the power spectrum for the scalar perturbations is somewhat hard to obtain because in the case of the holonomy correction, the anomaly free equations are still to be found [225]. Therefore, in the following discussion, we will focus on the tensor power spectrum of LQG and pursue the constraints obtainable on the model from B-mode observations.

Due to the pre-inflationary contracting period, the tensor power spectrum for LQG can be calculated numerically. In [222], a simple parameterized form of the power spectrum is introduced as follows

$$P_t = \frac{2}{\pi^2}\left(\frac{H}{\mathrm{M_{pl}}}\right)^2 \frac{1}{1+(k_*/k)^2}\left[1+\frac{4R-2}{1+(k/k_*)^2}\right], \tag{4.32}$$

where H is the Hubble parameter during the inflationary stage, k_* is the position of the highest peak in the power spectrum, and the quantity R is related to the mass of the scalar field as

$$R = (8\pi)^{0.32}\left[\frac{\mathrm{M_{pl}}}{m}\right]^{0.64}. \tag{4.33}$$

It is interesting to note that Eq. (4.32) reduces to the SFI result of Eq. (4.19) for $k_* \to 0$. In this Chapter, for simplicity, we consider the tensor power spectrum (Eq. 4.32) with a constant H in the early stage of inflation, which corresponds to the specific case of de Sitter inflation.

In this model, we assume that inflation is driven by the potential $V(\phi) = m^2\phi^2/2$. The Hubble parameter is related to this potential via

$$H^2 = \frac{1}{3\mathrm{M_{pl}^2}}V(\phi) = \frac{1}{6\mathrm{M_{pl}^2}}m^2\phi_i^2, \tag{4.34}$$

where ϕ_i is the initial value of the scalar field at the beginning of inflation. The number of e-folds can be calculated as (using the slow-roll approximation $3H\dot{\phi} = -V'$)

$$\begin{aligned} N_e &= \int_i^f H dt \\ &= -\frac{1}{\mathrm{M_{pl}^2}}\int_i^f \frac{V}{V'}d\phi \\ &= -\frac{1}{4\mathrm{M_{pl}^2}}\left(\phi_f^2 - \phi_i^2\right). \end{aligned} \tag{4.35}$$

Since $\phi_i \gg \phi_f$, the above equation is approximately given by $\phi_i^2 \simeq 4N_e\mathrm{M_{pl}^2}$. The Hubble parameter is then (from Eq. (4.34))

$$H^2 \simeq \frac{2}{3}N_e m^2. \tag{4.36}$$

Substituting this into Eq. (4.32), we arrive at the following expression for the tensor power spectrum:

$$P_t = \frac{4N_e}{3\pi}\left(\frac{m}{\mathrm{M_{pl}}}\right)^2 \frac{1}{1+(k_*/k)^2}\left[1+\frac{4\times(8\pi)^{0.32}\times(m/\mathrm{M_{pl}})^{-0.64}-2}{1+(k/k_*)^2}\right], \tag{4.37}$$

where N_e is the number of e-folds which we fix at $N_e \simeq 60$. Finally, we use Eq. (4.6) to project the perturbation modes onto the CMB sphere to find C_l^{BB} for the LQG model.

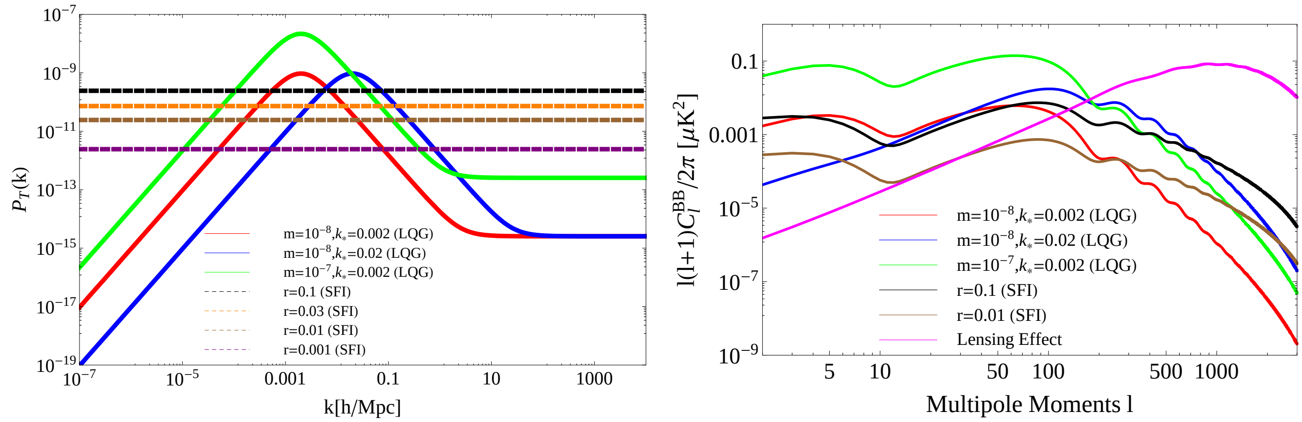

Figure 4.8: Left: the primordial tensor power spectrum for different models of inflation. Right: the corresponding B-mode angular power spectrum generated by different inflationary models. Note the lensing B-mode signal which acts as an effective noise for detecting the primordial C_l^{BB} signal. The units for m and k_* are $\mathrm{M_{pl}}$ and Mpc^{-1} respectively.

In the left panel of Fig. 4.8, for a number of representative sets of parameters, we plot the primordial tensor power spectrum for the LQG model alongside the signal expected in an SFI model for a number of different values of r. For the SFI model, since the power spectrum tilt n_t is very small ($n_t = 0$ for de Sitter inflation), the power spectrum is very flat on all scales. In comparison, the tensor power spectrum of LQG exhibits a bump feature, which is in fact the signature of the pre-inflationary contraction period. Very large scale modes stretched out of the Hubble horizon during the contracting period before inflation, and can be described by the solution in the Minkowski vacuum $f_k = e^{-ik\eta}/\sqrt{2k}$ [221; 222]. Thus, the power spectrum at very large scale takes the form $P_t(k) \sim k^3 |f_k|^2 \sim k^2$ [221; 222]. In contrast, the small scale modes are well within the Hubble horizon and so the power on small scales is similar to the scale-invariant power spectrum of the SFI model. The bump in the power spectrum on larger scales is characterized by the magnitude of k_*. As k_* increases, the bump is shifted to smaller scales and vice versa. The amplitude of the spectrum and the width of the bump are determined by the mass parameter m. We will link these two important parameters to the energy scale of inflation and the current Hubble horizon scale in the next subsection.

The right panel of Fig. 4.8 shows that the bump in the primordial power spectrum results in a peak in the CMB B-mode power spectrum, which is slightly different to that of the SFI model. In addition, if the peak of the LQG spectrum is normalized to the same magnitude as that of SFI, the small scale power will be suppressed in the LQG model, as compared to the SFI model.

4.4.2 Constraints from current data

In this subsection, we use the BICEP and QUaD data to constrain the parameters of LQG models. Before we perform the parameter estimation, we link the two parameters m and k_* with the energy scale of inflation, and with the current Hubble horizon scale.

The parameter m relates to the energy scale of inflation in LQG as follows

$$V^{\frac{1}{4}} = 3.02 \times 10^{15}\mathrm{GeV}\left(\frac{m}{10^{-7}\mathrm{M_{pl}}}\right)^{1/2}, \tag{4.38}$$

where 10^{15} GeV is around the GUT energy scale. Therefore, a detection of $m > 10^{-7}\mathrm{M_{pl}}$ would strongly suggest that the energy scale of inflation is above the GUT scale.

The parameter k_* describes the position of the peak in the primordial power spectrum. We can compare it with the current Hubble wavenumber, which is $k_H \equiv H_0 \simeq 2.33 \times 10^{-4}\mathrm{Mpc}^{-1}$. If $k_* > k_H$, then modes with physical wavelengths (λ_*) equal to the Hubble horizon at the beginning of inflation will have wavelengths less than the current Hubble horizon, whereas if $k_* < k_H$ their wavelengths will be larger than the current horizon scale. Thus, if $k_* > k_H$, we would expect to be able to find pre-inflationary fluctuations within our current Hubble horizon [221; 222]. Conversely, as $k_* \to 0$, the primordial tensor power spectrum (Eqs. (4.32) and (4.37)) reduces to the scale-invariant tensor power spectrum as noted above. Therefore, a non-zero detection of k_* would strongly indicate the existence of a bounce and of a contracting period before inflation.

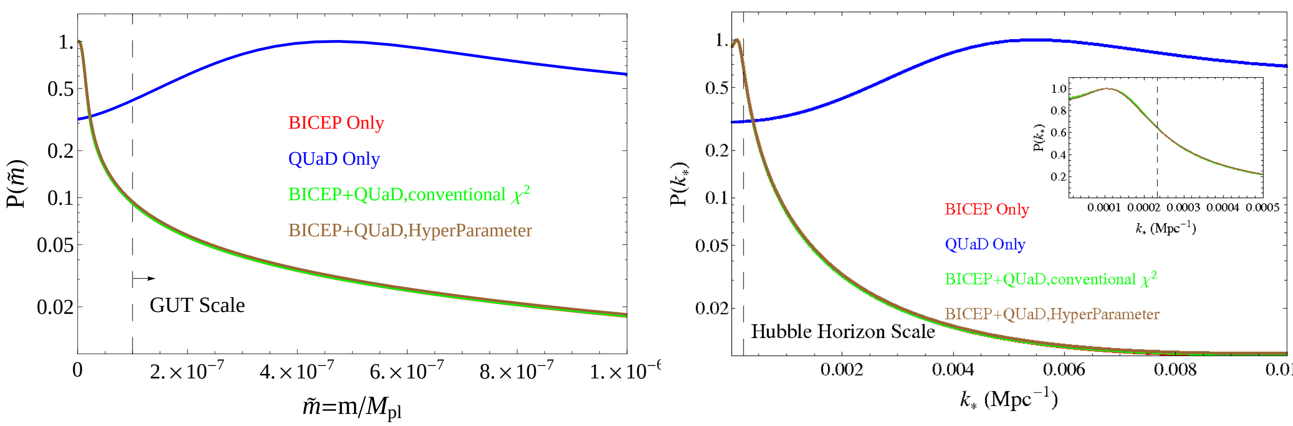

Figure 4.9: Probability distribution function (PDF) for the parameters in the LQG model. Left: constraints on the mass parameter $\tilde{m} = m/\mathrm{M_{pl}}$. Right: constraints on k_*. The red, green, and brown curves overlap with each other, indicating that the vast majority of the constraining power for the combined data sets comes from the BICEP data.

The current constraints on the parameters k_* and m are shown in Fig. 4.9. In the left panel, we have marginalized over the parameter k_* and we plot the PDF for the mass parameter m. The 1σ upper bound is $m \leq 1.36 \times 10^{-8}\mathrm{M_{pl}}$. The detailed results are listed in the second and third rows of Table 4.1. We note that the GUT scale mass $m \simeq 10^{-7}\mathrm{M_{pl}}$ is excluded at the 2σ level, but is still well within 3σ. As was the case with the SFI models, the small-scale QUaD data is unable to constrain the LQG models. Once again, the combined constraints are dominated by the BICEP data as is clear from the figure and from the results listed in Table 1.

In the right panel of Fig. 4.9, we show the PDF for k_* (marginalized over the m parameter).

Once again the results are dominated by BICEP. From this plot, wee see that there is a peak in the PDF at $k_* = 1.07 \times 10^{-4}\text{Mpc}^{-1}$. Although it is not statistically significant, a detection of such a feature would be an interesting result for the pre-inflationary bouncing behavior, since the bounce of the primordial tensor power spectrum is characterized by a non-zero k_* as we have already discussed. We further note that the peak value of k_* is only slightly smaller than the current Hubble wavenumber k_H, which would indicate that modes which had the same length scale as the Hubble horizon at the beginning of inflation have not evolved into the Hubble horizon yet. In that case, the bump in the tensor power spectrum of LQG is a super-horizon feature. However, we stress again that all of our results are upper limits only and our formal constraint is $k_* < 2.43 \times 10^{-4}\text{Mpc}^{-1}$ (1σ CL).

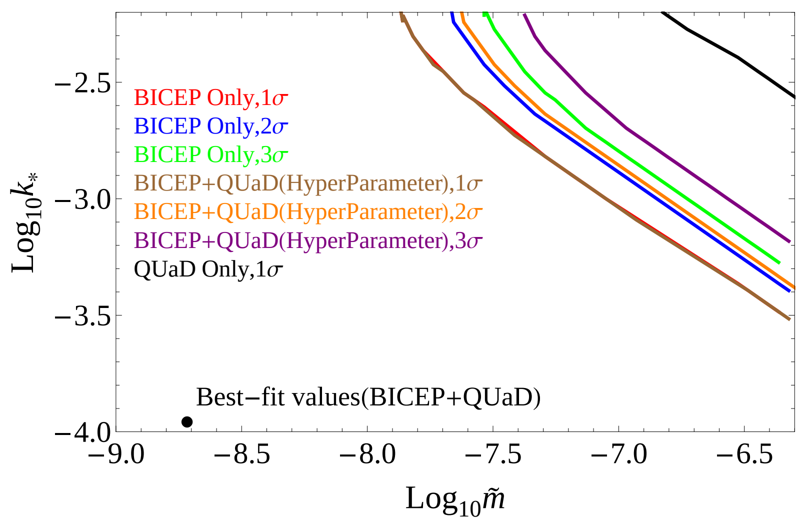

Figure 4.10: 2D constraints on the parameters $\tilde{m} = m/\text{M}_{\text{pl}}$ and $k_*[\text{Mpc}^{-1}]$ of the LQG model. The red line (BICEP 1σ CL) overlaps with the brown line (BICEP+QUaD, 1σ CL).

In Fig. 4.10, we plot the two-dimensional constraints on the parameters m and k_* on a log scale. Clearly, the current data is unable to provide strong constraints on the joint distribution of these two parameters and can only provide upper limits. Once again, as expected, the constraints are dominated by the BICEP data.

4.4.3 Prospects for future experiments

We now investigate the prospects for detection of LQG signatures with future CMB experiments by studying the projected constraints on the two parameters m and k_*. Once again, we use the Fisher matrix approach described in Section 4.2.3.2 and as in Section 4.3.3, we fix the background parameters at their WMAP 7-year best-fit values [72].

In Fig. 4.11, we plot the projected signal-to-noise ratio for the parameters m (left panel) and k_* (right panel) for forthcoming experiments. In the left panel, we plot the signal-to-noise ratio $m/\Delta m$ as a function of m. For this plot, we have kept k_* fixed at $k_* = 0.002$ Mpc^{-1}. We find

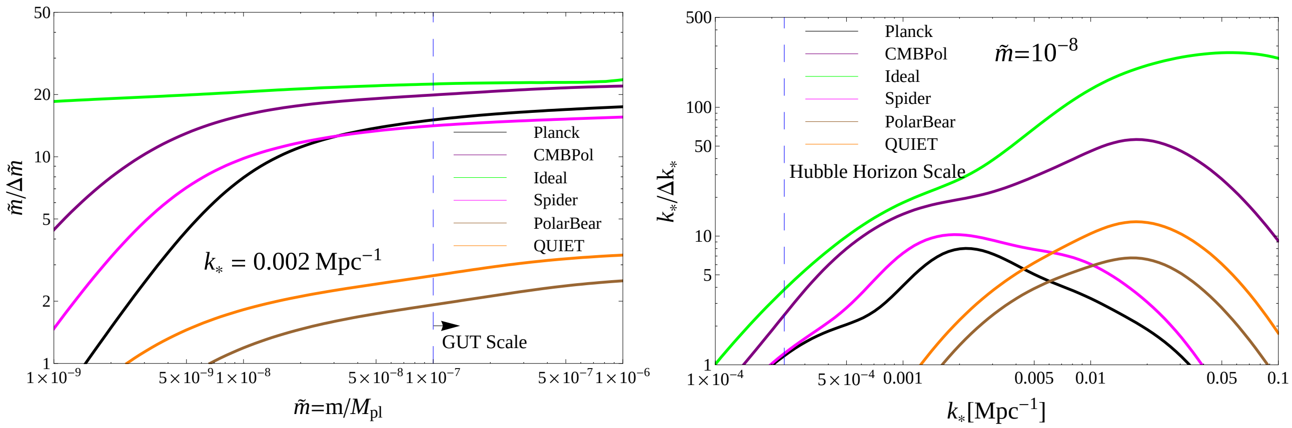

Figure 4.11: Predicted signal-to-noise ratios for the parameters in LQG for forthcoming and future experiments. Here $\tilde{m}$ is the mass parameter, and k_* is the position of the bump in the BB power spectrum.

that, if $m > 10^{-7}$ M_{pl}, i.e. the energy scale of inflation is higher than the GUT scale, then Planck, Spider and CMBPol could potentially detect the LQG signal at more than 10σ due to their large sky coverage. In contrast, the smaller scale experiments (PolarBear and QUIET) would only detect the signal at the 2—3σ level. For $m = 10^{-8}$ M_{pl}, close to the upper bound of the current 1σ confidence level, the large scale survey experiments (Planck, Spider and CMBPol) can still detect the signal at more than 5σ. For this mass parameter and value of k_*, the ground-based experiments, PolarBear and QUIET, would be insensitive to the signal since the B-mode power spectrum from LQG falls off extremely rapidly with increasing l. However, for larger values of k_*, the peak of the LQG C_l^{BB} power spectrum moves to smaller scales. We therefore expect a general trend whereby the large-scale experiments will be sensitive to models with small values of k_* and small-scale experiments will be sensitive to models with larger values of k_*.

This is illustrated in the right-hand panel of Fig. 4.11 where we plot forecasts for $k_*/\Delta k_*$ as a function of k_*. For these results, we have fixed $m = 10^{-8}$ M_{pl}. We find that the signal-to-noise ratio of k_* does not monotonically increase with increasing k_* for any single experiment. Since this parameter controls the angular scale at which the LQG B-mode signal peaks, as we vary k_* we move between the sensitivity ranges of different experiments. For example at $k_* \approx 0.002$ Mpc^{-1}, both Planck and Spider could detect the signal at more than 5σ whereas PolarBear and QUIET would achieve only a marginal detection. Conversely, if $k_* \approx 0.02$ Mpc^{-1}, the reverse is true: PolarBear and QUIET would make strong ($\gtrsim 5\sigma$) detections while Planck and Spider would struggle to detect a signal.

In Fig. 4.12, we plot the two-dimensional constraints on the parameters m and k_* for two typical models. The left panel shows the forecasted constraints for a model with $k_* = 0.002$ Mpc^{-1} and the right panel shows the constraints for a model with $k_* = 0.0002$ Mpc^{-1}. In both cases, a fiducial value of $m = 10^{-8}$ M_{pl} was adopted. We find that the former case can be well

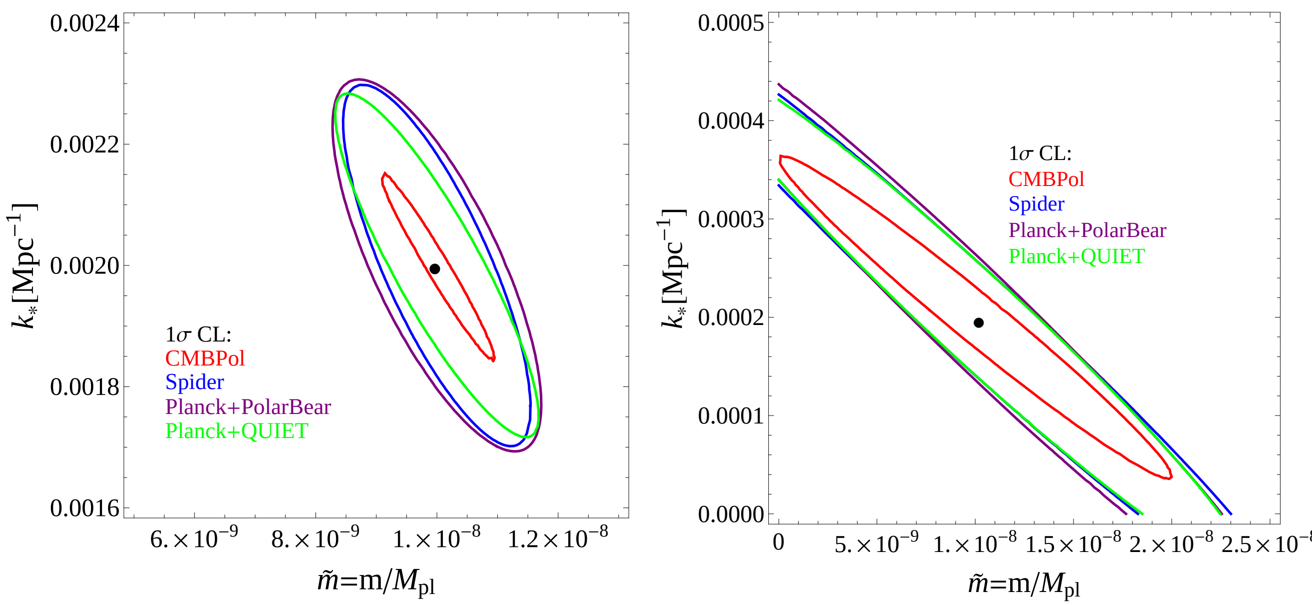

Figure 4.12: Forecasted 2D constraints for the LQG model. The input models are indicated with the black points. (Left: $\tilde{m} = 10^{-8}$ and $k_* = 0.002\text{Mpc}^{-1}$. Right: $\tilde{m} = 10^{-8}$ and $k_* = 0.0002\text{Mpc}^{-1}$).

constrained by either Spider, CMBPol, Planck+PolarBear or Planck+QUIET while the latter case can only be meaningfully constrained by the CMBPol mission.

4.5 Cosmic strings and their detection

4.5.1 B-mode polarization from cosmic strings

Cosmic strings have been proposed as a possible source of the inhomogeneities in the Universe [226]. Although current observations of the CMB temperature and polarization power spectra prefer inflation than cosmic strings as the main source of the primordial density perturbations [72], there is still significant motivation to search for the signature of cosmic strings from both theoretical and observational considerations.

Cosmic strings can be formed in several inflationary pictures, and particularly in Brane inflation models [50; 190; 191; 227]. Brane inflation arises from the framework of high dimensional string theory and is a further important model for sourcing the dynamics of inflation. In this model, the high dimensional Brane and anti-Brane collided and annihilated and cosmic strings were produced at the end of the inflationary epoch. If this scenario is correct, the resulting strings would have made an observable imprint on the CMB sky by way of the Kaiser-Stebbins effect [228].

Although current observations suggest that inflation sources the majority of the CMB anisotropy, one cannot rule out a significant (up to $\sim 10\%$) contribution from cosmic strings [229]. In this section, we will use CMB data to constrain the cosmic strings tension. In contrast to other works (see e.g. [229]), we focus on the possible detection of cosmic strings through the B-mode power spectrum alone. B-mode polarization can only be generated in the early Universe by vector and tensor perturbations, which provides a complementary route for detecting cosmic strings. Although the contribution of scalar perturbations from cosmic strings is subdominant ($< 10\%$) compared to the contribution from SFI, the contributions of vector and tensor perturbations from cosmic strings may constitute a very significant fraction of the B-mode polarization power on small angular scale (high multipoles) [230].

To predict the C_l^{BB} power spectrum generated by cosmic strings, one must understand the evolution of a cosmic string network and it is important to know the characteristics of the scaling regime which needs to be assumed in the numerical simulation. There are two popular ways of making progress. One is to solve the Nambu equations of motion for a string in an expanding universe and ignore the effects of radiation backreaction (hereafter the Nambu-String model); the other is to solve the equations of motion for the Abelian-Higgs (AH) model, but to limit the dynamical range of the simulation. In this work, we will consider only the Nambu-String model but we note that the Abelian-Higgs model can be constrained in a similar way [229].

In order to calculate the B-mode power spectrum, including the contributions of both vector and tensor perturbations, we use the publicly available code CMBACT [203; 204] to generate a fiducial C_l^{BB} for cosmic strings with the tension of the strings set to $G\mu_0 = 10^{-7}$. Since the amplitude of the B-mode power spectrum generated by cosmic strings is simply proportional to the square of the cosmic string tension, we can scale the fiducial spectrum to any other value for the cosmic string tension using

$$C_l^{BB} = C_l^{BB,0}\left(\frac{G\mu}{G\mu_0}\right)^2, \tag{4.39}$$

where $C_l^{BB,0}$ is the power spectrum normalized at $G\mu_0 = 10^{-7}$.

4.5.2 Constraints from current data

In Fig. 4.13, we show the current constraints on the cosmic string tension $G\mu$ from the BICEP and QUaD C_l^{BB} data. The upper bound from BICEP alone is $G\mu \leq 9.961 \times 10^{-7}$ (2σ CL). Using the QUaD data alone the result is $G\mu = 7.60^{+2.63}_{-3.60} \times 10^{-7}$($2\sigma$ CL), shown as the blue curve in Fig. 4.13. Taken at face value, the QUaD result represents a 2.8σ detection of the cosmic string tension. Referring back to Fig. 4.1 and the discussion in Section 4.3.2, this result is likely coming from the apparent excess of power seen in the QUaD data on scales $300 < l < 500$. To investigate further, we have repeated the analysis with the $l < 500$ QUaD data removed. This results in the likelihood function for $G\mu$ shown as the brown curve in Fig. 4.13. Excluding the $l < 500$ QUaD data shifts the peak of the likelihood significantly towards a smaller value (best-fit $G\mu = 4.32\times10^{-7}$), and the constraint is now consistent with zero at the 1σ CL. The 2σ upper limit becomes $G\mu < 8.57\times10^{-7}$ (see Table 4.1 for the full set of results). The fact that the QUaD result changes drastically when

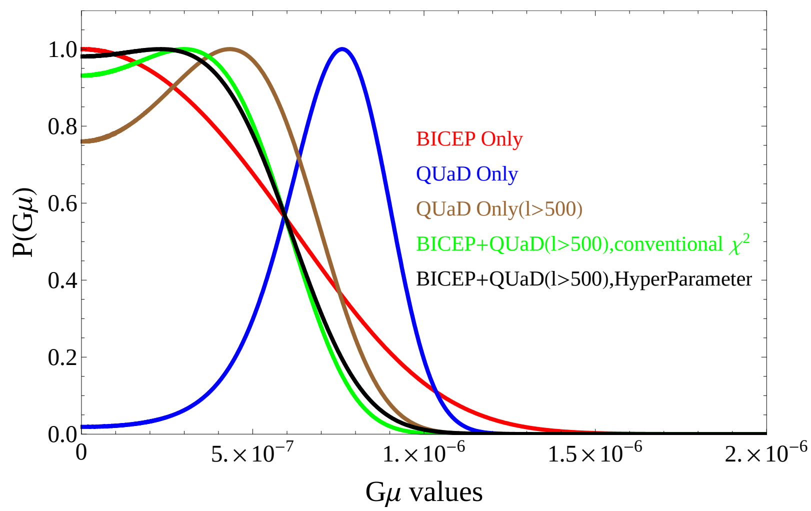

Figure 4.13: Current constraints from B-mode polarization on the cosmic string tension. To obtain the constraints, we have fixed the wiggling parameter at $\alpha = 1.9$.

we remove the $l < 500$ measurements suggests a problem with the $l < 500$ data. As in the case of the SFI constraints presented earlier, we note that the shape of the QUaD data at $l < 500$ is clearly inconsistent with the expected B-mode signal for cosmic strings. Once again, we suspect that the anomalous signal seen in the QUaD data between $l \approx 300$ and $l \approx 500$ is likely due to unquantified systematics. We therefore consider the QUaD result restricted to $l > 500$ to be a more robust constraint and consequently we quote this as our main result.

We now examine the constraints obtained from combining the BICEP data with the $l > 500$ QUaD data. Since the peaks of the two likelihood functions do not overlap, we will carefully consider both the conventional χ^2 analysis and the hyper-parameter χ^2. When we use the conventional χ^2, the peak of the combined likelihood lies midway between the peaks of the two individual likelihoods (green line in Fig. 4.13), and the resulting constraint is $G\mu < 7.72 \times 10^{-7}$ (2σ CL). If we use the hyper-parameter χ^2, the peak of the joint distribution moves slightly further towards zero, and the best-fit is $G\mu < 8.01 \times 10^{-7}$ (2σ CL). Since the conventional and hyper-parameter approaches give very similar results, this suggests that the BICEP and $l > 500$ QUaD data are mutually consistent which adds confidence to the joint constraint.

A number of previous works have also attempted to constrain cosmic strings through their imprint on CMB (TT, TE, EE), large scale structure and gravitational waves data [231; 232; 233; 234; 235; 236]. In a recent work [229], constraints on the cosmic string tension were obtained from a combination of CMB data (including the WMAP 5-year, ACBAR, BOOMERGANG, CBI, QUAD and BIMA observations), matter power spectrum data from the SDSS Luminous Red Galaxies sample, and Big Bang Nucleosynthesis constraints on the baryon fraction from measurements of deuterium at high redshift. They obtained a combined upper limit of $G\mu < 2.2 \times 10^{-7}$ (2σ) in the Nambu-String case.

As expected, this limit is much tighter than what we have obtained from B-modes alone since current measurements of the TT, TE and EE power spectra are much stronger than the BB data that we have used here. However, we note that in the analysis of Ref. [229], the main constraining power comes from the CMB TT and SDSS data and ultimately constraints from such data will be limited by degeneracies with other parameters (most notably, the spectral index n_s). As is the case for SFI models, the advantage of using the BB power spectrum to constrain the cosmic string tension is that C_l^{BB} is only very weakly dependent on the other cosmological parameters, e.g. n_s. Our constraint is therefore an independent check of other constraints obtained on $G\mu$ using different data and our result, although weaker, is consistent with previous analyses. Cosmic string constraints from forthcoming CMB polarization experiments will likely close the gap with other techniques in terms of constraining power. We now turn to examining the constraints achievable with these forthcoming experiments.

4.5.3 Prospects for future experiments

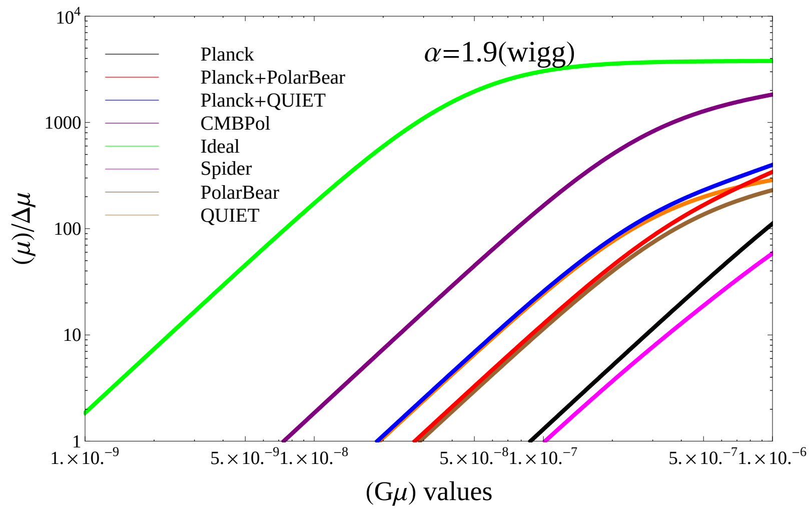

Figure 4.14: Forecasts of the signal-to-noise ratio for the cosmic string tension $G\mu$ potentially achievable with future CMB polarization experiments.

In this subsection, we forecast the detectability of the cosmic string tension $G\mu$ for future experiments. Once again, we use the Fisher matrix formalism described in Section 4.2.3.2. In Fig. 4.14, we plot the signal-to-noise ratio for a measurement of $G\mu$ for the various experiments. As one might expect, the Planck and Spider experiments are unable to tightly constrain the cosmic string tension since neither experiment will produce sensitive B-mode measurements on small scales where the string signal peaks.

For example, the Planck satellite can detect a cosmic string signal at the 3σ level only if $G\mu \gtrsim 2 \times 10^{-7}$ is satisfied. The ground-based experiments, PolarBear and QUIET, will obviously be better at constraining $G\mu$ than Planck and Spider. PolarBear should be able to detect $G\mu >$

5.0×10^{-8} (at the 3σ level) while QUIET should be able to detect $G\mu > 4.0 \times 10^{-8}$ (again at 3σ). Adding Planck to either of these experiments does not change the results significantly. CMBPol is much more sensitive than the other experiments for all fiducial $G\mu$ values, and its 3σ detection limit is $G\mu \gtrsim 1.5 \times 10^{-8}$. Finally, we find that the ideal CMB experiment can detect cosmic strings at the 3σ level if $G\mu \gtrsim 1.5 \times 10^{-9}$ is satisfied, which represents the fundamental detection limit for CMB B-mode polarization experiments.

4.6 Conclusion

In this Chapter, we have examined the observational signatures of three different models of the early Universe related to the inflationary process. These three models are in turn motivated by three different aspects of microscopic physics: single field slow-roll inflation from effective field theory (SFI), loop quantum cosmology from loop quantum gravity (LQG) and cosmic strings from Brane inflation and/or high dimensional string theory. We have discussed their potential observational signatures in the B-mode polarization of the CMB, and we have constrained the parameters of each model using the latest CMB polarization data from the BICEP and QUaD experiments. Using a Fisher matrix formalism we have forecasted the constraints achievable on these models using future CMB polarization observations from a number of experiments including Planck (space), PolarBear (ground), QUIET (ground), Spider (balloon), CMBPol (space) and an idealized experiment.

We first discussed the SFI model. From the Lyth bound relation, we know that $r \sim 0.01$ is an important benchmark value to link the energy scale of inflation with GUT scale. The constraints we obtained from current B-mode measurements are shown in Fig. 4.3. Using the BICEP data alone, we find $r = 0.01^{+0.31}_{-0.26}$ (1σ CL) in close agreement with the BICEP team's own analysis [182]. As expected, this constraint does not change significantly on the addition of the small-scale QUaD data. Looking to the future, we find that the Planck satellite may be able to detect $r \sim 0.05$ (at the 3σ CL), while the Spider, QUIET and PolarBear experiments all have the potential to make a 5σ detection of $r \sim 0.05$. The possible future satellite mission, CMBPol could detect $r \sim 0.01$ at the 20σ CL, and could even detect $r \sim 0.002$ at the $\sim 3\sigma$ CL. (All of these forecasts are for the case where the tensor spectral index is held fixed at $n_t = 0$.) In summary, we find that all future experiments can potentially constrain the value of r with sufficient sensitivity to allow the SFI model from effective field theory to be tested in an interesting way.

We have also discussed the LQG model, which predicts a pre-inflationary bouncing era. Before the bounce, the Universe was contracting and dominated by vacuum energy. Its tensor power spectrum is characterized by two parameters: m and k_*, where the mass parameter m controls the magnitude of the B-mode power spectrum, and k_* controls the scale of the peak in the B-mode spectrum. Our joint likelihood analysis using current data yields $m < 6.16 \times 10^{-8}\,\mathrm{M_{pl}}$ and $k_* < 7.05 \times 10^{-4}$ Mpc^{-1} (both 2σ CL upper limits). The PDF for the parameter k_* exhibits a peak at position $k_* = 1.07 \times 10^{-4}$ Mpc^{-1}. Although this peak is not statistically significant, we note that were the value of k_* to be around this value, this would constitute evidence for a pre-inflationary bounce. We have also presented forecasts for constraining the LQG model using future CMB experiments. We find that if the value of k_* is as large as 0.002 Mpc^{-1}, a number of ongoing and future experiments (Planck, Spider and CMBPol) could potentially detect the signal as long as $m > 2.5 \times 10^{-9}$ M$_{\rm pl}$. However, if the value of k_* were to be as low as 0.0002 Mpc^{-1} (as is mildly indicated by current data), then the signature of LQG becomes quite difficult to detect. We find that, for a typical choice of $m = 10^{-8}$ M$_{\rm pl}$, only CMBPol and the ideal experiment could detect the signal for such a low value of k_*.

Finally, we have presented current and prospective constraints on the cosmic string tension. We find that the BICEP and QUaD data constrain the cosmic string tension to be $G\mu \leq 9.96 \times 10^{-7}$ and $G\mu \leq 8.57 \times 10^{-7}$ respectively (both 2σ CL upper limits). The combined constraint is $G\mu < 8.01 \times 10^{-7}$, which is weaker, but comparable to the constraints from the CMB temperature anisotropy power spectrum. In terms of forecasts for the future, we find that the high-resolution ground-based experiments, PolarBear and QUIET, are more useful for constraining $G\mu$ (as compared to e.g. Planck and Spider) since they are much more sensitive to the B-mode power spectrum on small angular scales. These two experiments could detect $G\mu \sim 10^{-7}$ at more than 10σ CL. We also find that CMBPol can detect the signal of cosmic strings if $G\mu > 1.5 \times 10^{-8}$ at 3σ CL, and the ideal CMB experiment can detect the signal at the 3σ level even if the tension of cosmic string is as low as $G\mu = 1.5 \times 10^{-9}$.

Although the B-mode polarization derived constraints which we have presented in this Chapter are currently only upper limits, they are nevertheless already reached strong constraining power. In terms of constraining the parameters of early Universe models, B-mode polarization is clearly a very powerful tool and will likely overtake other early Universe probes with the advent of the next generation of CMB polarization experiments. In this Chapter, we have not directly considered the issue of model selection. However, it is likely that, in addition to constraining model parameters, future sensitive B-mode observations will also allow us to distinguish between models of the early Universe such as those considered in this Chapter.

Chapter 5

Peculiar Velocity Field: Constraining the tilt of the Universe

5.1 Introduction

The bulk flow, i.e. the streaming motion of galaxies or clusters, is a sensitive probe of the density fluctuation on very large scales. Recently there have been several observations of a large amplitude of the bulk flow on hundred Mpc scales, which are in conflict with the predictions of the Lambda cold dark matter (ΛCDM) model [244; 245]. The bulk flow is measured with respect to a frame in which the cosmic microwave background (CMB) temperature dipole vanishes. We define this as the *CMB rest frame*. It is usually assumed that the CMB rest frame coincides with the *matter rest frame* which we define to be the frame in which the velocities of matter in our horizon volume are isotropic.

It is possible that the two reference frames actually do not coincide with each other, resulting in a "tilted universe" [246; 247; 248]. If the inflationary epoch lasted just a little more than the 60 or so e-folds needed to solve the horizon problem, the observable "remnants" of the preinflationary Universe may still exist on very large scales of the CMB. As a result, there could be some fraction of the CMB dipole due to the intrinsic fluctuations rather than observer's kinetic motion. Therefore, when the observed dipole is subtracted from the galaxy peculiar velocity data, the subtraction induces a mismatch between the CMB rest frame and matter rest frame. We define the *intrinsic* CMB dipole to be the CMB dipole measured in the matter rest frame. The recent finding of such a mismatch between the directions of the observed CMB dipole and reconstructed velocity dipole [249; 250] suggested the possible existence of the intrinsic CMB dipole on the sky.

Preinflationary fluctuations in a scalar field may produce an intrinsic dipole anisotropy. In this scenario, the observed CMB dipole would be a sum of the dipole from our motion in the matter rest frame and the intrinsic CMB dipole caused by a large scale perturbation. This intrinsic dipole can be produced by a large scale isocurvature perturbation [1], but not a large scale adiabatic perturbation [251]. Note that our local motion relative to the matter rest frame is caused by small scale inhomogeneity (up to about the 100 Mpc scale) and will be negligibly affected by the very large scale ($\gg$ 10 Gpc) perturbation that would cause a tilt effect.

In this Chapter, we estimate the tilted velocity ($\mathbf{u}$) between the two rest frames using galaxy peculiar velocity data. This opens a new window on testing early-Universe models from observations of large scale structure.

5.2 Likelihood and mock catalogues

In order to use the galaxy peculiar velocity catalogues (see the following descriptions of the data), we need to model the velocity of galaxies in different rest frames. For each galaxy velocity survey, we first subtract off our local motion with respect to the CMB as estimated from the CMB dipole. However, if there is a non-negligible intrinsic CMB dipole, the CMB defined rest frame will not correspond to the matter rest frame and thus there will be a residual dipole in the galaxy peculiar velocity survey. To test this we estimate the line-of-sight velocity S_n of each galaxy n in the CMB rest frame with measurement noise σ_n. Suppose the CMB rest frame has a tilt velocity $\mathbf{u}$ with respect to the matter rest frame, then the line-of-sight velocity of each galaxy with respect to the matter rest frame becomes $p_n(\mathbf{u}) = S_n - \hat{r}_{n,i}u_i$, where $\hat{r}_{n,i}u_i$ is the projected component of the 3-D Cartesian coordinate $\mathbf{u}$ onto the line-of-sight direction of galaxy n. After subtracting out the "tilted velocity", we model the galaxy line-of-sight velocity with respect to the matter rest frame as $p_n = v_n + \delta_n$, where v_n is the galaxy line-of-sight velocity in the matter rest frame, and δ_n is a superimposed Gaussian random motion with variance $\sigma_n^2 + \sigma_*^2$, where σ_* accounts for the 1-D small scale nonlinear velocity. It can also compensate for an incorrect estimation measurement noise σ_n [244; 245]. Therefore, the covariance matrix of $p_n(\mathbf{u})$ becomes

$$
\begin{aligned}
G_{mn} &= \langle v_m v_n \rangle + \delta_{mn}(\sigma_n^2 + \sigma_*^2) \\
&= \langle (\hat{\mathbf{r}}_m \cdot \mathbf{v}(\mathbf{r}_m)) \, (\hat{\mathbf{r}}_n \cdot \mathbf{v}(\mathbf{r}_n)) \rangle + \ \delta_{mn}(\sigma_n^2 + \sigma_*^2),
\end{aligned}
\tag{5.1}
$$

in which the cosmic variance term is [252]

$$
\langle (\hat{\mathbf{r}}_m \cdot \mathbf{v}(\mathbf{r}_m)) \, (\hat{\mathbf{r}}_n \cdot \mathbf{v}(\mathbf{r}_n)) \rangle = \frac{\Omega_m^{1.1} H_0^2}{2\pi^2} \int dk P(k) f_{mn}(k), \tag{5.2}
$$

where

$$
f_{mn}(k) = \int \frac{d^2\hat{k}}{4\pi} \left(\hat{\mathbf{r}}_m \cdot \hat{\mathbf{k}} \right) \left(\hat{\mathbf{r}}_n \cdot \hat{\mathbf{k}} \right) \times \exp \left(ik\hat{\mathbf{k}} \cdot (\mathbf{r}_m - \mathbf{r}_n) \right), \tag{5.3}
$$

[1] In our context, an isocurvature perturbation is distinguished from an adiabatic perturbation in that the ratios of the number of photons to baryons and cold dark matter particles are not spatially invariant.

which can be calculated analytically (Appendix C).

Therefore, the likelihood of the tilted vector and the small scale velocity dispersion σ_* can be written as

$$L(\mathbf{u}, \sigma_*) = \frac{1}{(\det G_{mn})^{\frac{1}{2}}} \exp\left(-\frac{1}{2} p_m(\mathbf{u}) G^{-1}_{mn} p_n(\mathbf{u})\right), \tag{5.4}$$

where we fix the cosmological parameters at the WMAP 7-yr best-fit values ($\Omega_b = 0.0449$, $\Omega_c = 0.222$, $h = 0.71$, and $\sigma_8 = 0.801$ [72]).

We parameterize the velocity as $\mathbf{u} = \{u, \cos(\theta), \phi\}$ where in Galactic coordinates $\phi = l$ and $\theta = \pi/2 - b$. In order for our marginalized prior on u to be uniform we set Prior$(\mathbf{u}, \sigma_*) \propto 1/u^2$. Then the posterior distribution of the parameters $(\mathbf{u}, \sigma_*)$ given the data (D) is Pr$(\mathbf{u}, \sigma_*|\mathrm{D}) \propto$ Prior$(\mathbf{u}, \sigma_*) L(\mathbf{u}, \sigma_*)$.

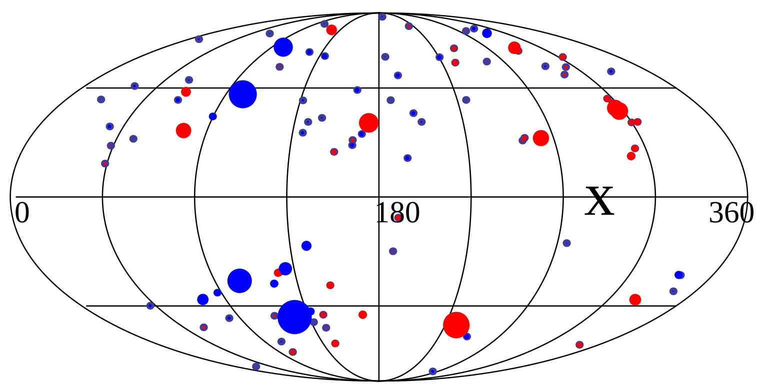

Figure 5.1: The SN data plotted in Galactic coordinates.. The red points are moving away from us and the blue ones are moving towards us. The size of the points is proportional to the magnitude of the line-of-sight peculiar velocity. "X" is our estimate of the direction of the tilted velocity estimated from the SN data.

Before we perform the likelihood analysis for the real data, we have tested this likelihood from mock catalogues. We input a set of fiducial values of (σ_*,$\mathbf{u}$) and generate 300 simulations of the underlying velocity field ($P_v(k) \sim P(k)/k^2$). The average likelihood of these simulations (Fig. 5.2) for each parameter exactly peaks at the input values, with the appropriate width determined by cosmic variance, instrumental noise and small scale velocity dispersion.

5.3 Data Analysis

We studied five different catalogues of galaxy peculiar velocities to constrain the tilted velocity $\mathbf{u}$ and the velocity dispersion σ_*. The five data sets are (see [244] for the procedure of excluding outliers):

- ENEAR is a survey of fundamental plane (FP) [269] distances to nearby early-type galaxies [253]. After the exclusion of 4 outliers, there are distances to 698 field galaxies or groups.

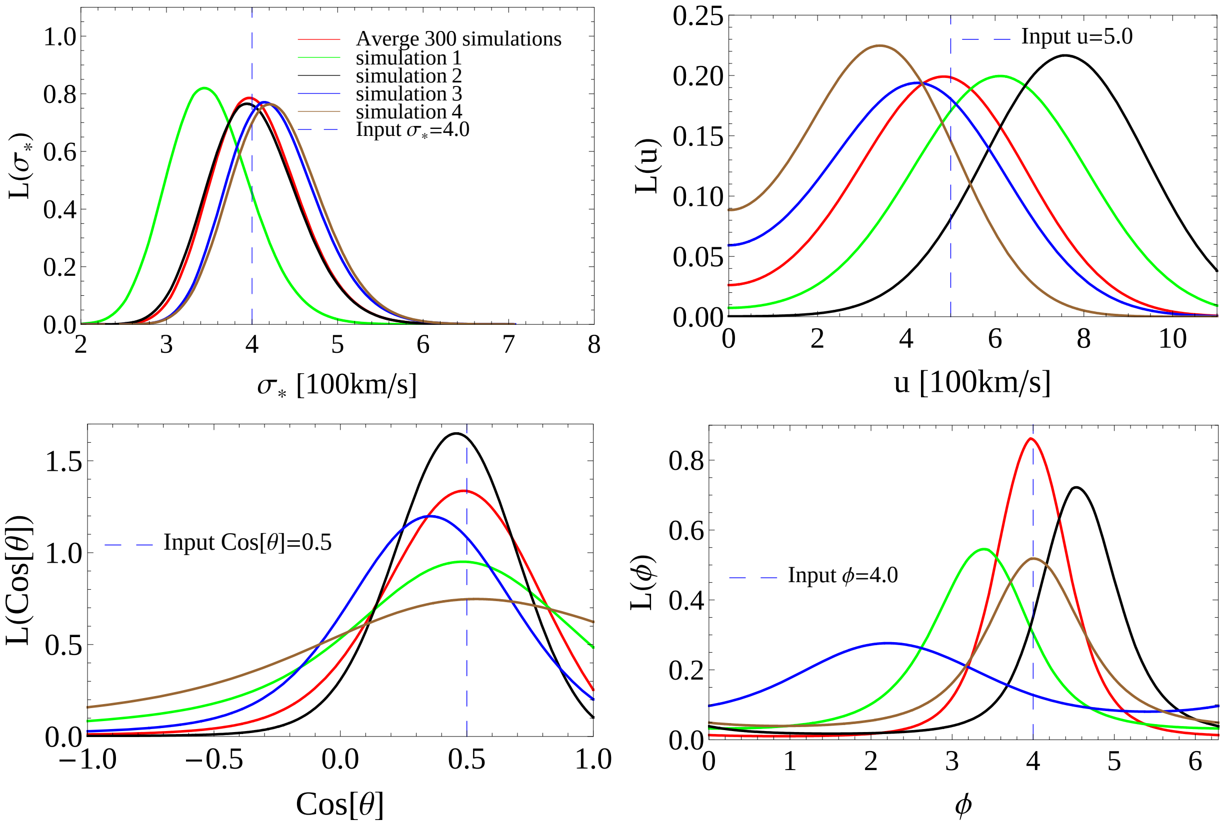

Figure 5.2: The simulation of the bulk flow velocity and test of likelihood (5.4). We input a particular set of parameters (σ_*, $\mathbf{u}$) and do 300 simulations of the underlying density field with the mean value of this set of parameters. One can see that the peaks of the average likelihood are very close to the input values ([Blue] dashed lines).

For single galaxies, the typical distance error is 20%. The characteristic depth of the sample is 29 h^{-1}Mpc.

- SN are 103 Type Ia supernovae distances [254], limited to a distance of $\lesssim$150 h^{-1}Mpc. SN distances are typically precise to 8%. The characteristic depth is 32 h^{-1}Mpc. See Fig. 5.1.

- SFI++ [255], based on the Tully-Fisher (TF) [269] relation, is the largest and densest peculiar velocity survey considered here. After rejection of 38 (1.4%) field and 10 (1.3%) group outliers, our sample consist of 2720 field galaxies and 736 groups, so we divide it into two subsamples, field samples SFI++$_F$, and group samples SFI++$_G$. The characteristic depth is 34 h^{-1}Mpc.

- SMAC [256] is an all-sky fundamental plane (FP) [269] survey of 56 clusters, with characteristic depth 65 h^{-1}Mpc.

- COMPOSITE is the combined catalogues (4536 data in total, compiled in [244; 245]) which has the characteristic depth of 33 h^{-1}Mpc. It is a combination of SN, SFI++, SMAC,

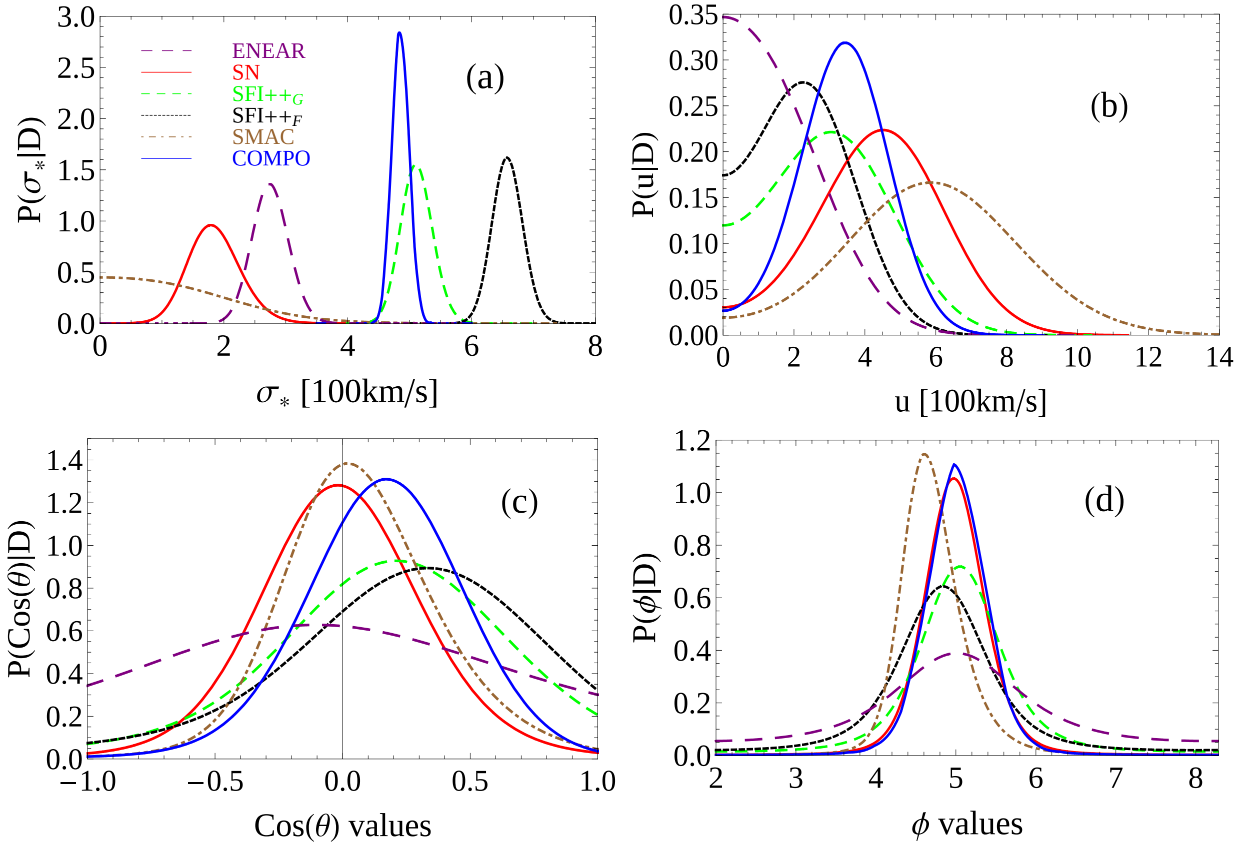

Figure 5.3: The 1-D marginalized posterior probability distribution functions of the parameters : (a) σ_*, (b) magnitude of $\mathbf{u}$, (c) Cos(θ), (d) ϕ.

ENEAR and also the samples from SBF [257] (69 field and 23 group galaxies, characteristic depth 17 h^{-1}Mpc), EFAR [258] (85 clusters and groups, characteristic depth 93 h^{-1}Mpc), SC [259] (TF-based survey of spiral galaxies in 70 clusters, characteristic depth 57 h^{-1}Mpc), and Willick [260] (Tully-Fisher based survey of 15 clusters, characteristic depth 111 h^{-1}Mpc).

In Fig. 5.3, we show the marginalized 1-D posterior probability distribution functions of the small scale velocity and intrinsic dispersion σ_*, and the velocity vector $\mathbf{u}$. The best-fit and marginalized error bars are listed in Table 5.1. In panel (a) of Fig. 5.3, we see that different surveys prefer different σ_*. For the SN catalogue, there is a smaller σ_*, because the supernovae light curves can be used to calibrate the distance measurement very precisely, so the scatter of the line-of-sight velocity is small. In the COMPOSITE catalogue, $\sigma_* \sim 450$ km/s reflects the average value of σ_* of all of the catalogues, which can be treated as the average value of the small scale velocity and the intrinsic dispersion. Using a single σ_* should not have a significant effect, in general, because the catalogues are of typical depth $> 40\ h^{-1}$Mpc or in better units > 4000 km/s, and the distance indicators have typically 20% error in the measurement which means that typically $\sigma_n > 800$ km/s. So whether σ_* is 400 km/s or 600 km/s is not of much consequence if $\sigma_n > \sigma_*$.

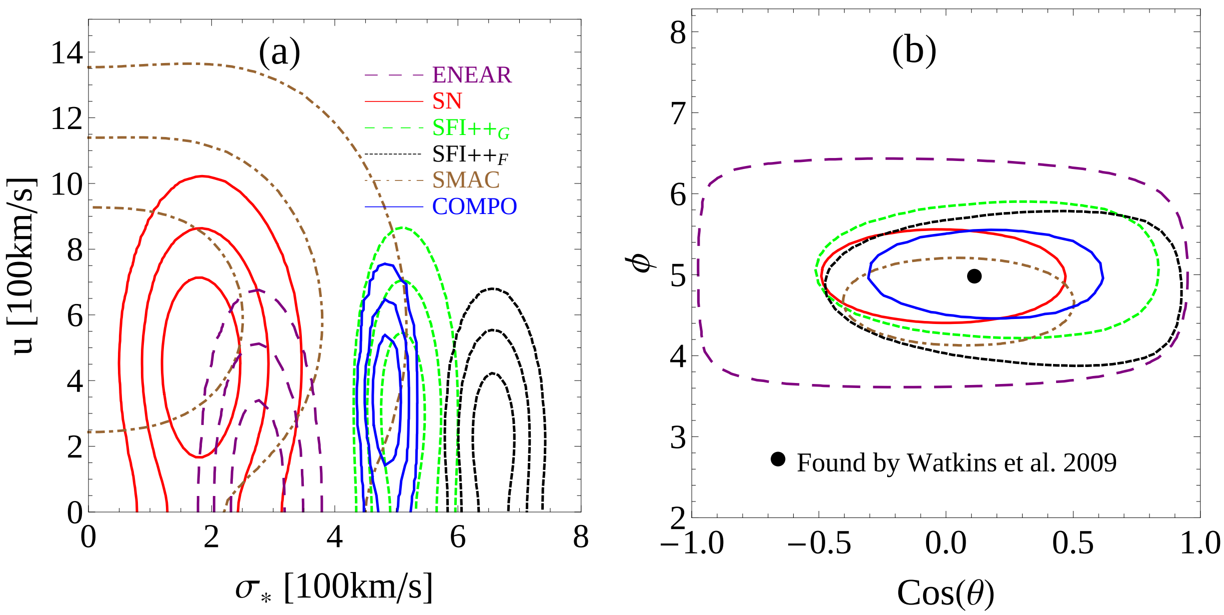

Figure 5.4: (a) The 68%, 95% and 99.7% Bayesian confidence interval contours for parameters σ_*-u. (b) The 68% contours for Cos(θ)-ϕ. The black dot is the direction of the bulk flow found by [244].

In panel (b) of Fig. 5.3, we show the marginalized 1-D distribution of the magnitude of the $\mathbf{u}$. Also, from Table 5.1 we can see that the SFI++ and ENEAR catalogues can provide fairly tight upper bounds on u, and ENEAR peaks at zero while the SFI++ catalogues contain zero velocity within 2σ. It should be noticed that the SN and the larger COMPOSITE catalogue can provide a nonzero 2σ lower bound on u, in which the latter provides the tightest constraints. In panels (c) and (d) of Fig. 5.3, we show the marginalized 1-D probability distribution of the direction of the relative velocity $(\cos(\theta), \phi)$. We see that the distribution of $\cos(\theta)$ and ϕ are very close to Gaussian, and the four catalogues predict a very similar direction of the velocity (Fig. 5.4 and Table 5.1). We should also notice that the various catalogues give consistent constraints on the tilted velocity.

In panel (a) of Fig. 5.4, we plot 2-D contours of σ_* and u, and we find that, in the posterior distribution, σ_* and u are not correlated. The reason is easy to understand: the "tilted Universe" velocity $\mathbf{u}$ describes superhorizon dipole modulation of CMB photons, whereas σ_* describes the subhorizon modes for small scale velocities and the intrinsic dispersion of each individual galaxy, so they come from completely different origins therefore without much correlation. Thus, even though there might be a possibility that the instrumental noise σ_n has been underestimated, the distribution of σ_* would be shifted to smaller values, but that will not change the constraints on u significantly. Thus, our constraint on u is pretty robust with respect to the estimate of small scale instrumental noise. In panel (b) of Fig. 5.4, we plot the 1σ contour of Cos(θ) and ϕ. We can see that the directions of tilted velocity found by different surveys are very consistent with each other, and also very consistent with the results from Watkins et al. [244].

5.4 Discussion

We should notice that, the direction of the large bulk flow velocity found by [244] is within the 1σ confidence level of the tilted velocity here, which therefore can provide a physical origin of the large bulk flow in [244]. In [245] they evaluated that the probability of getting a higher bulk flow within ΛCDM with WMAP7 parameter values to be less than 2%. In our analysis, the bulk flow of a galaxy survey should be accounted for in the error bars by the cosmic variance term (Eq. 5.2). So an alternative explanation might be that there is a feature in the matter power spectrum which would increase the cosmic variance. However, as the shear and octupole moments of the peculiar velocity field are not anomalously large, this is disfavored by the data [261].

In addition, the direction we find is consistent with that found in [262] which used the dipole of the kinetic Sunyaev-Zeldovich (kSZ) measurements to estimate the bulk flow on Gpc scales, but our magnitude is lower than what they found. However, there is an additional level of uncertainty in converting the kSZ dipole into a bulk flow which makes it difficult to estimate the magnitude of the bulk flow from the kSZ dipole [262]. In the bulk flow approach, Ref. [245] suggests that the bulk flow comes from scales $> 300\ h^{-1}$Mpc. If [262] proves correct it will be strong support for the tilt explanation since the tilted velocity should be the same regardless of the scale probed to measure it. A tilted Universe scenario was also proposed in [248] to explain the kSZ measurement.

An intrinsic dipole on the CMB sky caused by a tilted Universe may be explained by a preinflationary relic isocurvature inhomogeneity. If inflation lasts for only a few e-folds longer than required to solve the horizon problem, the scales that were superhorizon at the initial point of inflation are not very far outside our current horizon today. Inflation requires that there was initially a fairly smooth region of order of the inflationary Hubble horizon. A physical scale of such a region at the onset of inflation $l = e^p H_i^{-1}$ will have the physical scale $L = e^P H_0^{-1}$ today, where $P = p + N - N_{\rm min}$ ($N_{\rm min}$ is the minimal number of e-folds to solve the horizon problem and is generally assumed to be around 60) [246]. In the short inflationary case where N is not much larger than $N_{\rm min}$, a remnant of a preinflationary Universe still exists on superhorizon scales which may be detectable. The quadrupole effect, aka the Grishchuk-Zel'dovich effect [263], is also part of the effect of this large scale inhomogeneity.

An isocurvature perturbation can produce the "tilted Universe" effect, which arises in inflationary models due to the perturbations of quantum fields other than the inflaton, such as the axion, whose energy density is subdominant compared to that of the inflaton.

There are strong constraints on subhorizon isocurvature perturbations and thus if they are responsible for the tilt it would require them to be much larger on very large scales than they are on smaller scales. Although multifield models will not generically produce such a sharp breaking in scale invariance or result in isocurvature modes in the later Universe, there are double inflation

Catalogues	Characteristic Depth (h^{-1}Mpc)	σ_* [100km/s]	u [100km/s]	l (degrees)	b (degrees)	ΔN (2σ)
ENEAR	29	$2.8^{\pm}0.3$	$0^{+2.2}_{\times}$	$287.2^{+68.9}_{-68.3}$	$-3.8^{+37.5}_{-36.0}$	$\Delta N \geq 7$
SN	32	1.8 ± 0.4	$4.5^{+1.8}_{-1.9}$	$284.9^{+22.9}_{-22.1}$	$-1.0^{+18.8}_{-18.3}$	$6 \leq \Delta N \leq 9$
SFI++$_G$	34	$5.10^{+0.7}_{-0.3}$	$3.1^{+1.6}_{-1.9}$	289.7 ± 34.9	$10.3^{+26.8}_{-25.5}$	$\Delta N \geq 6$
SFI++$_F$	34	$6.6^{+0.3}_{-0.2}$	$2.3^{+1.2}_{-1.6}$	$276.8^{+40.1}_{-39.0}$	$15.8^{+28.4}_{-27.1}$	$\Delta N \geq 6$
SMAC	65	$0.0^{+1.7}_{\times}$	5.9 ± 2.4	$263.8^{+23.6}_{-18.5}$	$1.1^{+18.6}_{-16.0}$	$6 \leq \Delta N \leq 8$
COMPOSITE	33	$4.8^{+0.2}_{-0.1}$	3.4 ± 1.3	$285.1^{+23.9}_{-19.5}$	$9.1^{+18.5}_{-17.8}$	$6 \leq \Delta N \leq 8$

Table 5.1: The best-fit and 1σ confidence level for the velocity dispersion σ_*, the magnitude (u) and the direction (l, b) of the tilted velocity, and the 2σ constraints on the number of e-folds of inflation. The "$\times$" means that the value is less than zero.

models which can achieve this [247].

The dipole anisotropy is associated with the isocurvature fluctuation as follows [246; 247] [1]

$$\frac{u}{c} \simeq \frac{H_0^{-1}}{L}\frac{\delta\varphi}{\varphi_0}, \tag{5.5}$$

where $\delta\varphi$ is the fluctuation of the quantum field, and φ_0 is the background field. An inflationary scenario that results in isocurvature perturbations in the later Universe, such as in Ref. [247], is required. Assume that at the onset of inflation, the isocurvature quantum fluctuation satisfies $\delta\varphi/\varphi_0 \simeq 1$ [Constants of $\mathcal{O}(1)$ will not affect the results much], thus the Hubble horizon at the onset of the inflation is $p = 0$, $l = H_i^{-1}$, and $L = e^{\Delta N} H_0^{-1}$, where $\Delta N = N - N_{\rm min}$ is the excess number of inflationary e-folds beyond $N_{\rm min}$. The constraints on a "tilted Universe" lead to the constraints on the number of e-folds of inflation $u/c \simeq H_0^{-1}/L \simeq e^{-\Delta N}$. Therefore, an observable "tilted Universe" velocity requires that inflation should last a modest number of e-folds, which should not be too long nor too short— if inflation lasts too long, such perturbation effects would be washed out, if inflation is too short, the dipole effect will be too large, making the Universe over-tilted. We show the constraints on the number of e-folds in the last column of Table 5.1. We find that the required extra number of e-folds is at least 6 for all catalogues, and SN, SMAC and COMPOSITE can also provide a 2σ upper bound on ΔN given their data.

Note that our study provides a similar constraint to the Grishchuk-Zel'dovich effect (which can arise from either adiabatic or isocurvature perturbations) which requires that the extra number of e-folds should be greater than about 7 at the 95% confidence interval [264]. Also, correlations in the CMB multipoles may be used to estimate, from the Planck data, the tilt with an error bar similar to what we obtained here [265]. In the future, there is the potential to use the large number of SNe measured by the Large Synoptic Survey Telescope to constrain u with a standard deviation of about 30 km/s [266]. So it may be possible to explore the duration of inflation and the preinflationary quantum state at quite a precise level. The peculiar velocity field, is therefore a powerful tool to probe the very early-Universe in a manner not accessible by CMB observations alone.

5.5 Conclusion

In this Chapter, we developed a model and a statistical method to justify whether the apparent bulk flow motion of galaxies in our surveys is due to the subtraction of the intrinsic dipole on the CMB sky. In the conventional bulk flow scenario, the galaxies in the local region ($\lesssim 150\ h^{-1}$Mpc) are moving toward a direction ($l = 287^o \pm 9^o$, $b = 8^o \pm 6^o$) in which $v = 407 \pm 81$ km/s seems in tension with the ΛCDM predictions. However, we point out that some fraction of the CMB

[1] There may be some factors of order unity in this equation for different models, but they have negligibly small effect on the ΔN constraints due to the exponential. The same holds for $\delta\varphi/\varphi_0 \simeq 1$.

dipole can be intrinsic due to large scale inhomogeneities generated by preinflationary isocurvature fluctuations, so that in the CMB rest frame, all of the galaxies have streaming velocity towards the particular direction, resulting in the tilted Universe.

We modeled an intrinsic CMB dipole as a tilted velocity $\mathbf{u}$ and developed a statistical tool to constrain its magnitude and direction. We found that (1) the magnitude of the tilted velocity u is around 400 km/s, and its direction is close to what was found in previous bulk flow studies. For SN, SMAC and COMPOSITE catalogues, $u = 0$ is excluded at about the 2.5σ level, which can explain the apparent flow; (2) there is little correlation between the tilted velocity $\mathbf{u}$ and the galaxy's small scale velocity and intrinsic dispersion σ_*, which confirms our assumption.

Furthermore, assuming that primordial isocurvature modes lead to an intrinsic dipole anisotropy, constraints on the magnitude of the tilted velocity can result in constraints on the duration of inflation, due to the fact that inflation can neither be too long (no dipole effect) nor too short (very large dipole effect). Under this assumption, the constraints on the tilted velocity require that inflation lasts at least 6 e-folds longer (at the 95% confidence interval) than that required to solve the horizon problem.

Finally, we should point out that if there is an intrinsic fluctuation, the free electrons in clusters should be able to "see" the modulation on the sky, which can be tested through the kSZ effect. Therefore, the results from the South Pole telescope [158] and the Atacama cosmology telescope [267; 268] may shed some light on the intrinsic fluctuations. Such work is in progress.

Chapter 6

Cosmic Mach Number as A Sensitive Test of Growth of Structure

6.1 Introduction

The Cosmic Mach Number (hereafter CMN) can provide a robust measure of the shape and growth rate of the peculiar velocity power spectrum of the galaxies in the universe. One considers a region of a given size r in the universe, and compares the bulk motion of the sphere with the random velocities within that region. The bulk motion provides a measurement of the forces on the region from irregularities external to it, thereby measuring the amplitude of perturbations on scales much larger than the region. The random motions within the comoving region reflect gravitational perturbations on scales smaller than r. Thus their ratio, the CMN $M(r)$, depends only on the shape of the perturbation spectrum and not on its amplitude.

The concept was introduced by Ostriker and Suto in 1990 [270] as a cosmological metric that would be relatively independent of the "bias" of the test particles being observed and also relatively independent of the then quite uncertain perturbation amplitude. They concluded that although the existing data were poor, they gave estimates for the CMN that appeared to be inconsistent with the then popular CDM model with $\Omega_m = 1$ but seemed to prefer the open universe model instead. In a certain sense, the application of this test, correctly predicted the currently best validated cosmological models which have a value for Ω_m in the range $0.2 - 0.3$.

Subsequent to the original paper, Strauss et al (1993) [271] found again that the CDM models with $\Omega_m = 1$ remained inconsistent with the better data they used, but some non-standard models passed the test (see also [272]). Nagamine et al (2001) [273] looked at ΛCDM models and found better agreement, but the then ΛCDM model with $\Omega_m = 0.37$ again produced too high values of M over the range of $3 - 40$Mpc/h, whereas a model with $\Omega_m \sim 0.2$ (actually closer to WMAP 7-yr constraint [72]) was more consistent with the observations. In addition, there are various other papers discussing the issues around the CMN, such as non-linear clustering properties of dark matter on the CMN measurement [274], and constraint on the CMN from Sunyaev-Zeldovich effect [275].

This history leads us to re-examine the issue in light of the much better knowledge now available of both the new peculiar velocity data and the range of cosmological models remaining plausible given the current cosmological constraints. In this Chapter, we will develop a new statistical tool to measure the CMN from the peculiar velocity surveys, and investigate the power of the CMN to distinguish various cosmological models, especially in the aspects of differentiating the ΛCDM model from variance with non-trivial growth function provided by Modified Gravity (hereafter MG) models, and from models with massive neutrinos.

6.2 Statistics of Cosmic Mach Number

In linear perturbation theory, the power spectrum of the velocity divergence ($\theta \equiv \nabla \cdot \mathbf{v}$) is related to the power spectrum of density fluctuations via $P_{\theta\theta}(k,z) = f^2(k,z)P(k,z)$, where $f(k,z) \equiv -d\ln\delta/d\ln(1+z)$, and δ is the density perturbation of matter. Since the data in our application are at very low-redshift, we assume that they have the same redshift $z=0$ throughout and drop the z dependence for brevity [1]. The mean square velocity dispersion $\langle\sigma^2(r)\rangle$ and mean square bulk flow $\langle V^2(r)\rangle$ in a window of size r can be calculated as [270; 273; 277]

$$\begin{aligned}
\left\langle V^2(r)\right\rangle &= \frac{H_0^2}{2\pi^2}\int_0^\infty dk P_{\theta\theta}(k)W(kr), \\
\left\langle \sigma^2(r)\right\rangle &= \frac{H_0^2}{2\pi^2}\int_0^\infty dk P_{\theta\theta}(k)\left[1-W(kr)\right],
\end{aligned}$$

where $W(x)$ is a top-hat window function $W(x) = [3(\sin x - x\cos x)/x^3]^2$. Note that $W(x) \sim 1 (x \lesssim 1)$ and W drops to 0 quickly when $x > 1$. Thus W effectively changes the integral limits of the above formula,

$$\begin{aligned}
\left\langle V^2(r)\right\rangle &\simeq \frac{H_0^2}{2\pi^2}\int_0^{1/r} dk P_{\theta\theta}(k), \\
\left\langle \sigma^2(r)\right\rangle &\simeq \frac{H_0^2}{2\pi^2}\int_{1/r}^\infty dk P_{\theta\theta}(k),
\end{aligned} \tag{6.1}$$

The CMN on different scales of the patches is defined as

$$M(r) \equiv \left(\frac{\langle V^2(r)\rangle}{\langle\sigma^2(r)\rangle}\right)^{\frac{1}{2}}. \tag{6.2}$$

Thus it basically measures the shape of $P_{\theta\theta}$ by contrasting $\int dk P_{\theta\theta}(k)$ on large, and small scales.

[1] If the CMN technique is used on structure formation at high redshift, one needs to consider the contribution from the relative velocity between baryons and dark matter [276].

It is important to notice that this derivation assumes that one studies many patches of size r and separately observes $\langle V^2(r)\rangle$ and $\langle \sigma^2(r)\rangle$. In fact our observational data is restricted to our neighborhood galaxies so one can only use $V(r_0)$, i.e. our local bulk motion. Therefore, one needs to take into account the cosmic variance when comparing our local CMN with the global definition (6.2).

For a particular catalogue with N objects, the CMN M can be written as $M = |\mathbf{u}|/\sigma_*$, where $\mathbf{u}$ denotes the bulk flow velocity, which is a streaming motion of galaxies towards some particular direction, and σ_* stands for the small scale velocity dispersion. Unfortunately, neither $\mathbf{u}$ nor σ_* is a direct observable. For each galaxy peculiar velocity catalogue, what we observe is the line of sight velocity S_n with measurement error σ_n for the nth galaxy. Then one can construct a joint likelihood function for $\mathbf{u}$ and M by contrasting S_n with the line-of-sight projection of the bulk flow $\hat{r}_{n,i}u_i$. The uncertainty in $(S_n - \hat{r}_{n,i}u_i)$ is simply $(\sigma_n^2 + \sigma_*^2)^{\frac{1}{2}}$, where $\sigma_* = |\mathbf{u}|/M$ is given by the definition of the CMN. Therefore, the likelihood function takes the form of,

$$L(\mathbf{u},M) = \prod_{n=1}^{N} \frac{1}{[\sigma_n^2 + (|\mathbf{u}|/M)^2]^{\frac{1}{2}}} \exp\left(-\frac{(S_n - \hat{r}_{n,i}u_i)^2}{2(\sigma_n^2 + (|\mathbf{u}|/M)^2)}\right). \tag{6.3}$$

One can then marginalise over the 3D bulk flow vector $\mathbf{u}$ to obtain the distribution of M for each survey.

We use five different catalogues of galaxy peculiar velocity surveys, namely, SBF [257], ENEAR [253], Type Ia Supernovae (SN) [254], SC [259], and SFI++$_F$ [255], to constrain the CMN by using Eq. (6.3) [1]. We marginalise over the 'bulk flow' velocity $\mathbf{u}$ in the 4-D parameter space and obtain the 1-D posterior distribution of M as shown in panel (a) of Fig. 6.1. In the panel (a), one can see that the distribution of the CMN is very Gaussian, and the width depends primarily on the number of data entries in each catalogue. In addition, since each catalogue probes the CMN on various depths, different catalogues form a complimentary set of tests of cosmic structures.

In panel (b) of Fig. 6.1, we put together the old (1990) and current CMN data with various predictions computed from theoretic models: The [Blue] triangle data points are the current CMN values computed from likelihood (6.3) by using the five-catalogues. The [Red] square data are the ones used by Ostriker and Suto [270] in 1990, whose depths have been emulated by the current data.

The ΛCDM model with WMAP 7-yr best-fit parameters ($\Omega = 0.271$, $h = 0.704$, $n_s = 0.967$, $\Omega_b = 0.0455$, black solid line) is mildly consistent with the current CMN data at 3σ CL. In comparison, we overplot the theoretical $M(r)$ ([Green] dashed line) by using 1990's 'popular' CDM parameters. One can immediately understand the reason why Refs. [270; 271] claimed that there was a strong conflict between the data ([red] points) and popular CDM model ([Green]

[1] These catalogues are described in each individual paper in detail, also see [244]. To calculate the characteristic depth of each catalogue, we use error-weighted depth as $\overline{r} = \sum_n w_n r_n / \sum_n w_n$, where $w_n = 1/(\sigma_n^2 + \sigma_*^2)$.

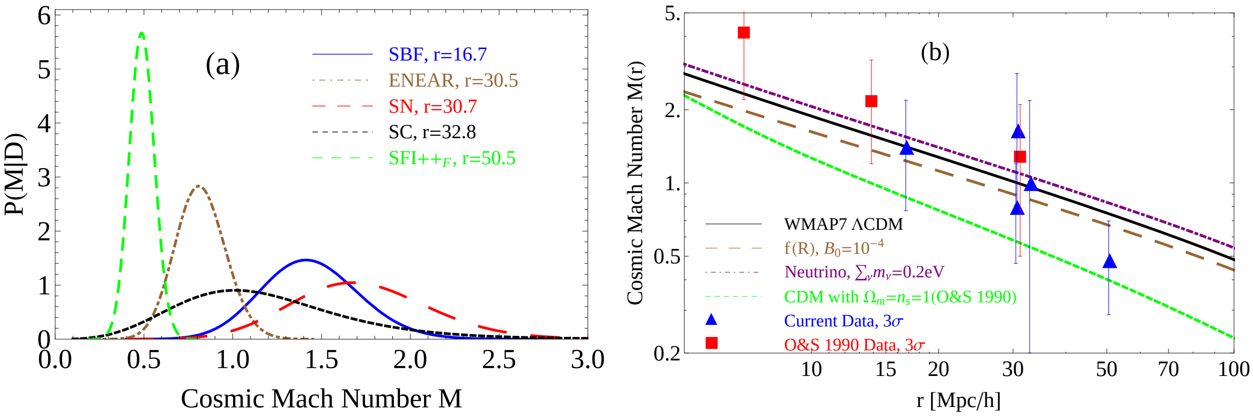

Figure 6.1: (a): The 1-D posterior distribution of the CMN $M(r)$ from 5 different catalogues. The unit of r is [Mpc/h]. (b): The comparison between the CMN data (3σ CL.) and theoretic prediction: blue data points are the CMN data from posterior distributions shown in panel (a); red data points are the data used in Ostriker and Suto 1990 [270]; the black line is the CMN prediction from WAMP 7-yr best-fit values [72]; the green dashed line is calculated by using 'popular' CDM cosmological parameters $n_s = \Omega_m = 1$ and $h = 0.5$ in 1990s [270]; the brown dashed and purple dot-dashed lines are the CMN from $f(R)$ model with $B_0 = 10^{-4}$ and from ΛCDM model with neutrino mass $\sum_\nu m_\nu = 0.2$eV.

dashed line). There was in fact no inconsistency between data and a model with $\Omega \approx 0.25$ and $n_s = 1$. However, with the up-to-date data and strongly constrained ΛCDM cosmology, one can see that the CMN data is consistent with the CMN prediction out to scale around 50Mpc/h. In addition, we plot the CMN for $f(R)$ theory with $B_0 = 10^{-4}$ as brown dashed line, and the ΛCDM model with massive neutrino $\sum_\nu m_\nu = 0.2$eV as purple dot-dashed line. These variations of growth factor exhibit some substantial difference from the standard ΛCDM model. We should notice that due to the large uncertainty of small scale non-linear velocity, we plot linear $P_{\theta\theta}$ on scales $k \gtrsim 1$h/Mpc in panel (b), but in reality, the nonlinear growth of structures on these scales may suppress the CMN values over $r \lesssim 15$Mpc/h.

To investigate the prospective accuracy of the CMN achievable in future surveys, we perform a forecast for the on-going 6dF peculiar velocity survey [278]. The redshift distribution of galaxies for the 6dF survey is $n_g(z) = Az^\gamma e^{-(z/z_p)^\gamma}$, where $z_p \simeq 0.0446$, $\gamma \simeq 1.6154$ and $A \simeq 622978$ [278]. It peaks around $z \approx 0.05$ and extends till $z \approx 0.15$. We make an optimistic assumption that the sub-catalogue of peculiar velocity field [1], which comprises about 12000 brightest early-type galaxies, are located at $z \lesssim 0.05$, corresponding to the depth $r \lesssim 150$Mpc/h. We further assume that the measurement error for line-of-sight velocity is around 20%, which is a typical error for the fundamental plane distance measurement. We divide these data into different redshift bins, and in each shell $(r, r + dr)$, we calculate the Fisher Matrix value for the CMN F_{MM} from Eq.(6.3)

[1]Although the total number of 6dF galaxies is 125071, the sub-catalogue galaxies with peculiar velocities comprises 10% of the whole sample [278].

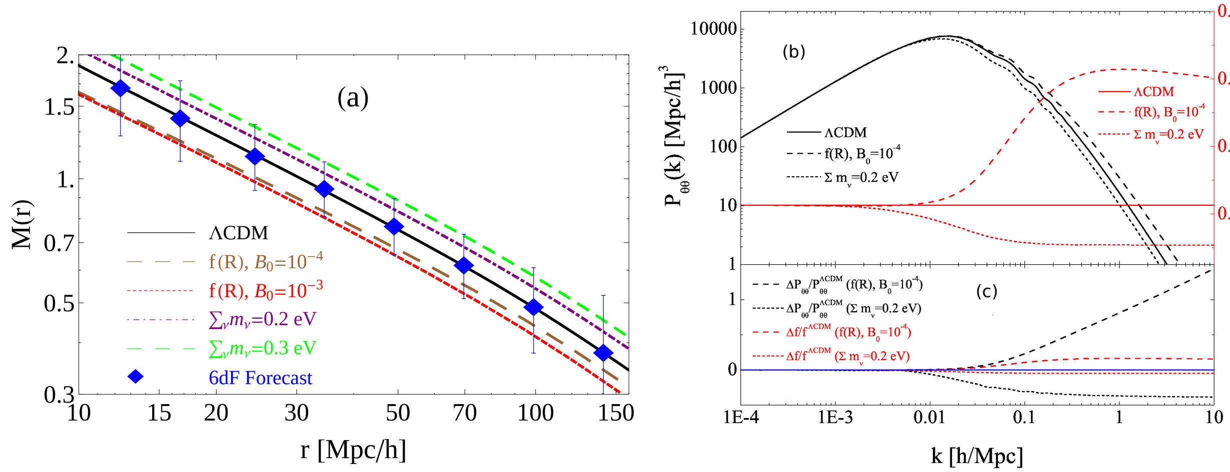

Figure 6.2: (a): Forecast 1σ errors of the CMN from 6dF survey, in which we assume the data is around our local region of the universe. Beside ΛCDM model, we plot $B_0 = 10^{-4}$ ([Brown] dashed line) and 10^{-3} ([Red] dashed line) for the $f(R)$ model, and $\sum_\nu m_\nu = 0.2$eV ([Purple] dot-dashed line) and 0.3eV ([Green] dashed line). (b): $P_{\theta\theta}$ [Black], and $f(k,a)$ [Red] in ΛCDM (real line), $f(R)$ (dashed line) and massive neutrino (dot-dashed line) models. (c): fractional difference between the $f(R)$ and massive neutrino models with ΛCDM.

which leads to the forecasted error of the CMN as

$$\sigma_{M(r)} \simeq \frac{M(r)}{\sqrt{2N(r)}}\left[1+\frac{\sigma_n^2}{(u(r)/M(r))^2}\right], \tag{6.4}$$

where $N(r)$ is the number of data points in the shell (r,$r+dr$), and $u(r)$ is the average bulk flow magnitude on depth r. We plot these forecast data in the panel (a) of Fig. 6.2. Comparing with panel (b) of Fig. 6.1, we find the full range of the CMN data on scales [10,150] (Mpc/h) from 6dF can improve the constraint on the variation of the scale-dependent growth factor significantly. We summarize the experimental conditions for future experiment that can sharpen the CMN test: (1) there should be considerably more galaxy samples ($\gtrsim 10^4$) on scales $[10, 150]$Mpc/h; (2) the smaller the measurement error σ_n is, and more homogeneous sky it can cover, the better it can reduce the overall error of M. One should also notice that, when the CMN data is used to constrain cosmology, the cosmic variance should be taken into account, since the bulk flow in our local patch is greater than expected from ΛCDM model [244], i.e. as notes earlier, there can be significant variance between a specific measurement of bulk flow $V^2(r_0)$ and its global average $\langle V^2(r)\rangle$.

6.3 A sensitive test of growth of structure

Since the CMN measures the shape of the peculiar velocity power spectrum $P_{\theta\theta}$ by design, it is sensitive to any distortion of $P_{\theta\theta}$. In the ΛCDM model, the growth is scale-independent. However, in the modified gravity models, and models with massive neutrinos, the growth is generically scale-dependent, thus $P_{\theta\theta}$ for these models is a distorted version of that for the ΛCDM model, making the CMN an ideal tool to distinguish these models from ΛCDM. Let us consider the $f(R)$ model and ΛCDM model with massive neutrinos as examples.

In a viable $f(R)$ model, where the Einstein-Hilbert action is extended to be a general function of the Ricci scalar R, the effective value of Newton's constant $G_{\rm eff}$ has both time and scale dependence, namely, $G_{\rm eff} = \mu(a,k)G$, where $\mu(a,k) = (1+\frac{4}{3}\lambda^2k^2a^4)/(1+\lambda^2k^2a^4)$, and G is the Newton's constant in general relativity (GR) [279; 280]. The only free parameter is λ^2, which quantifies the Compton wavelength of the scalar field $f_R \equiv df/dR$ and characterises the scale-dependence of the growth. It is more convenient to use a redefination of λ^2, which is $B_0 = 2H_0^2\lambda^2/c^2$, and $B_0 = 0$ for GR [280]. The current constraint on B_0 is $B_0 < 0.4$ (95% CL.) using the combined data of CMB, Integrated Sach-Wolfe (ISW) effect and Type Ia Supernovae [280].

In panels (b) and (c) of Fig. 6.2, we show $P_{\theta\theta}$ and f for a $f(R)$ models with $B_0 = 10^{-4}$ (dashed lines), in comparison with that of ΛCDM model (solid lines). As we see, the growth is enhanced at $k \gtrsim 0.01$ h/Mpc, which can be seen by the CMN. In panel (a), we compare the CMN ($f(R)$) to the CMN (ΛCDM), with the forecasted 6dF data points overplotted. As discussed before, for a survey with depth $r \in [10, 150]$ Mpc/h, the growth on scales $k \sim 1/r \in [0.01, 0.1]$ h/Mpc can be efficiently probed by the CMN. Also note that the CMN is determined by the integral of $P_{\theta\theta}$ (see Eq. (6.1)), thus even a small distortion in $P_{\theta\theta}$ can leave an amplified imprints on the CMN. This is why a 0.01% change in B_0 from $B_0 = 0$ can produce a 20% suppression in the CMN, which is potentially observable by 6dF.

Similarly, the CMN is sensitive to the neutrino mass. When neutrinos became non-relativistic and the Universe was deeply in the matter dominated era, neutrino thermal velocities damped out the perturbation under the characteristic scale $k_{\rm nr} \simeq 0.018\Omega_m^{1/2}(\sum_\nu m_\nu/1{\rm eV})$h/Mpc, suppressing the power spectrum on small scales. On scales greater than $k_{\rm nr}$, neutrinos affect the overall expansion of the Universe and therefore shift the peak of power spectrum to larger scales. We normalize power spectrum on very large scale from WMAP 7-yr result [72] and plot the $P_{\theta\theta}(k)$ and $f(k,a)$ in panels (b) and (c) of Fig. 6.2. We can see that a neutrino mass of 0.2eV can suppress the power spectrum on scales of $k \gtrsim 0.01$h/Mpc quite significantly, which exactly falls in the detection window of the CMN. Therefore, the cumulative 'integral' effect of the CMN can manifest the neutrino free-streaming effect by enhancing its value on all scales. Comparing with panel (b) of Fig. 6.1 and panel (a) of Fig. 6.2, we find that future CMN data is potentially able to distinguish the nonzero neutrino mass. It is true that the parameter degeneracy, such as among $B_0, \sum_\nu m_\nu, n_s, \Omega_m$ might dilute the constraints, but the degeneracy can be easily broken with the aid of other data. For example, we find that to mimic the same effect on CMN produced by $B_0 = 10^{-4}$, the spectral index n_s has to be changed by 10% from its best fit value of WMAP7[72] , which is not allowed by CMB data at 5σ level.

6.4 Conclusion

In this Chapter, we provide a statistical tool to measure the CMN, and further demonstrate that it is a sensitive probe of the structure growth. By design, the CMN is immune to the uncertainty in the overall amplitude of the density perturbation, and to linear galaxy bias. Also it is highly sensitive to any scale-dependent distortion of $P_{\theta\theta}$ since any small distortion can be amplified via the integral effect. Therefore it is an excellent tool to test alternative theories of gravity, and models with a neutrino mass.

We first perform a likelihood analysis of the CMN from the current peculiar velocity field data, and further confront the ΛCDM model with WMAP 7-yr parameters and popular CDM model with parameters in 1990 with the current data and old data from [270]. We confirm that the ΛCDM model prediction is consistent with current CMN data at 3σ CL. level. Based on our forecast for 6dF, we find that the CMN can improve the constraints on the modified gravity parameter B_0 by orders of magnitude, and it can also tighten the present constraints on the neutrino mass.

Chapter 7

Conclusions and Outlook

Over the last several decades, cosmology has been transformed into precision science. The standard hot Big-Bang scenario, which was originally supported by three fundamental observations (Hubble expansion, abundance of light elements, and CMB radiation), has been tested and confirmed by a wealth of new precise observations, such as the cosmic microwave background anisotropies, Type-Ia supernovae, and the large scale clustering of galaxies. The observational data provide strong support for a Universe which is spatially flat and accelerating at the present day, consisting of approximately 73% dark energy, 23% percent cold dark matter, and 4% baryons, which leads to the concordance model ΛCDM.

Testing this concordance model and exploring unknown physics beyond this model (for example, the nature of dark energy) have become important tasks for cosmologists. This thesis has addressed four important questions in order to test ΛCDM model from different perspectives.

- The inflation paradigm predicts a nearly scale-invariant and statistically isotropic primordial power spectrum. Do the current WMAP data favour statistical isotropy, and to what extent will the more accurate data from the Planck satellite improve on WMAP?

- Simple inflationary models, such as single-field slow-roll $V \sim \phi^2$ inflation, predict a nearly scale-invariant tensor power spectrum with a tensor-to-scalar ratio of about 0.01. How well, will the Planck satellite, as well as sub-orbital and ground-based experiment (such as SPIDER, PolarBear and QUIET) be able to constrain this signal? In addition, what is the detection limit for these experiments?

- Measurements of the peculiar velocities of various samples of galaxies suggest a very large bulk flow on scales of 50 Mpc/h or more. It has been claimed that these observations are in conflict with the prediction of the concordance ΛCDM model. If true, what are the physical implications of the bulk flows?

- The peculiar velocity field is an important prediction from the linear perturbation theory. How can we use current galaxy peculiar velocity data to test the growth of structure on different scales, and to constrain alternative theories of gravity and neutrino masses?

We have tackled the above questions in Chapters 2 to 6. The results of this thesis suggest the following directions for future research.

Although we have studied large angular correlations in the WMAP data in some detail, several authors have cast doubt on the accuracy of the low-multipoles measured by WMAP [281; 282; 283]. Refs. [281; 282; 283] argue that quadrupole is not cosmological, but due to a small error in the dipole direction and antenna pointing direction in the WMAP scanning scheme. If their concerns were to be confirmed, it could clearly be very difficult to accommodate a vanishing quadrupole within the statistically-isotropic ΛCDM scenario.

Fortunately, we live at a time when results from complimentary experiments will soon be available. The Planck satellite was launched by the European Space Agency in the 14$^{\text{th}}$ May, 2009, and the collaboration team will release the first full-sky CMB map in January 2013. Since Planck has 9 frequency bands, extending over a wide frequency range than WMAP's 5 bands, it provides much more information on Galactic foregrounds. One should therefore be able to reconstruct the CMB reliably to lower Galactic latitude, therefore obtain a more stable reconstruction of the all sky CMB.

So far, people have been searching for the statistical anisotropic power spectrum in the WMAP temperature maps [173]. The WMAP polarization maps cannot be used to test departures from statistical isotropy because they have very large noise and beam asymmetries. As Planck will release high precision polarization maps, a direct extension of the work from Chapter 3 would be to investigate the anisotropic power spectrum in the polarization map, and provide complimentary checks of the temperature analysis, particularly if the temperature data suggest a nonzero result.

Distinguishing between different scenarios of the early Universe requires new experiments that can give more powerful constraints on the primordial fluctuations. The Square Kilometer Array [284] is such an example. This is a radio telescope array with an effective collecting area more than 30 times greater than the largest array ever built. The HI redshift survey of SKA will lead to significant improvements in the galaxy power spectrum at large scales over current observations. A precise determination of the power spectrum on large scales may, for example, reveal sharp features in the primordial power spectrum that are not possible to detect in CMB experiments. Since different models of the early Universe may produce imprints on the cosmic structure at large scales (e.g. models in light of trans-Planckian physics [285], thermal initial states [286; 287], as well as particle production [288]), the SKA has the potential to discriminate between them. By applying the Fisher matrix technique as used in Chapter 4, one can forecast the possible constraints on these early Universe models from SKA.

As an extension of our analysis of large scale bulk flows, one needs to carefully test the consistency of bulk flows with ΛCDM model. One of the major concerns with the analysis described in [244; 245] is that different catalogues with very different depths and observational errors are directly combined to obtain the posterior distribution of cosmological parameters. This approach would be sensitive to systematics in the data, because each of the catalogues may prefer very dif-

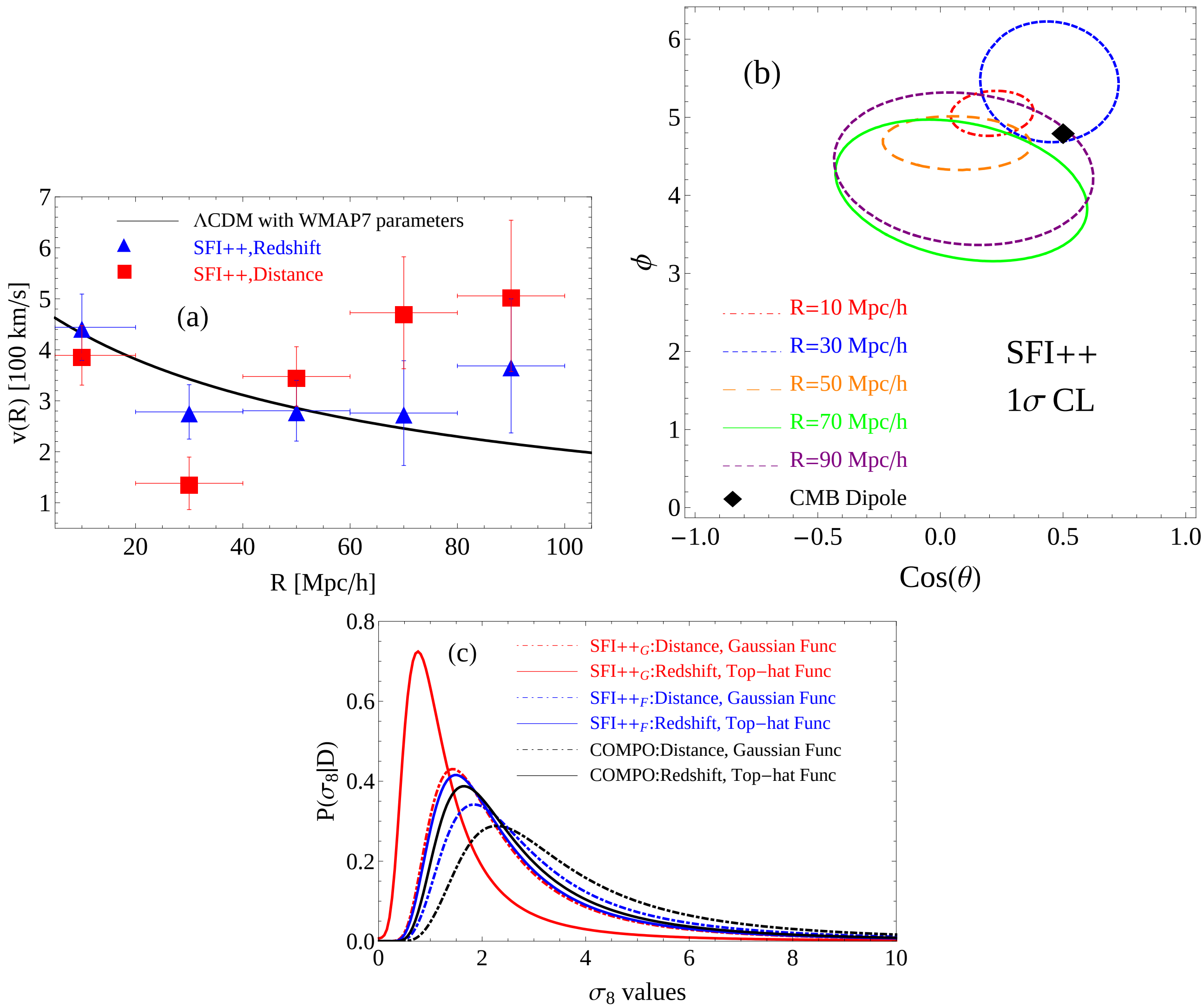

Figure 7.1: Demonstration of potential effects associated with Malmquist bias. Panel (a): bulk flow magnitude as a function of depth R. By placing the galaxies at their redshifts ([Blue] triangle points) rather than distance ([Red] square points), the bulk flow magnitude is consistent with ΛCDM prediction. However, if we place the galaxies at their TF distances, we find large flows on scales $\gtrsim$ 50Mpc/h. Panel (b): If we place the galaxies at their redshifts, the directions of the observed bulk flow at different depths is consistent with CMB dipole direction. Panel (c): Parameter estimation of σ_8 by using the COMPOSITE catalogue, SFI++ group galaxies (SFI++$_{\rm G}$), and SFI++ field galaxies (SFI++$_{\rm F}$) (see description of the catalogues in [244] for details). By using COMPOSITE catalogue, placing the galaxies at TF distance, and generating mock catalogues from Gaussian window function, Ref.[244] obtains the distribution ([Black] dashed line) which excludes WMAP 5-yr best-fit $\sigma_8 = 0.796$ at 3σ CL. However, by using the redshift as the true distances and adopting a top-hat window function, one finds a consistency with ΛCDM ([Black] solid line). Here we fix the cosmological parameters to be WMAP 5-yr results ($\Omega_m = 0.258$, $h = 0.719$, $n_s = 0.963$, $\Omega_b = 0.0441$) in order to compare with the results in [244].

ferent parameters. In addition, since Malmquist bias can also be a problem for peculiar velocity surveys, it is important to model the Malmquist bias and to ensure that the distance estimations are accurate. Figure 7.1 shows some preliminary results of an investigation of these effects.

In Fig. 7.1, we show the potential problem of Malmquist bias in the Tully-Fisher (TF) distance of SFI++ catalogues. In panel (a), we separate the SFI++ catalogue (see descriptions of the catalogue in Sec.5.3 in Chapter 5) into different radial distance bins, and calculate the bulk flow magnitude in each of them. If we place the galaxies at their TF distances, there are clearly large flows on scales of $\gtrsim$ 50Mpc/h. However, if we place the galaxies at their redshifts, the magnitude of the flows are consistent with ΛCDM predictions on different scales. This indicates that the potential problem of the inhomogeneous Malmquist bias gives spurious flows. In panel (b) of Fig. 7.1, we show that if we place the galaxies at their redshifts, the direction of the bulk flows on different depths are consistent with the CMB dipole direction.

Besides the potential problem of Malmquist bias, there is another potential issue around the analysis in [244]. In order to weight the data sets and calculate the bulk flow velocity, Ref. [244] uses a 'Minimum Variance' method. This method is to calculate the weight function of the data catalogues by minimizing the variance between it and ideal surveys of different depths. Therefore, Ref. [244] needs to first simulate ideal surveys at different depths. The galaxy redshift distribution of an ideal survey in [244] is assumed to be Gaussian and isotropic $n(r) \propto \exp(-r^2/2R^2)$. However, this would make the bulk flow at 50Mpc/h 'contaminated' by galaxies at much larger radii (perhaps $\gtrsim$ 100Mpc/h), for which the observational errors may be significant and observational errors themselves may be underestimated. As an alternative, one could instead use top-hat window function, i.e. calculate the bulk flow within some radius r as

$$\mathbf{B}(\mathbf{r}) = \frac{3}{4\pi r^3}\int_{x<r} \mathbf{v}(\mathbf{x}) d^3x. \tag{7.1}$$

In panel (c), we show the comparison between the TF distance+ Gaussian window function (used in [244]) and our corrections for redshifts+ top-hat window function. In this panel, the [Black] dashed line is the COMPOSITE catalogue if using the convention of [244], which excludes the WMAP 5-yr best-fit value $\sigma_8 = 0.796$ at 3σ confidence level. After correcting for both the top-hat window function, and the galaxy redshifts, one can see that the distribution of σ_8 from COMPOSITE catalogue is shifted to lower value of σ_8 ([Black] solid line) which is consistent with WMAP 5-yr best-fit value. Other catalogues also have similar situations, such as SFI++$_{\rm F}$ and SFI++$_{\rm G}$, whose likelihoods, after the corrections, are all consistent with WMAP 5-yr σ_8.

In Chapter 4, we have developed the hyper-parameter technique to combine different catalogues with different systematics. This technique should be applied to the combination of peculiar velocity catalogues. This project is now in progress.

In addition to the above analysis, it is also important to test whether the peculiar velocity field is consistent with density field. The density field at different depths can be reconstructed from infrared surveys, such as IRAS/PSCz [289] and future surveys based on WISE [290]. Once the density field is reconstructed, one can apply linear perturbation theory to predict velocity field. Therefore, one can compare the reconstructed velocity field from linear perturbation theory, with the smoothed velocity field from SFI++ survey. This would give a direct test of whether the observed peculiar velocity data is consistent with the linear perturbation theory with the hyper-parameter analysis described above [291].

In the near future, we would like to use the 6dF data [1] to study the Cosmic Mach Number on different scales. By applying this technique, with the combination of CMB and Type-Ia Supernovae data, it may be possible to improve on the results of Chapter 6.

[1] The analysis of 6dF is on-going in the collaboration team, and the peculiar velocity catalogue for the brightest ~ 12000 galaxies will be released soon.

Appendix A

Instrumental Characteristics of CMB Experiments

To calculate the total noise power spectrum N_l^{BB} (Section 4.2.3.2), we require the experimental specifications of each experiment, including the levels of both residual foreground noise and instrumental noise. We list the instrumental noise for each frequency channel the experiments we have considered in Table A.1-A.5. The effective noise power spectrum N_l^{BB} is given by the optimal combination of the channels [201]

$$[N_l^{BB}]^{-2} = \sum_{i \geq j} \left[(N_{\mathrm{fg},l}^{BB}(i) + N_{\mathrm{ins},l}^{BB}(i))(N_{\mathrm{fg},l}^{BB}(j) + N_{\mathrm{ins},l}^{BB}(j)) \frac{1}{2}(1 + \delta_{ij}) \right]^{-1}, \tag{A.1}$$

where $N_{\mathrm{ins},l}^{BB}(i)$ and $N_{\mathrm{fg},l}^{BB}(i)$ are the instrumental and residual foreground noise power spectra, respectively. Note that the noise power spectra $N_{\mathrm{ins},l}^{BB}(i)$ listed in the tables do not include the window function of the instrumental beam $\exp[l(l+1)\theta_F^2/(8\ln 2)]$.

To model polarized foregrounds, we focus on diffuse synchrotron (S) and dust (D) emission. The foreground contamination can be quantified by the parameter σ^{fg} which multiplies the power spectra $C_{S,l}^{BB}(i)$, $C_{D,l}^{BB}(i)$ of the foreground models. The smaller the value of σ^{fg} the deeper the

Band center [GHz]	30	44	70	100	143	217	353
FWHM [arcmin]	33	24	14	10.0	7.1	5.0	5.0
$N_{\mathrm{ins},l}^{BB}(i)$ $[10^{-6}\mu\mathrm{K}^2]$	2683	2753	2764	504	279	754	6975
f_{sky}	0.65						

Table A.1: Instrumental parameters for the Planck satellite (space-based experiment) [27]. Here we have assumed 4 sky surveys (28 months).

Band center [GHz]	90	150	220
FWHM [arcmin]	6.7	4.0	2.7
$N^{BB}_{\mathrm{ins},l}(i)$ $[10^{-6}\mu\mathrm{K}^2]$	5.2	4.3	44.0
f_{sky}	0.024		

Table A.2: Instrumental parameters for the ground-based PolarBear experiment [30].

Band center [GHz]	40	90
FWHM [arcmin]	23	10
$N^{BB}_{\mathrm{ins},l}(i)$ $[10^{-6}\mu\mathrm{K}^2]$	0.26	0.64
f_{sky}	0.04	

Table A.3: Instrumental parameters for the ground-based QUIET experiment [31]. Here we have assumed the phase-2 experiment.

Band center [GHz]	100	145	225	275
FWHM [arcmin]	58	40	26	21
$N^{BB}_{\mathrm{ins},l}(i)$ $[10^{-6}\mu\mathrm{K}^2]$	84.4	47.4	395	1170
f_{sky}	0.5			

Table A.4: Instrumental parameters for the balloon-borne Spider experiment [33]. Here we have assumed a 30-day LDB flight.

Band center [GHz]	30	45	70	100	150	220	340
FWHM [arcmin]	26	17	11	8	5	3.5	2.3
$N^{BB}_{\mathrm{ins},l}(i)$ $[10^{-6}\mu\mathrm{K}^2]$	31.21	5.79	1.48	0.89	0.83	1.95	39.46
f_{sky}	0.8						

Table A.5: Instrumental parameters for the mid-cost (EPIC-2m) CMBPol satellite mission [201].

Parameter	Synchrotron	Dust
$A_{S,D}$	4.7×10^{-5} $\mu\mathrm{K}^2$	1.2×10^{-4} $\mu\mathrm{K}^2$
ν_0	30 GHz	94 GHz
l_0	350	900
α	-3	2.2
β^{BB}	-2.6	-1.4

Table A.6: Assumptions for foregrounds parameters [201] foreground cleaning. Throughout this paper, we adopt $\sigma^{\mathrm{fg}} = 0.1$. The residual foreground noise is given by (see [201] for instance)

$$N^{BB}_{\mathrm{fg},l}(i) = \sum_{f=S,D} \left[C^{BB}_{f,l}(i)\sigma^{\mathrm{fg}} + \mathcal{N}^{BB}_{f,l}(i) \right] , \tag{A.2}$$

where $\mathcal{N}^{BB}_{f,l}(i)$ is the noise power spectrum arising from the cleaning procedure itself in the presence of instrumental noise.

Following [201; 237; 238], we model the scale (l) and frequency (ν_i) dependence of the synchrotron and dust emission as

$$C^{BB}_{S,l}(i) = A_S \left(\frac{\nu_i}{\nu_0}\right)^{2\alpha_S} \left(\frac{l}{l_0}\right)^{\beta_S} \tag{A.3}$$

and

$$C^{BB}_{D,l}(i) = p^2 A_D \left(\frac{\nu_i}{\nu_0}\right)^{2\alpha_D} \left(\frac{l}{l_0}\right)^{\beta^{BB}_D} \left[\frac{e^{h\nu_0/kT} - 1}{e^{h\nu_i/kT} - 1}\right]^2 . \tag{A.4}$$

In Eq. (A.4), p is the dust polarization fraction, estimated to be 5% [237], and T is the temperature of the dust grains, assumed to be constant across the sky with $T = 18\mathrm{K}$ [237]. Other parameters in Eqs. (A.3), (A.4) are specified in Table A.6 taken from [201].

The noise term $\mathcal{N}^{BB}_{f,l}(i)$ ($f = S, D$) entering Eq. (A.2) is calculated in [201; 237]

$$\mathcal{N}^{BB}_{f,l}(i) = \frac{N^{BB}_{\mathrm{ins},l}(i)}{n_{\mathrm{chan}}(n_{\mathrm{chan}} - 1)/4} \left(\frac{\nu_i}{\nu_{\mathrm{ref}}}\right)^{2\alpha} . \tag{A.5}$$

Here, n_{chan} is the total number of frequency channels used in making the foreground template map, and ν_{ref} is the frequency of the reference channel. In the case of dust, ν_{ref} is the highest frequency channel included in the template making, while in the case of synchrotron, ν_{ref} is the lowest frequency channel. The value of α is given in Table A.6 for different foreground models. We note that the ground-based experiments are insensitive to the largest angular scales, so when calculating the Fisher matrix using Eq. (4.13), we sum over the l from 21 to 3000. In addition, for ground-based experiments, the small scale fluctuations are not very sensitive to the residual foreground noise, and we can also pick out relatively clean patchs of sky where the foreground contamination is minimal. Therefore, to forecast the results for PolarBear and QUIET, we have not included a residual foreground noise term.

In addition to instrumental and residual foreground noise, gravitational lensing converts E-mode polarization into B-modes on small angular scales, contaminating the primordial B-mode signal [239; 240; 241; 242]. The lensed $C^{BB}_l(\mathrm{lens})$ will also contribute to the total noise power spectrum N_l^{BB}. The total noise power spectrum therefore becomes

$$N_{l,tot}^{BB} \equiv N_l^{BB} + C_l^{BB}(\text{lens}). \tag{A.6}$$

For the ideal case, we assume that there is no instrumental or foreground noise, and that we can successfully de-lens the CMB observations to a level of about 1/40 of the lensing signal [202]. In this case, the total effective noise power spectrum is

$$N_{l,tot}^{BB} = 1/40 \times C_l^{BB}(\text{lens}). \tag{A.7}$$

Finally, we adopt $f_{\text{sky}} = 0.8$ for the ideal experiment, which is the same as that used to model CMBPol.

Appendix B

Statistics of the conventional χ^2 and the hyper-parameter χ^2

In this appendix, we first review the basic results of conventional χ^2 statistics and then generalize the analysis to the hyper-parameter technique.

B.1 χ^2 statistics

A conventional joint χ^2 analysis will minimize the following combined χ^2

$$\chi^2_{tot} = \sum_j \chi^2_j, \tag{B.1}$$

where each χ^2_n follows the chi-square distribution

$$f(\chi^2_n) = \frac{1}{2^{\frac{n}{2}}\Gamma\left(\frac{n}{2}\right)}(\chi^2_n)^{\frac{n}{2}-1}\exp(-\frac{1}{2}\chi^2_n). \tag{B.2}$$

It is easy to show that this chi-square distribution is properly normalized, i.e.

$$\int_0^\infty f(\chi^2_n)d\chi^2_n = 1, \tag{B.3}$$

and the expectation value and the variance are

$$E(\chi^2_n) = n,\ V(\chi^2_n) = 2n. \tag{B.4}$$

Therefore, the minimum χ^2 value of a properly constrained model should satisfy the following relation

$$1-\frac{\sqrt{V(n)}}{E(n)} \leq \frac{\chi^2_{\text{min}}}{E(\chi^2_n)} \leq 1+\frac{\sqrt{V(n)}}{E(n)}. \tag{B.5}$$

For the χ^2 with order n, this is

$$1-\sqrt{\frac{2}{n}} \leq \frac{\chi^2_{\text{min}}}{n} \leq 1+\sqrt{\frac{2}{n}}. \tag{B.6}$$

If the $\chi^2_{\text{min}}/n \geq 1+\sqrt{\frac{2}{n}}$, we can say that the model does not provide a good fit to the data, whereas if $\chi^2_{\text{min}}/n \leq 1-\sqrt{\frac{2}{n}}$, we say that the model overfits the data, which may mean that the model has redundant free parameters.

If there are m constraints on the n random variables, then χ^2_n still follows the chi-square distribution, but with order $n-m$ [243]

$$f(\chi^2_n) = \frac{1}{2^{\frac{n-m}{2}}\Gamma\left(\frac{n-m}{2}\right)}(\chi^2_n)^{\frac{n-m}{2}-1}\exp(-\frac{1}{2}\chi^2_n). \tag{B.7}$$

It is straightforward to verify, that the shape of the distribution does not change, but the expectation value and the variance are changed simply as $n \to n-m$.

B.2 Hyper-parameter χ^2

The hyper-parameter approach to combining the constraints from different data sets can be useful in the case where the different data sets have different levels of systematics. To weight each data set, one should multiply each χ^2 by a free parameter,

$$\chi^2_{\text{hyper}} = \sum_j \alpha_j \chi^2_j, \tag{B.8}$$

where α_j is the weight parameter for each data set. One can marginalize these weight parameters in a Bayesian analysis, and in [205], the authors found that instead of minimizing the combined χ^2, one should instead minimize the following quantity

$$\chi^2_{\text{hyper}} = \sum_j n_j \ln \chi^2_j, \tag{B.9}$$

where n_j is the number of degrees of freedom for each data set. If we only consider one data set, the hyper-parameter statistic becomes

$$\chi^2_{\text{hyper}} = n \ln \chi^2_n. \tag{B.10}$$

From Eq. (B.2), using the following transformation

$$f_Y = f_X \left| \frac{dY}{dX} \right|, \tag{B.11}$$

one can show that the distribution of the hyper-parameter statistic is given by

$$g(\chi^2_{\text{hyper}}) = \frac{1}{n \cdot 2^{\frac{n}{2}} \Gamma\left(\frac{n}{2}\right)} \exp(\frac{1}{2}\chi^2_{\text{hyper}}) \exp(-\frac{1}{2}\exp(\frac{1}{n}\chi^2_{\text{hyper}})), \tag{B.12}$$

which has already been properly normalized. (When calculating the integral, one should use the transformation $\exp(\frac{x}{n}) = y$). One can then show that the expectation value and variance of the Hyper-parameter distribution is

$$E(\chi^2_{\text{hyper}}) = n\left(\ln 2 + \psi_0\left(\frac{n}{2}\right)\right), V(\chi^2_{\text{hyper}}) = n^2\psi_1\left(\frac{n}{2}\right), \tag{B.13}$$

where $\psi_n(x)$ is the "digamma function" defined as derivatives of the log Gamma function

$$\psi_n(x) = \frac{d^{n+1}}{dx^{n+1}} \ln \Gamma(x). \tag{B.14}$$

If there are m constraints on the n random variables (e.g. m parameters), then the distribution of the conventional χ^2_n follows Eq. (B.7). It is then easy to show that the form of the distribution is unchanged only if the χ^2_{hyper} is defined as

$$\chi^2_{\text{hyper}} = (n-m) \ln \chi^2_n. \tag{B.15}$$

Proof From Eqs. (B.7) and (B.11), one can derive the following PDF

$$\begin{aligned} g(\chi^2_{\text{hyper}}) &= f(\chi^2_n)\frac{d\chi^2_n}{d\chi^2_{\text{hyper}}} \\ &= f\left(\exp\left(\frac{\chi^2_{\text{hyper}}}{n-m}\right)\right)\frac{1}{n-m}\exp\left(\frac{\chi^2_{\text{hyper}}}{n-m}\right) \end{aligned}$$

$$
\begin{aligned}
&= \frac{1}{n-m}\exp\left(\frac{\chi^2_{\mathrm{hyper}}}{n-m}\right)\frac{1}{2^{\frac{n-m}{2}}\Gamma\left(\frac{n-m}{2}\right)} \\
&\quad \times \left[\exp\left(\frac{\chi^2_{\mathrm{hyper}}}{n-m}\right)\right]^{\frac{n-m}{2}-1}\exp\left(-\frac{1}{2}\exp\left(\frac{\chi^2_{\mathrm{hyper}}}{n-m}\right)\right) \\
&= \frac{1}{n-m}\frac{1}{2^{\frac{n-m}{2}}\Gamma\left(\frac{n-m}{2}\right)}\exp\left(\frac{\chi^2_{\mathrm{hyper}}}{2}\right)\exp\left(-\frac{1}{2}\exp\left(\frac{\chi^2_{\mathrm{hyper}}}{n-m}\right)\right).
\end{aligned}
\tag{B.16}
$$

Therefore, in the case of m constraints, the distribution keeps its form, and the expectation value and variance become

$$
E(\chi^2_{\mathrm{hyper}}) = (n-m)\left(\ln 2 + \psi_0\left(\frac{n-m}{2}\right)\right), V(\chi^2_{\mathrm{hyper}}) = (n-m)^2\psi_1\left(\frac{n-m}{2}\right). \tag{B.17}
$$

Thus, to ensure that the form of the χ^2_{hyper} distribution function is unchanged, the χ^2_{hyper} needs to be defined as

$$
\chi^2_{\mathrm{hyper}} = \sum_j n_j \ln \chi^2_{n_j}, \tag{B.18}
$$

where $n_j = n_{\mathrm{data}} - m$ is the number of degree of freedom.

The hyper-parameter approach is an objective way to weight each data set when producing joint constraints. The value of the weight is simply the value of the effective hyper-parameter, which is defined as [205]

$$
\alpha_{\mathrm{A}} = \frac{n_{\mathrm{A}}}{\chi^2_{\mathrm{A}}}, \tag{B.19}
$$

where A specifies a particular data set. Therefore, the larger the value of α, the larger the weight that the particular data set takes (see Table 4.3).

Appendix C

Analytic formulas of the correlated Window Function $f_{12}(k)$

The correlated window function $f_{12}(k)$

$$f_{12}(k) = \int \frac{d^2\hat{k}}{4\pi} \left(\hat{\mathbf{r}}_1 \cdot \hat{\mathbf{k}}\right) \left(\hat{\mathbf{r}}_2 \cdot \hat{\mathbf{k}}\right) \times \exp\left(ik\hat{\mathbf{k}} \cdot (\mathbf{r}_1 - \mathbf{r}_2)\right), \tag{C.1}$$

can be calculated analytically, by transforming it into harmonic space and using the property of spherical harmonics. The final integral should only depend on: (a) the angle α between $\mathbf{r}_1$ and $\mathbf{r}_2$ (therefore $\mathbf{r}_1$ and $\mathbf{r}_2$ should be symmetric); (b) r_1 and r_2 (amplitude of the vector); (c) k ($\mathbf{k}$'s amplitude). Therefore, we can specify $r_1 = (0, 0, 1)$, $r_2 = (0, \sin\alpha, \cos\alpha)$, where α is the relative angle between r_1 and r_2. Therefore,

$$\mathbf{A} = \mathbf{r}_1 - \mathbf{r}_2 = (0, -r_2 \sin\alpha, r_1 - r_2 \cos\alpha). \tag{C.2}$$

So its direction and amplitude become

$$\hat{\mathbf{A}} = \frac{1}{A}(0, -r_2 \sin\alpha, r_1 - r_2 \cos\alpha), \tag{C.3}$$

and

$$A = [r_1^2 + r_2^2 - 2r_1 r_2 \cos\alpha]^{\frac{1}{2}}. \tag{C.4}$$

We can set

$$\hat{\mathbf{k}} =(\sin\theta\cos\phi, \sin\theta\sin\phi, \cos\theta), \tag{C.5}$$

therefore,

$$\hat{\mathbf{k}}\cdot\hat{\mathbf{A}} =\frac{1}{A}\left((-r_2\sin\alpha)\sin\theta\sin\phi + (r_1 - r_2\cos\alpha)\cos\theta\right). \tag{C.6}$$

Now we can use spherical harmonic function $Y_{lm}(\theta,\phi)$ to decompose the integrand as follows.

$$\begin{aligned}\left(\hat{\mathbf{r}}_1\cdot\hat{\mathbf{k}}\right)\left(\hat{\mathbf{r}}_2\cdot\hat{\mathbf{k}}\right) &= \cos\theta(\sin\alpha\sin\theta\sin\phi + \cos\alpha\cos\theta)\\ &= i\sqrt{\frac{2\pi}{15}}\sin\alpha\left(Y_{2,1}+Y_{2,-1}\right) + \frac{4}{3}\sqrt{\frac{\pi}{5}}\cos\alpha Y_{2,0} + \frac{1}{3}\cos\alpha,\end{aligned} \tag{C.7}$$

$$\exp(ik\hat{\mathbf{k}}\cdot(\mathbf{r_1}-\mathbf{r_2})) = \sum_l i^l(2l+1)j_l(kA)P_l(\hat{\mathbf{k}}\cdot\hat{\mathbf{A}}), \tag{C.8}$$

in which we can just consider $l = 0, 2$ two terms in the summation. The reason is that the mixing angle between $\mathbf{k}$ and $\mathbf{A}$ just causes the mixing between different m modes in the spherical harmonics in Eq. (C.8), so the final non $l = 0$ and $l = 2$ terms vanish due to the orthogonality. Therefore, Eq. (C.8) becomes

$$\exp(ik\hat{\mathbf{k}}\cdot(\mathbf{r_1}-\mathbf{r_2})) = j_0(kA) - 5j_2(kA)P_2(\hat{\mathbf{k}}\cdot\hat{\mathbf{A}}), \tag{C.9}$$

where $j_l(kA)$ is spherical bessel function.

$$\begin{aligned}P_2(\hat{\mathbf{k}}\cdot\hat{\mathbf{A}}) &= \frac{1}{2}\left(3(\hat{\mathbf{k}}\cdot\hat{\mathbf{A}})^2 - 1\right)\\ &= -\frac{3}{2A^2}\sqrt{\frac{2\pi}{15}}(r_2\sin\alpha)^2\left(Y_{2,2}+Y_{2,-2}\right)\\ &+ \frac{2}{A^2}\sqrt{\frac{\pi}{5}}\left((r_1 - r_2\cos\alpha)^2 - \frac{1}{2}(r_2\sin\alpha)^2\right)Y_{20}\\ &- \frac{3}{A^2}(r_2\sin\alpha)(r_1 - r_2\cos\alpha)\\ &\times i\sqrt{\frac{2\pi}{15}}\left(Y_{2,1}+Y_{2,-1}\right).\end{aligned} \tag{C.10}$$

Note that there is no zero order term in $P_2(\hat{\mathbf{k}}\cdot\hat{\mathbf{A}})$. Then we use the orthogonality property of Y_{lm} $\int d^2\hat{\mathbf{k}}Y_{lm}Y^*_{l'm'} = \delta_{ll'}\delta_{mm'}$ and $Y^*_{lm} = Y_{l,-m}(-1)^m$ and get the final result

$$f_{12}(k) = \frac{1}{3}\cos\alpha(j_0(kA) - 2j_2(kA)) + \frac{1}{A^2}j_2(kA)r_1r_2\sin^2\alpha. \tag{C.11}$$

It is clear that this integration has the three properties we listed above and the window function f_{12} depends only on (r_1,r_2,k,α). This is an independent and simplified but equivalent result to Eq.(9.32) in [44].

References

[1] D. H. Spergel et al., ApJS.148 (2003) 175-194. 1, 55, 56, 58, 72

[2] D. N. Spergel et al., ApJS, 170 (2007) 377. 1, 4

[3] E. Komatsu et al., ApJS. 180 (2009) 330. x, xii, 1, 4, 20, 27, 28, 33, 70, 71, 74

[4] S. Cole et al., MNRAS.362 (2005) 505. 1, 2

[5] M. Tegmark et al. ApJ.606 (2004) 702. x, 1, 2, 30

[6] D. Eisenstein et al. ApJ. 633 (2005) 560. 1, 2

[7] S. Perlmutter et al., ApJ.517 (1999) 565. 1

[8] A. Riess, ApJ. 607 (2004) 665. 1

[9] P. Astier, Astron.Astrophys. 447 (2006) 31. 1

[10] C. Reichardt et al. ApJ. 694 (2009) 1200. 1, 75

[11] D. Bacon, R. Massey, A. Refregier, R. Ellis, MNRAS. 344 (2003) 673. 1

[12] C. Heymans et al., MNRAS. 361 (2005) 160. 1

[13] E. Semboloni et al., Astron.Astrophys., 452 (2006) 51. 1

[14] S. Allen, R. Schmidt, A. Fabian, H. Ebeling, MNRAS. 342 (2003) 287. 1

[15] N. Bahcall, P. Bode, ApJ. 588 (2003) L1-L4. 1

[16] A. Voevodkin, A. Vikhlinin, ApJ. 601 (2004) 610. 1

[17] S. Allen et al., MNRAS. 383 (2008) 879. 1

[18] R. Croft et al., ApJ. 581 (2002) 20. 1

[19] M. Viel, M. Haehnelt, V. Springel, MNRAS. 354 (2004) 684. 1

[20] T. Jena et al., MNRAS. 361 (2005) 70. 1

[21] U. Seljak et al., Phys. Rev. D71 (2005) 103515. 1

[22] A. Guth, Phys. Rev. D 23 (1981) 347. 1

[23] A. Linde, Reports of Progress in Physics, 47 (1984) 925. 1

[24] U. Seljak and M. Zaldarriaga, ApJ 469 (1996) 437. 2, 33

[25] http://camb.info; A. Lewis, A. Challinor and A. Lasenby, ApJ, 538 (2000) 473. 2, 33, 92

[26] P. J. E. Peebles, AJ, 75 (1970) 13. 1

[27] The Planck Collaboration, 2005, *'The Scientific Programme of Planck'*, eds. G. Efstathiou, C. Lawrence, and J. Tauber, ESA-SCI(2005), ESA Publications. 1, 17, 28, 29, 30, 50, 51, 76, 79, 92, 141

[28] H. T. Nguyen. et al., Proc. SPIE, 7020 (2008) 70201F. 1, 92

[29] J. A. Rubino-Martin et al., arXiv: 0810.314; http://www.iac.es/project/cmb/quijote/. 1, 92

[30] http://bolo.berkeley.edu/POLARBEAR/index.html. 1, 50, 92, 142

[31] D. Samtleben, arXiv: 0802.2657; http://quiet.uchicago.edu/. 1, 50, 92, 142

[32] http://groups.physics.umn.edu/cosmology/ebex/index.html. 2, 30, 92

[33] B. P. Crill, et al., arXiv:0807.1548. 2, 30, 92, 142

[34] E. Hubble, Proceedings of the National Academy of Science, 15 (1929) 168. 4

[35] W. Freedman et al., ApJ, 553 (2001) 47. 4

[36] G. Gamov, Physical Review, 70 (1946) 572. 4

[37] M. Pettini and D. Browen, ApJ, 560 (2001) 41. 4

[38] K. Olive and E. Skillman, ApJ, 617 (2004) 29. 4

[39] A. Penzias and R. Wilson, ApJ, 142 (1965) 419. 4

[40] R. Dicke, P. Peebles, R. Roll, and D. Wilkinson, ApJ, 142 (1965) 414. 4

[41] G. Smoot et al., ApJ, 396 (1992) L1. 4, 55

[42] A. Riotto, astro-ph/0210162. ix, 4, 8, 11, 12, 14, 15, 95, 96

[43] H. Peiris, Cosmology Lecture Notes, http://camd05.ast.cam.ac.uk/Cosmology/. 6

[44] S. Dodelson, Modern Cosmology, Academic Press 2003. x, 6, 16, 19, 22, 23, 31, 34, 36, 43, 45, 151

[45] N. Kaloper, A. Linde and R. Bousso, Phys. Rev. D 59 (1999) 043508. 6

[46] D. Baumann and H. Peiris, 0810.3022 [astro-ph]. 7, 19, 30

[47] N. T. Jones, H. Stoica and S. H. Tye, JHEP 0207, (2002) 0513. 16, 88

[48] S. Sarangi and S. H. Tye, Phys. Lett. B 536, (2002) 185. 16, 88

[49] L. McAllister and E. Silverstein, Gen. Rel. Grav. 40 (2008) 565. 16

[50] Y.Z. Ma and X. Zhang, JCAP 03 (2009) 006. 16, 87, 111

[51] M. Nolta et al., ApJS, 180 (2009) 296. 27

[52] D. Larson et al., ApJS.192 (2011) 16. ix, x, 19, 27

[53] S. Dodelson, AIP Conf. Proc. 689 (2003) 184-196. x, 27

[54] G. Efstathiou and S. Gratton, JCAP 01 (2009) 011, 0903.0345 [astro-ph] 30, 98

[55] G. Efstathiou, S. Gratton and F. Paci, MNRAS 397 (2009) 1355-1373, 0902.4803 [astro-ph]. 30, 98

[56] D. Baumann et al., AIP Conf.Proc.1141 (2009) 10-120. 10, 11, 12, 25, 27, 29, 30, 95, 96

[57] J. M. Bardeen, Phys. Rev. D 22 (1980) 1882. 10

[58] D. Fixsen et al., ApJ. 473 (1996) 576, astro-ph/9605054. 19

[59] D. Fixsen, J. Mather, ApJ, 581 (2002) 817. 19

[60] J. Mather et al., ApJ, 420 (1994) 439. 19

[61] C. Bennett et al., ApJS. 148 (2003) 1, astro-ph/0302207. 55, 75, 87

[62] A. Challinor, Large Scale Structure formation Notes, Cambridge, 2008. ix, 10, 11, 12, 16, 17, 20, 21, 22, 23, 24, 25, 34, 35, 37

[63] D. H. Lyth, Phys. Rev. Lett. 78 (1997) 1861, hep-ph/9606387. 13, 97

[64] G. Efstathiou and K. J. Mack, JCAP 0505 (2005) 008, astro-ph/0503360. 13, 97

[65] J. Silk, Astrophys. J. 151 (1968) 459. 25

[66] S. Dodelson, W. H. Kinney and E. W. Kolb, Phys. Rev. D. 56 (1997) 3207, astro-ph/9702166. ix, 15

[67] A. Albrecht and P. J. Steinhardt, Phys. Rev. Lett 48 (1982) 1220. 14, 15

[68] A. D. Linde, Phys. Lett. B 129 (1983) 177. 14, 15

[69] K. Freese, J. Frieman and A. Olinto, Phys. Rev. Lett. 65 (1990) 3233. 15

[70] A. Riotto, Nucl. Phys. B 515 (1998) 413. 15

[71] A. D. Linde and A. Riotto, Phys. Rev. D 56 (1997) 1841. 15

[72] E. Komatsu et al., ApJS, 192 (2011) 18. ix, x, xv, 11, 15, 18, 20, 28, 29, 30, 59, 87, 88, 92, 96, 98, 101, 103, 104, 109, 111, 119, 127, 130, 132

[73] M. Liguori et al., Phys. Rev. D 73 (2006) 043505. 17

[74] G. I. Rigopoulos, E. P. S. Shellard, and B. J. W. van Tent. Phys. Rev., D 73 (2006)083522. 17

[75] P. P. Avelino, E. P. S. Shellard, J. H. P. Wu, and B. Allen, ApJ., 507 (1998) L101. 17

[76] W. Hu and M. J. White, New Astrono. 2 (1997) 323, astro-ph/9706147. ix, 25, 26, 79

[77] A. G. Riess, et al. ApJ, 708 (2010) 645. 29

[78] W. J. Percival, et al. MNRAS 401 (2010) 2148. 29

[79] T. Padmanabhan, Structure formation in the universe, Cambridge University Press 1993. 31, 34, 36, 38, 39, 41

[80] H. J. Mo, F. V. D. Bosch and S. White, Galaxy Formation and Evolution, Cambridge University Press, 2010. 39

[81] D. Eisenstein and W. Hu, ApJ, 496 (1998) 605. 33

[82] R. K. Sheth and G. Tormen, MNRAS, 308 (1999) 119. 45

[83] A. Loeb, How did the first stars and galaxies form?, Princeton University Press 2010. 41, 43, 45, 46, 49, 50

[84] M. J. Rees and J. P. Ostriker, MNRAS 179 (1977) 541-559. 46

[85] D. Lynden-Bell, MNRAS 136 (1967) 101. 41

[86] W.H.Press and P.Schechter, ApJ 187 (1974) 425. 43

[87] http://adsabs.harvard.edu/abs/2007hsct.confE..69V xi, 44

[88] J. R. Bond, S. Cole, G. Efstathiou and N. Kaiser, ApJ 379 (1991) 440. 45

[89] S. White, G. Efstathiou and C. Frenk, MNRAS, 262 (1993) 1023. 45

[90] J. Primack, 0909.2021 [astro-ph]. 46, 47, 48, 49

[91] M. Viel et al., Phys. Rev. Lett, 100 (2008) 041304. 48

[92] A. Kravtsov, 0906.3295 [astro-ph]. 46

[93] H. Pagels and J. R. Primack, Phys. Rev. Lett, 48 (1982) 223-226. 47

[94] F. Zwicky, Helvetica Physica Acta 6 (1933) 110C127; F. Zwicky, ApJ 86 (1937) 217. 46

[95] V. Rubin, W. K. Ford, ApJ 159 (1970) 379. 46

[96] S. Dodelson and L. Widrow, Phys. Rev. Lett. 72 (1994) 17-20. 48

[97] T. Asaka, M. Laine and M. Shaposhnikov, JHEP 0701 (2007) 091. 48

[98] A. Boyarsky et al., Phys. Rev. Lett. 97 (2006) 261302. 48

[99] A. Boyarsky, J. Nevalainen and O. Ruchayskiy, Astron. Astrophys. 471 (2007) 51-57. 48

[100] J. Pritchard and A. Loeb, Phys. Rev. D 78 (2008) 103511. 50

[101] G. Steigman and M. S. Turner, Nucl. Phys. B 253 (1985) 375-386. 47

[102] M. Dine, W. Fiscler and M. Srednicki, Phys. Lett. B, 104 (1981) 199. 47

[103] M. Kustler, G. Raffelt and B. Beltran, editors, Axions: Theory, cosmology and experimental searches, Springer Lecture Notes in Physics 741, Berlin: Springer 2008. 47

[104] J. Simon and M. Geha, ApJ 670 (2007) 313-331. xi, 47

[105] L. Strigari et al., Nature 454 (2008) 1096-1097. 47

[106] W.J.G. de Blok et al.,AJ, 136 (2008) 2648-2719. 48

[107] E. Ramano-Diaz, I. Sholsman, C. Heller, and Y. Hoffman, ApJ, 685 (2008) L105-L108. 48

[108] E. Ramano-Diaz, I. Sholsman, C. Heller, and Y. Hoffman, ApJ 702 (2009) 1250-1267. 48

[109] O. Y. Gnedin and H. Zhao,MNRAS, 333 (2002) 299-306. 49

[110] S. Mashchenko, J. Wadsley, and H. M. P. Couchman, Science, 319 (2008) 174-177. 49

[111] J.E. Gunn and B.A. Peterson, ApJ, 142 (1965) 1633-1641. 50

[112] R.H. Becker et al., AJ 122 (2001) 2850-2857. 50

[113] http://www.lofar.org/ 50

[114] P. Steinhardt and N. Turok, Science, 296 (2002) 1436-1439. 50

[115] LHC: http://lhc.web.cern.ch 51

[116] CDMS: http://cdms.berkeley.edu 51

[117] http://bigboss.lbl.gov 51

[118] G. Efstathiou, Nuovo Cim. B 122 (2007) 1423-1435, 0712.1513 [astro-ph]. 51

[119] E. L. Wright et al., ApJ, 396 (1992) L13. 55

[120] G. Hinshaw et al., ApJ, 464 (1996) L25. 55

[121] G. Efstathiou, MNRAS, 348 (2004) 885. 55, 56, 58, 59, 60, 61, 68

[122] G. Hinshaw et al., ApJS, 148 (2003) 135. 55

[123] G. Hinshaw et al., ApJS, 180 (2009) 225. 56

[124] C. J. Copi, D. Huterer, D. J. Schwarz, G. D. Starkman, Phys. Rev. D, 75 (2007) 3507. 56, 60, 69

[125] C. J. Copi, D. Huterer, D. J. Schwarz, G. D. Starkman, MNRAS, 399 (2009) 295. 56, 57, 59, 60, 69, 72, 73, 74

[126] M. Tegmark, A. de Oliveira-Costa, A. J. Hamilton, Phys. Rev. D, 68 (2003) 13523. 56, 75

[127] D. J. Schwarz, G. D. Starkman, D. Huterer, C. J. Copi, Phys. Rev. Lett. 93 (2004) 1301. 56

[128] K. Land, J. Magueijo, Phys. Rev. Lett. 95 (2005) 071301. 56, 75

[129] K. Land, J. Magueijo, MNRAS, 362 (2005) 838. 56

[130] A. de Oliveira-Costa, M. Tegmark, M. Zaldarriaga, A. Hamilton, Phys. Rev. D, 69 (2004) 063516. 56

[131] A. de Oliveira-Costa, M. Tegmark, Phys. Rev. D, 74 (2006) 023005. 56, 63, 67

[132] C. L. Francis, J. A. Peacock, MNRAS 406 (2010) 14, 0909.2495 [arXiv:astro-ph]. xii, 56, 72, 73

[133] C. L. Bennett et al., ApJS 192 (2010) 17, 1001.4758 [arXiv:astro-ph]. 56, 76

[134] A. Pontzen, H. V. Peiris, Phys. Rev. D, 81 (2010) 103008, 1004.2706 [arXiv:astro-ph]. 56, 58, 61, 74

[135] S. Basak, A. Hajian, T. Souradeep, Phys. Rev. D, 74 (2006) 021301. 57

[136] G. Efstathiou, MNRAS, 349 (2004) 603. 58, 61, 67, 86

[137] K. M. Gorski, ApJ, 622 (2005) 759. 58, 79

[138] B. Gold et al., ApJS 180 (2009) 265. 59

[139] E. J. Groth, P. J. E. Peebles, ApJ, 310 (1986) 499. 61

[140] S. D. Landy, A. Szalay, ApJ, 412 (1993) 64L. 61

[141] A. Hamilton, ApJ, 417 (1993) 19. 61

[142] S. J. Maddox, G. Efstathiou, W. J. Sutherland, MNRAS, 283 (1996) 1227. 61

[143] P. Bielwicz, K. M. Gorski, A. J. Banday, MNRAS, 355 (2004) 1283. 62

[144] B. D. Wandelt, D. L. Larson, A. Lakshminarayanan, Phys. Rev. D, 70 (2004) 3511. 62

[145] H. K. Eriksen et al., ApJS, 155 (2004) 227. 62

[146] K. T. Inoue, P. Cabella, E. Komatsu, Phys. Rev. D, 77 (2008) 123539. 62

[147] K. Gorski, ApJ, 430 (1994) L85. 62

[148] K. Gorski et al., ApJ, 430 (1994) L89. 62

[149] D. J. Mortlock, A. D. Challinor, M. P. Hobson, MNRAS, 330 (2002) 405. 62

[150] M. Tegmark, Phys. Rev. D, 55 (1997) 5985. 67

[151] A. Hajian, 2007, arXIv:astro-ph/0702723. 69

[152] R. K. Sachs, A. M. Wolfe, ApJ, 147 (1967) 73. 73

[153] V. Mukhanov, Physical Foundations of Cosmology, Cambridge University Press 2005. 73

[154] T. Jarrett, Publications of the Astronomical Society of Australia, 21 (2004) 396. 73

[155] G. Hinshaw et al., ApJS, **170**, 288 (2007), astro-ph/0603451. 75, 87

[156] M.L. Brown et al., ApJ, **705**, 978 (2009), arXiv:0906.1003 [astro-ph]. 75, 87, 88, 91, 92

[157] The ACT Collaboration: J.W. Fowler et al., ApJ 722 (2010) 1148 , arXiv:1001.2934 [astro-ph]. 75

[158] N.R. Hall et al., ApJ, **718**, 632 (2010), arXiv:0912.4315 [astro-ph]. 75, 126

[159] P. Bielewicz, K. M. Gorski and A. J. Banday, Mon. Not. Roy. Astron. Soc. **355**, 1283 (2004), astro-ph/0405007. 75

[160] C. J. Copi, D. Huterer, D. J. Schwarz and G. D. Starkman, Mon. Not. Roy. Astron. Soc. **367**, 79 (2006), astro-ph/0508047. 75

[161] F. K. Hansen et al., ApJ 704 (2009) 1448, arXiv: 0812.3795 [astro-ph]. 75

[162] H. K. Eriksen et al., Astrophys. J. **605**, 14 (2004), astro-ph/0307507. 75

[163] M. Cruz et al., ApJ **655**, 11 (2007), astro-ph/0603859. 75

[164] M. Cruz et al., Science **318**, 1612 (2007), arXiv: 0710.5737. 75

[165] C. J. Copi et al., Adv. Astron. Astrophys. **2010** 2010 847541, arXiv: 1004.5602 [astro-ph]. 76

[166] L. Ackerman, S. M. Carroll and M. B. Wise, Phys. Rev. D **75**, 083502 (2007), astro-ph/0701357. 76

[167] B. Himmetoglu, C.R. Contaldi, and M. Peloso, Phys. Rev. D **79**, 063517 (2009), arXiv:0812.1231 [astro-ph]. 76

[168] B. Himmetoglu, C.R. Contaldi, and M. Peloso, Phys. Rev. Lett. **102**, 111301 (2009), arXiv: 0809.2779 [astro-ph]. 76

[169] A. L. Erickcek, M. Kamionkowski and S. M. Carroll, Phys. Rev. D. **78**, 123520 (2008), arXiv: 0806.0377 [astro-ph]. 76

[170] A. L. Erickcek, C.M. Hirata, and M. Kamionkowski Phys. Rev. D. **80**, 083507 (2009), arXiv:0907.0705 [astro-ph]. 76

[171] C. Gordon, W. Hu, D. Huterer and T. Crawford, Phys. Rev. D **72**, 103002 (2005), astro-ph/0509301. 76

[172] C. Dvorkin, H. V. Peiris and W. Hu, Phys. Rev. D **77**, 063008 (2008), arXiv: 0711.2321 [astro-ph]. 76

[173] N. E. Groeneboom and H. K. Eriksen, ApJ 690 (2009) 1807, arXiv: 0807.2242 [astro-ph]. 76, 136

[174] D. Hanson and A. Lewis, Phys. Rev. D, **80**, 063004 (2009), arXiv: 0908.0963 [astro-ph]. 76, 77, 78, 79, 86

[175] N. E. Groeneboom, L. Ackerman, I. K. Wehus, and H. K. Eriksen, ApJ 722 (2010) 452, arXiv: 0911.0150 [astro-ph]. 76

[176] D. Hanson, A. Lewis, and A. Challinor, Phys. Rev. D., **81**, 103003 (2010), arXiv:1003.0198 [astro-ph]. 76, 82, 85

[177] K.M. Huffenberger, B.P. Crill, A.E. Lange, K.M. Gorski, C.R. Lawrence, Astron. Astrophys. 510, A58, 2010, arXiv: 1007.3468 [astro-ph]. 76

[178] A. R. Pullen and M. Kamionkowski, Phys. Rev. D **76** 103529 (2007), arXiv:0709.1144 [astro-ph]. 76, 80

[179] M. Zaldarriaga, Phys. Rev. D., **55**, 1822 (1997), astro-ph/9608050. 81

[180] K. M. Smith, O. Zahn, O. Doré, Phys. Rev. D., **76**, 043510 (2007), arXiv:0705.3980 [astro-ph]. 86

[181] A. Lewis and A, Challinor, Phys. Rept. 429 (2006) 1-65. 92

[182] H. C. Chiang et al., Astrophys. J. 711 (2010) 1123. 87, 88, 91, 92, 93, 97, 115

[183] J. Kovac et al., Nature (London) 420 (2002) 772. 87

[184] A. C. S. Readhead et al., Science 306 (2004) 836. 87

[185] C. Bischoff et al. (CAPMAP Collaboration), ApJ. 684 (2008) 771. 87

[186] W. C. Jones et al., ApJ. 647 (2006) 823. 87

[187] J. H. P. Wu et al., ApJ. 665 (2007) 55. 87

[188] A. Borde and A. Vilenkin, Phys. Rev. Lett. 72 (2004) 3305. 87

[189] V. F. Mukhanov, H. A. Feldman and R. H. Brandenberger, Phys. Rept. 215 (1992) 203; R. H. Brandenberger, Lect. Notes Phys. 646 (2004) 127. 87

[190] S. Kachru, R. Kallosh, A. Linde and S. P. Trivedi, Phys. Rev. D, 68 (2003) 046005. 87, 111

[191] S. Kachru, R. Kallosh, A. Linde, J. M. Maldacena, L. McAllister and S. P. Trivedi, JCAP 0310 (2003) 013. 87, 111

[192] M. Bojowald, Living Rev. Relativity, 11 (2008) 4. 88

[193] W. Zhao, D. Baskaran and L. P. Grishchuk, Phys. Rev. D 79 (2009) 023002; 80 (2009) 083005 (2009); W. Zhao, Phys. Rev. D 79 (2009) 063003. 88

[194] S. Chandrasekhar, *in Radiative Transfer* (Dover: New York, 1960). 89

[195] M. Zaldarriaga and U. Seljak, Phys. Rev. D, 55 (1997) 1830. 89

[196] http://lambda.gsfc.nasa.gov/. ix, 5, 91

[197] http://bicep.caltech.edu/. 91

[198] http://find.uchicago.edu/quad/. 91

[199] B-Pol Collaboration, Exper. Astron. 23 (2009) 5; http://www.b-pol.org/index.php. 92

[200] http://cmbpol.kek.jp/litebird/. 92

[201] D. Baumann et al., AIP Conf. Proc. 1141 (2009) 10. 92, 101, 141, 142, 143

[202] U. Seljak and C. M. Hirata, Phys. Rev. D, 69 (2004) 043005. 92, 144

[203] http://www.sfu.ca/ levon/cmbact.html. 92, 112

[204] L. Pogosian and T. Vachaspati, Phys. Rev. D, 60 (1999) 083504. 112

[205] O. Lahav et.al, Mon. Not. Roy. Astron. Soc. 315 (2000) L45. 93, 94, 146, 148

[206] M. P. Hobson, S. L. Bridle, O. Lahav, Mon. Not. Roy. Astron. Soc. 335 (2002) 377. 93

[207] M. G. Kendall and A. Stuart, The Advanced Theory of Statistics, Volume II (Griffin, London, 1969). 94, 95

[208] M. Tegmark, A. Taylor and A. Heavens, Astrophys. J. 480 (1997) 22; M. Tegmark, Phys. Rev. Lett. 79 (1997) 3806. 94, 95

[209] M. Zaldarriaga, D. Spergel and U. Seljak, Astrophys. J. 488 (1997) 1. 94

[210] A. H. Jaffe, M. Kamionkowski and L. Wang, Phys. Rev. D, 61 (2000) 083501. 94

[211] L. P. Grishchuk, Zh. Eksp. Teor. Fiz. 67 (1974) 825 (1974) [Sov. Phys. JETP 40 (1975) 409 (1975)]. 95

[212] L. P. Grishchuk, 'Discovering Relic Gravitational Waves in Cosmic Microwave Background Radiation', chapter in *General Relativity and John Archibald Wheeler*, Eds. I. Ciufolini and R. Matzner (Springer, 2010, 151-199) [arXiv: 0707.3319]. 95

[213] A. R. Liddle, D. H. Lyth, Phys. Rep. 231 (1993) 1. 96, 102

[214] W. Zhao, D. Baskaran and L. P. Grishchuk, Phys. Rev. D, 82 (2010) 043003, 1005.4549 [arXiv:astro-ph]. 98

[215] W. Zhao and D. Baskaran, Phys. Rev. D 79 (2009) 083003; W. Zhao and W. Zhang, Phys. Lett. B 677 (2009) 16. 101

[216] L. P. L. Colombo, E. Pierpaoli and J. R. Pritchard, arXiv: 0811.2622. 101

[217] H. V. Peiris et al., Astrophys. J. Suppl. 148 (2003) 213. 103

[218] L. Alabidi and D. Lyth, JCAP, 0605 (2006) 016; L. Alabidi and D. Lyth, JCAP, 0608 (2006) 013. 104

[219] A. Sen, J. Math. Phys. 22 (1981) 1781. 105

[220] A. Ashtekar, Phys. Rev. Lett. 57 (1986) 2244. 105

[221] J. Grain and A. Barrau, Phys. Rev. Lett. 102 (2009) 081301. 105, 107, 108

[222] J. Mielczarek, T. Cailleteau, J. Grain and A. Barrau, Phys. Rev. D, 81 (2010) 104049. 105, 106, 107, 108

[223] P. Singh, K. Vandersloot and G. V. Vereshchagin, Phys. Rev. D, 74 (2006) 043510. 105

[224] K. A. Meissner, Class. Quant. Grav. 21 (2004) 5245. 105

[225] J. Mielczarek, M. Kamionka, A. Kurek and M. Szydlowski, arXiv: 1005.0814. 105

[226] A. Vilenkin and E. P. S. Shellard, Cosmic Strings and Other Topological Defects, Cambridge University Press 2000. 111

[227] G. R. Dvali and S. H. H. Tye, Phys. Lett. B, 450 (1999) 72. 111

[228] N. Kaiser and A. Stebbins, Nature, 310 (1984) 391. 111

[229] R. Battye and A. Moss, arXiv: 1005.0479. 111, 112, 113, 114

[230] L. Pogosian and M. Wyman, Phys. Rev. D, 77 (2008) 083509. 112

[231] R. R. Caldwell and B. Allen, Phys. Rev. D, 45 (1992) 3447. 113

[232] R. R. Caldwell, R. A. Battye and E. P. S. Shellard, Phys. Rev. D, 54 (1996) 7146. 113

[233] B. Abbott et al. [LIGO Scientific Collaboration], Phys. Rev. D, 80 (2009) 062002. 113

[234] M. Wyman, L. Pogosian and I. Wasserman, Phys. Rev. D, 72 (2005) 023513; L. Pogosian, I. Wasserman and M. Wyman, astro-ph/0604141. 113

[235] N. Bevis, M. Hindmarsh, M. Kunz and J. Urrestilla, Phys. Rev. Lett. 100 (2008) 021301. 113

[236] J. Sievers et al., arXiv: 0901.4540. 113

[237] L. Verde, H. Peiris and R. Jimenez, J. Cosmol. Astropart. Phys. 0601 (2006) 019. 143

[238] M. Tucci, E. Martinez-Gonzalez, P. Vielva and J. Delabrouille, Mon. Not. R. Astron. Soc. 360 (2005) 926. 143

[239] M. Zaldarriaga and U. Seljak, Phys. Rev. D, 58 (1998) 023003. 143

[240] M. Kesden, A. Cooray and M. Kamionkowski, Phys. Rev. Lett. 89 (2002) 011304. 143

[241] L. Knox and Y. S. Song, Phys. Rev. Lett. 89 (2002) 011303. 143

[242] W.Hu, M. M. Hedman and M. Zaldarriaga, Phys. Rev. D, 67 (2003) 043004. 143

[243] K. Riley, M. P. Hobson and S. J. Bence, Mathematica Methods for Physics and Engineering, Cambridge University Press 2005. 146

[244] R. Watkins, H. Feldman and M. Hudson, MNRAS 392, 743 (2009). xv, 117, 118, 119, 120, 122, 123, 129, 131, 136, 137, 138

[245] H. Feldman, R. Watkins and M. Hudson, MNRAS, 407, 2328 (2010). 117, 118, 120, 123, 136

[246] M. Turner, Phys. Rev. D. 44 (1991) 3737. 117, 123, 125

[247] D. Langlois and T. Piran, Phys.Rev. D 53 (1996) 2908-2919; D. Langlois, Phys. Rev. D54 (1996) 2447-2450. 117, 125

[248] A. Kashlinsky et al., Astrophys.J.,**686**, L49 (2008). 117, 123

[249] P. Erdogdu et al., MNRAS 373 (2006) 45-64, [astro-ph/0610005]. 117

[250] G. Lavaux, R. B. Tully, R. Mohayaee, S. Colombi, ApJ.709 (2010) 483-498, 0810.3658 [astro-ph]. 117

[251] J. P. Zibin and D. Scott, Phys. Rev. D **78**, 123529 (2008); A. L. Erickcek, S. M. Carroll and M. Kamionkowski, Phys. Rev. D **78**, 083012 (2008). 118

[252] K. Gorski, Astrophys.J., **332** (1988) L7. 118

[253] L. N. da Costa et al., Astron. J, 120 (2000) 95; M. Bernardi, et al., Astron. J, 123 (2002) 2990.; G. Wenger et al., Astron. J, 126 (2003) 2268. 119, 129

[254] J. L. Tonry, et al., Astrophys.J., 594 (2003) 1. 120, 129

[255] C. M. Springob, et al., ApJ Supp, 172 (2007) 599. 120, 129

[256] M. J. Hudson, PASP, 111 (1999) 57; M. J. Hudson, MNRAS, 352 (2004) 61. 120

[257] J. L. Tonry et al., Astrophys.J., 546 (2001) 681. 121, 129

[258] M. Colless et al., MNRAS 321 (2001) 277. 121

[259] R. Giovanelli et al., Astron. J, 116 (1998) 2632; D. A. Dale, Astron. J, 118 (1999) 1489. 121, 129

[260] J. A. Willick et al., ApJ 522 (1999) 647. 121

[261] E. Macaulay et al., arXiv:1010.2651 [astro-ph.CO]. 123

[262] A. Kashlinsky, et al., Astrophys.J. **712**, L81 (2010). 123

[263] L. P. Grishchuk, Ya. B. Zel'dovich, Astron. Zh. 55, 209 (1978). 123

[264] P. G. Castro, M. Douspis and P. G. Ferreira, Phys. Rev. D **68**, 127301 (2003). 125

[265] A. Kosowsky and T. Kahniashvili, arXiv:1007.4539 [astro-ph.CO]; L. Amendola et al., arXiv:1008.1183 [astro-ph.CO]. 125

[266] C. Gordon, K. Land and A. Slosar, MNRAS, 387, (2008), 371. 125

[267] S. Das, et al. arXiv:1009.0847 [astro-ph]. 126

[268] J. Dunkley, et al. arXiv:1009.0866 [astro-ph]. 126

[269] Fundamental Plane (FP) and Tully-Fisher (TF) are phenomenological procedures to determine the galaxies' intrinsic brightness and thus their distance independently of their redshift. 119, 120

[270] J. P. Ostriker and Y. Suto, ApJ, **348** (1990) 378-382. xv, 127, 128, 129, 130, 133

[271] M.A. Strauss, R. Cen and J.P. Ostriker, ApJ, **408** (1993) 389-402. 127, 129

[272] Y. Suto, N. Gouda and N. Sugiyma, ApJS, **74** (1990) 665-674; Y. Suto, R. Cen and J.P. Ostriker, ApJ, **395** (1992) 1-20. 127

[273] K. Nagamine, J.P. Ostriker and R. Cen, ApJ, **553** (2001) 513-527. 127, 128

[274] M. Gramann, N. A. Bahcall, R. Cen and J. R. Gott, ApJ, 441 (1995) 449-457. 128

[275] F. Atrio-Barandela, A. Kashlinsky and J. P. Mucket, ApJ, 601 (2004) 111-114. 128

[276] D. Tseliakhovich and C. Hirata, Phys. Rev. D 82 (2010) 083520; D. Tseliakhovich, R. Barkana and C. Hirata,1012.2574 [astro-ph.CO] 128

[277] J. Peebles, *Principles of Physical Cosmology*, 1993. Princeton. Univ. Press. 128

[278] D. H. Jones et al., MNRAS 399 (2009) 683-698. 130

[279] G. B. Zhao, L. Pogosian, A. Silvestri, and J. Zylberberg, Phys. Rev. D 79 (2009) 083513. 132

[280] T. Giannantonio, M. Martinelli, A. Silvestri, A. Melchiorri, JCAP, 04 (2010) 030. 132

[281] H. Liu and T. P. Li, ApJ, 732 (2011) 125. 136

[282] H. Liu, S. L. Xiong and T. P. Li, MNRAS 413 (2011) L96-L100. 136

[283] H. Liu, S. L. Xiong and T. P. Li, 1003.1073 [arXiv:astro-ph.CO]. 136

[284] C. A. Blake, F. B. Abdalla, S. L. Bridle and S. Rawlings, New Astron. Rev. 48 (2004) 1063-1077. 136

[285] J. Martin and C. Ringeval, Phys. Rev. D 69 (2004) 083515. 136

[286] K. Bhattacharya, S. Mohanty and R. Rangarajan, Phys. Rev. Lett. 96 (2006) 121302. 136

[287] Pedro G. Ferreira and J. Magueijo, Phys. Rev. D 78 (2008) 061301. 136

[288] N. Barnaby, Z. Huang, L. Kofman, and D. Pogosyan, Phys. Rev. D., 80 (2009) 043501. 136

[289] M. I. Schmoldt et al., Astron. J. 118 (1999) 1146-1160. 138

[290] E. L. Wright et al., Astron. J. 140 (2010) 1868. 138

[291] H. Wang et al., MNRAS, **394** (2009) 398-414. 139